# Modelling of Spray Combustion with Doubly Conditional Moment Closure

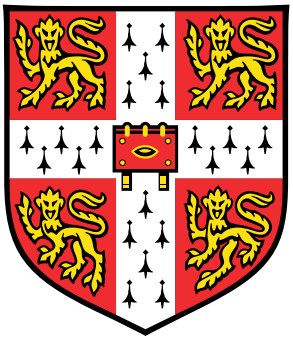

**Michael Philip Sitte**

Department of Engineering

University of Cambridge

This dissertation is submitted for the degree of

*Doctor of Philosophy*

Fitzwilliam College

25 September 2018

*To my parents*

# Declaration

I hereby declare that except where specific reference is made to the work of others, the contents of this dissertation are original and have not been submitted in whole or in part for consideration for any other degree or qualification in this, or any other university. This dissertation is my own work and contains nothing which is the outcome of work done in collaboration with others, except as specified in the text and Acknowledgements.

This dissertation was estimated to contain approximately 65 000 words and 64 figures.

Michael Philip Sitte
25 September 2018

# Acknowledgements

The work presented in this dissertation could not have been carried out without the help of many people, to whom I am very grateful. First and foremost I would like to express my gratitude to Prof. Epaminondas Mastorakos for his continuous support and guidance throughout my PhD. I admire his expertise and enthusiasm for Science, which have profoundly shaped my own approach to research. I am thankful for his suggestions and advice, and, in particular, for his optimism and trust in my abilities.

I would like to thank Prof. Swaminathan from Cambridge and Prof. Lindstedt from Imperial College for assessing this work and providing valuable suggestions. I would like to acknowledge all those who have participated in the development of the CMC code. Among the contributors to the CMC code, I am particularly grateful to Drs Andrea Giusti and Huangwei Zhang who have given me important guidance for the use of CFD and CMC. I am very thankful to Peter Benie for his help with computational resources – without his support the work presented in this thesis could not have been completed. I would also like to thank Prof. Nilanjan Chakraborty for his role in allocating the HPC resources used in this work through the UKCTRF.

I am grateful to a long list of people, whom I have been fortunate enough to meet during my studies at Cambridge. I would like to especially mention Anh Khoa Doan, Pedro Magalhães de Oliveira and Dr Andrea Giusti whom I value most highly on an academic and personal level. Of course, I am also thinking about Drs Huangwei Zhang, Ivan Langella, Luca Magri, Patton Allison and Zhi Chen, and the most recent additions to our lab, Ingrid El Helou, Jenna Foale and Savvas Gkantonas – they have been great colleagues and are dear friends to me, who strongly contributed towards making my PhD a truly exceptional experience. Several people outside of Engineering deserve to be mentioned as well: Adrián Báez Ortega, and Drs Liron Shmilovits and Marc Jansen have become great friends and broadened my point of view in many ways. I would also like to express very warm thanks to Dr Teresa Segura Garcia for her kindness and the support she has given me.

My eternal gratitude is to my parents, Sonja and Christian, and my sister Kerstin, for their constant support and unconditional love. My parents have always encouraged

my curiosity and interest in Science, which has sparked in me my passion for academic research and eventually led me to pursue this PhD.

The experimental data used for comparison in this thesis and information about experimental set-ups was kindly provided by Dr James Kariuki from Cambridge University and Dr Bruno Renou from INSA de Rouen.

I am thankful to the Gates Cambridge Trust (https://www.gatescambridge.org) for providing me with funding to undertake my doctoral research. This work used the ARCHER UK National Supercomputing Service (http://www.archer.ac.uk) with computational time provided by the UK Consortium on Turbulent Reacting Flows (UKCTRF).

# Abstract

Turbulent spray combustion is characterised by a strong coupling of evaporation, mixing and chemical reaction. This leads to a wide spectrum of combustion regimes, where self-propagating premixed flames and diffusion-controlled non-premixed flames may occur simultaneously within the same flame. The physical processes involved in spray combustion and their interaction take place over a broad range of scales, which makes their modelling in numerical simulations challenging.

This thesis presents the development of Doubly Conditional Moment Closure (DCMC) for the modelling of turbulent spray combustion. This modelling approach allows us to consider the effects of finite-rate chemistry and spray evaporation on the flame. Using a parametrisation of the flame structure, based on mixture fraction and reaction progress variable permits us to resolve premixed, non-premixed and intermediate combustion modes.

In the first part of this thesis, the model development is presented. With its foundation as a statistical model, DCMC does not require any strong assumption in terms of the combustion mode or regime. The DCMC equation is derived in a general form, which involves only a minimum number of modelling assumptions about the physical processes involved. Closure for the DCMC equation is discussed and a complete set of models is suggested. Since little experience exists in the modelling of doubly-conditional terms, the closure models were generalised from conventional Conditional Moment Closure (CMC) or adapted from other combustion models with similar parametrisation.

In the second part, the DCMC model is validated for two test flames. The DCMC model was first applied to the Cambridge spray jet flame using the Reynolds-Averaged Navier-Stokes (RANS) approach. This flame is characterised by significant pre-vaporisation and behaves as a propagating spray flame, with similarities to premixed flames, but with small-scale inhomogeneity in the gaseous mixture and the presence of liquid droplet interacting with the flame – a problem which requires the doubly-conditional description of the flame structure employed in the DCMC model. The role

of the spray terms on the flame structure and mixing field were assessed using RANS and promising results were obtained.

Finally, a Large-Eddy Simulation (LES) with DCMC acting as sub-grid scale combustion model was applied to the Rouen spray jet flame. LES-DCMC was found to accurately predict the spray statistics, lift-off height and flame shape. Small-scale effects of the spray on the flame could be resolved thanks to the doubly-conditional parametrisation of the flame structure. Temporal fluctuations and spatial variations of the flame structure were investigated. Spatial gradients of the doubly-conditional flame structure were small and convective transport was found to play a minor role on the flame structure compared to the effects of micro-mixing and chemical reaction in the DCMC equation. The findings of this work suggest that, besides spray combustion, DCMC shows great potential for the modelling of partially premixed flames and extinction.

# Publications

The work from this thesis has been published in the following articles:

### Journal articles

- Sitte, M. P. & Mastorakos, E. (2017). Modelling of spray flames with Doubly Conditional Moment Closure. *Flow, Turbulence and Combustion*, 99(3): 933–954.
- Sitte, M. P. & Mastorakos, E. (2019). Large Eddy Simulation of a spray jet flame using Doubly Conditional Moment Closure. *Combustion and Flame*, 199: 309–323.

### Conference paper

- Sitte, M. P. & Mastorakos, E. (2016). Modelling of spray flames with Doubly Conditional Moment Closure. *11th International ERCOFTAC Symposium on Engineering Turbulence Modelling and Measurements (ETMM)*, 21–23 September 2016, Palermo, Italy.

# Table of contents

# List of figures

# Nomenclature

### Roman letters

| | |
|---|---|
| $a$ | Thermal diffusivity, $\equiv \lambda/(\rho C_p)$ [$m^2/s$] |
| $c$ | Reaction progress variable [-] |
| $d_d$ | Droplet diameter |
| $d_N$ | Nozzle diameter, = 42 mm in Chapter 6 |
| $\mathbf{f}$ | Body force vector [$N/m^3$] |
| $\mathbf{g}$ | Gravitational acceleration vector |
| $h$, $h_s$, $h_t$ | Enthalpy, sensible enthalpy, total enthalpy, $\equiv h + (1/2)\ \mathbf{u} \cdot \mathbf{u}$, [J/kg] |
| $k$ | Turbulent kinetic energy [$m^2/s^2$] |
| $m_d$ | Droplet mass |
| $p$ | Pressure |
| $p$, $\overline{\overline{p}}$, $\bar{p}$, $\tilde{p}$ | Probability density function or filtered density function (in LES) |
| $\mathbf{q}$ | Heat flux vector |
| $r$ | Radial coordinate, radius |
| $t$ | Time |
| $\mathbf{u}$ | Velocity vector, $= (u_x, u_y, u_z)$ |
| $u'$ | Turbulent velocity fluctuation |
| $\mathbf{x}$ | Cartesian coordinate vector, $= (x, y, z)$ |
| $x$ | Cross-stream coordinate |
| $z$ | Axial coordinate |
| | |
| $C_L$ | Liquid heat capacity [J/kg/K] |
| $C_p$ | Isobaric specific heat capacity [J/kg/K] |
| $D$ | Mass diffusivity [$m^2/s$] |
| Da | Damköhler number, $\equiv \tau_p/\tau_c$ |
| $E_a$ | Activation energy [J/mol] |
| $\mathbf{F}$ | Force vector [N] |
| $\mathbf{I}$ | Identity matrix |

| | |
|---|---|
| Le | Lewis number, $\equiv a/D$ |
| Ka | Karlovitz number, $\equiv \tau_c/\tau_K$ |
| $L_T$ | Integral (turbulent) length scale |
| $L_V$ | Heat of evaporation [J/kg] |
| $N_\xi$, $N_c$, $N_{\xi c}$ | Scalar dissipation rates and cross-scalar dissipation rate [$s^{-1}$] |
| Nu | Nusselt number |
| Pr | Prandtl number, $\equiv \nu/a$ |
| $Q_\alpha$, $Q_h$, $Q_T$ | Conditional means of mass fraction $Y_\alpha$, enthalpy and temperature |
| $\dot{Q}$ | External heat source term [$W/m^3$] |
| Re | Reynolds number |
| $R_u$ | Universal gas constant, $\approx 8.314$ J/mol/K |
| $\mathbf{S}$ | Strain rate tensor |
| $S_h$ | Spray source term in the enthalpy equation [W/kg] |
| $\mathbf{S}_u$ | Spray source term in the momentum equation [$N/m^3$] |
| $S_\xi^-$, $S_c^-$ | Spray terms in $\xi$ and $c$ equation, defined in Eqns 3.18 and 3.19, [$s^{-1}$] |
| Sc | Schmidt number, $\equiv \nu/D$ |
| Sh | Sherwood number |
| $S_L$ | Laminar flame speed |
| $T$ | Temperature |
| $T_a$ | Activation temperature |
| $U_b$ | Bulk velocity |
| $\mathbf{U}_d$, $\mathbf{U}_p$ | Droplet ($d$) or particle ($p$) velocity vector |
| $V$ | Volume |
| $\mathbf{V}$ | Diffusion velocity vector |
| $Y$ | Mass fraction |
| $X$ | Mole fraction |
| $W$ | Molar mass |

**Greek letters**

| | |
|---|---|
| $\delta$ | Delta function |
| $\delta_{\alpha\mathrm{F}}$, $\delta_{\psi\mathrm{F}}$ | Kronecker delta, with species $\alpha$, $\psi$ and fuel |
| $\delta_L$ | Laminar flame thickness |
| $\varepsilon$ | Turbulent dissipation rate [$m^2/s^3$] |
| $\zeta$ | Sample space varaible of $c$ |
| $\eta$ | Sample space varaible of $\xi$ |
| $\eta_K$ | Kolmogorov length scale |

| | |
|---|---|
| $\theta$ | Phase indicator function |
| $\lambda$ | Thermal conductivity [W/m/K] |
| $\mu$ | Dynamic viscosity [Pa $\cdot$ s] |
| $\nu$ | Kinematic viscosity, $= \mu/\rho$ [m$^2$/s] |
| $\xi$ | Mixture fraction [-] |
| $\xi_{\text{lean}}$, $\xi_{\text{rich}}$, $\xi_{\text{st}}$ | Lean and rich flammability limit and stoichiometric mixture fraction |
| $\rho$ | Density |
| $\boldsymbol{\sigma}$ | Cauchy stress tensor |
| $\tau$ | Time scale |
| $\boldsymbol{\tau}$ | Deviatoric stress tensor |
| $\phi$ | Equivalence ratio |
| $\phi_{\text{ov}}$ | Overall equivalence ratio (total amount of liquid and gaseous fuel) |
| $\dot{\omega}_\alpha$, $\dot{\omega}_\psi$ | Reaction rate for species $\alpha$ and $\psi$, [s$^{-1}$] |
| $\dot{\omega}_c^*$, $\omega_c$, $\omega_p$ | Apparent reaction rate and its contributions, defined in Eqn. 3.16 |
| | |
| $\Gamma$ | Gamma function |
| $\Delta$ | LES-filter width |
| $\mathit{\Pi}$ | Volumetric evaporation rate per unit volume [s$^{-1}$] |
| $\mathit{\Psi}$ | Fine-grained PDF |

**Subscript indices**

| | |
|---|---|
| $b$ | burned |
| cmc | concerning the resolution of the CMC (or DCMC) |
| $d$ | droplet |
| F | fuel |
| $G$ | gaseous |
| $L$ | liquid or laminar |
| les | concerning the resolution of LES |
| res | resolved (by LES) |
| sat | saturation |
| sgs | sub-grid scale (unresolved by LES) |
| $T$ | turbulent |
| $u$ | unburned |
| | |
| $\alpha$ | chemical species |
| $\psi$ | chemical species associated with the reaction progress variable |

### Superscript indices and overbar symbols

| | |
|---|---|
| $'$ | Fluctuations around the conventional mean, $Y' = Y - \bar{Y}$ |
| $''$ | Fluctuations around density-weighted mean, $Y'' = Y - \tilde{Y}$, or fluctuations around the conditional mean, $Y'' = Y - Q$ |
| $\bar{}$ | Reynolds average, or LES-filtering |
| $\tilde{}$ | Density-weighted Favre average |

### Acronyms

| | |
|---|---|
| ATF | Artificially Thickened Flame |
| CFD | Computational Fluid Dynamics |
| CFL | Courant-Friedrichs-Lewy (number), $\equiv u\ \delta t/\delta x$ |
| CMC | Conditional Moment Closure |
| CSE | Conditional Source-term Estimation |
| DCMC | Doubly Conditional Moment Closure |
| DNS | Direct Numerical Simulation |
| FDF | Filtered density function (= sub-grid PDF in LES) |
| FGM | Flamelet Generated Manifold |
| FPV | Flamelet Progress Variable |
| GRT | Global Rainbow Refractometry Technique |
| HRR | Heat release rate [W/m$^3$] |
| LES | Large-Eddy Simulation |
| LDA | Laser Doppler Anemomentry |
| MMC | Multiple Mapping Closure |
| OH-PLIF | OH Planar Laser Induced Fluorescence |
| OS | Operator splitting |
| PDA | Phase Doppler Anemomentry |
| PDF | Probability density function |
| PIV | Particle Image Velocimetry |
| RANS | Reynolds-Averaged Navier-Stokes |
| RMS | Root mean square |
| SDR | Scalar dissipation rate |
| SF | Stochastic Field |
| SGS | Sub-grid scale |
| TCS | (Workshop on) Turbulent Combustion of Sprays |

# Chapter 1

# Introduction

## 1.1 Motivation

For more than 200 years fossil fuels have been the main source of primary energy. Combustion is used to turn this primary energy into useful energy, namely heat, mechanical and electrical energy. Combustion processes are at the centre of a vast number of technical applications, including domestic heating, industrial furnaces, power applications and transportation. Even though the share of fossil fuels in the global energy mix is expected to decrease from today's 86 % of primary energy supply [BP plc, 2017a; IEA, 2017], they will most likely be the dominant energy source in 2035. In fact, the total amount of energy supplied from fossil fuels is likely to increase due to global population and GDP growth. It is estimated that world-wide reserves of fossil fuel will suffice to satisfy this demand for more than a century. As a result, combustion of fossil fuels is expected to play an important role in global energy supplies in the decades to come [BP plc, 2017b]. In this context Bilger [2011] pointed out the responsibility to develop viable combustion technologies to supply clean energy, at least for a period of transition in the global energy supply.

Liquid fuels play a dominant role in transportation [BP plc, 2017b], mainly as fuel for internal combustion (IC) engines and aviation gas turbines. The use of liquid fuels is advantageous in mobile applications for their high energy density and relatively safer storage properties, and because very compact combustion devices can be built. Liquid fuels are not likely to be replaced in the case of long-distance transport and air crafts but substitution with bio-fuels might be possible [Agarwal, 2007; Blaschek et al., 2010]. With growing population and GDP, there is also an increasing need and demand for transportation. For instance, global air traffic is expected to double within the next 15 years [Airbus SAS, 2017].

Technical combustion processes are virtually always turbulent, since high mixing rates in turbulent flows permit the design of high-power applications in compact combustion devices. The combustion of liquid fuels usually involves the atomisation of the liquid into a finely dispersed spray to allow for a fast evaporation and mixing with the oxidiser [Jenny et al., 2012]. This underlines the need for research on liquid fuel combustion in general, and of turbulent spray combustion in particular.

The implementation of more stringent emission regulations has driven the development of new combustion technologies. For instance, in aviation gas turbines, modern concepts like Lean Premixed Prevaporised (LPP) and Rich Quench Lean (RQL) are used to reduce emissions of nitric oxides and soot [Lefebvre & Ballal, 2010]. The implementation of new combustion technologies is often complicated by the fact that they push combustion systems closer to their operation limits. In this case, careful design and tight control of the combustion process is necessary to ensure safe ignition and stable operation, while avoiding oscillations or extinction.

In most areas of engineering, numerical simulations are widely used to assist design and product development. Confronted with the above-mentioned challenges, there is a need for computational tools that can reliably predict the behaviour of complex combustion systems. At present, industrial combustor development still relies heavily on testing in experimental rigs, while numerical simulations are largely secondary. This clearly constitutes a handicap in the development of combustor design, relative to other parts of a thermal system where computational investigations are employed routinely [Bilger, 2011]. With recent growth in computational power major progress has been made in the field of computational fluid dynamics (CFD), which is developing into a reliable tool for flow prediction. However, the case of turbulent reacting flows remains particularly challenging, due to the interaction between turbulence, small-scale mixing and chemical reactions. These phenomena occur at scales that cannot be resolved numerically in most practical combustion applications, requiring the use of combustion modelling.

Further challenges arise in the numerical modelling of liquid-fuelled combustion systems, which include injection, atomisation, dispersion of droplets and evaporation. These processes span a wide range of time and length scales and are inter-connected. Consequently, there is to date no numerical tool that can describe the complete spray combustion process [Gutheil, 2011]. Injection and atomisation on the one side, and the turbulent combustion on the other side, are commonly viewed as two separate modelling problems. The focus of this thesis is on the modelling of the spray combustion process.

In spray combustion, a strong coupling exists between the evaporation and chemical reaction: the liquid fuel needs to evaporate first to provide gaseous fuel for the chemical reaction, which causes heat release and in turn leads to more evaporation. Both the evaporation and the chemical reaction are influenced by the turbulence, and occur localised on very small scales [Hayashi & Mizobuchi, 2011; Jenny et al., 2012].

In recent years, significant progress in the numerical modelling of spray combustion has been made. Nevertheless, the modelling uncertainties are significantly larger than in simulations of gaseous flames. Modelling of the physical effects and interaction that are present in turbulent spray flames is the topic of this thesis.

## 1.2 Strategy

This thesis describes the modelling of turbulent spray combustion in the case of a dilute spray. Limiting the scope of this work is necessary since spray combustion is, in general, very rich in terms of the physical processes involved. The focus on fully formed dilute spray excludes modelling of the spray formation, liquid break-up, droplet collision and agglomeration, which is an entirely separate fields of research. The main focus lies on combustion modelling, the modelling of chemical reaction in a turbulent flame and the impact of turbulence and evaporation on it. This study requires the use of further modelling tools for turbulent flows, turbulent dispersion of droplets and evaporation – these models are used but are not developed further in the present work. The modelling principles for turbulent dilute spray flames have been reviewed by Jenny et al. [2012].

The Euler-Lagrangian framework is employed for the numerical modelling of the two phase flow. It represents the natural approach for flows with a finely dispersed liquid phase and, thus, it is common practice in spray flame modelling. This involves the solution of the continuous gas phase in a Eulerian framework, and tracking of the dispersed liquid phase in a Lagrangian way assuming a point-particle approach. An overview of solver strategies for two phase flows is given by Balachandar & Eaton [2010].

The turbulent flow field of the continuous phase is solved with the Reynolds-Averaged Navier-Stokes (RANS) approach and the Large-Eddy Simulation (LES) [Poinsot & Veynante, 2005]. In the RANS approach only mean flow fields are resolved and all turbulent fluctuations are modelled. RANS is still used extensively in practical engineering applications for its moderate needs of computational resources, but it is limited by validity of the assumptions at the basis of the closure models used for

turbulence and combustion. LES solves the (spatially) filtered instantaneous flow field, resolving the large scales of turbulent motion explicitly, while the small scales are modelled using sub-grid scale closure. Since large scales of turbulence, which depend strongly on the specific geometry of the flow, are resolved, more general models can be used to provide closure for the small scales, which have more universal features than the large eddies. From the point of view of combustion modelling, LES provides more accurate mixing fields and allows for the modelling of of transient combustion phenomena. LES is the state-of-the-art of turbulent reacting flow modelling, but it requires significantly larger computational resources than RANS [Pitsch, 2006; Poinsot & Veynante, 2005]. In both RANS and LES of turbulent reacting flows, closure for the highly non-linear chemical reaction source term is required. Even though LES resolves the large scales of turbulence and provides improved predictions of passive scalar mixing, LES is usually not able to resolve the chemical reaction in turbulent flows, and a sub-grid scale combustion model for the filtered reaction rate is necessary [Bray, 1996; Givi, 1989; Pitsch, 2006; Pope, 1991]. Providing closure for this mean (or filtered) reaction source term is the objective of combustion modelling, which is in the scope of this thesis.

Traditionally, combustion modelling has often made a distinction between *premixed* flames where fuel and oxidiser are fully mixed before chemical reaction, and *non-premixed* flames where they are injected separately. In turbulent spray combustion, where the fuel is injected in liquid form and reaction is preceded by evaporation and mixing, this distinction cannot generally be made. Spray flames can simultaneously exhibit premixed and non-premixed modes of combustion [Réveillon & Vervisch, 2005]. The wide range of length and time scales involved and the strong coupling of turbulence, evaporation and chemical reaction [Jenny et al., 2012; Sirignano, 1983], manifest in complex spray combustion regimes [Réveillon & Vervisch, 2005] and a diverse palette of macroscopic phenomena, including flame propagation [Bradley et al., 2014; Hayashi et al., 1977; Myers & Lefebvre, 1986], ignition characteristics [Mastorakos, 2017] and extinction [Yuan et al., 2018] that differ from common experience with gaseous flames. For instance, depending on droplet diameter and spacing a spray flame may be smooth and propagate like a gaseous premixed flame, or may be rugged and propagate via the ignition of individual droplets [Burgoyne & Cohen, 1954; Neophytou et al., 2012]; for ignition energy needs to be provided to evaporate the liquid fuel first [Mastorakos, 2017]; for extinction the flame-droplet interaction, evaporation and mixing play an important role [Giusti & Mastorakos, 2017]. Therefore, in order to reproduce the behaviour of turbulent spray flames in a numerical simulation, an advanced combustion model is

required. The modelling approach needs to be applicable to different combustion modes and regimes. Furthermore, it should include the effect of evaporation and micro-mixing on the flame structure, and resolve finite rate chemical effects [Jenny et al., 2012].

In the present work, the Conditional Moment Closure (CMC) method is employed. The CMC approach for turbulent flame modelling has been developed independently by Bilger [1993a] and Klimenko [1990]. The model is founded on the conditional average. The model was originally developed for non-premixed flames, where a strong correlation of the reactive scalars with the mixture fraction is utilised. Then most fluctuations of the temperature and other reactive scalars can be associated with fluctuations of the mixture fraction. Using the mixture fraction as conditioning variable, fluctuations around the conditional mean of the reactive scalars are small and simple (first-order) closure for the highly non-linear chemical reaction source term can be provided. The CMC approach has been demonstrated to be consistent with the frozen limit and the fast chemistry limit [Klimenko & Bilger, 1999]. As a consequence of solving for the temporal and spatial evolution of conditionally averaged flame structure, CMC appears to be able to predict finite-rate chemistry effects in non-premixed combustion [Kronenburg & Mastorakos, 2011]. The main advantages of the CMC method for the modelling of turbulent reacting flows are (i) the sound derivation involving only mild modelling assumptions, and (ii) the capability to handle detailed chemistry at moderate computational cost.

The method has been reviewed by Klimenko & Bilger [1999] and more recently by Kronenburg & Mastorakos [2011]. CMC modelling of non-premixed combustion is well-established and has been applied to a wide range of combustion problems. Conventional first-order CMC has been used extensively with RANS, including the works by Roomina & Bilger [1999, 2001], Kim et al. [2005b, 2000], Fairweather & Woolley [2004] and Kim & Mastorakos [2005]. More recently, with the establishment of LES as the state-of-the-art of turbulent reacting flow modelling, CMC has been adopted to the LES-framework [Kim & Pitsch, 2005; Navarro-Martinez et al., 2005], where CMC takes the role of the sub-grid scale combustion model. LES-CMC has been successfully applied to various combustion problems in non-premixed, including auto-ignition [Stanković et al., 2013], forced ignition [Triantafyllidis et al., 2009; Tyliszczak & Mastorakos, 2013; Zhang et al., 2019], the stabilisation of lifted non-premixed jet flames [Navarro-Martinez & Kronenburg, 2011], and local extinction [Garmory & Mastorakos, 2011; Zhang et al., 2015] and blow-off [Zhang & Mastorakos, 2016]. The CMC method has been applied to spray flames with a non-premixed character, i.e. flames whose structures are well characterised by the mixture fraction. Applications of CMC to

spray flames include RANS simulations of spray auto-ignition [Borghesi et al., 2011; Kim & Huh, 2002] and LES-CMC of spray jet flames [Ukai et al., 2013, 2014, 2015], and LES-CMC of forced ignition [Tyliszczak & Mastorakos, 2013], local extinction [Giusti & Mastorakos, 2017] and blow-off [Giusti & Mastorakos, 2016] in liquid fuelled bluff-body flames. CMC has also been applied to premixed flames using a reaction progress variable as conditioning variable. Only a small number of applications to premixed flames exist, including several RANS simulations [Amzin & Swaminathan, 2013; Amzin et al., 2012; Martin et al., 2003]. LES-CMC has been used successfully to simulate the behaviour of premixed flames approaching blow-off [Farrace et al., 2018, 2017]. Furthermore, the CMC model has also been applied outside of the classic combustion context. These applications include laminar chaotic flows [Vikhansky & Cox, 2007], chemical reaction in the liquid-phase [Mortensen, 2004], in porous media [Klimenko & Abdel-Jawad, 2007] and in atmospheric flows [Brown & Bilger, 1998].

In the above-mentioned cases, a single conditioning variable was used to parametrise the flame structure, either the mixture fraction or the reaction progress variable in the rare cases where CMC was applied to a premixed flame. The statistical foundation of CMC ensures that it is, in principle, not limited to a specific combustion mode. In practice, CMC closure for the chemical reaction source term requires the flame to be reasonably well parametrised by the conditioning variable so that fluctuations around the conditional mean remain sufficiently small [Klimenko & Bilger, 1999]. For example in a mixture fraction-based approach this assumption breaks down in the case of ignition and extinction, or in the case of a partially premixed flame that propagates along mixture fraction iso-contours. Consequently, conventional singly-conditioned CMC models are limited to cases that are either premixed or predominantly non-premixed, which is also the case of the above-mentioned spray flames that were simulated using CMC.

In contrast, a general type of spray flame can span a broad range of combustion modes from non-premixed to almost fully pre-vaporised and premixed, which may also co-exist within a single flame [Domingo et al., 2005; Réveillon & Vervisch, 2005]. In particular, turbulent spray flames with increasing degrees of premixed behaviour have recently received more attention from an experimental [Kariuki & Mastorakos, 2017; Masri & Gounder, 2010] and numerical point of view [Wacks et al., 2018; Wacks & Chakraborty, 2016a; Wacks et al., 2016]. This reflects modern design trends, for example, in aviation gas turbine combustors, which operate in partially premixed conditions in order to reduce pollutant formation and improve combustion efficiency.

This motivates the development of Doubly Conditional Moment Closure (DCMC) where two conditioning variables provide a sufficient parameter space for the flame structure. To date, DCMC has only been applied at the level of fundamental feasibility studies where DCMC was tested against a Direct Numerical Simulation (DNS) while closure for the DCMC equation was provided from DNS results. These studies focused on predicting extinction [Cha et al., 2001; Kronenburg, 2004; Kronenburg & Papoutsakis, 2005] and the effect of temperature inhomogeneity on ignition [Behzadi et al., 2018; Salehi et al., 2017] and have so far demonstrated a great potential of the modelling approach for predicting complex, transient combustion phenomena. Kronenburg [2004] showed that the use of mixture fraction and reaction progress variable could be advantageous for the prediction of local extinction. So far, DCMC has not been used for simulations of lab-scale flames with RANS or LES. One of the main obstacles has been the complexity related to providing closure for DCMC. From a broader perspective, the strategy of double-conditioning has also been recently employed in the CMC-related modelling approach of Conditional Source-term Estimation (CSE) for the simulation of gaseous flames using RANS [Dovizio et al., 2016; Dovizio & Devaud, 2016; Dovizio et al., 2015].

CMC modelling allows to consider the effects of droplet evaporation on the flame structure. This includes direct effects due to the generation of fuel vapour and evaporative cooling, and indirect effects via micro mixing on the flame structure. Modelling of the direct effects of evaporation is challenging and has so far only been attempted for singly-conditional CMC in a small number of publications [Borghesi et al., 2011; Giusti et al., 2016; Giusti & Mastorakos, 2017; Tyliszczak et al., 2014; Ukai et al., 2013, 2014, 2015].

## 1.3 Objectives

The present work focuses on the development of a Doubly Conditional Moment Closure (DCMC) model for spray combustion. In detail, the objectives of this thesis are:

- Derive the DCMC equation for spray combustion. Aim for a derivation in the most general form and relax limiting assumptions where possible to provide the basis for future developments. Select a pair of conditioning variables that allows to parametrise the whole range from non-premixed to fully premixed flames. Derive the doubly-conditional terms that allows to incorporate the effects of evaporation on the flame structure.

- Provide closure for the DCMC equation. Chose simplifying assumption and propose sub-models for unclosed terms, namely the doubly-conditional scalar dissipation rates and spray terms. Additionally, provide closure for the Reynolds-averaged/LES-filtered equations of the flow field solver.

- Implement the method in a way that is computationally efficient and allows the performance of large scale simulations.

- Validate the method. Performing simulations of benchmark cases for turbulent spray combustion. Demonstrate the ability of DCMC to reproduce their features in the simulation.

- Discuss the solutions of the DCMC equation. Explore the term balance of the DCMC equation.

## 1.4 Outline

The structure of the thesis is as follows. Chapter 2 contains a literature review that introduces the basics of turbulent spray modelling, and provides a more detailed summary of the concepts presented in this introduction, concerning turbulent spray combustion and the Conditional Moment Closure method for turbulent combustion. It also contains a short overview of recent work on turbulent spray combustion modelling with different models.

Chapter 3 contains the main theoretical contribution of this thesis. It presents the development of the DCMC model for spray combustion. The framework for the mathematical description of two-phase flow is described, and the DCMC equation is derived. At the end simplifying assumptions are made and closure models are discussed.

In Chapter 4 the implementation of the present modelling approach is detailed. The governing equations for the flow field solver are presented. The equations and closure models are first given for simulations in the RANS framework, then in the LES framework. The modelling of the spray and the coupling with the gaseous phase is presented. At the end of the chapter the implementation of the DCMC model and its coupling with the flow field solver is detailed.

In Chapter 5, solutions of the DCMC equation are explores in a special case of spatial homogeneity, denoted as "DCMC-0D". This simple case is used for an *a priori* assessment of DCMC. Furthermore, the modelling of spray terms in DCMC and effect of evaporation on the flame structure are discussed.

Chapter 6 shows the first application of the DCMC method to a lab-scale flame using RANS. The chapter contains a comparisons with experimental results. The DCMC model is used to provide closure for the mean spray terms in the transport equations of the conditioning variables and the effect of spray evaporation is discussed. The insight gained is used to propose simpler modelling of the spray terms, which is used in Chapter 7.

In Chapter 7, LES-DCMC results for the Rouen spray jet flame are shown and compared with experimental results. This study constitutes the main validation of the DCMC approach for turbulent spray combustion.

Chapter 8 contains the summary and conclusions of this thesis. At the end, recommendations for future work are made.

# Chapter 2

# Literature review

## 2.1 Introduction

This chapter contains a summary of the topics relevant to the research presented in this thesis. First, the governing equations of a turbulent reacting flow are given. Second, the numerical modelling of turbulent reacting flows is discussed. The problem of modelling the chemical reaction source term in a turbulent flow accurately is discussed. Thus, the objective of turbulent combustion modelling is introduced. Third, spray combustion is reviewed. This section describes the features of spray flames and finishes with modelling strategies for multi-phase flow. Fourth, the CMC framework for turbulent combustion modelling is reviewed. Finally, a brief summary of recent work concerned with the modelling of turbulent spray combustion is given.

## 2.2 Turbulent reacting flows

In most practical combustion applications, the chemical reaction takes place within a turbulent flow. Turbulence is critical in all high-power applications to achieve fast mixing and high burning rates. Turbulent combustion is characterised by a two-way interaction of turbulence and and chemical reaction. On the one hand, turbulence has an effect on the flame structure, which can increase the reaction rate or in extreme case lead to extinction. On the other hand, the heat-release and dilatation from the flame affects the turbulent flow [Poinsot & Veynante, 2005].

### 2.2.1 Governing equations

The governing equations of a (single-phase) turbulent reacting flow consisting of $N_\alpha$ chemical species are presented in the form of transport equations, state equation and constitutive relations. All equations presented in this sections are taken from Williams [1985b], Poinsot & Veynante [2005] and Echekki & Mastorakos [2011], unless marked otherwise, and more details and discussions can be found in these references. The transport equations represent the conservation of mass, momentum and energy:

- Equation of mass conservation

$$\frac{\partial \rho}{\partial t} + \nabla \cdot (\rho \mathbf{u}) = 0 \tag{2.1}$$

- Equation of momentum[1]

$$\frac{\partial \rho \mathbf{u}}{\partial t} + \nabla \cdot (\rho \mathbf{u}\mathbf{u}) = -\nabla p + \nabla \cdot \boldsymbol{\tau} + \rho \sum_{\alpha=1}^{N_\alpha} Y_\alpha \mathbf{f}_\alpha \tag{2.2}$$

- Equation of mass conservation for species $\alpha$

$$\frac{\partial \rho Y_\alpha}{\partial t} + \nabla \cdot (\rho \mathbf{u} Y_\alpha) = -\nabla \cdot (\rho \mathbf{V}_\alpha Y_\alpha) + \rho \dot{\omega}_\alpha, \qquad \alpha = 1 \ ... \ N_\alpha \tag{2.3}$$

- Equation of energy conservation, written in terms of the enthalpy[2]

$$\frac{\partial \rho h}{\partial t} + \nabla \cdot (\rho \mathbf{u} h) = -\nabla \cdot \mathbf{q} + \dot{Q} + \frac{\partial p}{\partial t} + \nabla \cdot (p\mathbf{u}) + \boldsymbol{\tau} : \nabla \mathbf{u} + \rho \sum_{\alpha=1}^{N_\alpha} Y_\alpha \mathbf{f}_\alpha \cdot \mathbf{V}_\alpha \tag{2.4}$$

In these equations, $\rho$ is the density, $\mathbf{u}$ is the velocity vector, $p$ is the hydrostatic pressure, $\boldsymbol{\tau}$ is the deviatoric stress tensor, which is related to the Cauchy stress tensor (true stress tensor),

$$\boldsymbol{\sigma} = \boldsymbol{\tau} - p\mathbf{I} \tag{2.5}$$

[1]Here $\mathbf{uu}$ denotes the outer product. The outer product of two vectors results in a second rank tensor. It can also be written as $\mathbf{a}\mathbf{b}^\intercal = \mathbf{a} \otimes \mathbf{b} = a_i b_j$. The divergence of a second rank tensor is a first rank tensor (vector), since $\nabla \cdot \mathbf{a}\mathbf{b}^\intercal = (\nabla \cdot \mathbf{a})\mathbf{b} + \mathbf{a} \cdot \nabla \mathbf{b}$. In tensor notation the advective term is, $\nabla \cdot (\rho \mathbf{u}\mathbf{u}) = \partial(\rho u_i u_j)/\partial x_j$, and the viscous shear term is $\nabla \cdot \boldsymbol{\tau} = \partial \tau_{ij}/\partial x_i$.

[2]The double dot product is defined as $\mathbf{A} : \mathbf{B} = A_{ij} B_{ij} = \sum_i \sum_j A_{ij} B_{ij}$. In tensor notation the term can be written as $\boldsymbol{\tau} : \nabla \mathbf{u} = \tau_{ij} \ \partial u_i / \partial x_j$

$Y_\alpha$ is the mass fraction of species $\alpha$, $\mathbf{V}_\alpha$ is the diffusion velocity of species $\alpha$, $\mathbf{f}_\alpha$ is the external force per unit mass acting on species $\alpha$ and $\dot{\omega}_\alpha$ is the production of species $\alpha$ by chemical reaction. For the mass fractions, diffusive fluxes and reaction rates the following conditions apply:

$$\sum_{\alpha=1}^{N_\alpha} Y_\alpha = 1, \qquad \sum_{\alpha=1}^{N_\alpha} Y_\alpha \mathbf{V}_\alpha = 0, \qquad \sum_{\alpha=1}^{N_\alpha} \dot{\omega}_\alpha = 0 \tag{2.6}$$

The energy equation is written in terms of the enthalpy $h$. In its transport equation $\mathbf{q}$ is the energy flux, $\boldsymbol{\tau} : \nabla \mathbf{u}$ is the viscous heating term and $\dot{Q}$ is a heat source term, for instance due to radiation or a spark.

The conservation equations of a reacting flow were given in general form. In addition to the conservation equations plus their initial and boundary conditions, the equation of state and constitutive relations are required to describe a turbulent reacting flow fully.

The equation of state relates the thermodynamic state variables. In the general form for a multicomponent mixture it is written as

$$p = p(\rho, T, Y_1, Y_2 \ ... \ Y_{N_\alpha}) \tag{2.7}$$

The *ideal gas law* is commonly used and the equation of state becomes

$$p = \rho R_u T \sum_{\alpha=1}^{N_\alpha} \frac{Y_\alpha}{W_\alpha} \tag{2.8}$$

where $R_u \approx 8.314$ J/mol/K is the universal gas constant and $W_\alpha$ is the molecular mass of species $\alpha$.

Assuming an ideal gas, the (internal) energy $e$ and the enthalpy $h = e + p/\rho$ are given as functions of temperature only. For a system composed of $N_\alpha$ species, the enthalpy $h$ is

$$h = \sum_{\alpha=1}^{N_\alpha} Y_\alpha h_\alpha(T), \qquad h_\alpha = \Delta h^0_{\alpha=1} + \int_{T_0}^{T} C_{p,\alpha}(T') \, \mathrm{d}T' \tag{2.9}$$

where $\Delta h^0_\alpha$ is the reference enthalpy of species $\alpha$ at the reference temperature $T_0$. The enthalpy is related to the total (or stagnation) enthalpy $h_t$ and the sensible enthalpy $h_s$ as

$$h_t \equiv h + (1/2) \ \mathbf{u} \cdot \mathbf{u}, \qquad h_s \equiv h - \sum_{\alpha=1}^{N_\alpha} Y_\alpha \Delta h^0_\alpha \tag{2.10}$$

Assuming linear dependence of viscous stresses on local strain rate for a *Newtonian fluid*, the deviatoric stress tensor can be written as

$$\boldsymbol{\tau} = \mu \left(\nabla \mathbf{u} + (\nabla \mathbf{u})^{\intercal}\right) + \left(\kappa - \frac{2}{3}\mu\right)(\nabla \cdot \mathbf{u})\,\mathbf{I} \tag{2.11}$$

where $\mu$ is the dynamic viscosity and $\kappa$ is the bulk viscosity. In many applications it can be assumed that $\kappa = 0$. Using this expression of the viscous stress tensor, the momentum equation takes the form of the famous *Navier-Stokes equation*.

In the case where gravity is the only external force, the volume force term in the equation of momentum can be written as

$$\rho \mathbf{g} = \rho \sum_{\alpha=1}^{N_\alpha} Y_\alpha \mathbf{f}_\alpha \tag{2.12}$$

where $\mathbf{g}$ is the gravitational acceleration.

The diffusion velocity $\mathbf{V}_\alpha$ in a multicomponent mixture can be determined from the following expression derived from the kinetic theory of gases [Williams, 1985b]:

$$\begin{aligned} \nabla X_\alpha = \sum_{\beta=1}^{N_\alpha} \frac{X_\alpha X_\beta}{\mathcal{D}_{\alpha\beta}}(\mathbf{V}_\beta - \mathbf{V}_\alpha) + (Y_\alpha - X_\alpha)\frac{\nabla p}{p} + \frac{\rho}{p}\sum_{\beta=1}^{N_\alpha} Y_\alpha Y_\beta(\mathbf{f}_\alpha - \mathbf{f}_\beta) \\ + \sum_{\beta=1}^{N_\alpha} \frac{X_\alpha X_\beta}{\rho \mathcal{D}_{\alpha\beta}}\left(\frac{\mathcal{D}_{th,\beta}}{Y_\beta} - \frac{\mathcal{D}_{th,\alpha}}{Y_\alpha}\right)\frac{\nabla T}{T}, \qquad \alpha = 1 \ldots N_\alpha \end{aligned} \tag{2.13}$$

where $X_\alpha$ is the mole fraction of species $\alpha$, $\mathcal{D}_{\alpha\beta}$ are the binary diffusion coefficients and $\mathcal{D}_{th,\alpha}$ are the thermal diffusion coefficients. In general, it contains effects due to pressure gradients, external forces and temperature gradients. The last term describes the effect of mass diffusion due to temperature gradients, called *Soret effetc*. The general expression for the thermal flux is

$$\mathbf{q} = -\lambda \nabla T + \rho \sum_{\alpha=1}^{N_\alpha} h_\alpha Y_\alpha \mathbf{V}_\alpha + R_u T \sum_{\alpha=1}^{N_\alpha}\sum_{\beta=1}^{N_\alpha} \frac{X_\beta \mathcal{D}_{th,\alpha}}{W_\alpha \mathcal{D}_{\alpha\beta}}(\mathbf{V}_\alpha - \mathbf{V}_\beta) \tag{2.14}$$

The last term describes the effect of heat diffusion due to species gradients, termed *Dufour effect*.

It is often possible to assume that Soret, Dufour and pressure gradient effects are negligible and that the external force is the same on all species [Williams, 1985b]. Still, detailed modelling of the diffusion velocity is complex since it requires solving of a large linear system. In practice, simplified approaches with first-order approximations

like *Hirschfelder's law* or *Fick's* law are mostly used [Poinsot & Veynante, 2005]. In many application the following form of *Fick's law* is used for its simplicity:

$$\mathbf{V}_\alpha = -\frac{D_\alpha}{Y_\alpha}\nabla Y_\alpha \tag{2.15}$$

This form is theoretically only valid for binary mixing, or for multicomponent mixing if all binary diffusion coefficients are equal [Williams, 1985b]. The main issue with first-order approximations is that summing over all species mass fraction equations the continuity equation is not recovered, and mass conservation is not guaranteed. This problem can circumvented by introducing a correction velocity $\mathbf{V}^{(c)}$ [Ern & Giovangigli, 1994]:

$$\mathbf{V}_\alpha = -\frac{D_\alpha}{Y_\alpha}\nabla Y_\alpha + \mathbf{V}^c \tag{2.16}$$

where $\mathbf{V}^c = \sum_{\alpha=1}^{N_\alpha}(D_\alpha/Y_\alpha)\nabla Y_\alpha$, which ensures the condition, $\sum_{\alpha=1}^{N_\alpha}\mathbf{V}_\alpha Y_\alpha = 0$. Alternatively, the approximation in Eqn. 2.15 can be used only solving for $N_\alpha - 1$ species equations, and determining the last species from $Y_{N_\alpha} = 1 - \sum_{\alpha=1}^{N_\alpha-1} Y_\alpha$. This approximation may be acceptable in cases where one species exists in abundance, as for instance $N_2$ in combustion with air [Poinsot & Veynante, 2005].

The chemical reaction is represented by the source term $\dot{\omega}_\alpha$. Considering a reactive system consisting of $N_\alpha$ species and $N_R$ elementary reactions, the elementary reactions can be generally prescribed as [Poinsot & Veynante, 2005]

$$\sum_{\alpha=1}^{N_\alpha}\nu'_{\alpha,r}\mathrm{A}_\alpha \rightleftharpoons \sum_{\alpha=1}^{N_\alpha}\nu''_{\alpha,r}\mathrm{A}_\alpha, \qquad r = 1 \ldots N_R \tag{2.17}$$

where $\mathrm{A}_\alpha$ denotes the species, and $\nu'_{\alpha,r}$ and $\nu''_{\alpha,r}$ are their stoichiometric coefficients in the elementary reaction $r$ on the reactants and products side (e.g. $2\,\mathrm{H} + \mathrm{H_2O} \rightleftharpoons \mathrm{H_2} + \mathrm{H_2O}$). The net reaction source term of species $\alpha$ is obtained by summing over all elementary reactions:

$$\omega_\alpha = \frac{W_\alpha}{\rho}\sum_{r=1}^{N_R}\left\{(\nu''_{\alpha,r} - \nu'_{\alpha,r})\left[k_{f,r}\prod_{\alpha=1}^{N_\alpha}[X_\alpha]^{\nu'_\alpha} - k_{b,r}\prod_{\alpha=1}^{N_\alpha}[X_\alpha]^{\nu''_\alpha}\right]\right\} \tag{2.18}$$

where $[X_\alpha] = \rho Y_\alpha/W_\alpha$ is the molar concentration and $k_{f,r}$ and $k_{b,r}$ are the rate constants of the forward and backward reaction respectively. The rate constant is given by the *Arrhenius law*:

$$k_{f,r} = A_r T^{\beta_r}\exp\left(-\frac{E_{a,r}}{R_u T}\right), \qquad k_{b,r} = \frac{k_{f,r}}{K_{c,r}} \tag{2.19}$$

with the pre-exponential constant $A_r$, the temperature exponent $\beta_r$, the activation energy $E_{a,r}$ (or written with the activation temperature $T_{a,r} = E_{a,r}/R_u$) and the concentration-based equilibrium constant $K_{c,r}$.

### 2.2.2 Numerical simulations of turbulent reacting flows

In general, it is very difficult to study combustion processes using analytical techniques. In practice this makes numerical simulations the tool of choice. Still, numerical simulations of turbulent reacting flows are complex and rely on the tools provided by Computational Fluid Dynamics (CFD). For the simulation of a turbulent reacting flow there are three levels of simulation within the continuum limit [Echekki & Mastorakos, 2011; Poinsot & Veynante, 2005; Pope, 2000; Swaminathan & Bray, 2011].

#### Direct Numerical Simulation

In a Direct Numerical Simulation (DNS), the local instantaneous balance equations (Eqns 2.1, 2.2, 2.3 and 2.4) are solved directly, resolving all scales of turbulent motion and chemical reaction. In order to resolve the smallest scales of turbulent motion, a spatial resolution smaller than the Kolmogorov length scale $\eta_K$ is required. The Kolmogorov length scale can be estimated as a function of the turbulent Reynolds number $Re_T$ [Tennekes & Lumley, 1972]:

$$\eta_K \sim L_T Re_T^{-3/4} \tag{2.20}$$

where $L_T$ is the integral length scale, which is typically of the same order as the characteristic length scale of the flow. Hence the total number of nodes required to fully resolve a homogeneous turbulence field in a three-dimensional domain scales as $N^3 \sim \mathrm{Re}_T^{9/4}$. Furthermore, the time step scales as $\delta t \sim \delta x/u'$ with $\delta x = L_T/N$, since a small CFL number is necessary for accurate temporal integration, and the duration of the simulation scales as $\tau_T \sim L_T/u'$ to achieve convergence of the turbulence statistics. Then the number of time steps that need to be performed scales as $N_{\delta t} \sim \tau_T/\delta t \sim N$. Therefore, the computation cost of (non-reacting) DNS scales as $N^4 \sim \mathrm{Re}_T^3$ (or $\sim \mathrm{Re}_\lambda^6$) [Pope, 2000, p. 346ff.].

In the case of a turbulent reacting flow, DNS also has to resolve the chemical time and length scales. In many cases, this can be a more stringent requirement than resolving all scales of turbulence. In combustion DNS with a one-step chemical mechanism at least 20 nodes are required to resolve the inner flame structure whose thickness is of the order $O(0.1\ \mathrm{mm})$. Then the total number of nodes scales as $N^3 \sim (L_T/\delta_L)^3 \sim (\mathrm{Re}_T\ \mathrm{Da})^{3/2}$,

and the number of time steps scales as $N_{\delta t} \sim \tau_T/\tau_c = \mathrm{Da}$ [Poinsot & Veynante, 2005, p. 159ff.]. More complex multi-step chemical mechanisms require even finer spatial resolution, since steeper concentration gradients need to be resolved, and smaller time steps. The computational cost per node has been found to increases linearly with the number of species [Lu & Law, 2009]. In combustion DNS with hydrocarbon chemistry, the temporal resolution of the fastest reactions requires very small time steps of the order of $10^{-9}$ s, and typical simulations requires $10^5$ to $10^6$ explicit time steps [Echekki & Mastorakos, 2011].

DNS allows for the most accurate description of a turbulent reaction flow. Since DNS resolves all scales of turbulent motion, it is often perceived as a way to conduct "numerical experiments". However, due to the rapid increase of computational cost with Reynolds number, even DNS of non-reacting flows with realistic Reynolds numbers, for example in gas turbines of the order $O(10^6)$, are still infeasible [Swaminathan & Bray, 2011]; for comparison, one of the largest DNS of non-reacting flow by Ishihara et al. [2016] reaches $\mathrm{Re}_\lambda = 2300$ ($\mathrm{Re}_T \approx 150,000$). In combustion DNS further concessions have to be made in terms of the chemical mechanism used to describe the combustion process. Detailed chemical schemes for hydrocarbon combustion consists of hundreds of species far out of reach for DNS, and, consequently, reduced chemical mechanism have to be employed. Even with reduced chemistry, state-of-the-art combustion DNS are mostly limited to small domains with a simple geometry, which typically are at least one order of magnitude smaller in linear scale than laboratory flames or practical combustion devices [Echekki & Mastorakos, 2011], for instance a recent DNS of a premixed jet flame with jet Reynolds number $\mathrm{Re} = 10,500$ (based on jet diameter, 1.5 mm, and bulk velocity, 110 m/s) by Wang et al. [2018].

### Reynolds-Averaged Navier-Stokes

The Reynolds-Averaged Navier-Stokes (RANS) framework is the classical approach for the computation of turbulent flows in practical engineering applications. The approach has its origin in the *Reynolds-decomposition* of the flow variables in a mean $\bar{\Phi}$ and a turbulent fluctuation $\Phi'$, as already introduced by Reynolds [1895] (see also Tennekes & Lumley [1972, p. 27ff]):

$$\Phi = \bar{\Phi} + \Phi' \tag{2.21}$$

RANS is based on an ensemble average, which is equivalent to a time average in statistically stationary flows. In the RANS approach, transport equations for mean flow variable are solved. This means that all scales of turbulent motion are unresolved

and need to be modelled. Namely, the transport equations of the Reynolds-averaged mean contain the unclosed Reynolds stresses, $\overline{\mathbf{u}'\mathbf{u}'}$, and turbulent scalar fluxes, $\overline{\mathbf{u}'\Phi'}$. Since all scales of turbulent motion are modelled, a coarse spatial resolution of the order of 1 mm and small grids with $O(10^5)$ points are usually sufficient for most flows of engineering interest [Poinsot & Veynante, 2005, p. 134ff].

In turbulent reacting flows, density fluctuations are often important and it is not possible to neglect terms like $\bar{\mathbf{u}}\overline{\rho'\mathbf{u}'}$ or $\overline{\rho'\mathbf{u}'\Phi}$. Then it is convenient to introduce density-weighted *Favre-averaging* [Favre, 1969]:

$$\tilde{\Phi} \equiv \frac{\overline{\rho\Phi}}{\bar{\rho}} \tag{2.22}$$

In this way averaged transport equations can be obtained that do not contain correlations with the density fluctuations (see also discussion by Bilger [1975]).

The modelling of turbulent reacting flows requires the solution of the Reynolds-averaged species mass balance, which includes the chemical reaction source as mean reaction rate term $\overline{\dot{\omega}}_\alpha$ (note that the present discussion also applies to the Favre-average $\widetilde{\dot{\omega}}_\alpha$). The reaction rate $\dot{\omega}_\alpha$ is a non-linear function of species and temperature (Eqn. 2.19), and consequently for its mean one has

$$\overline{\dot{\omega}}_\alpha \neq \dot{\omega}_\alpha(\bar{Y}_1, \bar{Y}_2 \ ... \ \bar{Y}_{N_\alpha}, \bar{T}) \tag{2.23}$$

Williams [1985a, p. 106f] and Borghi [1988, p. 257] made a more general argument, which showed that *moment methods*, based on a Taylor expansion of the reaction rate term[3],

$$\begin{aligned}\overline{\dot{\omega}}_\alpha = \dot{\omega}_\alpha(\bar{Y}_1 \ ... \ \bar{Y}_{N_\alpha}, \bar{T}) + \frac{1}{2}\frac{\partial^2\dot{\omega}_\alpha}{\partial Y_i \partial Y_j}\bigg|_{(\bar{Y}_1 ... \bar{Y}_{N_\alpha}, \bar{T})} \overline{Y_i' Y_j'} + \frac{\partial^2\dot{\omega}_\alpha}{\partial Y_i \partial T}\bigg|_{(\bar{Y}_1 ... \bar{Y}_{N_\alpha}, \bar{T})} \overline{Y_i' T'} \\ + \frac{1}{2}\frac{\partial^2\dot{\omega}_\alpha}{\partial T^2}\bigg|_{(\bar{Y}_1 ... \bar{Y}_{N_\alpha}, \bar{T})} \overline{T'^2} + \ ...\end{aligned} \tag{2.24}$$

cannot be successful to compute the mean reaction rate, for the following reasons: (i) moment approaches require the solution of transport equation for higher moments with the related closure problem. However, even if perfect transport equations could be obtained, (ii) problems arise from the sensitivity of the term $\exp(-T_{a,r}/T)$, and the expansion in Eqn. 2.24 not being valid for $T'/\bar{T} > 1$, leading to large errors, particularly

[3]Here the Einstein summation convention was used for species indices $i$ and $j$. First-order terms do not appear because $\overline{Y'} = 0$. Note that the $\overline{Y_i' T'}$-terms do not have the factor $\frac{1}{2}$ because $\frac{\partial^2\dot{\omega}_\alpha}{\partial Y_i \partial T} = \frac{1}{2}\frac{\partial^2\dot{\omega}_\alpha}{\partial Y_i \partial T} + \frac{1}{2}\frac{\partial^2\dot{\omega}_\alpha}{\partial T \partial Y_i}$.

for high activation temperature. Finally, the results are not only inaccurate but (iii) produce physically impossible results that violate necessary conditions like $\tilde{Y} \geq 0$, $\overline{Y''^2} \geq 0$, $-(\overline{Y_i''^2}\ \overline{Y_j''^2})^{1/2} \leq \overline{Y_i'' Y_j''} \leq (\overline{Y_i''^2}\ \overline{Y_j''^2})^{1/2}$ and $\dot{\omega} \geq 0$ for an irreversible reaction. For these reasons the moments approach has been abandoned. It is the objective of turbulent combustion modelling to accurately predict the mean reaction rate.

### Large-Eddy Simulation

The Large-Eddy Simulation (LES) represent an intermediate concept between RANS and DNS, where the unsteady motion of large eddies is explicitly calculated, while the effects of small-scale turbulence are modelled. LES allows for a more accurate description of the flow than RANS and a significantly coarser spatial resolution can be used than in DNS. Compared to DNS the requirements for a 3D-grid in LES are reduced by a factor $\mathrm{Re}_\Delta^{9/4}$ where $\mathrm{Re}_\Delta \equiv u'_{\mathrm{sgs}}\Delta/\nu$ is the sub-grid Reynolds number [Pitsch, 2006]. However, instantaneous LES-filtered transport equations need to be solved so that the computational cost is about 100 to 1000 times higher than in RANS [Poinsot & Veynante, 2005, p. 136]

Historically, LES has its origins in meteorological applications with the early work by Smagorinsky [1963]. The first application of LES in an engineering context, to a turbulent channel flow, was carried out by Deardorff [1970]. Since LES only resolves the large scales of turbulence, a sub-grid scale (SGS) turbulence model for the small scales is required. The most popular SGS closure is the Smagorinsky model, where the SGS Reynolds stresses are modelled based on resolved strain rate tensor [Lilly, 1967; Smagorinsky, 1963]. Other SGS turbulence models are the dynamic model [Germano et al., 1991] and the scale similarity model [Bardina et al., 1980]. The *scale invariance* or *scale similarity* hypothesis implies that certain features of the flow are invariant with length scale within the inertial range of the turbulent energy spectrum [Meneveau & Katz, 2000].

Interest in LES of turbulent reacting flows started to come up in the 1990s. One of the earliest applications of LES to a reacting flow was carried out by Schumann [1989], however, not considering SGS scalar fluctuations. The main challenge with LES for reacting flows lies in the modelling of the spatially filtered reaction rate term, similar to the closure problem for the mean reaction rate in RANS, as first mentioned by Givi [1989, p. 99], and further commented upon by Pope [1991, p. 595] and Bray [1996, p. 19]: LES does not solve the closure problem for the non-linear reaction rate term, since the interaction of chemical reaction and molecular diffusion takes place at small sub-grid length scales. DesJardin & Frankel [1998] showed in an *a priori* test

that closure of the reaction rate term without SGS model gave poor results compared to DNS. Notably, the scale-similarity assumption used for modelling of turbulent fluxes [Meneveau & Katz, 2000], is not applicable to combustion processes which originate at unresolved scales [Pitsch, 2006]. Therefore, an SGS combustion model is necessary. Early suggestions of SGS combustion modelling include the work by DesJardin & Frankel [1998], Colucci et al. [1998], Bushe & Steiner [1999], Branley & Jones [2001], Pitsch & Steiner [2000], Hawkes & Cant [2000], Colin et al. [2000] and others (see review by Pitsch [2006]).

LES constitutes the state-of-the-art of turbulent combustion modelling. The advantages of LES for turbulent combustion modelling compared to RANS are discussed in Pitsch [2006] and Poinsot & Veynante [2005]: primarily, LES provides significantly improved predictions of the flow field, since large scales are explicitly computed, which allows better predictions of complex swirling and recirculating flows, common in combustion applications. LES also provides improved accuracy of the scalar mixing and dissipation rates, critical for combustion modelling. Moreover, the modelling impact is considerably smaller in LES compared to RANS since only the small scales, corresponding to a small fraction of turbulent kinetic energy and scalar variance, require modelling. These small scales of turbulence can be expected to have more uniform features than the large scales that depend on the exact geometry, and thus models with general formulations might be more suitable to describe them. Finally, LES allows to model transient combustion phenomena, including instabilities, acoustic activity, ignition and extinction.

### 2.2.3 Turbulent combustion modelling

The objective of turbulent combustion modelling is to provide closure for the mean reaction rate in numerical simulations of turbulent reacting flows. Technical combustion processes can be subdivided in terms of the mixing, distinguishing premixed and non-premixed combustion [Peters, 2000]. This distinction is useful from a theoretical point of view and is utilised in a wide range of classic modelling approaches for turbulent combustion.

#### Non-premixed combustion

In non-premixed combustion the fuel and the oxidiser are injected into the combustion chamber separately. Practical examples are furnaces, diesel engines, gas turbines

and fires. Non-premixed flames are also called *diffusion flames* since diffusion is the rate-controlling process [Peters, 2000].

The flame establishes at the most favourable location between fuel and oxidiser where the mixture exists in stoichiometric proportions. Fuel and oxidiser diffuse towards the reaction zone and heat diffuses outwards. Unless fuel and oxidiser are pushed against each other by the flow, the flame spreads in time until it extinguishes in the products due to the lack of fresh reactants. Therefore two important characteristics of non-premixed flames are the lack of a reference thickness and the absence of propagation [Peters, 2000; Poinsot & Veynante, 2005].

A useful tool for the study of non-premixed flames is the notion of a conserved scalar. Conserved scalars are defined as a linear combinations of $Y_\alpha$ and other scalars that are constructed so that the reaction source term cancels out in the transport equation of the conserved scalar. For instance, a conserved scalar can be defined as the elemental mass fractions of carbon, hydrogen and oxygen [Bilger, 1976; Peters, 1984]

$$Z_\mathrm{C} \equiv \sum_{\alpha=1}^{N_\alpha} \frac{n_{\mathrm{C},\alpha} W_\mathrm{C}}{W_\alpha} Y_\alpha, \qquad Z_\mathrm{H} \equiv \sum_{\alpha=1}^{N_\alpha} \frac{n_{\mathrm{H},\alpha} W_\mathrm{H}}{W_\alpha} Y_\alpha, \qquad Z_\mathrm{O} \equiv \sum_{\alpha=1}^{N_\alpha} \frac{n_{\mathrm{O},\alpha} W_\mathrm{O}}{W_\alpha} Y_\alpha \tag{2.25}$$

where $n_{\mathrm{C},\alpha}$, $n_{\mathrm{H},\alpha}$ and $n_{\mathrm{O},\alpha}$ are the number of carbon, hydrogen and oxygen atoms in a molecule of species $\alpha$ respectively. The mixture fraction is a normalised conserved scalar with $\xi = 1$ in the fuel stream and 0 in the oxidiser stream. Bilger [1989] used the following definition of the mixture fraction for a hydrocarbon of the type $\mathrm{C}_m\mathrm{H}_n$,

$$\xi \equiv \frac{\beta - \beta_\mathrm{Ox}}{\beta_\mathrm{Fu} - \beta_\mathrm{Ox}} \tag{2.26}$$

with

$$\beta \equiv \frac{Z_\mathrm{C}}{m W_\mathrm{C}} + \frac{Z_\mathrm{H}}{n W_\mathrm{H}} - \frac{Z_\mathrm{O}}{(m + n/4) W_\mathrm{O}} \tag{2.27}$$

where $\beta_\mathrm{Ox}$ and $\beta_\mathrm{Fu}$ are the values of $\beta$ for the oxidiser and fuel stream respectively.

A simpler alternative explanation of the mixture fraction can be given: in a two stream problem, with a fuel and oxidiser stream, the mixture fraction is the local fraction of mass originating from the fuel stream, $\xi \equiv m_\mathrm{Fu}/(m_\mathrm{Fu} + m_\mathrm{Ox})$ [Peters, 2000]. The above definition was introduced to evaluate this quantity in a reacting flow.

Due to its definition, the mixture fraction is governed by a transport equation without reaction rate

$$\frac{\partial \rho \xi}{\partial t} + \nabla \cdot (\rho(\mathbf{u} + \mathbf{V}_\xi)\xi) = 0 \tag{2.28}$$

For the theoretical study of laminar diffusion flames, the *passive scalar approach* is an important concept, based on the mixture fraction [Bilger, 1989; Peters, 1984]. This approach allows to separate the problem of computing a laminar diffusion flame, i.e. finding $Y_\alpha(\mathbf{x}, t)$, $T(\mathbf{x}, t)$, into (i) a mixing problem for $\xi(\mathbf{x}, t)$ and (ii) a flame structure problem, where it is assumed that $Y_\alpha(\xi, t)$ and $T(\xi, t)$. In the Burke-Schumann limit of irreversible infinitely fast chemistry, reaction only takes place at the mixture fraction corresponding to a stoichiometric mixture, $\xi_{\mathrm{st}}$.

The *passive scalar approach* is also used as basis in several methods for the modelling of turbulent non-premixed combustion. In *presumed-PDF methods* the turbulent mixing problem is solved for the mean and variance of mixture fraction to compute the PDF. Different methods for the solution of the flame structure problem exist, including flamelet models and CMC discussed later.

### Premixed combustion

In premixed combustion, fuel and oxidiser are mixed to the molecular level before reacting. Practical examples are spark ignition engines, power gas turbines and household burners [Peters, 2000].

A homogeneous mixture of fuel and oxidiser is characterised by its equivalence ratio $\phi$, which is related to the mixture fraction,

$$\phi \equiv \frac{\xi}{1-\xi} \, \frac{1-\xi_{\mathrm{st}}}{\xi_{\mathrm{st}}} \tag{2.29}$$

so that $\phi = 1$ corresponds to stoichiometric mixture. A stable flame can only form if the equivalence ratio is within the flammable domain, which depends on the fuel, temperature and pressure, but at ambient condition is typically $0.5 < \phi < 1.5$ [Peters, 2000].

The key characteristic of this type of flame is its propagation towards the unburned mixture in the direction normal to the flame. The propagation is a result of the asymmetric structure of a premixed flame, leading to transport of heat and species into the un-reacted gases. The flame thickness and the propagation rate relative to the unburned reactants in a one-dimensional geometry are well-defined. The propagation rate is called the laminar flame speed $S_L^0$. In the unstrained, adiabatic case $S_L^0$ depends on temperature, composition of the fresh gases and pressure. In the general case, the burning velocity also depends on strain and curvature, and the flame's response to them changes with the Lewis number [Cant & Mastorakos, 2008; Poinsot & Veynante, 2005].

For premixed turbulent combustion different regime diagrams have been proposed [Abdel-Gayed et al., 1989; Borghi, 1985; Peters, 1988; Poinsot et al., 1991]. These regimes are distinguished in terms of the interaction of flame and turbulence, which depends on length and time scales of the flow and the flame. The regimes include laminar flames, different flamelet regimes, and flames with thin and broken reaction zones. These regimes can be described by a set of non-dimensional numbers: the turbulent Reynolds number, comparing inertial and viscous forces in the largest scales of turbulence, the turbulent Damköhler number, comparing the turbulent integral time scale, $\tau_T = L_T/u'$, with the chemical time scale, $\tau_c = \delta_L^0/S_L^0$, and the Karlovitz number comparing the chemical time scale with the Kolmogorov time scale $\tau_K = u'_K/\eta_K$ [Peters, 2000]:

$$\mathrm{Re}_T \equiv \frac{u' L_T}{\nu}, \qquad \mathrm{Da} \equiv \frac{\tau_T}{\tau_c} = \frac{S_L^0 L_T}{u' \delta_L^0}, \qquad \mathrm{Ka} \equiv \frac{\tau_c}{\tau_K} = \frac{\delta_L^2}{\eta_K^2} \tag{2.30}$$

where $\delta_L^0$ is the laminar flame thickness. In the limit $\mathrm{Da} \gg 1$ the chemical time scale is short leading to a thin reaction zone, which is advected and distorted by the flow. For $\mathrm{Ka} > 1$ turbulent eddies can enter the flame and change the inner flame structure.

For the modelling of premixed combustion, a reaction progress variable can be defined, which was first introduced by Bray & Moss [1977]. The concept was subsequently further developed by Bray, Moss and Libby [Bray et al., 1985]. A reaction progress variable is a normalised scalar that increases monotonically from zero in fresh reactants to unity in fully-burned products. In a fully premixed flow, the progress variable can be based on a species mass fraction or, in an adiabatic case, on the temperature [Cant, 2011; Swaminathan & Bray, 2011]:

$$c(\mathrm{x}, t) \equiv \frac{Y(\mathrm{x}, t) - Y_u}{Y_b - Y_u} \quad \text{or} \quad c(\mathrm{x}, t) \equiv \frac{T(\mathrm{x}, t) - T_u}{T_b - T_u} \tag{2.31}$$

where the subscripts $u$ and $b$ represent the value in unburned and burned mixture respectively. For instance, the progress variable can be based on the mass fraction of products or fuel or a combination of species. Using a progress variable based on the temperature can be problematic in some cases, because the temperature may also be affected by heat loss, differential diffusion, acoustic activity etc. [Cant, 2011]. For non-adiabatic systems Bilger [1993b] proposed another definition based on enthalpy (see also Klimenko & Bilger [1999, p. 683]). The introduction of a progress variable is convenient, since it describes the complete thermochemical state of the system. Therefore, it has a similar role to the mixture fraction in a diffusion flame.

### Partially premixed combustion

Partially premixed combustion denotes an intermediate case, where compositional inhomogeneity in the range of flammable and non-flammable mixtures lead to the establishment of diffusion-like reaction zones and propagating flame fronts. The canonical case of partially premixed combustion is the triple flame [Kioni et al., 1993].

Often the term *partially premixed combustion* is used ambiguously. In his review Masri [2015] defined *partially premixed* as a situation where fluid particles contain compositional inhomogeneities, spanning a wider range of mixture fractions with flammable and non-flammable mixture. *Stratified flames* are defined as a special case of partially premixed combustion, where compositional inhomogeneities are within the flammable range.

Non-premixed and premixed combustion denote two extreme cases in terms of mixing. Practical combustion applications usually involves partial premixing [Masri, 2015; Peters, 2000]. On the one hand, perfect mixing is difficult to achieve and some inhomogeneity usually remains, and on the other hand, non-premixed flames contain some partial premixing, for instance at the base of lifted flames, in edge flames, before auto-ignition and after local extinction. In particular, lifted jet flames have been studied extensively. In that case, fuel and oxidiser are mixed unevenly upstream of the flame stabilisation point, resulting in a partially premixed flow, where premixed and non-premixed flames occur simultaneously, which has been shown in both experiments [Lyons & Watson, 2000] and DNS [Domingo et al., 2002; Mizobuchi et al., 2002]. Moreover, many modern combustion concepts specifically operate in partially premixed combustion modes to minimise pollutant formation while ensuring stable operation. These technologies include the rich-quench-lean (RQL) and lean-premixed and prevaporised (LPP) concept in aeronautical gas turbines [Lefebvre & Ballal, 2010].

For theoretical studies of partially premixed combustion, the Takeno Flame Index, $\text{F.I.} \equiv \nabla Y_\text{F} \cdot \nabla Y_\text{O}$, has been suggested [Yamashita et al., 1996] as an identifier for the combustion mode, where $Y_\text{F}$ and $Y_\text{O}$ are the mass fractions of fuel and oxidiser. In the normalised form it can be written as [Masri, 2015]

$$G_\text{FO} \equiv \frac{\nabla Y_\text{F} \cdot \nabla Y_\text{O}}{\|\nabla Y_\text{F} \cdot \nabla Y_\text{O}\|} \tag{2.32}$$

Then the extreme values $+1$ and $-1$ refer to fully premixed and non-premixed respectively. In spite of critical views [Knudsen & Pitsch, 2009], Masri [2015, p. 1123] points out that "the Flame Index remains a useful tool to elucidate the extent of inhomogeneity in turbulent flames."

The parametrisation of partially premixed flames often involve the mixture fraction and a reaction progress variable, thus, combining the concepts used for premixed and non-premixed combustion. In a partially premixed flow, a normalised reaction progress variable can be defined [Bray et al., 2005]:

$$c(\mathbf{x},t) \equiv \frac{Y_u(\xi(\mathbf{x},t)) - Y(\mathbf{x},t)}{Y_u(\xi(\mathbf{x},t)) - Y_b(\xi(\mathbf{x},t))} \tag{2.33}$$

where the unburnt and burnt state, $Y_u(\xi)$ and $Y_b(\xi)$, may be given by the mixing line and the equilibrium composition respectively.

## 2.3 Spray combustion

### 2.3.1 General concepts

The essential characteristic of spray flames is that either fuel or oxidiser is injected in liquid form. Evaporation and diffusion have to occur prior to chemical reaction. In order to enhance the mixing, the liquid is atomised to create a spray of small droplets.

Spray combustion involves a rich palette of physical phenomena that are strongly inter-connected and span a wide range of length and time scales. Figure 2.1 shows a schematic of various processes and interactions in turbulent spray combustion [Jenny et al., 2012]: in the gas phase, the turbulence causes dispersion of the gas at the large turbulent scales (macro-mixing) and subsequently mixing continues at the small turbulent scales and subsequently to the molecular level (micro-mixing). The mixing of species and heat is directly coupled to chemical reaction (combustion), which in return impacts on micro-mixing and the turbulent flow. In addition to these interaction also found in gaseous single-phase combustion, for a spray flame, the turbulent motion of the gas induces irregular motion of the droplets (droplet turbulence). In return the motion of the droplets has an effect on the turbulent motion of the gas phase, due to the two-way momentum coupling. The irregular turbulent motion of droplets leads to their dispersion. Turbulent motion of gas and the droplets induces a relative velocity between gas phase and droplets, which enhances the evaporation. The evaporation is naturally coupled to the mixing in the gas phase and is sensitive to the heat released by the chemical reaction. Following the review by Jenny et al. [2012], a brief phenomenological description of the physical processes involved in spray combustion is given in the following.

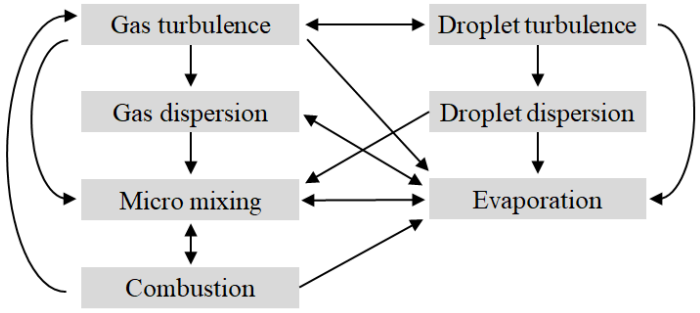


Fig. 2.1 Schematic of the phenomena and interactions involved in turbulent spray combustion. Adapted from Jenny et al. [2012].

The *atomisation* process breaks-up the injected liquid into a fine spray and thus provides the basis for the dispersion of the fuel, mixing and combustion. The combustion itself is strongly dependent on the droplet size distribution due to the break-up process [Lefebvre, 1989]. The liquid break-up occurs due to various physical mechanisms that include the absolute instability of a jet, capillary pinching and interfacial stress. Lin & Reitz [1998] provide a detailed review of the phenomena involved in atomisation. Liquid break-up can be classified into primary and secondary atomisation. *Primary atomisation* denotes the break-up of an injected liquid jet into large droplet and liquid ligaments through the development of Kelvin-Helmholtz instabilities and leading to Rayleigh-Taylor instabilities. *Secondary atomisation* denotes further disintegration into smaller droplets due to instabilities that result from aerodynamic forces arising from the relative inter-phase velocities. This process can be related to the Weber number, which compares inertial forces, $\rho_G \|\mathbf{U}_d - \mathbf{u}\|^2$, and surface tension forces, $\sigma/d_d$ [Lefebvre, 1989]:

$$\mathrm{We} \equiv \frac{\rho_G \|\mathbf{U}_d - \mathbf{u}\|^2 d_d}{\sigma} \tag{2.34}$$

where $\rho_G$ is the density of the gaseous carrier phase, $\|\mathbf{U}_d - \mathbf{u}\|$ is the relative velocity between droplet and the carrier phase, $d_d$ is the droplet diameter and $\sigma$ is the surface tension. The larger the Weber number, the higher the external deforming pressure forces compared to the reforming surface tension. In practice, the criterion for break-up is represented by a critical Weber number, which limits the maximum (stable) droplet size. The critical Weber number may depend on the liquid viscosity, introduced via the Ohnesorg number, and the turbulence intensity, given by the Reynolds number. In many cases $\mathrm{We}_{\mathrm{crit}} \sim O(1)$ [Lefebvre, 1989].

A coarse distinction of spray regimes is made in terms of the dispersed phase volume fraction: the *dense spray* regime is associated with dispersed phase volume fraction is

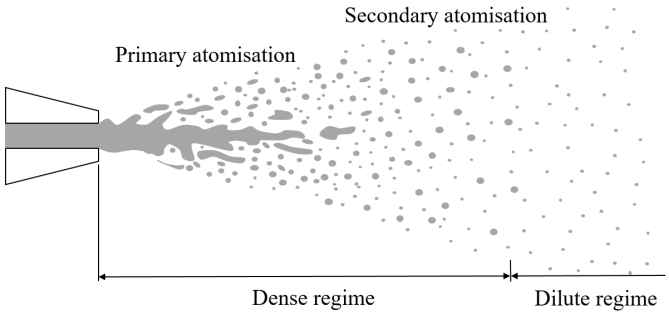


Fig. 2.2 Schematic of spray atomisation. Similar to Jenny et al. [2012].

above $10^{-3}$ and is dominated by atomisation phenomena, frequent droplet collision and coalescence. In contrast, in the *dilute regime*, with a dispersed phase volume fraction of less than $10^{-3}$, droplet collisions are considered negligible. In the *very dilute regime*, for a volume fraction of less than $10^{-6}$, the effect of the dispersed phase on the turbulence in the continuous phase becomes entirely negligible [Balachandar & Eaton, 2010; Jenny et al., 2012].

*Dispersion* of the droplets occurs by momentum exchange with the turbulent motion in the continuous phase. In return, the dynamics of the dispersed phase influence the mean flow and turbulence in the continuous phase. Two phenomena that arise from this dynamic coupling are (i) the modulation of carrier-phase turbulence and (ii) preferential concentration of particles [Balachandar & Eaton, 2010]. Several mechanisms are involved in the modulate of turbulence in the continuous phase. Inertia of particles and the dissipation due to particle drag have a damping effect in the carrier-phase turbulence. In contrast, wake formation and vortex shedding behind particles can generate turbulence. Since these phenomena act at difference scale, the particles can enhance and reduce different scales of turbulent motion at the same time. Vortex structures in the turbulent flow field lead to a preferential concentration of particles. Particles heavier than the carrier are driven outwards from the centre of the vortex by inertial forces and accumulate in regions between multiple vortices where the strain rate dominates over vorticity. This phenomenon is related to the particle *Stokes number*, defined as the ratio of the characteristic particle and flow time scales [Balachandar & Eaton, 2010]:

$$\mathrm{St} \equiv \frac{\tau_p}{\tau_f} \tag{2.35}$$

The particle relaxation time scale $\tau_p$, including virtual mass, is given by [Balachandar, 2003, 2009]:

$$\tau_p = \frac{(2\rho_p/\rho + 1)}{36} \frac{d_p^2}{\nu} \frac{1}{f(\mathrm{Re}_p)} \tag{2.36}$$

where $\rho_p/\rho$ is the particle-fluid density ratio, the function, $f(\mathrm{Re_p}) = 1 + 0.15\ \mathrm{Re}_p^{0.687}$, is the finite Reynolds number correction for Stokes drag, and the particle Reynolds number is defined as

$$\mathrm{Re}_p \equiv \frac{\|\mathbf{U}_p - \mathbf{u}\| d_p}{\nu} \tag{2.37}$$

The flow time scale is given by the characteristic velocity and length scale of the flow, $\tau_f = L_f/u_f$. For turbulent dispersion of particles, the time scale associated with the large eddies is $\tau_T = L_T/u'$, and for the Kolmogorov scale $\tau_K = \eta_K^2/\nu$ (since $\eta_K = (\nu^3/\varepsilon)^{1/4}$ and $\tau_K = (\nu/\varepsilon)^{1/2}$), and for any eddy of size $\eta_K < l_* < L_T$, the corresponding time scale is $\tau_* = \varepsilon^{1/3} l_*^{2/3}$ (since $\varepsilon = (u'_*)^3/l_*$) [Tennekes & Lumley, 1972]. The Stokes number describes how closely a particle follows the flow: for $\mathrm{St} \ll 1$, the particle follows the flow closely, like a tracer; for $\mathrm{St} \gg 1$, the flow have little effect the particles, which continue on their trajectories in a ballistic sense; for $\mathrm{St} \sim 1$, the particles are driven out of the eddy's vortex core by centrifugal forces and concentrate in regions with low vorticity, establishing the preferential concentration of particles [Balachandar & Eaton, 2010].

*Evaporation* and *micro mixing* directly affect the fuel distribution in the inter-droplet region and, thus, have a large effect on combustion [Jenny et al., 2012]. The classic theoretical problem is a spherically symmetric droplet evaporating in quiescent medium with only radial convection away from the droplet surface due to vaporisation (Stefan flow) [Sirignano, 1983]. Relative velocity of droplet and gas lead to increased heat and mass transfer. Moreover, the shear forces at the droplet surface induce internal circulation and droplet rotation [Sirignano, 1983]. In practice, the spherically symmetric case is usually modelled adding a corrections for convection [Faeth, 1979]. A overview of state-of-the-art droplet evaporation models for CFD can be gained from the review by Sazhin [2006], and an instructive comparison of equilibrium and non-equilibrium models was performed by Miller et al. [1998].

For groups of droplets in a spray, different scenarios can be distinguished [Jenny et al., 2012; Réveillon & Demoulin, 2007]. For a large distance between droplets, greater than 10 diameters in a dilute spray, evaporation proceeds in the same way as for an isolated droplet. If the droplets are also small and have a low Reynolds number, they behave like in the idealised case of spherical symmetry. For smaller distance, the mixing field around the droplets starts to interfere and evaporation-modulation occurs. This

may happen even in an overall dilute spray, since droplets tend to assume a preferential concentration in a turbulent flow. In these clusters the fuel vapour concentration reaches values close to saturation, which slows down further evaporation rate. In this case, evaporation can only occur if the fuel vapour concentration is reduced by mixing or if droplets are carried out of the cluster region by the flow. Hence, preferential concentration can have a strongly detrimental effect on the overall evaporation rate [Jenny et al., 2012].

*Combustion* phenomena in spray combustion are detailed in the following sections. First, the canonical case of an igniting single droplet and its combustion are presented in Section 2.3.2. Then the propagation of a flame in a mist of droplets is reviewed in Section 2.3.3. Finally, the spray combustion regimes are discussed in Section 2.3.4.

### 2.3.2 Single droplet combustion

Single droplet combustion has been studied as canonic case for spray combustion. At the same time, single droplet combustion is also representative of practical cases where the distance of droplets is large (see Section 2.3.4). Single droplets have been studied extensively from a theoretical, numerical and experimental point of view. Several reviews of single droplet evaporation [Sazhin, 2006] and combustion [Faeth, 1979; Law, 1982; Sirignano, 1983; Williams, 1973] and single droplet ignition [Aggarwal, 2014] exist. Single droplet combustion is the canonic case characterised by the formation of a spherical diffusion flame around the droplet. Therefore, it is the case where spray combustion is approached using the theoretical framework from non-premixed combustion.

The scenario of single droplet combustion can be described as follows [Law, 1982]. A cold droplet placed in a hot environment is heated by conductive heat transfer. One part of the heat transferred to the liquid phase diffuses into the interior of the droplet; the other part is used to vaporise the liquid. Consequently, vapour at saturation concentration exists near the droplet surface. The vapour diffuses away from the surface. For an initially cold droplet, the evaporation rates are slow at first, but increase as the droplet heats up. A flame can be initiated by forced or auto-ignition. The heat released by a flame diffuses inwards and outwards, and the droplet heats up quickly. A spherically symmetric diffusion flame engulfing the droplet is established. A schematic of a single droplet flame is shown in Fig. 2.3 (left). In the spherically symmetric configuration, only Stefan flow is induced. In presence of forced or natural convection, the flame is distorted in the direction of the flow. For strong relative velocity, the fuel can be swept into the wake, so that the flame does not engulf the

droplet, and even extinction can occur. At the same time, the shear stress on the droplet surface can induce a circular motion in the liquid, which enhances evaporation rates significantly. During an initial heat-up period the droplet size hardly changes, and diameter might even increase due to thermal expansion if the boiling point is high and initial evaporation rates are low. This period is normally much shorter than the vigorous burning period. Following the ignition, the radius of the flame increases, as a result of fuel vapour accumulation between droplet surface and flame until a quasi-steady state is reached. Then the droplet temperature is almost constant. In the idealised case, under the assumption of quasi-steadiness and constant properties, it can be shown that the square of the droplet diameter decreases linearly, $d_d^2 = d_{d,0}^2 - K(t - t_0)$, which is called the $d^2$ *law* and constitutes the simplest model for droplet evaporation [Williams, 1985b]. Due to the strong assumptions involved, the linearity only holds approximately in realistic cases, but it provides useful insight and may be used as the basis for crude estimates. This relation of evaporation time and diameter was first observed experimentally by Sreznevsky [1882] and explained by Langmuir [1918]. Eventually the flame moves closer to the droplet surface until it collapses into the droplet leading to extinction. This is a finite-rate chemistry effect that can be explained defining a Damköhler number that compares the time scales of diffusive transport and chemical reaction [Law, 1982].

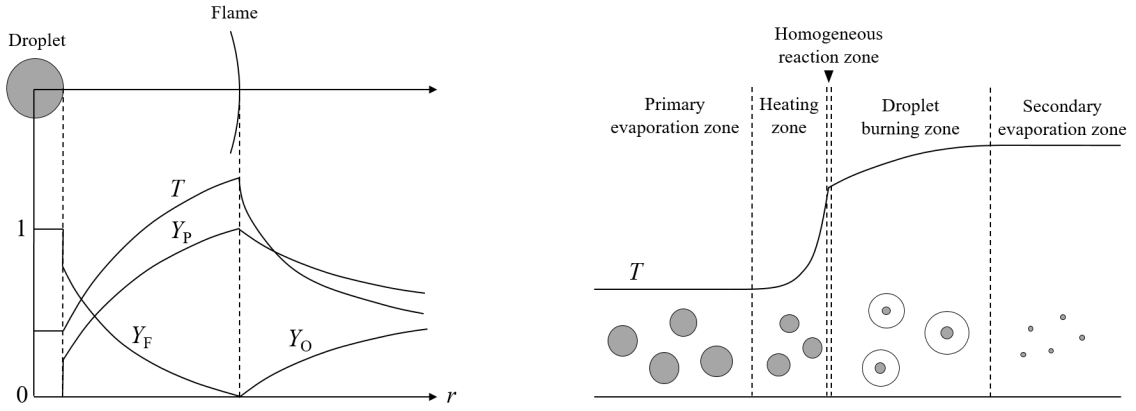


Fig. 2.3 Schematics of a single droplet flame with the flame-sheet approximation (left) and a one-dimensional freely propagating spray flame (right). Left image similar to Williams [1985b]; right image similar to Silverman et al. [1993] and Neophytou & Mastorakos [2009].

### 2.3.3 Propagating spray flames

The propagation of a flame in uniformly dispersed fuel droplets, or the equivalent case of a burner stabilised flame with incoming flow, has been studied extensively as the canonical problem of spray flames. In this canonical case, the spray flame is theoretically approached like a premixed flame, due to its propagating behaviour and considering the mist of fuel droplets as an inhomogeneous mixture of liquid droplets, vapour and oxidiser. This approach is funded on early experimental findings that the behaviour of a flame propagating in sprays was similar to gaseous premixed flames, when the droplet size is small [Burgoyne & Cohen, 1954].

In a theoretical analysis Silverman et al. [1993] distinguish five zones in the one-dimensional structure of a flame propagating in a poly-disperse spray (Fig. 2.3, right). The droplets evaporate upstream of the flame in the (i) *primary evaporation zone* where heat release of the flame is not felt, and in the (ii) *heating zone*. The fuel evaporated in the first two zones is consumed in the (iii) *homogeneous reaction zone*. Homogeneous reaction refers to chemical reaction in the gas phase. Therefore, an effective equivalence ratio $\phi_{\text{eff}}$ can be defined, based on the amount of fuel vapour and oxidiser at the location of the homogeneous reaction zone, in contrast to the overall equivalence ration $\phi_{\text{ov}}$, based the total amount of fuel in form of vapour and liquid. Even if the overall mixture is fuel-rich ($\phi_{\text{ov}} > 1$), slow evaporation, for low fuel volatility or large droplet diameter, can lead to effectively lean conditions for the homogeneous reaction zone ($\phi_{\text{eff}} < 1$). Sufficiently large droplets may survive and continue to evaporate in the hot gases downstream of the flame. If the combustion in the homogeneous reaction zone was fuel-lean ($\phi_{\text{eff}} < 1$), then oxidiser is left and the remaining droplets may burn individually or in clusters in the (iv) *droplet burning zone*. Droplet burning, controlled by the evaporation rate, is a relatively slow process, compared to homogeneous reaction. When the oxidiser is consumed and some droplets still exist, they continue to evaporate in the (v) *secondary evaporation zone*, slightly cooling the mixture. If the combustion in the homogeneous reaction zone was effectively rich ($\phi_{\text{eff}} > 1$), the oxidiser is fully consumed, no droplet burning can occur, and surviving droplets evaporate in the secondary evaporation zone.

Early experimental studies characterised the effect of droplet size one spray flames. Burgoyne & Cohen [1954] studied the flame propagation in mono-disperse tetralin (1,2,3,4-tetrahydronaphthalin, $C_{10}H_{12}$) droplets. For droplets with a diameter below 10 $\mu$m the flame behaved qualitatively like a gaseous premixed flame, for a diameter above 40 $\mu$m the droplets burned individually, and for intermediate diameters a transition occurred. Similarly, Cekalin [1961] describes flame propagation via a relay

mechanism by ignition of individual droplets. Hayashi et al. [1977] also observed smooth flames for ethanol and kerosene droplets of size 7 $\mu$m, and thickened corrugated flames for droplets of size 20 $\mu$m.

Numerous experimental studies have focused on the quantification of laminar burning velocities in sprays (e.g. Polymeropoulos & Das [1975], Hayashi et al. [1977], Ballal & Lefebvre [1981], Myers & Lefebvre [1986], Nomura et al. [2000]). In these experiments, gas and suspended droplets have zero relative velocity, and the burning velocity is defined relative to the fresh mixture. Key parameters of this problem specific to spray flames are the (overall) equivalence ratio, droplet size, fuel volatility, fuel vapour fraction (fuel vapour to total fuel). The following effects on the burning velocity have been described. First, it has been observed that in fuel-lean and stoichiometric cases ($\phi_{\text{ov}} \leq 1$) the burning velocity decreases with increasing droplet size; in (overall) fuel-rich cases ($\phi_{\text{ov}} > 1$) larger droplets may lead to higher burning velocities than in the equivalent gaseous mixtures. This has been explained with the concept of the effective equivalence ratio $\phi_{\text{eff}}$: in (overall) rich mixture, incomplete evaporation produces a gaseous mixture closer to stoichiometric conditions leading to faster burning velocities [Hayashi et al., 1977]. Second, it has been reported that in the presence of droplets with intermediate size ($\approx 10$ $\mu$m) higher burning velocities could be reached than for smaller droplets or purely gaseous premixed flames, even for lean overall mixtures [Hayashi et al., 1977; Nomura et al., 2000; Polymeropoulos & Das, 1975]. This has been attributed to the development of thermo-diffusive instabilities and associated wrinkling of the flame [Bradley et al., 2014]. Finally, it has been pointed out in a numerical study that the burning velocity might be enhanced in (overall) fuel-rich mixtures by the production of very reactive intermediate species due to pyrolysis and their diffusion towards the oxidation zone [Neophytou & Mastorakos, 2009; Neophytou et al., 2012].

### 2.3.4 Spray combustion regime diagrams

Several attempts have been made to categorise spray flames in a regime diagram. Chiu and co-workers [Chiu et al., 1982; Chiu & Liu, 1977] considered the flame forming in a spherical cloud of droplets in contact with hot oxidiser and classified four different regimes, which are distinguished by a single parameter, the group combustion number $G$. The group combustion number represents the ratio of characteristic speed of heat transfer in the gas phase and the speed of the heat transfer between the two phases, directly related to the characteristic evaporation speed. For most cases with high Péclet number, $G \approx 5N_d^{2/3}/S$ [Candel et al., 1999], where $N_d$ is the number of droplets and $S$

is the separation parameter. $S = \delta_s/\delta_{rf}$ is the ratio of the mean droplet spacing and the characteristic diffusion flame radius. For $G \ll 1$ the inter-droplet distance is large and flames form around individual droplets. In contrast, for $G \gg 1$, the droplets are closely spaced and heat transfer inside the cloud is weak. Then the flame is established around the entire cloud, while only the outer droplet evaporate. This regime is called *external sheath combustion*. Two intermediate regimes were proposed [Chiu et al., 1982]: for $G < 1$ a flame forms at the interior of the cloud, engulfing a group of droplets, called *internal group combustion*, while droplets outside of this flame burn in single droplet combustion mode; for $G > 1$ the flame establishes around the droplet cloud, with the flame also affecting the droplets at the centre of the cloud, called *external group combustion*. These concepts for the classification of spray flames have, however, been difficult to extend to configurations other than the spherical cloud in hot oxidiser [Jenny et al., 2012].

Another attempt to categorise spray flames was made by Borghi [1996a,b] who studied laminar flame propagation in homogeneously distributed poly-disperse droplets. The analysis was based on two non-dimensional parameters, the ratio of the evaporation time scale $\tau_v$ and the flame time scale $\tau_f$, and the ratio of the mean droplet distance $\delta_s$ and the flame thickness of a premixed flame $\delta_f$, where $\tau_f = \delta_f/S_L^0$. For $\tau_v/\tau_f \ll 1$ evaporation finishes before the droplets reach the reaction zone, leading to the formation of a premixed flame. For $\delta_s/\delta_f < 1$ and sufficient evaporation time, the droplets enter the reaction zone and thickening of the flame is expected. Beside these extreme cases, the penetration of the flame by some droplets leads to the formation of a secondary reaction zone behind the primary, partially premixed flame front. For this case different regimes are distinguished similar to Chiu's internal and external group combustion regimes.

Réveillon & Vervisch [2005] extended the concepts proposed by Borghi, proposing to add the overall equivalence ratio (based on the mass of injected liquid and oxidiser) as a third parameter of the regime diagram. In their DNS study of a droplet-laden jet, they distinguished three regimes, illustrated in Fig. 2.4. In the *external combustion* regime a single continuous flame engulfs all droplets (*closed external*) or two continuous flames form on both sides of the jet (*open external*); these flames had a predominantly premixed character. In the *group combustion* regime, independent flames formed around separate droplet clusters; both premixed and non-premixed burning modes were observed. In the intermediate *hybrid combustion* regime, premixed flames formed around droplet clusters and a continuous diffusion flame surrounded the whole droplet cloud.

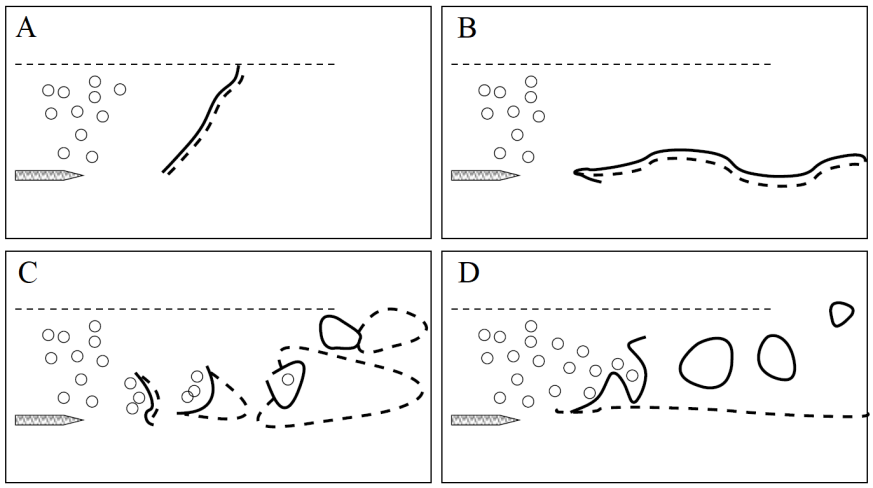


Fig. 2.4 Spray combustion regimes according to Réveillon & Vervisch [2005]: (A) closed external, (B) open external, (C) group and (D) hybrid combustion. Solid lines and dashed lines represent premixed and diffusion flames respectively. Figure from Réveillon & Vervisch [2005].

### 2.3.5 Modelling of dispersed multi-phase flows

Turbulent spray flames fall into the category of multi-phase flows. Dispersed multi-phase flows constitute a subcategory of multi-phase flows. In contrast to other multi-phase flows, for instance free-surface flows, in dispersed multi-phase flows, the evolution of the phase interface is considered secondary. Instead of tracking the interface, processes like break-up and agglomeration are taken into account via the particle-size spectrum [Balachandar & Eaton, 2010].

Different computational approaches for the modelling of turbulent dispersed multi-phase flows exist. Their applicability in a particular case can be related to the particles Stokes number, $\mathrm{St} \equiv \tau_p/\tau_f$ (Eqn. 2.35), comparing particle and flow time scales. The relevant flow time scale for DNS is the Kolmogorov time scale $\tau_K$ and the corresponding Stokes number is [Balachandar & Eaton, 2010]

$$\frac{\tau_p}{\tau_K} = \frac{(2\rho_p/\rho + 1)}{36} \frac{1}{f(\mathrm{Re}_p)} \left(\frac{d_p}{\eta_K}\right)^2 \tag{2.38}$$

and for LES the time scale of the smallest resolved eddy is $\tau_\Delta = \Delta/u'_{\mathrm{sgs}}$ and the corresponding Stokes number can be calculated as

$$\frac{\tau_p}{\tau_\Delta} = \frac{(2\rho_p/\rho + 1)}{36} \frac{1}{f(\mathrm{Re}_p)} \left(\frac{d_p}{\Delta}\right)^2 \left(\frac{\Delta}{\eta_K}\right)^{4/3} \tag{2.39}$$

where $\Delta$ is the LES-filter width and $u'_{\mathrm{sgs}}$ is the sub-gird velocity fluctuation. The following four categories of approaches can be distinguished [Balachandar & Eaton, 2010]:

In *equilibrium Eulerian approaches* it is assumed that particles are small and perfectly follow the carrier phase, so that the droplet-laden flow can be considered as a single fluid. Hence, this approach is only applicable for sufficiently small particles with a small time constant. This can be expressed by the particle Stokes number $\mathrm{St} \equiv \tau_{\mathrm{p}}/\tau_{\mathrm{K}}$ (or $\tau_p/\tau_\Delta$ for LES), the ratio of particle and Kolmogorov time scales. The approach was found to be reasonably accurate for $\mathrm{St} \lesssim 0.2$.

*Eulerian approaches* use a two-fluid formulation, which considers carrier and dispersed phase as inter-penetrating fluids media. In contrast to the equilibrium Eulerian approach, separate momentum and energy equations are solved for the dispersed phase; source/sink terms account for the transfer between the two phase. Consequently, the approach is applicable in cases with larger particles and the restriction on very low St can be relaxed. Still, the Eulerian approach assumes a unique field of particle velocity, temperature etc., implicitly restricting the range of possible St. This restriction can be alleviated by using a probabilistic framework. In general, Eulerian approaches are found to provide comparable results to Lagrangian approaches for $0.2 \lesssim \mathrm{St} \lesssim O(1)$.

The *Lagrangian point-particle approach* uses a Lagrangian description to solve the equations of motion, mass and energy of the individual particles. The assumption of unique fields is not required. Therefore, the approach is well suited for tracking large particles with $\mathrm{St} > 1$ and, of course, it is also suitable for particles with $\mathrm{St} < 1$. Moreover, it can handle a poly-disperse particle cloud easily.

The *fully resolved approach* does not require the point-particle assumption and is thus not restricted theoretically to particles smaller than the smallest resolved length scale of the flow. This approach has only been used for a single or few particles but is usually out of reach, even for most DNS applications.

In theory, the Lagrangian point-particle approach assumes that $d_p \ll \eta_K$ in DNS or $d_p \ll \Delta$ in LES. However, since the fully resolved approach is not practicable in most cases, even for $d_p \gtrsim \eta_K$, the point-particle approach may be the only option. In LES, the point-particle approach can be pushed to consider larger particles with $d_p \sim \Delta$ [Balachandar & Eaton, 2010].

In terms of modelling the dynamic coupling of the carrier phase and the dispersed particles, three levels can be distinguished [Elghobashi, 1994]: in cases where both the dispersed phase volume fraction and mass loading are small, the effect of the carrier-phase turbulence on the particle dynamics is dominant, while the particles hardly affect

the flow (*one-way coupling* between carrier and particles). When the particle volume fraction is small, but the particle and carrier phase mass are comparable the dynamic effects of the particles on the carrier become significant (*two-way coupling*). For even larger particle volume fraction, interactions between particles, collisions, agglomeration and break-up, become more likely and need to be considered (*four-way coupling*).

## 2.4 Conditional Moment Closure

Conditional Moment Closure (CMC) is an advanced model for turbulent combustion, which was developed independently by Klimenko [1990] and Bilger [1993a]. The method and early work have been reviewed in detail by Klimenko & Bilger [1999] and more recently by Kronenburg & Mastorakos [2011]. Additionally, a very instructive analysis of the CMC method in comparison to unsteady flamelet models has been published by Klimenko [2001]; differences between the two models are also pointed out by Swaminathan & Bilger [1999a].

### 2.4.1 Conventional CMC

CMC was originally developed as a model for non-premixed combustion, following a mixture fraction-based approach, hence splitting the turbulent combustion problem into (i) a mixing problem to find the mixture fraction field $\xi(\mathbf{x}, t)$ and (ii) a flame structure problem concerned with finding the species mass fractions $Y_\alpha$ and temperature $T$ as function of $\xi$.

In CMC the flame structure is formally described by the conditional means of the reactive scalars. The conditional mean $Q_\alpha$ is defined as the ensemble average of $Y_\alpha(\mathbf{x}, t)$ under the condition that the associated value $\xi(\mathbf{x}, t)$ is at the value $\eta$ [Bilger, 1993a]:

$$Q_\alpha(\eta; \mathbf{x}, t) \equiv \langle Y_\alpha(\mathbf{x}, t) | \xi(\mathbf{x}, t) = \eta \rangle \equiv \langle Y_\alpha | \eta \rangle \tag{2.40}$$

As a result of this averaging procedure, the instantaneous value of the reactive scalar can be decomposed into the conditional mean and a fluctuation around the conditional mean [Bilger, 1993a]:

$$Y_\alpha(\mathbf{x}, t) = Q_\alpha(\xi(\mathbf{x}, t); \mathbf{x}, t) + Y''_\alpha(\mathbf{x}, t) \tag{2.41}$$

If most fluctuations of $Y_\alpha$ are associated with fluctuations of $\xi$, the fluctuations around the conditional mean are small compared to fluctuations around the conventional

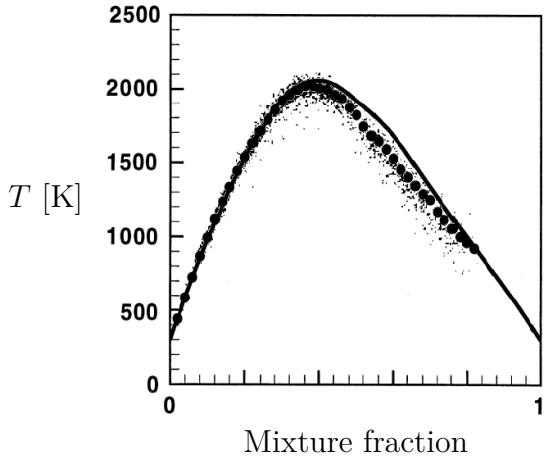


Fig. 2.5 Scatter plot and conditional mean of temperature from experimental measurements (symbols) [Barlow & Frank, 1998] and CMC solution (line) [Roomina & Bilger, 2001] for the Sandia D flame at $x/d = 30$. Adapted from Roomina & Bilger [2001] and Barlow & Frank [1998].

mean, $Y''_\alpha \ll Y'_\alpha$, where $Y'_\alpha = Y_\alpha - \langle Y_\alpha \rangle$. This is illustrated by Fig. 2.5, which shows temperature measurements and their conditional mean for a non-premixed jet flame (Sandia D flame) [Barlow & Frank, 1998].

The principle of the CMC method is to solve transport equations for the conditional means of the reactive scalars in order to obtain the flame structure. An exact transport equation for the conditional moments can be derived, and using only light modelling (assuming (i) high Reynolds number, (ii) the validity of the *primary closure hypothesis*, (iii) Fickian mass diffusion at the molecular level, (iv) unity Lewis number and (v) small conditional fluctuations of density) the following form of the equation is obtained [Klimenko & Bilger, 1999]:

$$\frac{\partial Q_\alpha}{\partial t} + \langle \mathbf{u}|\eta \rangle \cdot \nabla Q_\alpha = \langle N_\xi|\eta \rangle \frac{\partial^2 Q_\alpha}{\partial \eta^2} + \langle \dot{\omega}_\alpha|\eta \rangle - \frac{\nabla \cdot (\langle \rho|\eta \rangle \langle \mathbf{u}'' Y''_\alpha|\eta \rangle p(\eta))}{\langle \rho|\eta \rangle p(\eta)} \qquad (2.42)$$

Notably, the assumptions (iv) and (v) can be relaxed, including differential diffusion terms [Kronenburg & Bilger, 1997] and using density-weighted conditional averaging [Klimenko & Bilger, 1999, p. 623] respectively. The transport equation of the conditional mean (Eqn. 2.42), also called CMC equation, is a partial differential equation in space, time and the conditioning variable $\eta$. CMC equations need to be solved for the conditional means of all species mass fractions $Q_\alpha$ and temperature $Q_T \equiv \langle T|\eta \rangle$ or alternatively enthalpy $Q_h \equiv \langle h|\eta \rangle$. For $Q_h$ an equation similar to Eqn. 2.42 is derived

(further assuming (vi) low Mach number) [Klimenko & Bilger, 1999]:

$$\frac{\partial Q_h}{\partial t} + \langle \mathbf{u}|\eta\rangle \cdot \nabla Q_h = \langle N_\xi|\eta\rangle \frac{\partial^2 Q_h}{\partial \eta^2} + \frac{\langle \dot{Q}|\eta\rangle}{\langle \rho|\eta\rangle} + \frac{1}{\langle \rho|\eta\rangle}\left\langle \frac{\partial p}{\partial t}\middle|\eta\right\rangle - \frac{\nabla \cdot (\langle \rho|\eta\rangle \langle \mathbf{u}''h''|\eta\rangle p(\eta))}{\langle \rho|\eta\rangle p(\eta)} \tag{2.43}$$

The conditional mean of the density $\langle \rho|\eta\rangle$ is calculated from the equation of state.

From its conditional means the unconditional mean of a variable can be calculated as

$$\langle Y_\alpha(\mathbf{x},t)\rangle = \int_0^1 Q_\alpha(\eta;\mathbf{x},t)\ p(\eta;\mathbf{x},t)\ \mathrm{d}\eta \tag{2.44}$$

The mixture fraction PDF is usually presumed based on the mean and variance as $p(\eta;\langle\xi\rangle,\langle\xi'^2\rangle)$. Therefore, the CMC model also requires the solution of transport equations for the mean and variance of mixture fraction.

The motivation for the development of CMC was to provide closure for the non-linear chemical reaction source term in a turbulent reacting flow. In Eqn. 2.42, the reaction source term appears in the form of a conditional mean. If it can be assumed that the fluctuations around the conditional means are small, a very simple first-order closure can be used,

$$\langle \dot{\omega}_\alpha(Y_1, Y_2\ ...\ Y_{N_\alpha}, T)|\eta\rangle \approx \dot{\omega}_\alpha(Q_1, Q_2\ ...\ Q_{N_\alpha}, Q_T) \tag{2.45}$$

Figure 2.5 illustrates that CMC with first-order reaction rate closure [Roomina & Bilger, 2001] provides accurate results if the conditional fluctuations are small. In order to solve the CMC equation, further sub-models are required for the conditional velocity $\langle \mathbf{u}|\eta\rangle$, the conditional scalar dissipation rate, $\langle N_\xi|\eta\rangle = \langle D_\xi \nabla\xi \cdot \nabla\xi|\eta\rangle$, the turbulent transport term $\langle \mathbf{u}''Y_\alpha''|\eta\rangle$ and potentially for external source terms in the $Q_h$ equation; furthermore, a model for the PDF is needed. In practice, the models for the PDF and the conditional SDR are the most important. An overview of the closure models is given in Klimenko & Bilger [1999] and Kronenburg & Mastorakos [2011].

Theoretically, the modelling of the PDF and conditional SDR are not independent, since they are related through the PDF transport equation, which under the assumption of high Reynolds number (as Eqn. 2.42) becomes [Klimenko & Bilger, 1999]

$$\frac{\partial \langle \rho|\eta\rangle p(\eta)}{\partial t} + \nabla \cdot (\langle \rho|\eta\rangle \langle \mathbf{u}|\eta\rangle p(\eta)) = -\frac{\partial^2 \langle \rho|\eta\rangle \langle N_\xi|\eta\rangle p(\eta)}{\partial \eta^2} \tag{2.46}$$

Hence, closure for the conditional SDR can be theoretically found from Eqn. 2.46, if models for the PDF and $\langle \mathbf{u}|\eta\rangle$ are provided [Kronenburg et al., 2000a]. In practice, closure for the conditional SDR is often provided as $\langle N_\xi|\eta\rangle = \langle N_\xi\rangle\ F_{N_\xi}(\eta;\langle\xi\rangle,\langle\xi'^2\rangle)$

[Klimenko & Bilger, 1999]. For instance, a typical choice of sub-models is the $\beta$-function for the PDF and the Amplitude Mapping Closure (AMC) model [O'Brien & Jiang, 1991] for the conditional SDR, $\langle N_\xi|\eta\rangle = N_0 \exp(-2[\mathrm{erf}^{-1}(2\eta-1)]^2)$, where $N_0$ is the scaling factor. The shape predicted by the AMC model is not exactly equal but very close to the shape obtained using a $\beta$-PDF and integrating the PDF equation [Girimaji, 1992a].

CMC is a statistical model and its derivation is founded on the definition of the conditional mean. The CMC equation can be derived using the principle assumptions of (i) high turbulent Reynolds number and (ii) the validity of the primary closure hypothesis [Klimenko & Bilger, 1999]. High Reynolds number allows to neglect terms of molecular transport in physical space. Bilger [1993a] and Klimenko [1990] introduced two different primary closure hypotheses. A comparison and discussion can be found in Klimenko & Bilger [1999, p. 621f, 625f]. As primary closure hypothesis Klimenko [1990] assumed a diffusion approximation for the flux of the reactive scalar in conserved scalar space. Alternatively, $\langle Y''_\alpha N''_\xi|\eta\rangle = 0$ is a sufficient assumption, which might be too strict, however, and it stands in contrast to experience with second-order CMC where this term contributes strongly [Swaminathan & Bilger, 1998, 1999a].

The foundation of the CMC method as a statistical model has important implications, and gives a desirable feature to CMC. The derivation of the CMC equation itself does not require any assumption about the flame structure and its correlation with the conditioning variable, and is thus not *a priori* limited to a certain combustion mode or regime [Kronenburg & Mastorakos, 2011]. For instance, the assumption of a thin flame was not required. The CMC equation remains formally valid when the mixture fraction approach fails to fully describe the combustion mode, as for example in partially premixed combustion, or in the case of extinction and ignition. However, in this case large conditional fluctuations are expected, and first-order closure used for the chemical reaction source term would not yield accurate results. Hence, limitations may still arise from the assumptions behind the sub-models used for closure in the CMC equation, and in particular the reaction source term.

The CMC approach has been demonstrated to be consistent with the frozen limit, $\mathrm{Da} \to 0$, and the fast chemistry limit, $\mathrm{Da} \to \infty$, where the CMC solution converges towards the mixing line and the equilibrium composition respectively [Klimenko & Bilger, 1999, p. 630]. More recent studies seem to demonstrate the capability of CMC (in combination with RANS) to predict finite-rate chemistry effects in a wide range of non-premixed flames [Kronenburg & Mastorakos, 2011], including piloted jet flames [Fairweather & Woolley, 2004; Roomina & Bilger, 1999, 2001], lifted jet flames [Devaud

& Bray, 2003; Kim & Mastorakos, 2005] and bluff body-stabilised flames [Fairweather & Woolley, 2007a; Kim et al., 2000]. Kronenburg et al. [2000b] used CMC for the prediction of soot formation, following the suggestions of Kronenburg & Bilger [1997] for the inclusion of differential diffusion effects.

### 2.4.2 Second-order CMC

Since the early 2000s, most effort in CMC modelling has been dedicated to combustion problems where the local correlation between conditioning variables and the reactive scalars is weakened [Kronenburg & Mastorakos, 2011]. The consequence are larger fluctuations around the conditional mean, which is illustrated by Fig. 2.6 (left), showing that $Y_{\mathrm{CO}}$ correlates poorly with mixture fraction in the presence of local extinction and ignition. Other examples for weakened correlation of the reactive scalars with mixture fraction are cases with partial premixing. The implication is that the first-order closure of the chemical reaction term in CMC (Eqn. 2.45), based on the assumption of small conditional fluctuations, cannot provide accurate closure any more, as discussed by Bilger [1992]. Therefore, the strategy of a second-order closure for the chemical reaction term can be proposed, where first and second conditional moments of the reactive scalars are used to model the effect of the conditional fluctuations on the conditional mean of the chemical reaction rate [Bilger, 1992, 1993b]. The transport equation for the second conditional moments were first derived by Li & Bilger [1993] using the decomposition method and Klimenko [1993] using the joint-PDF method.

In second-order CMC, the CMC equation (Eqn. 2.42) is solved with a second-order closure for the chemical reaction term. The Taylor expansion of the reaction rate (compare with Eqn. 2.24) gives

$$\begin{aligned}\langle \dot{\omega}_\alpha|\eta\rangle \approx \dot{\omega}_\alpha(\mathbf{Q},Q_T) &+ \frac{1}{2}\frac{\partial^2\dot{\omega}_\alpha}{\partial Y_i\partial Y_j}\bigg|_{(\mathbf{Q},Q_T)}\langle Y_i''Y_j''|\eta\rangle + \frac{\partial^2\dot{\omega}_\alpha}{\partial Y_i\partial T}\bigg|_{(\mathbf{Q},Q_T)}\langle Y_i''T''|\eta\rangle \\ &+ \frac{1}{2}\frac{\partial^2\dot{\omega}_\alpha}{\partial T^2}\bigg|_{(\mathbf{Q},Q_T)}\langle T''^2|\eta\rangle\end{aligned} \tag{2.47}$$

with $\mathbf{Q} = (Q_1 \ ... \ Q_{N_\alpha})$. The explicit form of the coefficients for the Arrhenius law (Eqn. 2.19) can be found in Swaminathan & Bilger [1999a]. Bilger [1992] discussed that in contrast to conventional moment methods (see discussion following Eqn. 2.24, following Borghi [1988]), second-order closure was acceptable in CMC where $G_T^{1/2}/Q_T < 0.1$ and $G_{\mathrm{OH}}^{1/2}/Q_{\mathrm{OH}} < 0.2$ for the reaction $\mathrm{H_2 + O_2 \rightarrow H + OH}$. An alternative closure for the conditional reaction rate based on presumed PDFs was proposed for reduced two-, three- or four-step chemical mechanisms [Swaminathan & Bilger, 1999b] In any

case, second-order reaction rate closure requires knowledge of the conditional variances and co-variances, $\langle Y_i'' Y_j''|\eta\rangle$, $\langle Y_i'' T''|\eta\rangle$ and $\langle (T'')^2|\eta\rangle$, which can be obtained by solving additional transport equations for them.

Using similar modelling as for the conditional mean equation [Klimenko & Bilger, 1999, p. 665ff], the transport equation of the conditional variances and co-variances, $G_{ij} \equiv \langle Y_i'' Y_j''|\eta\rangle$, can be written as [Kim, 2002; Klimenko & Bilger, 1999]

$$\begin{aligned}\frac{\partial G_{ij}}{\partial t} + \langle \mathbf{u}|\eta\rangle \cdot \nabla G_{ij} = \langle N_\xi|\eta\rangle \frac{\partial^2 G_{ij}}{\partial \eta^2} - \frac{\nabla \cdot (\langle \rho|\eta\rangle \langle \mathbf{u}'' Y_i'' Y_j''|\eta\rangle p(\eta))}{\langle \rho|\eta\rangle p(\eta)} \\ + \langle \dot{\omega}_i'' Y_j''|\eta\rangle + \langle \dot{\omega}_j'' Y_i''|\eta\rangle - \langle \mathbf{u}'' Y_i''|\eta\rangle \cdot \nabla Q_j - \langle \mathbf{u}'' Y_j''|\eta\rangle \cdot \nabla Q_i \\ + \langle Y_i'' N_\xi''|\eta\rangle \frac{\partial^2 Q_j}{\partial \eta^2} + \langle Y_j'' N_\xi''|\eta\rangle \frac{\partial^2 Q_i}{\partial \eta^2} - 2\langle D \nabla Y_i'' \cdot \nabla Y_j''|\eta\rangle - \frac{1}{\langle \rho|\eta\rangle p(\eta)} \frac{\partial J_G}{\partial \eta}\end{aligned} \tag{2.48}$$

where the turbulent flux in conserved scalar space $J_G$ was introduced with the consistent primary closure hypothesis as discussed by Kim [2002]. An analysis of the term balance can be found in Swaminathan & Bilger [1998, 1999b]. Similar equations for $G_{Ti} \equiv \langle T'' Y_i''|\eta\rangle$ and $G_T = \langle T''^2|\eta\rangle$ can be obtained. These transport equations include various terms, notably $\langle \dot{\omega}_i'' Y_j''|\eta\rangle$, $\langle D \nabla Y_i'' \cdot \nabla Y_j''|\eta\rangle$ and $\langle Y_i'' N_\xi''|\eta\rangle$, which are unclosed and require modelling. *A priori* assessments of the sub-models against DNS data were performed by Swaminathan & Bilger [1999b] and Sreedhara et al. [2008]. A summary and discussion of common closure models can be found in Kronenburg & Mastorakos [2011].

In early applications a simplified second-order closure for a global (one-step) chemical mechanism was used [Kronenburg et al., 1998; Mastorakos & Bilger, 1998]. A generalised approach for multi-step chemical mechanisms was presented by [Kim & Huh, 2004] and Kim et al. [2005a]. A major challenge for the application of second-order CMC with multi-step chemical mechanisms is the large number of additional transport equations for the conditional correlations that needs to be solved, since the number of additional transport equations for the conditional variances and co-variances scales as $N_\alpha^*(N_\alpha^*+1)/2$, where $N_\alpha^*$ is the number of reacting species [Kronenburg & Mastorakos, 2011]. In order to alleviate this issue Kim & Huh [2004] proposed to apply second-order closure to rate limiting steps only, significantly reducing the number of additional transport equations. In contrast, De Paola et al. [2008a] used second-order CMC to simulate an auto-igniting plume, without reduction in dimensionality of the correlation matrix, thus solving for all conditional correlations of a multi-step mechanism.

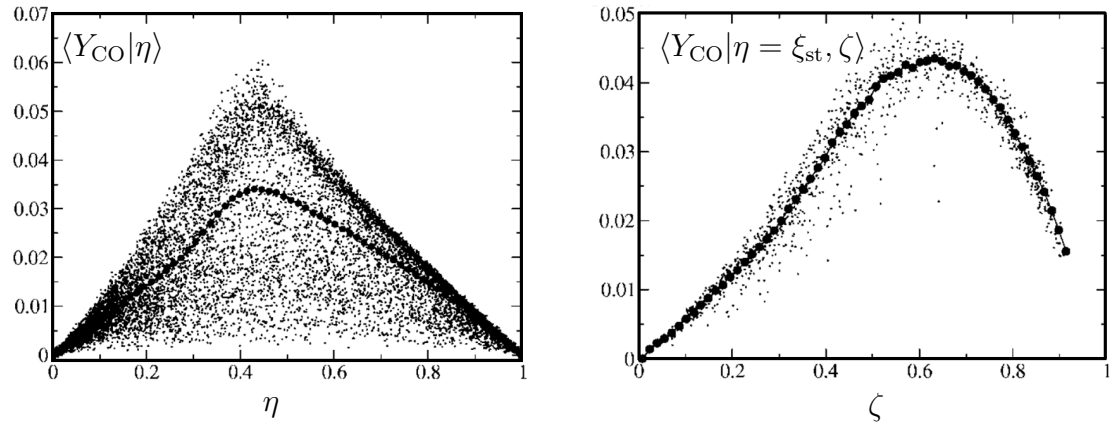


Fig. 2.6 Scatter plot and conditional mean (large symbosls) of $Y_{CO}$ from DNS with local extinction. Images from Kronenburg & Papoutsakis [2005].

Second-order CMC has achieved good agreement with DNS results for auto-ignition of a non-premixed flow [Mastorakos & Bilger, 1998], and a case with significant local extinction [Kim et al., 2002]. Furthermore, the approach has been applied with relative success to jet diffusion flames [Kim & Huh, 2004; Kronenburg et al., 1998] and flames with local extinction and re-ignition [Bradley et al., 2002; Fairweather & Woolley, 2007b; Kim & Huh, 2004]. In particular, in the case of local extinction second-order closure gave improved predictions of temperature and $O_2$ mass fraction, but some differences with the experiments remained. Sreedhara & Huh [2005] modelled a bluff-body flame, where second-order closure failed to improve the result significantly compared to first-order closure, even though conditional correlations were reasonably well predicted. The reason for these discrepancies is not clear, but Kronenburg & Mastorakos [2011, p. 100] conjectured that "corrections to the chemical source term may not suffice" in this case.

### 2.4.3 Doubly Conditional Moment Closure

An alternative strategy to provide accurate closure for the chemical reaction rate in cases where the correlation of the reactive scalars with the mixture fraction is weakened, is the introduction of a second conditioning variable. If most of the fluctuations around the (singly-) conditional mean, based on the mixture fraction, can be associated with the second conditional variable, then the fluctuation around the doubly-conditional mean, based on the mixture fraction and a second conditioning variable, are expected to be small. This is illustrated in Fig. 2.6: the correlation of $Y_{CO}$ with mixture fraction is weak as a result of local extinction, but most of the (singly-conditional) fluctuations

can be associated with fluctuations of sensible enthalpy. Consequently, the fluctuations around a doubly-conditional mean, based on mixture fraction and sensible enthalpy, would be small. Then a first-order closure for the chemical reaction rate based on the doubly-conditional means of the reactive scalars can be expected to be accurate. While second-order CMC attempted to model the effect of the conditional fluctuations, the strategy of double-conditioning aims to reduce the size of the conditional fluctuations.

The strategy of double-conditioning was fist proposed by Bilger [1992], who suggested conditioning on mixture fraction and a reaction progress variable such as temperature. This principle can be generalised by writing the CMC equation with multiple conditions. The reactive scalar $Y_\alpha$ can be conditionally averaged on a set of conditioning variables $\mathbf{Y}^c \equiv (Y_1^c, Y_2^c \ ... \ Y_{N_c}^c)$ and the conditional mean is defined as [Bilger, 1992]

$$Q_\alpha(\mathbf{Z}^c; \mathbf{x}, t) \equiv \langle Y_\alpha(\mathbf{x}, t) | \mathbf{Y}^c(\mathbf{x}, t) = \mathbf{Z}^c \rangle \tag{2.49}$$

where $\mathbf{Z}^c \equiv (Z_1^c, Z_2^c \ ... \ Z_{N_c}^c)$ contains the sample space variables, parametrising the $N_c$-dimensional conditional space. The transport equation of the conditional mean with multiple conditions (using similar assumptions as for Eqn. 2.42) can be written in a compact form with Einstein summation convention [Kronenburg & Mastorakos, 2011]:

$$\begin{aligned} \frac{\partial Q_\alpha}{\partial t} + \langle \mathbf{u} | \mathbf{Z}^c \rangle \cdot \nabla Q_\alpha = \langle \dot{\omega}_\alpha | \mathbf{Z}^c \rangle - \langle \dot{\omega}_{c,i} | \mathbf{Z}^c \rangle \frac{\partial Q_\alpha}{\partial Z_i^c} + \langle D \nabla Y_i^c \cdot \nabla Y_j^c | \mathbf{Z}^c \rangle \frac{\partial^2 Q_\alpha}{\partial Z_i^c \partial Z_j^c} \\ - \frac{1}{\langle \rho | \mathbf{Z}^c \rangle p(\mathbf{Z}^c)} \nabla \cdot (\langle \rho | \mathbf{Z}^c \rangle p(\mathbf{Z}^c) \langle \mathbf{u}'' Y_\alpha'' | \mathbf{Z}^c \rangle) \end{aligned} \tag{2.50}$$

where $\dot{\omega}_{c,i}$ is the reaction source term of the conditioning variable $Y_i^c$.

The development of Doubly Conditional Moment Closure (DCMC) was mainly motivated by the modelling of ignition and extinction. So far DCMC has only been applied in *a priori* tests where closure for conditional scalar dissipation rates was provided from a DNS dataset. Cha et al. [2001] used mixture fraction and scalar dissipation rate as conditioning variables. While extinction was well predicted, re-ignition occurred too early. This can be explained by the fact that (i) scalar dissipation rate does not correlate well with composition after extinction leading to large conditional fluctuations and that (ii) conditioning on the instantaneous scalar dissipation rate ignored the importance of the chemical time scales. Kronenburg [2004] used mixture fraction and sensible enthalpy as conditioning variables, following the suggestion by Bilger [1992]. This led to small conditional fluctuations and very good predictions of the composition and reaction rates, compared to the DNS. Hence, this study demonstrated that sensible

enthalpy was suitable second conditioning variable. Subsequently, Kronenburg & Papoutsakis [2005] managed to predicting accurately local extinction, the onset of re-ignition and global extinction observed in the DNS data. More recently Salehi et al. [2017] applied DCMC to study the effects of temperature inhomogeneities on ignition, using mixture fraction and scalar dissipation rate as conditioning variables. Relative to conventional CMC, DCMC gave improved results, but early ignition was also observed in both cases. Behzadi et al. [2018] studied the auto-ignition in a stratified mixture with DCMC, based on mixture fraction and sensible enthalpy, coupled to DNS. They compared DCMC with second-order CMC finding better performance of DCMC in the case of highly stratified mixture.

A comparison of the (i) second-order CMC and (ii) DCMC can be made, since both strategies were introduced for cases where fluctuations around the conditional mean render conventional CMC with first-order reaction rate closure inaccurate [Bilger, 1992, 1993b]. Second-order CMC refers to a correction of the conditional reaction rate closure to increase its accuracy for non-negligible conditional fluctuations. This strategy extends the capabilities of CMC, but the singly-conditional approach still assumes that the problem is predominantly described by the mixture fraction [Kronenburg & Mastorakos, 2011], and the second-order closure based on a Taylor expansion loses accuracy for large conditional fluctuations [Swaminathan & Bilger, 1999b]. In DCMC, a second conditioning variable is introduced, so that fluctuations around the doubly-conditional mean remain small enough for first-order closure. A DCMC formulation that uses sensible enthalpy as second conditioning variable, includes effects of heat and mass transport independent of the mixture fraction, and can accurately describe a combustion problem with arbitrary temperature fluctuations [Kronenburg, 2004]. A main challenge with DCMC is the closure problem, namely for the doubly-conditional scalar dissipation rates, as pointed out by Bilger [1992] and discussed by Kronenburg [2004].

Finally, it should be pointed out that the DCMC equation, under the assumption of spatial homogeneity, has similarities with the multi-dimensional flamelet equations derived by Nguyen et al. [2010] and Mittal et al. [2012]. Notably, Nguyen et al. [2010] suggested simple closure for the doubly-conditional SDRs.

### 2.4.4 LES-CMC

LES-CMC refers to the use of CMC within an LES-framework. In this case CMC takes the role of a sub-grid scale combustion model. The present section refers specifically to the adaptation of conventional CMC with first-order reaction rate closure to LES.

Nevertheless, LES-CMC deserves to be detailed in its own separate section, for its merit in tackle complex combustion problems, whose modelling would otherwise require a second-order CMC or DCMC approach. This section also explores the reason behind this success.

The use of LES as a means to obtain the flow and mixing field for CMC was already envisaged by Klimenko & Bilger [1999]. LES-CMC is based on the definition of the conditional filtering [Bushe & Steiner, 1999]. Navarro-Martinez et al. [2005] and Kim & Pitsch [2005] derived the CMC equation using an LES-consistent formulation. The resulting CMC equation is formally identical to Eqn. 2.42, but in the sense of LES $Q_\alpha$ is defined as the conditionally filtered variable and $p(\eta)$ is the filtered density function (FDF).

The coupling of LES and CMC, and the use of an LES-consistent framework for CMC has several advantages. First, LES provides a more accurate prediction of the flow and mixing field than RANS. In particular, improvements can be expected in complicated geometries, swirling and recirculating flows [Pitsch, 2006]. Second, LES resolves large-scale flow structures, leading to relatively small sub-grid scale variance of mixture fraction and narrow FDFs, which can be better approximated using a presumed PDF [Jiménez et al., 1997]. Finally, CMC is based on an LES-consistent (spatial) filtering procedure, and the evolution of the conditional moments due to large-scale flow structures is resolved in time. Therefore, an important aspect of LES-CMC is the transient solution of CMC coupled to the unsteady flow and mixing field. This is illustrated by Fig. 2.7, which shows LES-CMC results for the Sandia F flame [Garmory & Mastorakos, 2015] with considerable local extinction. Most of the scatter observed in the experiment is resolved by LES-CMC capturing the transient response of the local flame structure to the flow.

LES-CMC was first applied to a simple jet flame (Sandia D) [Navarro-Martinez et al., 2005], a bluff-body stabilised flame [Navarro-Martinez & Kronenburg, 2007] and a jet diffusion flame stabilised on a bluff body [Kim & Pitsch, 2006]. Navarro-Martinez & Kronenburg [2009, 2011] and Stanković et al. [2013] used LES-CMC to simulate lifted jet flames with auto-ignition. Coriton et al. [2015] and Kronenburg & Stein [2017] applied LES-CMC to a jet flame with partial premixing.

As detailed above, LES-CMC is well suited for simulating transient combustion phenomena. Triantafyllidis et al. [2009] simulated the ignition of a bluff-body stabilised flame and Tyliszczak [2015] modelled excited jet flames. More recently, Zhang et al. [2019] have used LES-CMC to simulated the ignition of a lifted jet, focusing on the edge flame propagation speed. The resolution of temporal fluctuations of the conditional

moments appears to be a key factor for the success of LES-CMC. The approach has been used successfully to predict local extinction in a piloted jet flame (Sandia F) [Garmory & Mastorakos, 2011] and bluff-body stabilised flames [Zhang et al., 2015; Zhang & Mastorakos, 2017]. In these cases, the simulation results showed good agreement with experimental measurements and, in particular, fluctuations of conditional temperature were well predicted. Zhang & Mastorakos [2016] simulated the global extinction in a bluff-body flame and predicted the blow-off velocity curve with reasonable accuracy, less than 25 % above the experimental values.

### 2.4.5 CMC for spray flames

As mixture fraction-based approach, CMC is a candidate for the modelling of spray flames where the combustion is mainly driven by the evaporation rate and the mixing of fuel and oxidiser. Notably, in a spray flame the mixture fraction is not a passive scalar since it is generated by evaporation. The CMC equation for a two-phase flow was rigorously derived (using the same assumptions as for Eqn. 2.42) by Mortensen & Bilger [2009]:

$$\begin{aligned}\frac{\partial Q_\alpha}{\partial t} + \langle \mathbf{u}|\eta\rangle \cdot \nabla Q_\alpha = \langle \dot{\omega}_\alpha|\eta\rangle + \langle N_\xi|\eta\rangle \frac{\partial^2 Q_\alpha}{\partial \eta^2} - \frac{\nabla \cdot (\langle\theta\rangle\langle\rho|\eta\rangle p(\eta)\langle \mathbf{u}'' Y_\alpha''|\eta\rangle)}{\langle\theta\rangle\langle\rho|\eta\rangle p(\eta)} \\ + \left(\delta_{\alpha \mathrm{F}} - Q_\alpha - (1-\eta)\frac{\partial Q_\alpha}{\partial \eta}\right)\frac{\langle \Pi|\eta\rangle}{\langle\theta\rangle} \\ - \frac{1}{\langle\theta\rangle\langle\rho|\eta\rangle p(\eta)}\frac{\partial}{\partial \eta}\left((1-\eta)\langle\rho|\eta\rangle p(\eta)\langle \Pi'' Y_\alpha''|\eta\rangle\right)\end{aligned} \tag{2.51}$$

where $\langle\theta\rangle$ is the gaseous volume fraction, with $\langle\theta\rangle \approx 1$ in a dilute spray, $\langle \Pi|\eta\rangle$ is the conditional volumetric evaporation rate per unit volume, and $\delta_{\alpha \mathrm{F}}$ is the Kronecker delta, equals unity for the fuel species, $\alpha = \mathrm{F}$, and zero otherwise.

In the CMC equation for two-phase flow, various terms are unclosed. In order to model the effect of the spray on the flame, these terms may require closure different from the gaseous case, with particular importance for $\langle \Pi|\eta\rangle$, $\langle N_\xi|\eta\rangle$ and the PDF [Mortensen & Bilger, 2009]. The term $\langle \Pi'' Y_\alpha''|\eta\rangle$ is assumed to be negligible [Borghesi et al., 2011]. In addition, the transport equation of the mixture fraction variance $\langle \xi'^2\rangle$ also requires closure for the terms $\langle \rho\xi\Pi\rangle$, $\langle \rho\xi^2\Pi\rangle$ and $\langle N_\xi\rangle$ [Mortensen & Bilger, 2009].

Early studies did not include spray source terms in the CMC equation and mixture fraction variance equation [De Paola et al., 2008b; Wright et al., 2005], or used a CMC equation with spray terms that were somewhat different [Kim & Huh, 2002; Sreedhara & Huh, 2007] from the terms derived by Mortensen & Bilger [2009]. Still, Wright

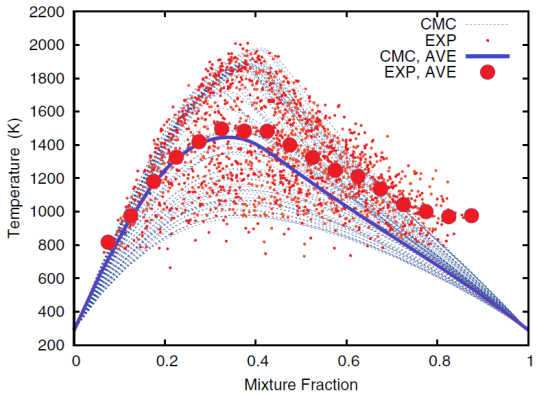


Fig. 2.7 Conditional temperature for the Sandia F flame at $y/d = 7.5$, $r = 6$ mm. Scatter plot and conditional mean from experiment [Barlow & Frank, 1998] compared to the instantaneous and time-averaged conditional mean from LES-CMC [Garmory & Mastorakos, 2011]. Adapted from Garmory & Mastorakos [2011].

et al. [2005] managed to accurately predict spray ignition, flame propagation and the establishment of a diffusion flame, and found good agreement of the autoignition delay with experiments for different temperatures and turbulent intensities. Various studies of spray combustion under IC-engine conditions using CMC have been performed by the ETH Zürich group, for instance Bolla et al. [2014, 2013]. Schroll et al. [2010] proposed to model $\langle \Pi | \eta \rangle$ as a $\delta$-functions at $\eta$ corresponding to the fuel vapour mass fraction at the droplet surface, and included spray terms in the mixture fraction variance equation. Borghesi et al. [2011] complemented this modelling approach, adding corrections to $\langle N_\xi | \eta \rangle$ and the PDF. In the simulation of an auto-igniting droplet-laden jet significant effects of the spray terms were found in regions with strong evaporation; effects on the temperature, corresponding to evaporative cooling, were more significant than effects on species mass fraction.

More recently LES-CMC has been applied to spray combustion. Bottone et al. [2012] simulated the auto-ignition of a Diesel spray. Spray terms were not included in the CMC equation or the mixture fraction SGS variance equation, but reasonable agreement with experiments in terms of the lift-off height was found. Ukai et al. [2013, 2014, 2015] performed LES-CMC of pilot-stabilised, spray jet flames (Sydney spray flames). The conditional evaporation rate $\langle \Pi | \eta \rangle$ was modelled as a $\delta$-function at the LES-filtered mean of mixture fraction. Moreover, LES-CMC has been applied to various transient combustion phenomena. Tyliszczak & Mastorakos [2013] simulated the forced ignition of a liquid-fuelled bluff-body swirl burner. Giusti & Mastorakos [2017] successfully predicted local extinction and lift-off, following preliminary studies

by Tyliszczak et al. [2014] and Giusti et al. [2016] and Giusti & Mastorakos [2016] predicted complete extinction in the same burner. In these studies, $\langle \Pi | \eta \rangle$ was modelled as a $\delta$-function at the droplet surface mixture fraction, and the effect of evaporation on the SGS-variance of mixture fraction was modelled.

### 2.4.6 CMC for premixed flames

The application of the CMC method to premixed flames, using a reaction progress variable as conditioning variable, seems natural and the first theoretical developments were already made by Bilger [1993b]. However, for a long time the development of CMC for premixed flames was held back by the issue of modelling of the conditional SDR, where progress was only made recently [Swaminathan & Bray, 2011].

For a suitable progress variable $c$, for instance based on sensible enthalpy and with $\mathrm{Le}_c = 1$, the transport equation of the conditional moment $Q_\alpha \equiv \langle Y_\alpha | c = \zeta \rangle$ can be written as follows [Bilger, 1993b; Mantel & Bilger, 1995; Swaminathan & Bilger, 2001]:

$$\begin{aligned} \frac{\partial Q_\alpha}{\partial t} + \langle \mathbf{u} | \zeta \rangle \cdot \nabla Q_\alpha = & \frac{1}{\mathrm{Le}_\alpha} \langle N_c | \zeta \rangle \frac{\partial^2 Q_\alpha}{\partial \zeta^2} + \langle \dot{\omega}_\alpha | \zeta \rangle - \langle \dot{\omega}_c | \zeta \rangle \frac{\partial Q_\alpha}{\partial \zeta} \\ & + \frac{1}{\langle \rho | \zeta \rangle p(\zeta)} \left( \frac{1}{\mathrm{Le}_\alpha} - 1 \right) \frac{\partial \langle \rho | \zeta \rangle \langle N_c | \eta \rangle p(\zeta)}{\partial \zeta} \\ & - \frac{1}{\langle \rho | \zeta \rangle p(\zeta)} \nabla \cdot \left[ \langle \rho | \zeta \rangle \langle \mathbf{u}'' Y_\alpha'' | \zeta \rangle p(\zeta) \right] \end{aligned} \tag{2.52}$$

where non-unity Lewis number effects are retained, since they are expected to be essential for the reaction-diffusion balance in premixed flames (otherwise using the same assumptions as for Eqn. 2.42).

In a first *a priori* test of premixed CMC against DNS, Swaminathan & Bilger [2001] showed that first-order closure for the reaction source provided good results. Nevertheless, very few applications of CMC to premixed flames exist. This is due to modelling issue that cannot be addressed in CMC, namely tracking the evolution of the reaction progress variable and its PDF in space and time. Even when using a presumed PDF approach, an accurate model for the mean SDR in turbulent premixed flame is required. In particular, the mean SDR of progress variable cannot be modelled like for a passive scalar, but dilatation effects were shown to be important [Swaminathan & Bray, 2005]. A model taking the dilatation into account was first proposed by Kolla et al. [2009].

Martin et al. [2003] used CMC (with RANS) to simulate an idealised aero-engine combustor. Yet, only a simple linear relaxation model was used for the mean SDR and unity Lewis number was assumed. Amzin et al. [2012] and Amzin & Swaminathan [2013] applied CMC to piloted, premixed jet flames, using a model for the mean SDR that considers dilatation effects [Kolla et al., 2009].

The first application of LES-CMC to premixed combustion was performed by Thornber et al. [2011], using a linear relaxation model for the (unconditionally) filtered SDR. Farrace et al. [2017] simulated premixed bluff-body flames approaching extinction, using an SDR model that considers dilatation effects [Dunstan et al., 2013]. Their results showed the right qualitative trends but the flame length was under-predicted. In a subsequent study, Farrace et al. [2018] included non-unity Lewis number effects in the CMC equation, and achieved very good agreement of CMC results with experiments.

## 2.5 Modelling approaches for turbulent spray flames

Various combustion models, other than CMC (see Section 2.4.5), have been applied to the modelling of turbulent spray flames. This section provides an overview of these models and some exemplary references for applications.

Presumed-PDF models with tabulated chemistry have been used in a large number of studies. Early applications to turbulent spray diffusion flames with flamelets and RANS include the work by Hollmann & Gutheil [1996, 1998], who used a tabulation based on mixture fraction and scalar dissipation rate. Various recent applications use a tabulation with the Flamelet Generated Manifold (FGM) model, developed by van Oijen & de Goey [2000] after original work by Bradley et al. [1988], and usually based on a tabulation of premixed flame calculations. The method has been applied to various spray flames, include simulations with RANS [Bekdemir et al., 2011; Ma & Roekaerts, 2016a] and LES [Chrigui et al., 2012, 2013; El-Asrag et al., 2016; Ma & Roekaerts, 2016a,b, 2017; Sacomano Filho et al., 2014]. The Flamelet/Progress Variable (FPV) approach [Pierce & Moin, 2004], in its original form uses a tabulation of diffusion flamelets. LES of spray combustion with the FPV approach include the work by De & Kim [2013] and El-Asrag et al. [2014]. Another recent work by Hu & Kurose [2018] used LES and a tabulation of premixed and non-premixed flamelets. Most of these applications with the FGM and FPV models use a tabulation based on mixture fraction and reaction progress variable, and potentially other quantities like enthalpy or pressure depending on the application.

The Artificially Thickened Flame (ATF) model, developed as an LES approach by Colin et al. [2000] after original work by Butler & O'Rourke [1977], has been applied to spray combustion. LES-applications include the work by Rittler et al. [2015] and Sacomano Filho et al. [2017], who used a hybrid approach of the ATF model with FGM tabulated chemistry.

Transported PDF methods have also been used for the modelling of turbulent spray flames. The transported PDF method with a Lagrangian algorithm [Pope, 1976] has been applied to spray combustion in combination with RANS by Ge & Gutheil [2008], who solved for the joint-PDF of mixture fraction and enthalpy, combined with a spray flamelet tabulation, Ma et al. [2016], who solved the PDF for mixture fraction and progress variable in combination with FGM tabulation, and Bhattacharjee & Haworth [2013] and Pei et al. [2013, 2015], who solved for the complete composition PDF. The transported PDF model in combination with LES, also denoted as transported Filtered Density Function (FDF) model or as LES/FDF, has been applied to spray flames by Heye et al. [2013] and Irannejad et al. [2015].

The Eulerian Stochastic Field (SF) method [Valiño, 1998], augmented with a stochastic spray implementation by Bini & Jones [2008], has been applied to various cases of turbulent spray combustion, including the early LES applications by Jones et al. [2011, 2012] and Prasad et al. [2013]. The Multiple Mapping Closure (MMC) model [Klimenko & Pope, 2003], which is both CMC and PDF-consistent, has only recently been applied to spray combustion with LES [Khan et al., 2018].

## 2.6 Summary

This Chapter contains a literature review of the topics most relevant to the research presented in this thesis. First, a brief introduction of general concepts of the numerical modelling of turbulent reacting flows was given. Second, a phenomenological overview of spray combustion was given, to reflect the modelling challenges associated with them. Most importantly, the complex structure of spray flames and the strong coupling of the physical processes involved were explained. In particular, this revealed the necessity to develop advanced combustion modelling tools in response to the multi-modal character of spray flames. Third, a detailed review of CMC modelling for turbulent reacting flows was provided. The CMC method has been used successfully to model a wide range of complex combustion problems. In particular, the strategy of double-conditioning appears very promising for the modelling of complex combustion phenomena. Finally,

some advanced combustion models, other than CMC, currently used for the modelling of turbulent spray flames were mentioned.

# Chapter 3

# DCMC Equation for Spray Combustion

## 3.1 Introduction

In the CMC framework, the composition of a turbulent reacting flow is described using the conditional mean of the reactive scalars. For these conditional means exact transport equations can be derived, which allow for accurate closure of the non-linear chemical source term. This chapter presents the DCMC equation for turbulent spray combustion – this is the transport equation of the conditional mean, based on two conditional variables, derived for a two-phase flow.

The DCMC equation is derived for the two conditioning variables, mixture fraction and reaction progress variable. Therefore, the DCMC equation for species mass fraction $Y_\alpha$ is the transport equation for the doubly-conditional mean $Q_\alpha$ defined as [Bilger, 1992]

$$Q_\alpha(\eta, \zeta; \mathbf{x}, t) \equiv \langle Y_\alpha(\mathbf{x}, t) | \xi(\mathbf{x}, t) = \eta, c(\mathbf{x}, t) = \zeta \rangle \equiv \langle Y_\alpha | \eta, \zeta \rangle \tag{3.1}$$

where $\eta$ and $\zeta$ are independent sample space variables of $\xi$ and $c$ respectively. The doubly-conditional mean is a function of space and time, and two independent conditioning variables.

The choice of conditioning variables, mixture fraction and reaction progress variable was first suggested by Bilger [1992]. Furthermore, the choice is supported by the wide-spread use of mixture fraction in conventional singly-conditional CMC for non-premixed combustion [Klimenko & Bilger, 1999], and the successful employment of the reaction progress variable in CMC for premixed flames [Amzin et al., 2012; Farrace et al., 2018, 2017]. Thus, a mixture fraction-progress variable approach appears to be

the most promising parametrisation for flames that involve premixed, non-premixed and intermediate burning modes. Moreover, Kronenburg [2004] showed that DCMC based on mixture fraction and a progress variable based on sensible enthalpy allowed to predict local extinction.

The mixture fraction-progress variables approach is also very commonly used for the parametrisation of tabulated chemistry, for instance in the FPV model [Pierce & Moin, 2004], the FGM model [van Oijen & de Goey, 2004], the multi-regime flamelet model [Knudsen & Pitsch, 2012] and the unstrained flamelet model [Ruan et al., 2014], later called FlaRe.

The derivation of the DCMC equation for spray combustion requires an accurate description of the local instantaneous fields in a two-phase flow. In the modelling of dilute spray flames, the effects of droplets on the gaseous phase are often introduced as simple source terms in the balance equations of the gaseous phase. This approach follows the point-particle assumption without considering the existence of an interface and introduces the effects of droplets in an average sense at the resolution of the flow field discretisation, or modelled otherwise. This approach is insufficient for the derivation of CMC equations. Instead a formalism for the local instantaneous description of a multi-phase flow is employed. In this way balance equation are obtained that are valid everywhere in an arbitrary multi-phase flow including the phase-interfaces. Transport equations for conditionally averaged fields are obtained by applying the appropriate averaging procedures to the local instantaneous balance equations [Mortensen & Bilger, 2009]. It should be mentioned that a rigorous framework for development of CMC for multi-phase flow is also found in Klimenko & Abdel-Jawad [2007].

The singly-conditional CMC equation for spray combustion has been derived by Mortensen & Bilger [2009]. The novel contribution of this chapter is the derivation of a DCMC equations for spray combustion, and the proposition of a complete set of closure models required for DCMC simulations with RANS and LES.

The chapter is organised as follows. First, the mathematical framework for the description of a multi-phase flow is introduced and the local instantaneous balance equations for a two-phase flow are given. Second, the DCMC equation for the species mass fraction is derived, using the local instantaneous balance equations for a two-phase flow. Third, the DCMC equation for enthalpy is presented. Fourth, comments are made about the derivation of the DCMC equation in the LES framework. Finally, closure for the DCMC equation is discussed and a set of closure models is suggested.

## 3.2 Local instantaneous balance equations

The governing equations of a single-phase turbulent reacting flow were detailed in Section 2.2.1. The local instantaneous balance equation for a multi-phase flow can be derived using a *two-fluid* (or *separated flow*) model, which is based on the assumption that the domain can be divided into two (or more) spatial domains that do not overlap, each one containing only one phase. The phase interfaces are assumed to be infinitely thin and without mass. Coupling of the two phases is effectuated by applying jump conditions at the phase-interfaces. The two-fluid formulation, developed by Kataoka [1986], is used here with the notation employed by Mortensen & Bilger [2009] for the derivation of the (singly-conditional) CMC equation for spray flames, to allow for a straight-forward comparison of the two equations. The formalism was also used by Zhu et al. [2000] to derive PDF transport equations for two-phase flows.

A phase-indicator function $\theta_k$ is used to distinguish different phase domains, $\theta_k = 1$ in the region occupied by phase $k$ and zero otherwise. A schematic clarifying the notation is shown in Fig. 3.1. Mathematically, the phase-indicator is defined as a Heaviside function.[1] Using this formalism, balance equations of a flow variable for a multi-phase flow can be simply obtained by multiplying the balance equation for a single-phase flow with $\theta_k$ and re-arranging; the phase-interface transfer terms occur naturally. The local instantaneous balance equations of the phase indicator function, density and species mass fraction are as follows [Kataoka, 1986; Mortensen & Bilger, 2009]:

$$\frac{\partial \theta_k}{\partial t} + \mathbf{u}_k \cdot \nabla \theta_k = \mathit{\Pi}_k \tag{3.2}$$

$$\frac{\partial \theta_k \rho_k}{\partial t} + \nabla \cdot (\theta_k \rho_k \mathbf{u}_k) = \rho_k \mathit{\Pi}_k \tag{3.3}$$

$$\frac{\partial \theta_k \rho_k Y_{k,\alpha}}{\partial t} + \nabla \cdot (\theta_k \rho_k (\mathbf{u}_k + \mathbf{V}_{k,\alpha}) Y_{k,\alpha}) = \theta_k \rho_k \dot{\omega}_{k,\alpha} + \rho_k Y_{k,\alpha} (\hat{V}_{k,\alpha} + \mathit{\Pi}_k) \tag{3.4}$$

Phase interface transfer is represented by the volumetric rate of phase change per unit volume, $\mathit{\Pi}_k \equiv -(\mathbf{u}_k - \mathbf{u}_I) \cdot \mathbf{n}_k a_I$, and the diffusion velocity across the phase-interface,

[1] The phase-indicator functions are defined as follows [Kataoka, 1986; Mortensen & Bilger, 2009]: a field variable $\beta$ is introduced, and the location of the interface is defined by the level-set condition $\beta(\mathbf{x}, t) = \beta_I$. The region occupied by phase 1 is defined where $\beta(\mathbf{x}, t) > \beta_I$ and the region of phase 2 where $\beta(\mathbf{x}, t) < \beta_I$. Hence, the phase indicator functions are defined as $\theta_1(\mathbf{x}, t) \equiv H(\beta(\mathbf{x}, t) - \beta_I)$ and $\theta_2(\mathbf{x}, t) \equiv 1 - H(\beta(\mathbf{x}, t) - \beta_I)$. It follows that the outward pointing normal vectors at the interface are defined as $\mathbf{n}_1 \equiv -\nabla\beta / \|\nabla\beta\|$ and $\mathbf{n}_2 \equiv \nabla\beta / \|\nabla\beta\|$. Note that this definition (phase 1: $\beta > \beta_I$; phase 2: $\beta < \beta_I$ ) follows Kataoka [1986]; Mortensen & Bilger [2009] defined the two phases in the opposite sense – the final result is unaffected.

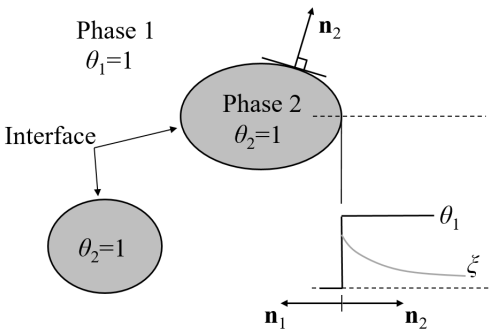


Fig. 3.1 Notation for the two-fluid model. The dashed line marks the orientation for the profiles of $\xi$ and $\theta_1$.

$\hat{V}_{k,\alpha} \equiv \mathbf{V}_{k,\alpha} \cdot \nabla\theta_k = -\mathbf{V}_{k,\alpha} \cdot \mathbf{n}_k a_I$, where $\mathbf{u}_I$ is the velocity of the interface, $a_I$ is the interfacial area concentration per unity volume[2] (area per volume), and $\mathbf{n}_k$ is the outward pointing normal vector of the interface, hence $\mathbf{n}_1$ pointing into phase 2. The normal vector is related to the phase indicator function[3], $a_I \mathbf{n}_k = -\nabla\theta_k$. The terms $\hat{V}_{k,\alpha}$ and $\mathit{\Pi}_k$ involve the spatial gradient of $\theta_k$ and are represented by a $\delta$-function at the interface.

The interface transfer terms, $\hat{V}_{k,\alpha}$ and $\mathit{\Pi}_k$, are zero everywhere, except for the phase-interfaces. Within the domain occupied by phase $k$ excluding the interface, $\theta_k = 1$ and the usual balance equations for density and species mass fraction for a single phase (Eqns 2.1 and 2.3) are re-covered. At the phase-interface the only non-zero terms are $\hat{V}_{k,\alpha}$ and $\mathit{\Pi}_k$. Since the interface is mass-less the balance of terms for the interface leads to the the jump conditions [Kataoka, 1986; Mortensen & Bilger, 2009],

$$\sum_{k=1}^{2} \rho_k \mathit{\Pi}_k = 0 \tag{3.5}$$

$$\sum_{k=1}^{2} \rho_k Y_{k,\alpha} (\hat{V}_{k,\alpha} + \mathit{\Pi}_k) = 0 \tag{3.6}$$

where it was assumed that no surface reaction takes place.

[2]The interfacial concentration per unit volume is defined as $a_I \equiv \|\nabla\beta\| \; \delta(\beta - \beta_I)$ [Kataoka, 1986; Mortensen & Bilger, 2009]

[3]The outward pointing normal vectors are defined as $\mathbf{n}_1 \equiv -\nabla\beta/\|\nabla\beta\|$ and $\mathbf{n}_2 \equiv \nabla\beta/\|\nabla\beta\|$. Recalling that the phase indicator functions are defined trough the Heaviside functions whose derivative is the $\delta$-function, $\nabla\theta_1 = \delta(\beta - \beta_I)\nabla\beta = -\delta(\beta - \beta_I)\|\nabla\beta\|\mathbf{n}_1$ and $\nabla\theta_2 = -\delta(\beta - \beta_I)\nabla\beta = -\delta(\beta - \beta_I)\|\nabla\beta\|\mathbf{n}_2$, hence, $\nabla\theta_k = -\delta(\beta - \beta_I)\|\nabla\beta\|\mathbf{n}_k = -a_I\mathbf{n}_k$ [Kataoka, 1986; Mortensen & Bilger, 2009].

Mortensen & Bilger [2009] pointed out how the equation for interface mass transfer in sprays, derived by Spalding [1955], is obtained from the jump conditions: the jump condition for the liquid (fuel) species is

$$\rho_G \Pi_G (Y_{G,s} - Y_L) = -(\rho_G Y_G \hat{V}_G)_s \tag{3.7}$$

where the subscripts represent the liquid ($L$) and gas ($G$) phase and the droplet surface ($s$). From the jump condition for mass it was used that $\rho_G \Pi_G = -\rho_L \Pi_L > 0$ for an evaporating droplet. Assuming Fickian diffusion, the following result, originally derived by Spalding [1955] is found (here, written in radial coordinates for a spherical droplet):

$$\dot{m}(Y_G - Y_L) = \rho_G D_G \nabla Y_G \cdot \mathbf{n}_L = \rho_G D_G \frac{\partial Y_G}{\partial r} \tag{3.8}$$

where $\mathbf{n}_L$ is the normal vector at the interface pointing into the gaseous phase and $\dot{m}$ is the evaporation rate per unity area, $\dot{m} \equiv -\rho_L(\mathbf{u}_I - \mathbf{u}_L) \cdot \mathbf{n}_L > 0$ for an evaporating droplet.

In the following, a separated flow model [Kataoka, 1986] is used to derive the local instantaneous balance equations of enthalpy, mixture fraction and reaction progress variable for a two-phase flow. The sub-script $k$ is omitted, since all equations are written for the gaseous phase, $\theta = \theta_G$, unless specifically indicated. Furthermore, Fick's law is assumed.

The local instantaneous balance equation of the enthalpy is

$$\begin{aligned} \frac{\partial \theta \rho h}{\partial t} + \nabla \cdot (\theta \rho h \mathbf{u}) = \nabla \cdot (\theta \lambda \nabla T) + \sum_{\alpha=1}^{N_\alpha} \nabla \cdot (\theta \rho h_\alpha D_\alpha \nabla Y_\alpha) \\ + \theta \frac{\partial p}{\partial t} + \theta \mathbf{u} \cdot \nabla p + \theta \boldsymbol{\tau} : \nabla \mathbf{u} + \theta \dot{Q} + \sum_{\alpha=1}^{N_\alpha} \theta \rho \ \mathbf{f}_\alpha \cdot (Y_\alpha \mathbf{V}_\alpha) \\ - \nabla \theta \cdot \lambda \nabla T + \sum_{\alpha=1}^{N_\alpha} \rho h_\alpha Y_\alpha \hat{V}_\alpha + \rho h \Pi \end{aligned} \tag{3.9}$$

where the spray source term (of the enthalpy equation in conservative form) is denoted as

$$\rho S_h = -\nabla \theta \cdot \lambda \nabla T + \sum_{\alpha=1}^{N_\alpha} \rho h_\alpha Y_\alpha \hat{V}_\alpha + \rho h \Pi \tag{3.10}$$

The mixture fraction $\xi$ is introduced as a passive scalar with respect to chemical reaction, $\xi = 0$ denoting pure air and $\xi = 1$ pure fuel vapour. It can be defined based on elemental mass fraction, as defined by Bilger [1976]. The local instantaneous balance

equations for mixture fraction is

$$\frac{\partial \theta \rho \xi}{\partial t} + \nabla \cdot (\theta \rho \mathbf{u} \xi) = \nabla \cdot (\theta \rho D \nabla \xi) + \rho \xi (\hat{V}_\xi + \mathit{\Pi}) \tag{3.11}$$

For the diffusivity of the mixture fraction $D$, usually unity Lewis number is assumed. The second term on the r.h.s. is the source term due to evaporation.

The reaction progress variable is defined as a linear function of a reactive scalar $Y_\psi$, where zero represents unburnt reactants $Y_\psi^u$, given by the mixing line, and one fully burnt mixture $Y_\psi^b$, taken equal to the equilibrium composition, $Y_\psi^{\mathrm{Eq}}$, as introduced by Bray et al. [2005]:

$$c(\mathbf{x}, t) \equiv c_\psi(\xi(\mathbf{x}, t), Y_\psi(\mathbf{x}, t)) \equiv \frac{Y_\psi^u(\xi(\mathbf{x}, t)) - Y_\psi(\mathbf{x}, t)}{Y_\psi^u(\xi(\mathbf{x}, t)) - Y_\psi^b(\xi(\mathbf{x}, t))} \tag{3.12}$$

As a direct consequence of this definition the mass fraction $Y_\psi$ is given as an exact function of $\xi$ and $c$:

$$Y_\psi(\xi, c) = (1 - c) Y_\psi^u(\xi) + c Y_\psi^b(\xi) \tag{3.13}$$

Different choices for $Y_\psi$ are found in various works, for instance the mass fraction of fuel, a product species, or a combination of species. In the present work $c$ is based on the mass fraction of carbon dioxide, $Y_\psi = Y_{\mathrm{CO2}}$. For illustrative purposes, the mass fraction of $CO_2$ at equilibrium as a function of mixture fraction, $Y_{\mathrm{CO2}}^{\mathrm{Eq}}(\xi)$, is shown in Fig. 3.2. The unburnt reactants do not contain any $CO_2$ and $Y_{\mathrm{CO2}}^u = 0$. The local instantaneous balance equation of the reaction progress variable is derived following Bray et al. [2005], also considering the phase-interface terms in the balance equations

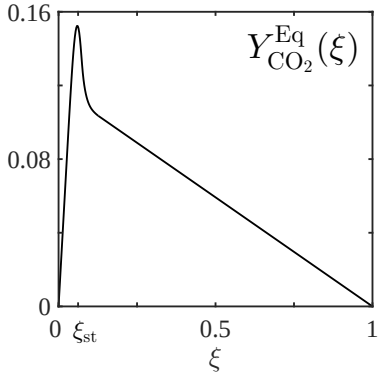


Fig. 3.2 Equilibrium mass fraction of $CO_2$ for combustion of n-heptane and air, approximated by a weakly strained non-premixed flamelet with the chemical mechanism by Smallbone et al. [2009].

of $\rho$, $\xi$ and $Y_\psi$:

$$\begin{aligned}\frac{\partial \theta\rho c}{\partial t} + \nabla\cdot(\theta\rho\mathbf{u}c) = \nabla\cdot(\theta\rho D\nabla c) \\ + \frac{\theta\rho}{\partial Y_\psi/\partial c}\left[\dot{\omega}_\psi + N_\xi\frac{\partial^2 Y_\psi}{\partial\xi^2} + 2N_{\xi c}\frac{\partial^2 Y_\psi}{\partial\xi\partial c} + N_c\frac{\partial^2 Y_\psi}{\partial c^2}\right] \\ + \frac{\rho}{\partial Y_\psi/\partial c}\left[Y_\psi\hat{V}_\psi - \xi\hat{V}_\xi\frac{\partial Y_\psi}{\partial\xi}\right] + \rho c\Pi\end{aligned} \tag{3.14}$$

where the scalar dissipation rates and cross-scalar dissipation rate are defined as

$$N_\xi \equiv D\nabla\xi\cdot\nabla\xi, \qquad N_c \equiv D\nabla c\cdot\nabla c, \qquad N_{\xi c} \equiv D\nabla\xi\cdot\nabla c \tag{3.15}$$

In the derivation of Eqn. 3.14, it is assumed that $c$ and $\xi$ have the same diffusivity $D$. It is important to consider this restriction when selecting a reactive scalar $Y_\psi$ as basis for the reaction progress variable. In principle, it is possible to relax this assumption but then additional terms appear and require modelling, which is not in the scope of this work. Due to the dependence of $c$ on $Y_\psi$ and $\xi$, in addition to the chemical reaction source term, present in perfectly premixed case, three terms appear that involve the scalar dissipation rates and cross-scalar dissipation rate. They are conveniently combined in the following term [Bray et al., 2005], which has been denoted as the *apparent reaction rate* [Ruan et al., 2012]:

$$\dot{\omega}_c^* \equiv \underbrace{\frac{1}{\partial Y_\psi/\partial c}\dot{\omega}_\psi}_{\dot{\omega}_c} + \underbrace{\frac{1}{\partial Y_\psi/\partial c}\left[N_\xi\frac{\partial^2 Y_\psi}{\partial\xi^2} + 2N_{\xi c}\frac{\partial^2 Y_\psi}{\partial\xi\partial c} + N_c\frac{\partial^2 Y_\psi}{\partial c^2}\right]}_{\dot{\omega}_p} \tag{3.16}$$

where $\dot{\omega}_c$ and $\dot{\omega}_p$ are introduced to distinguish the contribution of the direct chemical source term, $\dot{\omega}_c$, and effects of the scalar dissipation rates, $\dot{\omega}_p$. Note that the term $N_c\ \partial^2 Y_\psi/\partial c^2$ is zero for the usual linear definition of $c$ based on $Y_\psi$ (Eqn. 3.12). The term $\dot{\omega}_c$ is the reaction rate source term as it appears in fully premixed combustion; Chen et al. [2015] interpreted the term $N_\xi\ \partial^2 Y_\psi/\partial\xi^2$ as the contribution of the non-premixed burning mode. Moreover, the functional dependence of $c$ on $\xi$ and $Y_\psi$ leads to the appearance of evaporation source terms in Eqn. 3.14 (line 3). Note that the term $\rho c\Pi$ originated from the continuity equation, when writing the $c$-equation in conservative form. The presence of an evaporation source in the $c$-equation was discussed by Domingo et al. [2005].

For the evaporation source terms in Eqns 3.11 and 3.14, the diffusion velocity across the following jump conditions allow to relate the diffusion velocity across the interface

with the volumetric evaporation rate. Assuming a pure liquid fuel the jump conditions for mixture fraction, and for the species mass fractions, $Y_\psi$ and $Y_\alpha$, are

$$\xi\hat{V}_\xi = (1-\xi)\Pi, \qquad Y_\psi\hat{V}_\psi = (\delta_{\psi\mathrm{F}} - Y_\psi)\Pi, \qquad Y_\alpha\hat{V}_\alpha = (\delta_{\alpha\mathrm{F}} - Y_\alpha)\Pi \tag{3.17}$$

where the Kronecker delta was used, $\delta_{\alpha\mathrm{F}} = 1$ if $\alpha$ is the fuel species, zero otherwise, and similar for $\delta_{\psi\mathrm{F}}$.

We further define the following spray terms, which can be re-written using the jump conditions:

$$S_\xi^- \equiv \xi\hat{V}_\xi = (1-\xi)\Pi \tag{3.18}$$

$$S_c^- \equiv \frac{1}{\partial Y_\psi/\partial c}\left[Y_\psi\hat{V}_\psi - \xi\hat{V}_\xi\frac{\partial Y_\psi}{\partial\xi}\right] = \frac{1}{\partial Y_\psi/\partial c}\left[(\delta_{\psi\mathrm{F}} - Y_\psi) - (1-\xi)\frac{\partial Y_\psi}{\partial\xi}\right]\Pi \tag{3.19}$$

The purpose of these definitions will become apparent in the derivation of the DCMC equation (Sec. 3.3). So far it can be said that $S_\xi^-$ and $S_c^-$ are the spray source terms, as they occur in the $\xi$ and $c$-equation written in non-conservative form, which is obtained by subtracting the continuity equation times $\xi$ or $c$ from the respective transport equation.

## 3.3 Derivation of the DCMC equation

The DCMC equation equation can be derived in two different ways, using the decomposition method by Bilger [1993a] or the joint-PDF method by Klimenko [1990]. More details about both methods and a comparison is given in the review by Klimenko & Bilger [1999]. In the present work, the joint-PDF method is pursued. More specifically, the present derivation follows the derivation by Mortensen & Bilger [2009] to facilitate comparison.

The DCMC equation is derived for the two conditioning variables, mixture fraction and reaction progress variable. The doubly-conditional space is defined as

$$\mathbb{D} = \{(\eta,\zeta) \in \mathbb{R}^2 : 0 \le \eta \le 1, 0 \le \zeta \le 1\} \tag{3.20}$$

The derivation of the DCMC equation according to the joint-PDF method uses the *fine-grained PDF* [O'Brien, 1980; Pope, 1985], which is defined through the $\delta$-function

(see also Klimenko & Bilger [1999, p. 606]):

$$\Psi(\mathbf{x},t;\eta,\zeta) \equiv \delta(\eta - \xi(\mathbf{x},t))\ \delta(\zeta - c(\mathbf{x},t)) \tag{3.21}$$

Hence, $\Psi$ is zero for all $\xi$ and $c$, except for $(\xi, c) = (\eta, \zeta)$. The fine-grained PDF can be interpreted as the PDF for a single realisation of the flow [O'Brien, 1980]. The derivation method utilises the following two identities, relating the fine-grained PDF and the conventional mean to the PDF and the conditional mean [Klimenko & Bilger, 1999, pp. 606,608]:

$$\langle\Psi\rangle = p(\eta,\zeta), \qquad \langle\Psi F\rangle = \langle F|\eta,\zeta\rangle p(\eta,\zeta) \tag{3.22}$$

The fine-grained PDF is a generalised function, and the following rules for differentiation apply [Klimenko & Bilger, 1999, p. 610]:

$$\frac{\partial\Psi}{\partial t} = -\frac{\partial}{\partial\eta}\left(\Psi\frac{\partial\xi}{\partial t}\right) - \frac{\partial}{\partial\zeta}\left(\Psi\frac{\partial c}{\partial t}\right) \tag{3.23}$$

$$\nabla\Psi = -\frac{\partial}{\partial\eta}\left(\Psi\nabla\xi\right) - \frac{\partial}{\partial\zeta}\left(\Psi\nabla c\right) \tag{3.24}$$

Furthermore, the derivation uses the balance equations of $Y_\alpha$, $\xi$ and $c$ in the non-conservative form, obtained by subtracting Eqn. 3.3 from Eqns 3.4, 3.11 and 3.14 respectively:

$$\theta\rho\frac{\partial Y_\alpha}{\partial t} + \theta\rho\mathbf{u}\cdot\nabla Y_\alpha = \nabla\cdot(\theta\rho D_\alpha\nabla Y_\alpha) + \theta\rho\dot{\omega}_\alpha + \rho Y_\alpha\hat{V}_\alpha \tag{3.25}$$

$$\theta\rho\frac{\partial\xi}{\partial t} + \theta\rho\mathbf{u}\cdot\nabla\xi = \nabla\cdot(\theta\rho D\nabla\xi) + \rho S_\xi^- \tag{3.26}$$

$$\theta\rho\frac{\partial c}{\partial t} + \theta\rho\mathbf{u}\cdot\nabla c = \nabla\cdot(\theta\rho D\nabla c) + \theta\rho\dot{\omega}_c^* + \rho S_c^- \tag{3.27}$$

where Fick's law was assumed, with $\xi$ and $c$ having the same diffusivity. The apparent reaction rate, $\dot{\omega}_c^*$, is defined in Eqn. 3.16. Using the jump conditions, the spray terms are re-written as

$$S_\xi^- = (1-\xi)\Pi \tag{3.28}$$

$$S_c^- = \frac{1}{\partial Y_\psi/\partial c}\left[(\delta_{\psi\mathrm{F}} - Y_\psi) - (1-\xi)\frac{\partial Y_\psi}{\partial\xi}\right]\Pi \tag{3.29}$$

Hence, $S_\xi^-$ and $S_c^-$ are the spray source terms of the non-conservative form of the respective balance equations.

First the PDF transport equation is derived. One can start the derivation from [Klimenko, 1990]

$$\frac{\partial \theta\rho\Psi}{\partial t} = \Psi\frac{\partial \theta\rho}{\partial t} + \theta\rho\frac{\partial \Psi}{\partial t} \tag{3.30}$$

Using the differentiation rules in Eqns 3.23 and 3.24, and inserting from Eqns 3.3, 3.26 and 3.27 leads to the transport equation of the fine-grained PDF, as derived in Klimenko & Bilger [1999, p. 612], plus the phase-interface terms:

$$\begin{aligned}\frac{\partial \theta\rho\Psi}{\partial t} + \nabla\cdot(\theta\rho\mathbf{u}\Psi) = &-\nabla\cdot\left(\frac{\partial}{\partial\eta}(\Psi\theta\rho D\nabla\xi)\right) - \nabla\cdot\left(\frac{\partial}{\partial\zeta}(\Psi\theta\rho D\nabla c)\right)\\ &-\frac{\partial^2}{\partial\eta^2}(\Psi\theta\rho N_\xi) - \frac{\partial^2}{\partial\zeta^2}(\Psi\theta\rho N_c) - 2\frac{\partial^2}{\partial\eta\zeta}(\Psi\theta\rho N_{\xi c})\\ &-\frac{\partial}{\partial\zeta}(\Psi\theta\rho\dot\omega_c^*) - \frac{\partial}{\partial\eta}(\Psi\rho S_\xi^-) - \frac{\partial}{\partial\zeta}(\Psi\rho S_c^-) + \Psi\rho\Pi\end{aligned} \tag{3.31}$$

where $N_\xi \equiv D\nabla\xi\cdot\nabla\xi$, $N_c \equiv D\nabla c\cdot\nabla c$ and $N_{\xi c} \equiv D\nabla\xi\cdot\nabla c$ are the scalar and cross-scalar dissipation rates, and $S_\xi^-$ and $S_c^-$ are the evaporation source terms of the mixture fraction and reaction progress variable equations in non-conservative form. In Eqn. 3.31, the flow variables $\theta$, $\rho$, $\xi$ etc. are functions of $\mathbf{x}$ and $t$, and do not dependent of $\eta$ and $\zeta$. Consequently, they are cummutative with the derivatives $\partial/\partial\eta$ and $\partial/\partial\zeta$.

In order to obtain the PDF transport equation, the conventional average is applied to Eqn. 3.31 using the relation in Eqn. 3.22. The conventional average is commutative with differentiation. Since the homogeneous reaction associated with premixed and non-premixed combustion only takes place in the gaseous phase, the PDF and DCMC equations are derived for the gaseous phase only. For this purpose phase-averaging is used, only considering observations in the gaseous phase [Mortensen & Bilger, 2009]. Furthermore, density-weighted conditional averaging is applied to relax the assumption of small conditional fluctuations of the density [Klimenko & Bilger, 1999]. These averaging procedures are introduced as follows (compare with the definitions of phase-averaging in RANS in Section 4.2, and of phase-weighted filtering for LES in Section 4.3).

The conditional *phase-average* of an arbitrary flow variable $F$ is defined as [Klimenko & Abdel-Jawad, 2007; Mortensen & Bilger, 2009]

$$\overline{\langle F|\eta,\zeta\rangle} \equiv \frac{\overline{\overline{\langle\theta F|\eta,\zeta\rangle}}}{\overline{\overline{\langle\theta|\eta,\zeta\rangle}}} \tag{3.32}$$

where $\overline{\overline{\langle\theta|\eta,\zeta\rangle}}$ is the conditional ensemble average of $\theta$ considering both phases. The conditional average noted as $\overline{\overline{\langle\cdot|\eta,\zeta\rangle}}$ considers observations from both phases; $\overline{\langle\cdot|\eta,\zeta\rangle}$ is only representative of the phase corresponding to the phase indicator function $\theta$ – in the present case this is the gas phase.

The PDF considering observations from all phases is marked $\overline{\bar{p}}(\eta,\zeta)$. In the present case of a pure liquid, all observations from the liquid phase correspond to $\eta = 1$. The PDF of the gas phase (ignoring observations from the liquid phase) is defined as

$$\bar{p}(\eta,\zeta) \equiv \frac{\overline{\overline{\langle\theta|\eta,\zeta\rangle}}\ \overline{\bar{p}}(\eta,\zeta)}{\overline{\bar{\theta}}} \tag{3.33}$$

where $\overline{\bar{\theta}}$ is the ensemble average of $\theta$ over both phases.

The density-weighted conditional average is defined as [Klimenko & Bilger, 1999]

$$\widetilde{\langle F|\eta,\zeta\rangle} \equiv \frac{\overline{\langle\rho F|\eta,\zeta\rangle}}{\overline{\langle\rho|\eta,\zeta\rangle}} \tag{3.34}$$

where $\overline{\langle\rho|\eta,\zeta\rangle}$ is the conditional ensemble averaged of the density in the gas phase. Since the density-weighted average is applied after the phase-average, this is only the conditional average over the gas phase. The density-weighted PDF (of the gase phase) is defined as

$$\tilde{p}(\eta,\zeta) \equiv \frac{\overline{\langle\rho|\eta,\zeta\rangle}\ \bar{p}(\eta,\zeta)}{\bar{\rho}} \tag{3.35}$$

where $\bar{\rho}$ is the ensemble average of density in the gas phase, and $\bar{p}(\eta,\zeta)$ denotes the PDF of the gas-phase.

Applying the ensemble-average (over all phases), noted as $\langle\cdot\rangle$ and commutative with differentiation, to the fine-grained PDF leads to the following result. In a first step phase averaging is applied. Then the definition of the density-weighted average is applied to the gas phase. Finally, using the definitions of the gas-phase PDF and the density-weighted PDF leads to

$$\begin{aligned}\langle\Psi\theta\rho F\rangle &= \overline{\overline{\langle\theta\rho F|\eta,\zeta\rangle}}\ \overline{\bar{p}}(\eta,\zeta) = \overline{\overline{\langle\theta|\eta,\zeta\rangle}}\ \overline{\langle\rho|\eta,\zeta\rangle}\ \widetilde{\langle F|\eta,\zeta\rangle}\ \overline{\bar{p}}(\eta,\zeta) = \\ &= \overline{\bar{\theta}}\bar{\rho}\widetilde{\langle F|\eta,\zeta\rangle}\ \tilde{p}(\eta,\zeta)\end{aligned} \tag{3.36}$$

Note that Eqn. 3.32 is the general definition of phase-averaging but, assuming a pure fuel, all observations of the liquid phase corresponds to $\eta = 1$. If the conditional space was define as $0 \leq \eta < 1$, this would exclude the liquid phase, and $\theta$ could be omitted in the averaging: $\overline{\overline{\langle\theta|\eta,\zeta\rangle}}_{\eta<1} = 1$ and $\overline{\langle F|\eta,\zeta\rangle}_{\eta<1} = \overline{\overline{\langle\theta F|\eta,\zeta\rangle}}_{\eta<1}$. This was

similarly pointed out by Klimenko & Abdel-Jawad [2007]. In this case, the gas-phase PDF becomes $\bar{p} = \overline{\overline{p}}/\overline{\overline{\theta}}$, and the final result of averaging (Eqn. 3.36) is unchanged.

In the following the explicit distinction between these conditional averaging procedures is omitted. In this derivation, the phase-averaged and density-weighted conditional mean is marked as $\langle\cdot|\eta,\zeta\rangle$. The density-weighted DCMC equation for the gas phase can be identified by the occurrence of the mean gaseous volume fraction $\overline{\overline{\theta}}$, the mean density of the gas phase $\bar{\rho}$ and the density-weighted PDF of the gas phase $\tilde{p}(\eta,\zeta)$. Alternatively, if density-weighted conditional averaging was not used, the DCMC equation would contain $\langle\rho|\eta,\zeta\rangle\bar{p}(\eta,\zeta)$.

Averaging the transport equation of the fine-grained PDF (Eqn. 3.31) leads to the PDF transport equation. The result can be compared to the transport equation of the joint-PDF, derived by Dopazo & O'Brien [1974] and Pope [1976]. The transport equation for the density-weighted joint-PDF of $\xi$ and $c$ in a two-phase flow is as follows:

$$\begin{aligned}
&\frac{\partial\overline{\overline{\theta}}\bar{\rho}\tilde{p}}{\partial t}+\nabla\cdot(\overline{\overline{\theta}}\bar{\rho}\langle\mathbf{u}|\eta,\zeta\rangle\tilde{p}) = \\
&\quad -\nabla\cdot\left(\frac{\partial}{\partial\eta}(\overline{\overline{\theta}}\bar{\rho}\langle D\nabla\xi|\eta,\zeta\rangle\tilde{p})\right)-\nabla\cdot\left(\frac{\partial}{\partial\zeta}(\overline{\overline{\theta}}\bar{\rho}\langle D\nabla c|\eta,\zeta\rangle\tilde{p})\right) \\
&\quad -\frac{\partial^2}{\partial\eta^2}(\overline{\overline{\theta}}\bar{\rho}\langle N_\xi|\eta,\zeta\rangle\tilde{p})-\frac{\partial^2}{\partial\zeta^2}\overline{\overline{\theta}}\bar{\rho}\langle N_c|\eta,\zeta\rangle\tilde{p})-2\frac{\partial^2}{\partial\eta\zeta}(\overline{\overline{\theta}}\bar{\rho}\langle N_{\xi c}|\eta,\zeta\rangle\tilde{p}) \\
&\quad -\frac{\partial}{\partial\zeta}(\overline{\overline{\theta}}\bar{\rho}\langle\dot{\omega}_c^*|\eta,\zeta\rangle\tilde{p})-\frac{\partial}{\partial\eta}(\bar{\rho}\langle S_\xi^-|\eta,\zeta\rangle\tilde{p})-\frac{\partial}{\partial\zeta}(\bar{\rho}\langle S_c^-|\eta,\zeta\rangle\tilde{p})+\bar{\rho}\langle\Pi|\eta,\zeta\rangle\tilde{p}
\end{aligned} \tag{3.37}$$

In the next step the DCMC equation is derived. Multiplying Eqn. 3.31 with $Y_\alpha$, re-arranging and using Eqns 3.24 leads to

$$\begin{aligned}
&\frac{\partial\theta\rho Y_\alpha\Psi}{\partial t}+\nabla\cdot(\theta\rho\mathbf{u}Y_\alpha\Psi)=\nabla\cdot(\Psi\theta\rho D_\alpha\nabla Y_\alpha) \\
&\quad -\nabla\cdot\left(\frac{\partial}{\partial\eta}(\Psi\theta\rho Y_\alpha D\nabla\xi)\right)-\nabla\cdot\left(\frac{\partial}{\partial\zeta}(\Psi\theta\rho Y_\alpha D\nabla c)\right) \\
&\quad +\frac{\partial}{\partial\eta}(\Psi\theta\rho(D+D_\alpha)\nabla\xi\cdot\nabla Y_\alpha)+\frac{\partial}{\partial\zeta}(\Psi\theta\rho(D+D_\alpha)\nabla c\cdot\nabla Y_\alpha) \\
&\quad -\frac{\partial^2}{\partial\eta^2}(\Psi\theta\rho Y_\alpha N_\xi)-\frac{\partial^2}{\partial\zeta^2}(\Psi\theta\rho Y_\alpha N_c)-2\frac{\partial^2}{\partial\eta\zeta}(\Psi\theta\rho Y_\alpha N_{\xi c}) \\
&\quad +\Psi\theta\rho\dot{\omega}_\alpha-\frac{\partial}{\partial\zeta}(\Psi\theta\rho\dot{\omega}_c^*) \\
&\quad +\Psi\rho Y_\alpha\Pi+\Psi\rho Y_\alpha\hat{V}_\alpha-\frac{\partial}{\partial\eta}(\Psi\rho S_\xi^-)-\frac{\partial}{\partial\zeta}(\Psi\rho S_c^-)
\end{aligned} \tag{3.38}$$

Averaging leads to the transport equation of the doubly-conditional mean. This equation is exact – except for the assumption of Fick's law, which is used here to derive the scalar dissipation rate terms, but which is not required to obtain this result.

$$\begin{aligned}
&\frac{\partial\overline{\overline{\theta}}\bar{\rho}Q_\alpha\tilde{p}}{\partial t}+\nabla\cdot(\overline{\overline{\theta}}\bar{\rho}\langle\mathbf{u}Y_\alpha|\eta,\zeta\rangle\tilde{p})=\nabla\cdot(\overline{\overline{\theta}}\bar{\rho}\langle D_\alpha\nabla Y_\alpha|\eta,\zeta\rangle\tilde{p})\\
&\quad-\nabla\cdot\left(\frac{\partial}{\partial\eta}(\overline{\overline{\theta}}\bar{\rho}\langle Y_\alpha D\nabla\xi|\eta,\zeta\rangle\tilde{p})\right)-\nabla\cdot\left(\frac{\partial}{\partial\zeta}(\overline{\overline{\theta}}\bar{\rho}\langle Y_\alpha D\nabla c|\eta,\zeta\rangle\tilde{p})\right)\\
&\quad+\frac{\partial}{\partial\eta}(\overline{\overline{\theta}}\bar{\rho}\langle(D+D_\alpha)\nabla\xi\cdot\nabla Y_\alpha|\eta,\zeta\rangle\tilde{p})+\frac{\partial}{\partial\zeta}(\overline{\overline{\theta}}\bar{\rho}\langle(D+D_\alpha)\nabla c\cdot\nabla Y_\alpha|\eta,\zeta\rangle)\\
&\quad-\frac{\partial^2}{\partial\eta^2}(\overline{\overline{\theta}}\bar{\rho}\langle Y_\alpha N_\xi|\eta,\zeta\rangle\tilde{p})-\frac{\partial^2}{\partial\zeta^2}(\overline{\overline{\theta}}\bar{\rho}\langle Y_\alpha N_c|\eta,\zeta\rangle\tilde{p})-2\frac{\partial^2}{\partial\eta\zeta}(\overline{\overline{\theta}}\bar{\rho}\langle Y_\alpha N_{\xi c}|\eta,\zeta\rangle\tilde{p})\\
&\quad+\overline{\overline{\theta}}\bar{\rho}\langle\dot{\omega}_\alpha|\eta,\zeta\rangle\tilde{p}-\frac{\partial}{\partial\zeta}(\overline{\overline{\theta}}\bar{\rho}\langle\dot{\omega}_c^*|\eta,\zeta\rangle\tilde{p})\\
&\quad+\bar{\rho}\langle Y_\alpha\Pi|\eta,\zeta\rangle\tilde{p}+\bar{\rho}\langle Y_\alpha\hat{V}_\alpha|\eta,\zeta\rangle\tilde{p}-\frac{\partial}{\partial\eta}(\bar{\rho}\langle S_\xi^-|\eta,\zeta\rangle\tilde{p})-\frac{\partial}{\partial\zeta}(\bar{\rho}\langle S_c^-|\eta,\zeta\rangle\tilde{p})
\end{aligned}\tag{3.39}$$

In Eqn. 3.39, different terms of diffusive transport can be identified. Combining similar terms, the DCMC equation can be written in the following compact form:

$$\begin{aligned}
&\frac{\partial\overline{\overline{\theta}}\bar{\rho}Q_\alpha\tilde{p}}{\partial t}+\nabla\cdot(\overline{\overline{\theta}}\bar{\rho}\langle\mathbf{u}Y_\alpha|\eta,\zeta\rangle\tilde{p})=\nabla\cdot\mathbf{J}_D+\frac{\partial J_{Y\eta}}{\partial\eta}+\frac{\partial J_{Y\zeta}}{\partial\zeta}\\
&\qquad+\overline{\overline{\theta}}\bar{\rho}\langle\dot{\omega}_\alpha|\eta,\zeta\rangle\tilde{p}-\frac{\partial}{\partial\zeta}(\overline{\overline{\theta}}\bar{\rho}\langle\dot{\omega}_c^*|\eta,\zeta\rangle\tilde{p})\\
&\qquad+\bar{\rho}\langle Y_\alpha\Pi|\eta,\zeta\rangle\tilde{p}+\bar{\rho}\langle Y_\alpha\hat{V}_\alpha|\eta,\zeta\rangle\tilde{p}-\frac{\partial}{\partial\eta}(\bar{\rho}\langle S_\xi^-|\eta,\zeta\rangle\tilde{p})-\frac{\partial}{\partial\zeta}(\bar{\rho}\langle S_c^-|\eta,\zeta\rangle\tilde{p})
\end{aligned}\tag{3.40}$$

where $\mathbf{J}_D$ is the flux of molecular diffusion in physical space:

$$\mathbf{J}_D\equiv\overline{\overline{\theta}}\bar{\rho}\langle D_\alpha\nabla Y_\alpha|\eta,\zeta\rangle\tilde{p}-\frac{\partial}{\partial\eta}(\overline{\overline{\theta}}\bar{\rho}\langle Y_\alpha D\nabla\xi|\eta,\zeta\rangle\tilde{p})-\frac{\partial}{\partial\zeta}(\overline{\overline{\theta}}\bar{\rho}\langle Y_\alpha D\nabla c|\eta,\zeta\rangle\tilde{p})\tag{3.41}$$

and $J_{Y\eta}$ and $J_{Y\zeta}$ are the net diffusive fluxes of $Y_\alpha$ in conditional space, representative of small-scale diffusion processes. In contrast to conventional, singly-conditional CMC, in the present DCMC equation there are two fluxes, one for each direction of conditional space:

$$\begin{aligned}
J_{Y\eta}\equiv&(\overline{\overline{\theta}}\bar{\rho}\langle(D+D_\alpha)\nabla\xi\cdot\nabla Y_\alpha|\eta,\zeta\rangle\tilde{p})\\
&-\frac{\partial}{\partial\eta}(\overline{\overline{\theta}}\bar{\rho}\langle Y_\alpha N_\xi|\eta,\zeta\rangle\tilde{p})-\frac{\partial}{\partial\zeta}(\overline{\overline{\theta}}\bar{\rho}\langle Y_\alpha N_{\xi c}|\eta,\zeta\rangle\tilde{p})
\end{aligned}\tag{3.42}$$

$$
\begin{aligned}
J_{Y\zeta} \equiv & (\overline{\overline{\theta}}\bar{\rho}\langle(D+D_\alpha)\nabla c\cdot\nabla Y_\alpha|\eta,\zeta\rangle) \\
& -\frac{\partial}{\partial\zeta}(\overline{\overline{\theta}}\bar{\rho}\langle Y_\alpha N_c|\eta,\zeta\rangle\tilde{p}) - \frac{\partial}{\partial\eta}(\overline{\overline{\theta}}\bar{\rho}\langle Y_\alpha N_{\xi c}|\eta,\zeta\rangle\tilde{p})
\end{aligned}
\tag{3.43}
$$

These terms are unclosed.

In the molecular diffusion term $\nabla\cdot\mathbf{J}_D$, the first sub-term scales as $\mathrm{Re}_T^{-1}$ for finite Schmidt number $\mathrm{Sc}=\mu/(\rho D)$ [Bilger, 1993a]. The second and third sub-term scale as $\mathrm{Re}^{-1/2}N_\xi^{-1/2}$ and $\mathrm{Re}_T^{-1/2}N_c^{-1/2}$ respectively, and they are always smaller than the respective scalar dissipation rate terms [Navarro-Martinez et al., 2005]. In contrast the other terms of the DCMC equation are of the order one [Bilger, 1993a]. Consequently, the diffusion term $\nabla\cdot\mathbf{J}_D$ can be neglected in high Reynolds number flows, which is done in most CMC application. However, the small scale diffusion processes given by the fluxes $J_{Y,\eta}$ and $J_{Y\zeta}$ remain important. For this purpose the *primary closure hypothesis* is invoked to provide closure for $J_{Y\eta}$ and $J_{Y\zeta}$: Klimenko [1990] assumed that diffusion in conditional space was of Brownian nature, justifying the use of a first-order diffusion approximation. In DCMC, the linear diffusion relation, assumed by Klimenko [1990], becomes

$$
J_Y = A_1 Q_\alpha + A_2\frac{\partial Q_\alpha}{\partial\eta} + A_3\frac{\partial Q_\alpha}{\partial\zeta}
\tag{3.44}
$$

where the coefficients $A_1$, $A_2$ and $A_3$ must not depend on $Q_\alpha$ to preserve the linear properties of turbulent scalar transport. The coefficients can be determined by considering that the diffusion relation must hold in a simple mixing case without reaction. Then $Y_\alpha = a_1 + a_2\xi + a_3 c$, with constant $a_1$, $a_2$, $a_3$, is a solution of Eqn. 3.25. Inserting $Y_\alpha = a_1 + a_2\xi + a_3 c$ in Eqns 3.42 gives

$$
\begin{aligned}
J_{Y\eta} = & \, a_2(\overline{\overline{\theta}}\bar{\rho}\langle(D+D_\alpha)\nabla\xi\cdot\nabla\xi|\eta,\zeta\rangle\tilde{p}) + a_3(\overline{\overline{\theta}}\bar{\rho}\langle(D+D_\alpha)\nabla\xi\cdot\nabla c|\eta,\zeta\rangle\tilde{p}) \\
& - a_2\overline{\overline{\theta}}\bar{\rho}\langle N_\xi|\eta,\zeta\rangle\tilde{p} - (a_1+a_2\eta+a_3\zeta)\frac{\partial}{\partial\eta}(\overline{\overline{\theta}}\bar{\rho}\langle Y_\alpha N_\xi|\eta,\zeta\rangle\tilde{p}) \\
& - a_3\overline{\overline{\theta}}\bar{\rho}\langle N_{\xi c}|\eta,\zeta\rangle\tilde{p} - (a_1+a_2\eta+a_3\zeta)\frac{\partial}{\partial\zeta}(\overline{\overline{\theta}}\bar{\rho}\langle Y_\alpha N_{\xi c}|\eta,\zeta\rangle\tilde{p})
\end{aligned}
\tag{3.45}
$$

and inserting $Q_\alpha = a_1 + a_2\eta + a_3\zeta$ in Eqn. 3.44 gives

$$
J_{Y\eta} = A_1(a_1 + a_2\eta + a_3\zeta) + A_2 a_2 + A_3 a_3
\tag{3.46}
$$

Comparing the coefficients allows to determine $A_1$, $A_2$ and $A_3$ for the flux $J_{Y\eta}$; and similar for the other flux $J_{Y\zeta}$.

Thus a closed form of the diffusive fluxes is obtained:

$$\begin{aligned} J_{Y\eta} = & \left( \frac{\partial}{\partial \eta}(\overline{\overline{\theta}}\bar{\rho}\langle N_\xi|\eta,\zeta\rangle\tilde{p}) + \frac{\partial}{\partial \zeta}(\overline{\overline{\theta}}\bar{\rho}\langle N_{\xi c}|\eta,\zeta\rangle\tilde{p}) \right) Q_\alpha \\ & + \overline{\overline{\theta}}\bar{\rho}\langle D_\alpha \nabla\xi\cdot\nabla\xi|\eta,\zeta\rangle\tilde{p}\frac{\partial Q_\alpha}{\partial\eta} + \overline{\overline{\theta}}\bar{\rho}\langle D_\alpha\nabla\xi\cdot\nabla c|\eta,\zeta\rangle\tilde{p}\frac{\partial Q_\alpha}{\partial\zeta} \end{aligned} \tag{3.47}$$

$$\begin{aligned} J_{Y\zeta} = & \left( \frac{\partial}{\partial \eta}(\overline{\overline{\theta}}\bar{\rho}\langle N_{\xi c}|\eta,\zeta\rangle\tilde{p}) + \frac{\partial}{\partial \zeta}(\overline{\overline{\theta}}\bar{\rho}\langle N_{c}|\eta,\zeta\rangle\tilde{p}) \right) Q_\alpha \\ & + \overline{\overline{\theta}}\bar{\rho}\langle D_\alpha \nabla\xi\cdot\nabla c|\eta,\zeta\rangle\tilde{p}\frac{\partial Q_\alpha}{\partial\eta} + \overline{\overline{\theta}}\bar{\rho}\langle D_\alpha\nabla c\cdot\nabla c|\eta,\zeta\rangle\tilde{p}\frac{\partial Q_\alpha}{\partial\zeta} \end{aligned} \tag{3.48}$$

The DCMC equation (Eqn. 3.40) can be written in another, equivalent form by subtracting the PDF transport equation (Eqn. 3.37) times $Q_\alpha$:

$$\begin{aligned} \frac{\partial Q_\alpha}{\partial t} + \langle\mathbf{u}|\eta,\zeta\rangle\cdot\nabla Q_\alpha = & -\frac{1}{\overline{\overline{\theta}}\bar{\rho}\tilde{p}}\nabla\cdot(\overline{\overline{\theta}}\bar{\rho}\tilde{p}\langle\mathbf{u}''Y_\alpha''|\eta,\zeta\rangle) + \langle D_\alpha\nabla\xi\cdot\nabla\xi|\eta,\zeta\rangle\frac{\partial^2 Q_\alpha}{\partial\eta^2} \\ & + 2\langle D_\alpha\nabla\xi\cdot\nabla c|\eta,\zeta\rangle\frac{\partial^2 Q_\alpha}{\partial\eta\partial\zeta} + \langle D_\alpha\nabla c\cdot\nabla c|\eta,\zeta\rangle\frac{\partial^2 Q_\alpha}{\partial\zeta^2} \\ & + \langle\dot{\omega}_\alpha|\eta,\zeta\rangle - \langle\dot{\omega}_c^*|\eta,\zeta\rangle\frac{\partial Q_\alpha}{\partial\zeta} - \frac{1}{\overline{\overline{\theta}}\bar{\rho}\tilde{p}}\frac{\partial\overline{\overline{\theta}}\bar{\rho}\tilde{p}\langle Y_\alpha''\dot{\omega}_c^{*\prime\prime}|\eta,\zeta\rangle}{\partial\zeta} \\ & + (\delta_{\alpha\mathrm{F}} - Q_\alpha)\frac{\langle\mathit{\Pi}|\eta,\zeta\rangle}{\overline{\overline{\theta}}} - \frac{\langle S_\xi^-|\eta,\zeta\rangle}{\overline{\overline{\theta}}}\frac{\partial Q_\alpha}{\partial\eta} - \frac{\langle S_c^-|\eta,\zeta\rangle}{\overline{\overline{\theta}}}\frac{\partial Q_\alpha}{\partial\zeta} \\ & - \frac{1}{\overline{\overline{\theta}}\bar{\rho}\tilde{p}}\frac{\partial\bar{\rho}\tilde{p}\langle Y_\alpha''S_\xi^{-\prime\prime}|\eta,\zeta\rangle}{\partial\eta} - \frac{1}{\overline{\overline{\theta}}\bar{\rho}\tilde{p}}\frac{\partial\bar{\rho}\tilde{p}\langle Y_\alpha''S_c^{-\prime\prime}|\eta,\zeta\rangle}{\partial\zeta} \\ & + \mathcal{D}_{Q_\alpha} + \mathcal{D}_{D_\alpha} \end{aligned} \tag{3.49}$$

where $\mathcal{D}_{D_\alpha}$ is a differential diffusion term, which disappears for $D_\alpha = D$:

$$\begin{aligned} \mathcal{D}_{D_\alpha} \equiv & \frac{1}{\overline{\overline{\theta}}\bar{\rho}\tilde{p}}\frac{\partial\overline{\overline{\theta}}\bar{\rho}\tilde{p}\langle(D_\alpha - D)\nabla\xi\cdot\nabla\xi|\eta,\zeta\rangle}{\partial\eta}\frac{\partial Q_\alpha}{\partial\eta} \\ & + \frac{1}{\overline{\overline{\theta}}\bar{\rho}\tilde{p}}\frac{\partial\overline{\overline{\theta}}\bar{\rho}\tilde{p}\langle(D_\alpha - D)\nabla\xi\cdot\nabla c|\eta,\zeta\rangle}{\partial\eta}\frac{\partial Q_\alpha}{\partial\zeta} \\ & + \frac{1}{\overline{\overline{\theta}}\bar{\rho}\tilde{p}}\frac{\partial\overline{\overline{\theta}}\bar{\rho}\tilde{p}\langle(D_\alpha - D)\nabla\xi\cdot\nabla c|\eta,\zeta\rangle}{\partial\zeta}\frac{\partial Q_\alpha}{\partial\eta} \\ & + \frac{1}{\overline{\overline{\theta}}\bar{\rho}\tilde{p}}\frac{\partial\overline{\overline{\theta}}\bar{\rho}\tilde{p}\langle(D_\alpha - D)\nabla c\cdot\nabla c|\eta,\zeta\rangle}{\partial\zeta}\frac{\partial Q_\alpha}{\partial\zeta} \end{aligned} \tag{3.50}$$

and $\mathcal{D}_{Q_\alpha}$ represents molecular diffusion in physical space:

$$\begin{aligned}\mathcal{D}_{Q_\alpha} \equiv & \frac{1}{\bar{\bar{\theta}}\bar{\rho}\tilde{p}}\nabla\cdot(\bar{\bar{\theta}}\bar{\rho}\tilde{p}\langle D_\alpha\nabla Y_\alpha|\eta,\zeta\rangle) \\ & - \frac{1}{\bar{\bar{\theta}}\bar{\rho}\tilde{p}}\nabla\cdot\left(\frac{\partial\bar{\bar{\theta}}\bar{\rho}\tilde{p}\langle Y_\alpha D\nabla\xi|\eta,\zeta\rangle}{\partial\eta}\right) - \frac{1}{\bar{\bar{\theta}}\bar{\rho}\tilde{p}}\nabla\cdot\left(\frac{\partial\bar{\bar{\theta}}\bar{\rho}\tilde{p}\langle Y_\alpha D\nabla c|\eta,\zeta\rangle}{\partial\zeta}\right) \\ & + \frac{Q_\alpha}{\bar{\bar{\theta}}\bar{\rho}\tilde{p}}\nabla\cdot\left(\frac{\partial\bar{\bar{\theta}}\bar{\rho}\tilde{p}\langle D\nabla\xi|\eta,\zeta\rangle}{\partial\eta}\right) + \frac{Q_\alpha}{\bar{\bar{\theta}}\bar{\rho}\tilde{p}}\nabla\cdot\left(\frac{\partial\bar{\bar{\theta}}\bar{\rho}\tilde{p}\langle D\nabla c|\eta,\zeta\rangle}{\partial\zeta}\right)\end{aligned} \tag{3.51}$$

The conditional apparent reaction rate appears in closed form because $Y_\psi$ is a function of $\xi$ and $c$ (Eqn. 3.13), as a direct consequence of the definition of the progress variable (Eqn. 3.12), and, therefore, $Q_\psi = Y_\psi(\xi, c)$ and $Y''_\psi = Y_\psi - Q_\psi = 0$. The conditional apparent reaction rate becomes

$$\begin{aligned}\langle\dot{\omega}^*_c|\eta,\zeta\rangle = & \frac{1}{\partial Q_\psi/\partial\zeta}\langle\dot{\omega}_\psi|\eta,\zeta\rangle \\ & + \frac{1}{\partial Q_\psi/\partial\zeta}\left[\langle N_\xi|\eta,\zeta\rangle\frac{\partial^2 Q_\psi}{\partial\eta^2} + 2\langle N_{\xi c}|\eta,\zeta\rangle\frac{\partial^2 Q_\psi}{\partial\eta\partial\zeta} + \langle N_c|\eta,\zeta\rangle\frac{\partial^2 Q_\psi}{\partial\zeta^2}\right]\end{aligned} \tag{3.52}$$

and similar for the conditional spray source terms:

$$\langle S^-_\xi|\eta,\zeta\rangle = (1-\eta)\langle\Pi|\eta,\zeta\rangle \tag{3.53}$$

$$\langle S^-_c|\eta,\zeta\rangle = \frac{1}{\partial Q_\psi/\partial\zeta}\left[(\delta_{\psi\mathrm{F}} - Q_\psi) - (1-\eta)\frac{\partial Q_\psi}{\partial\eta}\right]\langle\Pi|\eta,\zeta\rangle \tag{3.54}$$

In Eqn. 3.49, term 2 represents convective transport and term 3 signifies turbulent transport in physical space. The terms 4–6 contain the SDRs and represent small-scale diffusion process; micro mixing terms are also included in the apparent reaction rate (term 8, detailed in Eqn. 3.52). The chemical reaction is represented by term 7 and the first part of term 8. Terms 10–14 represent the effect of spray evaporation. Term 15, denoted $\mathcal{D}_{D_\alpha}$, groups the terms of differential diffusion, which vanish in the case of unity Lewis number. Term 16, denoted $\mathcal{D}_{Q_\alpha}$, contains the molecular diffusion terms that are negligible at high Reynolds number.

## 3.4 DCMC equation for enthalpy

A similar equation can be derived for the conditional mean of the enthalpy $Q_h$. The $Q_h$-equation is derived starting from the enthalpy equation in non-conservative form:

$$\begin{aligned}\theta\rho\frac{\partial h}{\partial t} + \theta\rho\mathbf{u}\cdot\nabla h = \nabla\cdot(\theta\lambda\nabla T) + \sum_{\alpha=1}^{N_\alpha}\nabla\cdot(\theta\rho h_\alpha D_\alpha\nabla Y_\alpha) \\ + \theta\frac{\partial p}{\partial t} + \theta\mathbf{u}\cdot\nabla p + \theta\boldsymbol{\tau}:\nabla\mathbf{u} + \theta\dot{Q} + \sum_{\alpha=1}^{N_\alpha}\theta\rho\ \mathbf{f}_\alpha\cdot(Y_\alpha\mathbf{V}_\alpha) \\ - \nabla\theta\cdot\lambda\nabla T + \sum_{\alpha=1}^{N_\alpha}\rho h_\alpha Y_\alpha\hat{V}_\alpha\end{aligned} \tag{3.55}$$

Assuming a low Mach number flow allows to neglect terms two and three in the second line [Poinsot & Veynante, 2005]. Furthermore, the effect of the body force $\mathbf{f}_\alpha$ on $h$ (term five in the second line) is neglected. The diffusion terms in Eqn. 3.55 can be re-written, so differential diffusion appears explicitly:

$$\nabla\cdot(\theta\lambda\nabla T)+\sum_{\alpha=1}^{N_\alpha}\nabla\cdot(\theta\rho h_\alpha D_\alpha\nabla Y_\alpha) = \nabla\cdot(\theta\rho D\nabla h)+\sum_{\alpha=1}^{N_\alpha}\nabla\cdot(\theta\rho h_\alpha(D_\alpha-D)\nabla Y_\alpha) \tag{3.56}$$

where it was used that $\nabla h = C_p\nabla T + h_\alpha\nabla Y_\alpha$ and that $\mathrm{Le} = \lambda/(\rho C_p D) = 1$ for the diffusivity of the mixture fraction $D$.

Following the same derivation steps as detailed for the $Q_\alpha$-equation, leads to the transport equation for $Q_h$:

$$\begin{aligned}\frac{\partial Q_h}{\partial t} + \langle\mathbf{u}|\eta,\zeta\rangle\cdot\nabla Q_h = -\frac{1}{\overline{\bar{\theta}}\bar{\rho}\tilde{p}}\nabla\cdot(\overline{\bar{\theta}}\bar{\rho}\tilde{p}\langle\mathbf{u}''h''|\eta,\zeta\rangle) + \langle D\nabla\xi\cdot\nabla\xi|\eta,\zeta\rangle\frac{\partial^2 Q_h}{\partial\eta^2} \\ + 2\langle D\nabla\xi\cdot\nabla c|\eta,\zeta\rangle\frac{\partial^2 Q_h}{\partial\eta\partial\zeta} + \langle D\nabla c\cdot\nabla c|\eta,\zeta\rangle\frac{\partial^2 Q_h}{\partial\zeta^2} \\ - \langle\dot{\omega}_c^*|\eta,\zeta\rangle\frac{\partial Q_h}{\partial\zeta} - \frac{1}{\overline{\bar{\theta}}\bar{\rho}\tilde{p}}\frac{\partial\overline{\bar{\theta}}\bar{\rho}\tilde{p}\langle h''\dot{\omega}_c^{*\prime\prime}|\eta,\zeta\rangle}{\partial\zeta} \\ + \frac{\langle S_h|\eta,\zeta\rangle}{\overline{\bar{\theta}}} - \frac{\langle\Pi|\eta,\zeta\rangle}{\overline{\bar{\theta}}}Q_h - \frac{\langle S_\xi^-|\eta,\zeta\rangle}{\overline{\bar{\theta}}}\frac{\partial Q_\alpha}{\partial\eta} - \frac{\langle S_c^-|\eta,\zeta\rangle}{\overline{\bar{\theta}}}\frac{\partial Q_\alpha}{\partial\zeta} \\ - \frac{1}{\overline{\bar{\theta}}\bar{\rho}\tilde{p}}\frac{\partial\bar{\rho}\tilde{p}\langle h''S_\xi^{-\prime\prime}|\eta,\zeta\rangle}{\partial\eta} - \frac{1}{\overline{\bar{\theta}}\bar{\rho}\tilde{p}}\frac{\partial\bar{\rho}\tilde{p}\langle h''S_c^{-\prime\prime}|\eta,\zeta\rangle}{\partial\zeta} \\ + \mathcal{D}_{Q_h} + \mathcal{D}_{D_h} + \frac{1}{\bar{\rho}}\langle\dot{Q}|\eta,\zeta\rangle + \frac{1}{\bar{\rho}}\Big\langle\frac{\partial p}{\partial t}\Big|\eta,\zeta\Big\rangle\end{aligned} \tag{3.57}$$

where $\langle \dot{Q}|\eta,\zeta\rangle$ is a source/sink term due to a spark or radiation, for example. $\mathcal{D}_{D_h}$ contains the effects of differential diffusion,

$$\begin{aligned}\mathcal{D}_{D_h} = &\frac{1}{\overline{\overline{\theta}}\bar{\rho}\tilde{p}}\sum_{\alpha=1}^{N_\alpha}\frac{\partial\overline{\overline{\theta}}\bar{\rho}\tilde{p}\langle h_\alpha(D_\alpha - D)\nabla\xi\cdot\nabla\xi|\eta,\zeta\rangle}{\partial\eta}\frac{\partial Q_\alpha}{\partial\eta}\\ &+\frac{1}{\overline{\overline{\theta}}\bar{\rho}\tilde{p}}\sum_{\alpha=1}^{N_\alpha}\frac{\partial\overline{\overline{\theta}}\bar{\rho}\tilde{p}\langle h_\alpha(D_\alpha - D)\nabla\xi\cdot\nabla c|\eta,\zeta\rangle}{\partial\eta}\frac{\partial Q_\alpha}{\partial\zeta}\\ &+\frac{1}{\overline{\overline{\theta}}\bar{\rho}\tilde{p}}\sum_{\alpha=1}^{N_\alpha}\frac{\partial\overline{\overline{\theta}}\bar{\rho}\tilde{p}\langle h_\alpha(D_\alpha - D)\nabla\xi\cdot\nabla c|\eta,\zeta\rangle}{\partial\zeta}\frac{\partial Q_\alpha}{\partial\eta}\\ &+\frac{1}{\overline{\overline{\theta}}\bar{\rho}\tilde{p}}\sum_{\alpha=1}^{N_\alpha}\frac{\partial\overline{\overline{\theta}}\bar{\rho}\tilde{p}\langle h_\alpha(D_\alpha - D)\nabla c\cdot\nabla c|\eta,\zeta\rangle}{\partial\zeta}\frac{\partial Q_\alpha}{\partial\zeta}\end{aligned} \tag{3.58}$$

and $\mathcal{D}_{Q_h}$ is the term of molecular diffusion in physical space

$$\begin{aligned}\mathcal{D}_{Q_h} = &\frac{1}{\overline{\overline{\theta}}\bar{\rho}\tilde{p}}\nabla\cdot(\overline{\overline{\theta}}\bar{\rho}\tilde{p}\langle D\nabla h|\eta,\zeta\rangle)\\ &-\frac{1}{\overline{\overline{\theta}}\bar{\rho}\tilde{p}}\nabla\cdot\left(\frac{\partial\overline{\overline{\theta}}\bar{\rho}\tilde{p}\langle hD\nabla\xi|\eta,\zeta\rangle}{\partial\eta}\right)-\frac{1}{\overline{\overline{\theta}}\bar{\rho}\tilde{p}}\nabla\cdot\left(\frac{\partial\overline{\overline{\theta}}\bar{\rho}\tilde{p}\langle hD\nabla c|\eta,\zeta\rangle}{\partial\zeta}\right)\\ &+\frac{Q_h}{\overline{\overline{\theta}}\bar{\rho}\tilde{p}}\nabla\cdot\left(\frac{\partial\overline{\overline{\theta}}\bar{\rho}\tilde{p}\langle D\nabla\xi|\eta,\zeta\rangle}{\partial\eta}\right)+\frac{Q_h}{\overline{\overline{\theta}}\bar{\rho}\tilde{p}}\nabla\cdot\left(\frac{\partial\overline{\overline{\theta}}\bar{\rho}\tilde{p}\langle D\nabla c|\eta,\zeta\rangle}{\partial\zeta}\right)\end{aligned} \tag{3.59}$$

## 3.5 Derivation of the DCMC equation for LES

The DCMC equation is derived using the conditional averaging procedure. In the LES-context, a doubly-conditional filter can be defined as [Bushe & Steiner, 1999],

$$\langle F(\mathbf{x},t)|\eta,\zeta\rangle = \frac{\int_V F(\mathbf{x}',t)\;\delta(\eta-\xi(\mathbf{x}',t))\;\delta(\zeta-c(\mathbf{x}',t))\;G(\mathbf{x}-\mathbf{x}')\;\mathrm{d}V'}{p(\eta,\zeta)} \tag{3.60}$$

where the fine-grained PDF (Eqn. 3.21) was used, $G(\mathbf{x}-\mathbf{x}')$ is the spatial filter, and $p(\eta,\zeta)$ is the PDF of scalars $\eta$ and $\zeta$ at the sub-filter scale, denoted as the filtered density function (FDF). The filtered density function, first introduced by Pope [1991, p. 596] (see also Colucci et al. [1998]), is defined as

$$p(\mathbf{x},t;\eta,\zeta) = \int_V \delta(\eta-\xi(\mathbf{x}',t))\;\delta(\zeta-c(\mathbf{x}',t))\;G(\mathbf{x}-\mathbf{x}')\;\mathrm{d}V' \tag{3.61}$$

Starting from these definitions, conditional phase-averaging and density-weighted averaging can be defined analogue to Eqns 3.32 and 3.34.

Navarro-Martinez et al. [2005] pointed out that the derivation according to the *decomposition method* suggested by Bilger [1993a], was not consistent with the LES-filtering procedure. Consequently, the *joint-PDF method* [Klimenko, 1990] is employed. The DCMC equation is derived starting from the transport equation of the fine-grained PDF and then applying the LES filter. The derivation can be found in Appendix A.

The resulting DCMC equation is virtually identical to Eqn. 3.49 (also for the enthalpy with Eqn. 3.57). Instead of the conditional variances and co-variances that appear in Eqns 3.49 and 3.57, LES-consistent DCMC equation formally contains, for instance, $(\langle \mathbf{u} Y_\alpha | \eta, \zeta \rangle - \langle \mathbf{u} | \eta, \zeta \rangle Q_\alpha \rangle)$ etc.

## 3.6 Boundary and initial conditions for DCMC

The DCMC equation is a partial differential equation in time, space and the two conditioning variables, $\eta$ and $\zeta$. Boundary conditions are required in physical space, $(x, y, z)$, and in the doubly-conditional space, $(\eta, \zeta)$.

The doubly-conditional space $\mathbb{D}$ is delimited by four boundaries, where the following boundary conditions are applied: Dirichlet boundary conditions are applied at $\eta = 0$ corresponding to the composition of air and at $\eta = 1$ corresponding pure fuel vapour. Dirichlet boundary conditions are also applied at $\zeta = 0$ corresponding to the composition at the mixing line and at $\zeta = 1$ corresponding the equilibrium composition, as follows directly from the definition of the progress variable (Eqn. 3.12).

Hence, the boundary conditions of the doubly-conditional space are fixed in time and space. In certain cases it might be appropriate to relax these conditions and, for instance, let the boundary at $\zeta = 1$ evolve in time. This extension may be useful in flames with non-adiabatic effects or cases where the equilibrium composition is not representative. For completeness, the modifications to the DCMC equation that would occur in that case, can be found in Appendix B.

At the boundaries of the physical space the following boundary conditions are applied: at inlets a set of conditional moments, $Q_\alpha$ ($\alpha = 1...N_\alpha$) and $Q_h$, is fixed. For this purpose the flame structure of a weakly strained flame can be used, and the procedure for obtaining the corresponding set of conditional moments, is presented in Ch. 5. At walls and outlets zero-gradient boundary conditions are applied.

As initial condition a set of conditional moments, $Q_\alpha$ and $Q_h$ needs to be provided in the entire domain. The same set of conditional moments used at the inlet may be used.

## 3.7 Closure for the DCMC equation

Equation 3.49 is a very general form of the DCMC equation, obtained after making only very minor assumptions, mainly by invoking the *primary closure hypothesis*. In order to solve this equation, several simplifying assumptions are made in the following. Then the modelling of unclosed terms is discussed.

A dilute spray is assumed, so that the volume fraction of the gas phase $\overline{\overline{\theta}} \approx 1$. Unity Lewis number is assumed. Consequently $D_\alpha = D = a$ and the differential diffusion term vanishes. The modelling of differential diffusion is not in the scope of the present work, but can be considered in the future. The terms of molecular diffusion are neglected except for the first term in Eqn. 3.51, which is retained. In RANS the effect of this term is expected to be small, but in finely resolved LES the sub-grid scale turbulent viscosity $\mu_T$ can be of similar size as the molecular viscosity $\bar{\mu}$. This term was also retained in previous LES-CMC applications by Navarro-Martinez & Kronenburg [2007, 2009, 2011]. The other terms of molecular transport physical space are neglected, since they have been shown to be smaller than the SDR terms [Navarro-Martinez et al., 2005]. The term of transport in physical space was re-arranged as advective and dilatation term. The conditional correlations $\langle Y''_\alpha \dot{\omega}^{*\prime\prime}_c | \eta, \zeta \rangle$ can be re-written to make appear the terms $\langle Y''_\alpha \dot{\omega}''_\psi | \eta, \zeta \rangle$, $\langle Y''_\alpha N''_\xi | \eta, \zeta \rangle$, $\langle Y''_\alpha N''_c | \eta, \zeta \rangle$ and $\langle Y''_\alpha N''_{\xi c} | \eta, \zeta \rangle$, and consequently it is neglected as second-order term. In the context of first-order CMC, terms of this type are neglected. Notably, this term does not appear if the DCMC equation is derived following the *decomposition method* by Bilger [1993b]. In the same way the conditional correlation with the evaporation rate $\langle Y''_\alpha \Pi'' | \eta \rangle$ does not appear when using the *decomposition method*. Here $\langle Y''_\alpha \Pi'' | \eta \rangle$ is neglected, as in all previous work on the modelling of spray flames with CMC. This leads to the DCMC equation in the following form:

$$
\begin{aligned}
\frac{\partial Q_\alpha}{\partial t} + \nabla\cdot(\langle \mathbf{u}|\eta,\zeta\rangle Q_\alpha) &= Q_\alpha \nabla\cdot\langle \mathbf{u}|\eta,\zeta\rangle \\
&- \frac{1}{\bar{\rho}\tilde{p}(\eta,\zeta)} \nabla\cdot(\bar{\rho}\tilde{p}(\eta,\zeta)\langle \mathbf{u}'' Y''_\alpha|\eta,\zeta\rangle) + \frac{1}{\bar{\rho}\tilde{p}(\eta,\zeta)} \nabla\cdot(\bar{\rho}\tilde{p}(\eta,\zeta)\langle D\nabla Y_\alpha|\eta,\zeta\rangle) \\
&+ \langle N_\xi|\eta,\zeta\rangle \frac{\partial^2 Q_\alpha}{\partial \eta^2} + 2\langle N_{\xi c}|\eta,\zeta\rangle \frac{\partial^2 Q_\alpha}{\partial \eta \partial \zeta} + \langle N_c|\eta,\zeta\rangle \frac{\partial^2 Q_\alpha}{\partial \zeta^2} \\
&+ \langle \dot{\omega}_\alpha|\eta,\zeta\rangle - \langle \dot{\omega}^*_c|\eta,\zeta\rangle \frac{\partial Q_\alpha}{\partial \zeta} \\
&+ (\delta_{\alpha \mathrm{F}} - Q_\alpha)\langle \Pi|\eta,\zeta\rangle - \langle S^-_\xi|\eta,\zeta\rangle \frac{\partial Q_\alpha}{\partial \eta} - \langle S^-_c|\eta,\zeta\rangle \frac{\partial Q_\alpha}{\partial \zeta}
\end{aligned}
\tag{3.62}
$$

where $\langle\cdot|\eta,\zeta\rangle$ represents density-weighted conditional averaging, $\tilde{p}(\eta,\zeta)$ is the density-weighted PDF and $\bar{\rho}$ is the unconditionally averaged density. The definitions of $\langle\dot{\omega}_c^*|\eta,\zeta\rangle$, $\langle S_\xi^-|\eta,\zeta\rangle$ and $\langle S_c^-|\eta,\zeta\rangle$ are unchanged, as in Eqns 3.52, 3.53 and 3.54 respectively and the Kronecker delta $\delta_{\alpha\mathrm{F}}$ is used as previously introduced in Eqn. 3.17.

The conditional apparent reaction rate $\langle\dot{\omega}_c^*|\eta,\zeta\rangle$ consists of a term due to chemical reaction, $\langle\dot{\omega}_c|\eta,\zeta\rangle$, and a group of terms that contain the scalar dissipation rates, $\langle\dot{\omega}_p|\eta,\zeta\rangle$, as defined in Eqn. 3.16:

$$\langle\dot{\omega}_c^*|\eta,\zeta\rangle = \langle\dot{\omega}_c|\eta,\zeta\rangle + \langle\dot{\omega}_p|\eta,\zeta\rangle \tag{3.63}$$

where

$$\langle\dot{\omega}_c|\eta,\zeta\rangle = \frac{1}{\partial Q_\psi/\partial\zeta}\langle\dot{\omega}_\psi|\eta,\zeta\rangle \tag{3.64}$$

$$\langle\dot{\omega}_p|\eta,\zeta\rangle = \frac{1}{\partial Q_\psi/\partial\zeta}\left(\langle N_\xi|\eta,\zeta\rangle\frac{\partial^2 Q_\psi}{\partial\eta^2} + 2\langle N_{\xi c}|\eta,\zeta\rangle\frac{\partial^2 Q_\psi}{\partial\eta\partial\zeta} + \langle N_c|\eta,\zeta\rangle\frac{\partial^2 Q_\psi}{\partial\zeta^2}\right) \tag{3.65}$$

These terms are exact and, at this stage, do not contain any modelling. As a consequence of the definition of the progress variable (Eqn. 3.12), the mapping between $(\xi, c)$ and $Y_\psi$ is exact and for conditional fluctuations $Y_\psi'' = Y_\psi - Q_\psi = 0$ holds. Consequently, it was not necessary to apply the *primary closure hypothesis* to the terms grouped in $\langle\dot{\omega}_p|\eta,\zeta\rangle$.

The DCMC equation (Eqn. 3.62) includes the conditional velocity $\langle\mathbf{u}|\eta,\zeta\rangle$, the conditional turbulent flux $\langle\mathbf{u}''Y_\alpha''|\eta,\zeta\rangle$, the conditional molecular flux $\langle D\nabla Y_\alpha|\eta,\zeta\rangle$, the conditional SDRs $\langle N|\eta,\zeta\rangle$, conditional reaction rate $\langle\omega_\alpha|\eta,\zeta\rangle$ and the conditional evaporation rate $\langle\Pi|\eta,\zeta\rangle$, which require closure. The motivation for the development of CMC models has been to provide simple closure for the non-linear chemical source term. The models for the conditional SDR are, together with the model for the PDF, the most important closure models for CMC.

In the next step, a set of closure models for the DCMC equation is suggested. The closure problem has been pointed out to be a major challenge for the implementation of DCMC [Kronenburg & Mastorakos, 2011]. While the conditional reaction rate takes a very simple from, the models provided for the PDF and SDRs are most important in CMC modelling. In contrast to conventional singly-conditional CMC, DCMC closure needs to be provided for several other terms and, only very little experience with sub-models for doubly-conditional terms exists. In the present work, closure is provided by generalising sub-models used in conventional CMC or by adapting them from other

combustion models that use a similar parametrisation, such as for instance mixture fraction-progress variable flamelet models.

### 3.7.1 Conditional reaction rate

First-order closure constitutes the standard model for the reaction rate in conventional CMC. In order to yield accurate results, this model requires the flame to be well parametrised by the conditioning variable, so that conditional fluctuations, $Y''_\alpha = Y_\alpha - Q_\alpha$, are small. First-order closure has been successfully used in most applications with premixed and non-premixed (and spray) flames, including all recent LES-CMC applications (e.g. Zhang & Mastorakos [2017], Giusti & Mastorakos [2017], Ukai et al. [2013] and Farrace et al. [2017]). The assumption of small conditional fluctuations breaks down in the case of partial premixing or extinction/ignition when singly-conditional CMC is used.

However, introducing the progress variable as second conditioning variable in DCMC, the conditional fluctuations due to extinction have been shown to be small, so that first-order closure is appropriate [Kronenburg, 2004; Kronenburg & Papoutsakis, 2005]. Therefore, in the present work first-order closure for the conditional reaction rate is used

$$\langle \dot{\omega}_\alpha | \eta, \zeta \rangle = \dot{\omega}_\alpha(Q_1, Q_2 \ ... \ Q_{N_\alpha}, Q_T) \tag{3.66}$$

$$\langle \dot{\omega}_\psi | \eta, \zeta \rangle = \dot{\omega}_\psi(Q_1, Q_2 \ ... \ Q_{N_\alpha}, Q_T) \tag{3.67}$$

### 3.7.2 Probability density function

As a presumed-PDF method, DCMC requires a model for the joint-PDF, $\tilde{p}(\eta, \zeta)$. Together with the modelling of the conditional SDRs, the model for the presumed PDF constitutes the most important closure in all CMC approaches.

In most passive scalar based combustion models, including singly-conditional CMC, the mixture fraction PDF is normally presumed as a $\beta$-PDF [Poinsot & Veynante, 2005]. The advantages of the $\beta$-PDF are its flexibility, since it changes continuously from a bi-modal PDF to a mono-modal PDF, and simplicity since it is parametrised by its mean and variance. In particular, the presumed $\beta$-PDF has been shown to reproduce all stages of a two-scalar mixing problem in statistically-stationary, isotropic turbulence [Girimaji, 1991].

The density-weighted PDF $\tilde{p}(\eta)$ is usually not computed according to the definition, $\tilde{p}(\eta) \equiv \langle \rho | \eta \rangle \ \bar{p}(\eta)/\bar{\rho}$ (Eqn. 3.35), but it is directly presumed based on the density-

weighted moments, $\tilde{\xi}$ and $\widetilde{\xi''^2}$. The $\beta$-PDF with the mean $\tilde{\xi}$ and variance $\widetilde{\xi''^2}$ is defined as [Poinsot & Veynante, 2005]

$$p_\beta(\eta; \tilde{\xi}, \widetilde{\xi''^2}) \equiv \frac{\Gamma(a+b)}{\Gamma(a)\Gamma(b)}\ \eta^{a-1}\ (1-\eta)^{b-1} \tag{3.68}$$

where the $\Gamma$-function[4] was used and

$$a \equiv \tilde{\xi}\left[\frac{\tilde{\xi}(1-\tilde{\xi})}{\widetilde{\xi''^2}} - 1\right], \qquad b \equiv (1-\tilde{\xi})\left[\frac{\tilde{\xi}(1-\tilde{\xi})}{\widetilde{\xi''^2}} - 1\right] \tag{3.69}$$

For the variance the following theoretical limit applies:

$$\widetilde{\xi''^2} \leq \tilde{\xi}\ (1-\tilde{\xi}) \tag{3.70}$$

where equality corresponds to the case of two $\delta$-functions at the boundaries. Consequently, $a$ and $b$ are non-negative parameters. In the case of $a > 1$ and $b > 1$, the $\beta$-PDF takes the shape similar to a bell-curve, with one intermediate maximum and approaching zero for $\eta = 0$ and 1; for $a < 1$ the PDF goes to infinity at $\eta = 0$ and for $b < 1$ it is infinity at $\eta = 1$ (see Figs 1 and 2 in Liu et al. [2002]). A weakness of the $\beta$-PDF is that it cannot reproduce a shape with a singularity at $\eta = 0$ or 1 and an intermediate peak at $0 < \eta < 1$. More general presumed PDFs, like presumed mapping functions [Mortensen & Andersson, 2006], have been suggested but are significantly more complicated.

For spray flames, Mortensen & Bilger [2009] conjectured that the $\beta$-PDF would not perform well to capture the mixture fraction distribution in the laminar mixing layer around the droplet, but that it could provide reasonable results for low values of mixture fraction far from the droplet surface. Corrections of the $\beta$-PDF for spray flames have been proposed: Ge & Gutheil [2008] suggested to presume the $\beta$-PDF on the the interval $\eta \in [\eta_{\min},\ \eta_{\max}]$ in mixture fraction space instead of the interval $\eta \in [0,\ 1]$, however, in practice it is complicated to determine a value for $\eta_{\max}$. Another correction was suggested by Borghesi et al. [2011], who added a $\delta$-function at the mixture fraction corresponding to the droplet surface to the presumed $\beta$-PDF. Nevertheless, the standard $\beta$-PDF is used in most recent applications to spray flames, including CMC with RANS [Bolla et al., 2014] and LES-CMC [Giusti & Mastorakos, 2017; Ukai et al., 2013].

[4]The *Gamma function* is function with the property $\Gamma(n+1) = n!$, for $n \in \mathbb{N}$. For complex numbers with positive real part it is defined by the improper integral: $\Gamma(z) = \int_0^\infty t^{z-1}e^{-t}\mathrm{d}t$, for $z \in \mathbb{C}$ with $\mathrm{Re}(z) > 0$. The evaluation of the Gamma-function, usually uses the identity $\Gamma(z+1) = z\Gamma(z)$ [Press et al., 1992, Vol. 1, p. 206].

In the presumed PDF modelling of premixed flames $\beta$-PDFs are also used, besides other examples of presumed PDF shapes [Borghi, 1988; Bray et al., 1989]. The $\beta$-PDF is presumed based on the mean and variance of a progress variable, $p_\beta(\zeta; \tilde{c}, \widetilde{c''^2})$. Alternatively, it has also been suggested to construct the PDF from the pre-computed structure of premixed laminar flames [Salehi & Bushe, 2010] or from the Linear Eddy Model [Tsui & Bushe, 2014]. Nevertheless, $\beta$-PDFs were used in recent work on premixed flames, including RANS with flamelets [Kolla & Swaminathan, 2010b], RANS with CMC [Amzin & Swaminathan, 2013; Amzin et al., 2012], LES flamelet modelling [Langella & Swaminathan, 2016] and LES-CMC [Farrace et al., 2017].

For the modelling of the joint-PDF of mixture fraction and reaction progress variable it is often assumed that the two scalars are statistically independent. A necessary assumption for statistical independence is that $\widetilde{\xi'' c''} = 0$, which is a necessary but generally not a sufficient condition[5]. Then the joint-PDF can be constructed as the product of the marginal PDFs, $\tilde{p}(\eta, \zeta) = \tilde{p}(\eta)\ \tilde{p}(\zeta)$. However, simulations with the transported PDF method have shown that generally a correlation between mixture fraction and progress variable exists [Gutheil, 2011; Tian & Lindstedt, 2019]. The effect of the covariance was assessed for RANS [Chen et al., 2015; Darbyshire & Swaminathan, 2012; Ruan et al., 2014] and LES [Chen et al., 2018]. These studies have shown that considering the covariance is potentially important in a RANS simulations. Chen et al. [2015] investigated the effect of considering the covariance on the stabilisation of a lifted jet flame in RANS, and found two competing effects on lift-off height: (i) the size of the reaction zone with high reaction rate was reduced increasing the lift-off and (ii) the rich and lean branches of the flame were squeezed together reducing the lift-off, which partly balanced each other, but still caused a noticeable net effect. In LES, the effect of the SGS covariance on the FDF was found to gain importance for large filter size, but the overall results for the resolved LES-filtered reaction rate were similar, irrespectively if the covariance was considered [Chen et al., 2018]. In order to relax the assumption of statistical independence, the joint-PDF can be constructed using the conditional PDF, $\tilde{p}(\eta, \zeta) = \tilde{p}(\eta)\ \tilde{p}(\zeta|\eta)$ [Ihme & Pitsch, 2008], or using a *copula* that can take the cross-correlation $\widetilde{\xi'' c''}$ into account [Darbyshire & Swaminathan, 2012]. Ruan et al. [2014] and Chen et al. [2015] used the *copula* for modelling with unstrained

[5]Two events $A$ and $B$ are independent if the occurrence of the event $B$ does not changes the probability that event $A$ occurs, i.e. $P(A) = P(A|B)$. Hence, two events $A$ and $B$ are called independent if, and if only, $P(A \cap B) = P(A)\ P(B)$ [Grimmett & Stirzaker, 2001]. Hence the assumption of statistical independence is equivalent with $\tilde{p}(\eta, \zeta) = \tilde{p}(\eta)\ \tilde{p}(\zeta)$, and $\widetilde{\xi'' c''} = 0$ is a consequence thereof.

flamelets in RANS, and Ukai et al. [2015] used CMC to compute $\tilde{p}(\zeta|\eta) = \delta(\zeta - \langle c|\eta\rangle)$ in LES.

Most recent RANS and LES applications assumed statistical independence, $\tilde{p}(\eta,\zeta) = p_\beta(\eta)\ p_\beta(\zeta)$, for instance with unstrained flamelets [Chen et al., 2017], FGM [Donini et al., 2017; Ma & Roekaerts, 2016a] and doubly-conditional CSE [Dovizio et al., 2015]; Knudsen & Pitsch [2012] and Popp et al. [2015] used $p(\eta,\zeta) = p_\beta(\eta)\ \delta(\zeta - \tilde{c})$ with the FPV approach. The assumption on statistical independence in the sub-grid scale of LES cannot be generally justified, but the net effect of the covariance on resolved variables may be expected to be small when at least one marginal PDF is narrow. Hence, the approximation of the joint-PDF with two independent marginal PDFs may be more acceptable in LES than in RANS. Nevertheless, in most RANS simulations the same assumption is made, due to the complexity involved in more sophisticated PDF modelling.

In the present work, the density-weighted joint-PDF is constructed from two independent $\beta$-PDFs, presumed from the density-weighted mean and variance:

$$\tilde{p}(\eta,\zeta) = p_\beta(\eta;\tilde{\xi},\widetilde{\xi''^2}) \times p_\beta(\zeta;\tilde{c},\widetilde{c''^2}) \tag{3.71}$$

### 3.7.3 Conditional scalar dissipation rate of mixture fraction

One of the most popular models for the singly-conditional SDR of the mixture fraction $\langle N_\xi|\eta\rangle$ is the *Amplitude Mapping Closure* (AMC) model [O'Brien & Jiang, 1991], implied by the mapping closure model due to Chen et al. [1989]. The functional shape from the AMC model is identical with the counterflow conditional SDR commonly used for diffusion flamelets [Peters, 1984]. Notably, the shape of the conditional SDR is independent of the mixing rate. Another model is the presumed $\beta$-PDF model by Girimaji [1992b]. In principle, the AMC model assumes the presence of unmixed fluid in the flow, and Girimaji's model is derived for homogeneous flow conditions. A more general model, based on the PDF transport equation, was developed by Devaud et al. [2004]. Alternatively, Bushe & Steiner [1999] proposed to invert the integral $\widetilde{N}_\xi = \int_0^1 \langle N_\xi|\eta\rangle\ \tilde{p}(\eta)\ \mathrm{d}\eta$, looking for a best fit solution for the over-determined system. A simpler approach was used by Navarro-Martinez et al. [2005] for LES-CMC: since FDFs are usually narrow, they suggested $\langle N_\xi|\eta\rangle \approx \langle\widetilde{N}_\xi|\eta\rangle$, using conditional volume averaging in the CMC cells (see later for conditional volume averaging, Eqn. 4.93).

These models for the conditional SDR cannot be expected to reproduce the steep gradients in the laminar layer in contact with the droplet surface, but similar to the PDF models, the SDR models might be reasonable for low $\eta$-values [Mortensen &

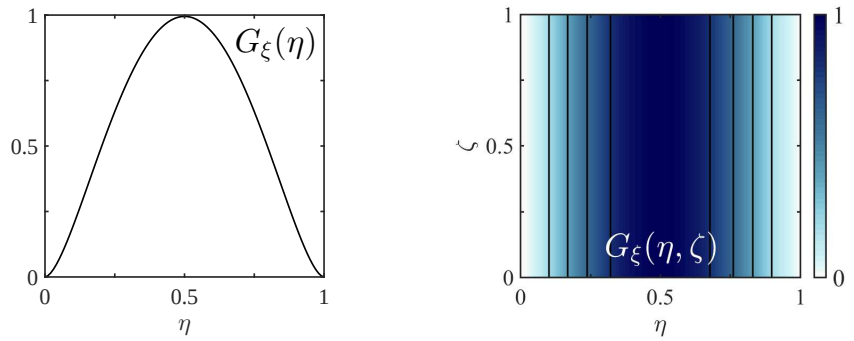


Fig. 3.3 Modelling of $\langle N_\xi|\eta,\zeta\rangle$. AMC model and presumed shape in doubly-conditional space (Eqn. 3.73).

Bilger, 2009]. However, the majority of CMC simulations of spray flames uses the same SDR models as in single-phase flow. Borghesi et al. [2011] suggested a modification of the AMC model with a $\delta$-function corresponding to the SDR on the droplet surface.

Only few suggestions on the modelling of $N_\xi$ in doubly conditional space exist. Nguyen et al. [2010] assumed a triple flame as the canonical case, and inferred that $N_\xi$ was primarily imposed by the flow with little dependence on chemical reaction. Consequently they neglected the influence of progress variable, and used the usual counterflow, bell-curve profile.

In the present work, the same closure as suggested by Nguyen et al. [2010] is used:

$$\langle N_\xi|\eta,\zeta\rangle = N_0 G_\xi(\eta) \tag{3.72}$$

where $G_\xi(\eta)$ is the bell-shaped function[6] given by the AMC model and $N_0$ is the scaling factor:

$$G_\xi(\eta) = \exp(-2[\mathrm{erf}^{-1}(2\eta-1)]^2), \qquad N_0 = \frac{\widetilde{N_\xi}}{\int_0^1\int_0^1 G_\xi(\eta)\tilde{p}(\eta,\zeta)\,\mathrm{d}\eta\,\mathrm{d}\zeta} \tag{3.73}$$

The presumed shape for $\langle N_\xi|\eta,\zeta\rangle$ is shown in Fig. 3.3.

[6]The *error function* is defined as follows: $\mathrm{erf}(x) = (2/\sqrt{\pi})\int_0^x e^{-t^2}\mathrm{d}t$. The function has the following symmetry and limiting values: $\mathrm{erf}(0) = 0$, $\mathrm{erf}(+\infty) = 1$ and $\mathrm{erf}(-x) = -\mathrm{erf}(x)$.
The inverse error function $\mathrm{erf}^{-1}$(x) is defined on $-1 < x < 1$; $\mathrm{erf}^{-1}(0) = 0$, $\mathrm{erf}^{-1}(+1) = +\infty$ and $\mathrm{erf}^{-1}(-\mathrm{x}) = -\mathrm{erf}^{-1}(\mathrm{x})$ [Press et al., 1992, Vol. 1, p. 213].

### 3.7.4 Conditional scalar dissipation rate of progress variable

Kolla & Swaminathan [2010a] suggested the profile obtained from unstrained laminar premixed flames as presumed shape for the singly-conditional SDR, $\langle N_c|\zeta\rangle$. Their analysis suggested that the shape of the conditional SDR, normalised by the peak value, was little influenced by the strain rate. In order to obtain the correct peak value of $\langle N_c|\zeta\rangle$, the presumed shape needs to be re-scaled, so as to integrate with the PDF to give $\widetilde{N}_c$. Hence, consistent modelling of the mean SDR is equally important to model $\langle N_c|\zeta\rangle$ correctly. A consistent model for $\widetilde{N}_c$ needs to include dilatation effects, as suggested by Kolla et al. [2009]. This model for $\langle N_c|\zeta\rangle$ has been used in various CMC studies of premixed flames using RANS [Amzin & Swaminathan, 2013; Amzin et al., 2012] and in LES-CMC [Farrace et al., 2018, 2017], suggesting that it provides an acceptable prediction of the conditional SDR in premixed flames.

The only attempt to model the doubly-conditional SDR of the reaction progress variable was undertaken by Nguyen et al. [2010]. They used the product of a bell-curve centred on the stoichiometric mixture fraction in $\eta$-space and a bell-curve centred on $\zeta = 0.5$, to approximated the SDR from a two-dimensional manifold created from freely-propagating laminar premixed flames.

It is not clear, if the above-mentioned models for fully premixed flames can be used in spray flames. The effect of sprays on $N_c$ has so far not been explored in depth. Some insight can be inferred from the DNS studies by Wacks et al. [2016] and Wacks & Chakraborty [2016b], suggesting that $\|\nabla c\|$ is lower in spray flames compared to fully premixed flames. No SDR models that include spray parameters have been developed so far. In this context, modelling of the SDR for spray combustion in the same way as for a gaseous flames is the only practical option. The exact modelling of $\langle N_c|\eta,\zeta\rangle$ is expected to be important to predict phenomena like extinction, which is, however, not in the scope of the present study.

In the present work, two different models are used. In Chapter 6 the simple model suggested by Nguyen et al. [2010] is used:

$$\langle N_c|\eta,\zeta\rangle = \frac{\widetilde{N}_c}{\int_0^1\int_0^1 G_c(\eta,\zeta)\tilde{p}(\eta,\zeta)\ \mathrm{d}\eta\ \mathrm{d}\zeta}\ G_c(\eta,\zeta) \tag{3.74}$$

where $G_c(\eta,\zeta)$ is the presumed shape:

$$G_c(\eta,\zeta) = g(\eta)\ \exp(-2[\mathrm{erf}^{-1}(2\zeta-1)]^2) \tag{3.75}$$

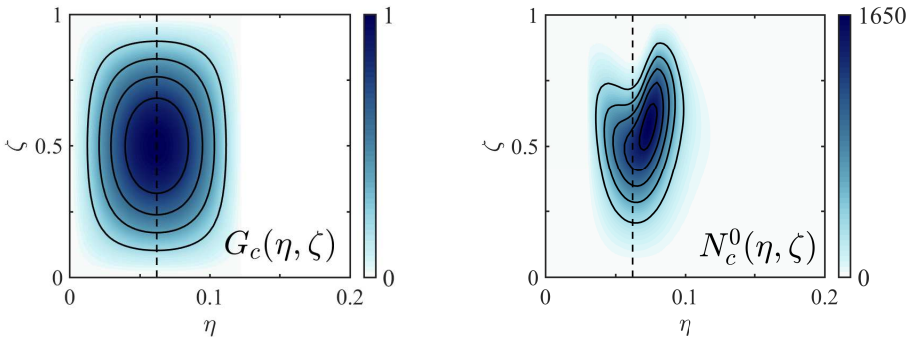


Fig. 3.4 Modelling of $\langle N_c|\eta,\zeta\rangle$. Model by Nguyen et al. [2010] (Eqn. 3.75) and tabulation of one-dimensional laminar premixed flames $N_c^0$ for heptane. The dashed line marks the stoichiometric mixture fraction $\xi_{\mathrm{st}} \approx 0.0622$ for heptane-air mixture.

with

$$g(\eta) = \begin{cases} \exp(-2[\mathrm{erf}^{-1}((\eta/\xi_{\mathrm{st}}) - 1)]^2) & \text{if } \eta < 2\xi_{\mathrm{st}} \\ 0 & \text{otherwise} \end{cases} \tag{3.76}$$

In Chapter 7, $\langle N_c|\eta,\zeta\ \rangle$ is modelled, using a tabulation the SDR from one-dimensional freely propagating laminar premixed flames $N_c^0(\eta,\zeta)$ as the presumed shape. This model is the generalisation of the modelling approach followed by Farrace et al. [2018, 2017] in singly-conditional CMC and based on the suggestion by Kolla & Swaminathan [2010a]:

$$\langle N_c|\eta,\zeta\rangle = \frac{\widetilde{N}_c}{\int_0^1 \int_0^1 N_c^0(\eta,\zeta)\tilde{p}(\eta,\zeta)\ \mathrm{d}\eta\ \mathrm{d}\zeta}\ N_c^0(\eta,\zeta) \tag{3.77}$$

The laminar premixed flames are computed using the commercial software Cosilab [Rotexo GmbH und Co. KG, 2012]. The presumed shapes for $\langle N_c|\eta,\zeta\rangle$ from both models are compared in Fig. 3.4; here, the presumed shapes shown are for heptane-air mixture. Note that the scaling ($\max(N_c^0) \approx 1650\ \mathrm{s}^{-1}$) has no effect since the presumed shape is re-scaled according to Eqn. 3.77. For consistency with the simplifying assumptions made for the DCMC equation (Eqn. 3.62), the premixed flames were computed for unity Lewis number. The same set of laminar flame computations was used to tabulate $S_L^0$, $\delta_L^0$ and $\tau$ for the algebraic model for $\widetilde{N}_c$ (Eqn. 4.22 for RANS and Eqn. 4.63 for LES).

### 3.7.5 Conditional cross-scalar dissipation rate

For the doubly-conditional cross-scalar dissipation rate $\langle N_{\xi c}|\eta,\zeta\rangle$, very few modelling suggestions exist, even though Kronenburg [2004] hypothesised that the cross-scalar

dissipation rate (CDR) played an important role to predict the level of extinction accurately. Modelling could follow the decomposition of the CDR as $N_{\xi c} = D\nabla\xi \cdot \nabla c = D\|\nabla\xi\| \, \|\nabla c\| \, \mathbf{n}_\xi \cdot \mathbf{n_c}$ where $\mathbf{n}_\xi = -\nabla\xi/\|\nabla\xi\|$ are the normal vectors to the respective iso-surfaces and $\mathbf{n}_\xi = -\nabla c/\|\nabla c\|$ [Domingo et al., 2002]. Kronenburg [2004] proposed $\langle N_{\xi c}|\eta,\zeta\rangle \approx \pm\sqrt{\langle N_\xi|\eta,\zeta\rangle}\sqrt{\langle N_c|\eta,\zeta\rangle}$ where the sign would be chosen from the sign of $\widetilde{\xi''c''}$. However, beside the two extreme cases for + and −, intermediate values are also possible. In this sense, the modelling suggestion by Kronenburg [2004] could be extended to propose the following model:

$$\langle N_{\xi c}|\eta,\zeta\rangle \approx \frac{\widetilde{N}_{\xi c}}{\sqrt{\widetilde{N}_\xi \widetilde{N}_c}}\sqrt{\langle N_\xi|\eta,\zeta\rangle}\sqrt{\langle N_c|\eta,\zeta\rangle} \tag{3.78}$$

where the pre-factor provides the sign and the scaling. Nguyen et al. [2010] neglected the conditional CDR.

In the present work, the doubly-conditional cross-scalar dissipation rate is modelled as

$$\langle N_{\xi c}|\eta,\zeta\rangle = 0 \tag{3.79}$$

for consistency with the modelling of the joint-PDF as the product of two independent marginal PDFs.

### 3.7.6 Conditional evaporation rate

The doubly-conditional volumetric evaporation rate $\langle \mathit{\Pi}|\eta,\zeta\rangle$ needs modelling. Since the other conditional spray terms are related to $\langle \mathit{\Pi}|\eta,\zeta\rangle$, the model provides closure for $\langle S_h|\eta,\zeta\rangle$, $\langle S_\xi^-|\eta,\zeta\rangle$ and $\langle S_c^-|\eta,\zeta\rangle$ as well.

In many CMC application to spray flames, the conditional evaporation source term is not considered. Different models for $\langle \mathit{\Pi}|\eta\rangle$ have been proposed [Kim & Huh, 2002; Schroll et al., 2010; Ukai et al., 2013]. Most recently, $\langle \mathit{\Pi}|\eta\rangle$ was usually modelled as a $\delta$-function in mixture fractions space. Schroll et al. [2010], Borghesi et al. [2011] and Tyliszczak et al. [2014] used $\langle \mathit{\Pi}|\eta\rangle = \mathit{\Pi}_0\delta(\eta - \xi_s)$, where $\xi_s$ is the mixture fraction at the droplet surface taken equal to the fuel mass fraction at saturation conditions $Y_{\mathrm{F}s}$. The assumption that $\xi_s = Y_{\mathrm{F}s}$ is only accurate as long as the droplet evaporate upstream of the flame. This model reflects the fact that evaporation only takes place at the surface of the droplet where the fuel mass fraction is given by saturation conditions. An issue with this modelling approach is that usually presumed $\beta$-PDFs fall short to predict the probability associated with the mixture fraction at the droplet surface accurately. Thus, Borghesi et al. [2011] proposed a correction of the PDF at $\eta = \xi_s$,

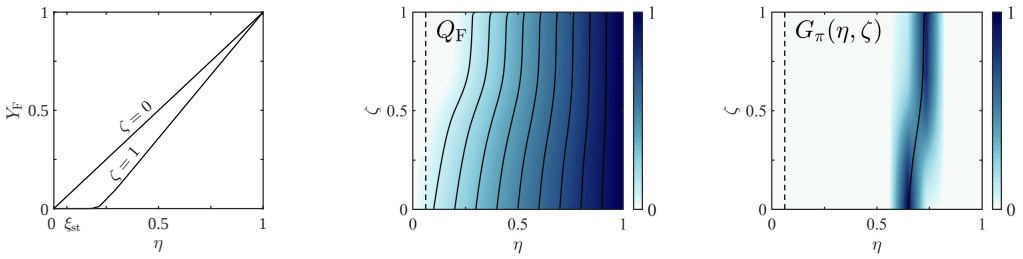


Fig. 3.5 Modelling of $\langle \mathit{\Pi} | \eta, \zeta \rangle$. Mixing line and equilibrium mass fraction of fuel (left), doubly-conditional moment of fuel $Q_{\mathrm{F}}$ (middle) and presumed shape $G_\pi(\eta, \zeta)$ for $Y_{\mathrm{Fs}} = 0.65$ (right) in the case of heptane.

which has, however, not been in continued use. Instead Ukai et al. [2013, 2014, 2015] circumvented this problem, modelling the term as $\langle \mathit{\Pi} | \eta \rangle = \mathit{\Pi}_0 \delta(\eta - \tilde{\xi})$. This assumes that the micro-mixing between droplet surface and carrier gas is infinitely fast.

In the present work the doubly-conditional evaporation source term $\langle \mathit{\Pi} | \eta, \zeta \rangle$ is modelled as a ridge in $(\eta, \zeta)$-space along the iso-contour given by $Q_{\mathrm{F}}(\eta, \zeta) = Y_{\mathrm{F}s}$, hence being the equivalent of the $\delta$-function used in conventional CMC. Figure 3.5 shows the conditional moment of fuel mass fraction and the presumed shape for the spray source term. This presumed shape of the conditional spray term is scaled, such that $\langle \mathit{\Pi} | \eta, \zeta \rangle$ integrates with the PDF to give the filtered value $\widetilde{\mathit{\Pi}}$,

$$\langle \mathit{\Pi} | \eta, \zeta \rangle = \mathit{\Pi}_0 G_\pi(\eta, \zeta) \tag{3.80}$$

where $G_\pi(\eta, \zeta)$ is the presumed shape and $\mathit{\Pi}_0$ is the scaling factor:

$$\mathit{\Pi}_0 = \frac{\widetilde{\mathit{\Pi}}}{\int_0^1 \int_0^1 G_\pi(\eta, \zeta)\ \tilde{p}(\eta, \zeta)\ \mathrm{d}\eta \mathrm{d}\zeta} \tag{3.81}$$

As pointed out in previous work for singly-conditional CMC [Borghesi et al., 2011; Giusti & Mastorakos, 2017], this source term needs to be limited to avoid numerical instability in the case where the probability associated with $[Q_{\mathrm{F}}(\eta, \zeta) = Y_{\mathrm{F}s}]$ is very low.

Having provided a model for $\langle \mathit{\Pi} | \eta, \zeta \rangle$, the conditional enthalpy evaporation source term can be closed using the same presumed shape,

$$\langle S_h | \eta, \zeta \rangle = \frac{\widetilde{S}_h}{\widetilde{\mathit{\Pi}}} \langle \mathit{\Pi} | \eta, \zeta \rangle \tag{3.82}$$

and the terms $\langle S_\xi^- | \eta, \zeta \rangle$ and $\langle S_c^- | \eta, \zeta \rangle$ are given by Eqns 3.53 and 3.54.

### 3.7.7 Transport of conditional means in physical space

The DCMC equation contains various terms that correspond to the transport of the conditional means in physical space. Closure is required for the conditional mean velocity $\langle \mathbf{u}|\eta,\zeta\rangle$, the conditional turbulent scalar flux $\langle \mathbf{u}''Y_\alpha''|\eta,\zeta\rangle$ and the conditional molecular flux $\langle D\nabla Y_\alpha|\eta,\zeta\rangle$.

For the conditional mean of velocity various model have been proposed. The most simple model assumes conditional independence of the velocity [Smith et al., 1992]. Other well-known models are the linear model [Kuznetsov & Sabel'nikov, 1990], the model by Li & Bilger [1994], the gradient diffusion model [Pope, 1976]. Sreedhara et al. [2008] compared the conditional independence model, the linear model and the gradient diffusion model for a simple jet flame, finding only small differences. More recently, Mortensen & de Bruyn Kops [2008] proposed a mapping closure model for the conditional mean velocity, which has not been validated against experiments so far.

In singly-conditional CMC applications to non-premixed flames using RANS, the linear model is commonly used. For spray flames Mortensen & Bilger [2009] and conjectured that the gradient diffusion model would be most suitable. Nevertheless, the linear model is commonly used in CMC simulations of spray flames using RANS [Borghesi et al., 2011; Kim & Huh, 2002; Wright et al., 2005].

For premixed flames, Mantel & Bilger [1995] showed that the conditional velocity $\langle \mathbf{u}|c=\zeta\rangle$ had a linear dependence. Swaminathan & Bilger [2001] performed *a priori* testing of different models, including the linear model and the gradient model, and found comparable performance. The linear model was subsequently used for singly-conditional CMC of premixed flames by Amzin et al. [2012] and Amzin & Swaminathan [2013].

Since DCMC applications have so far been limited to *a priori* tests where the modelling of the conditional mean velocity was not required. Thus, no models have been tested yet. However, most models previously used in singly-conditional CMC could be extended for DCMC.

In LES-CMC, Navarro-Martinez et al. [2005] neglected the sub-grid scale correlation of velocity and mixture fraction, hence assuming conditional independence of the mean velocity. This modelling approach was also followed by [Triantafyllidis et al., 2009] and most recent LES-CMC applications for non-premixed [Navarro-Martinez & Kronenburg, 2011], spray [Giusti & Mastorakos, 2017] and premixed flames [Farrace et al., 2017].

In the present work, conditional independence is assumed:

$$\langle \mathbf{u}|\eta,\zeta\rangle = \tilde{\mathbf{u}} \tag{3.83}$$

For LES applications this follows common modelling trends as detailed above and for RANS application this modelling choice can be justified based on the findings of Sreedhara et al. [2008], showing little difference in the performance of the models in a simple jet flame.

In conventional CMC, the conditional turbulent scalar flux is usually modelled based on the gradient diffusion assumption with conditionally independent turbulent diffusivity $\langle \mathbf{u}'' Y_\alpha'' | \eta \rangle = D_T \nabla Q_\alpha$ [Klimenko & Bilger, 1999]. In most CMC applications to non-premxied flames this model is used and Richardson et al. [2007] demonstrated its validity for high Reynolds number flow. Yet, shortcomings are known and Klimenko & Bilger [1999] advise caution using the model. In particular, counter-gradient transport was observed by Richardson et al. [2007] in expanding flames with propagating fronts at low turbulence levels. However, this study focused on the turbulent flux conditional on the mixture fraction – it does not necessarily imply the same for premixed CMC where the turbulent flux is conditioned on a progress variable $\langle \mathbf{u}'' Y_\alpha'' | c = \zeta \rangle$, which has not been assessed so far. Amzin et al. [2012] and Amzin & Swaminathan [2013] used the gradient diffusion model for CMC applications to premixed flames.

The gradient diffusion model is expected to perform reasonably well in spray flames dominated by non-premixed burning modes, except for high mixture fraction values in the near field of the droplet surface [Mortensen & Bilger, 2009], but this has not been demonstrated explicitly. The gradient diffusion model is used in most CMC simulations of spray flames, due to lack of alternatives.

In the present work, the gradient diffusion model is used:

$$\langle \mathbf{u}'' Y_\alpha'' | \eta, \zeta \rangle = -D_T \nabla Q_\alpha \tag{3.84}$$

The conditional molecular diffusion flux is rarely modelled in CMC, since it is commonly neglected for the high Reynolds number assumption. However, in LES-CMC this term can be of comparable size to the conditional turbulent flux. Navarro-Martinez & Kronenburg [2007, 2009, 2011] and Kim & Pitsch [2005, 2006] modelled it as $\langle D \nabla Y_\alpha | \eta \rangle = \bar{D} \nabla Q_\alpha$, where $\bar{D}$ is the diffusivity of the mixture fraction. In recent LES-CMC simulations of premixed flames, the term was not retained [Farrace et al., 2018, 2017].

In the present work, the term is modelled in the following way:

$$\langle D \nabla Y_\alpha | \eta, \zeta \rangle = \bar{D} \nabla Q_\alpha \tag{3.85}$$

## 3.8 Summary and discussion

The DCMC equation for spray combustion was derived and closed. The DCMC equation is based on two conditioning variables, mixture fraction and reaction progress variable – this choice is motivated by the successful use of this parametrisation in CMC and other turbulent combustion models.

A normalised reaction progress variable was used. While this definition leads to a more complicated transport equation for $c$ with additional terms that involve the scalar dissipation rates, it is advantageous in the present modelling approach: using a normalised progress variable, the doubly-conditional space takes a regular shape $[0,1] \times [0,1]$. This is advantageous for the discretisation and solution of the DCMC equation, and convenient when presuming the joint-PDF based on means and variances. The added complexity in the $c$ equation is not a major drawback. In any case, the SDRs need to be modelled for DCMC and, thus, are readily available to close the apparent reaction rate.

In the derivation of the transport equation for the normalised progress variable it was assumed that the diffusivity for $\xi$ and $c$ were equal. While this assumption is certainly limiting, the progress variable can be chosen accordingly. For instance, using a progress variable based in the mass fraction of $CO_2$, as chosen in the present work, approximately fulfils this requirement, assuming unity Lewis number for the mixture fraction.

Local instantaneous balance equations for a two-phase flow were rigorously derived using a *separate flow* model. DCMC equations are obtained by applying the conditional average; phase-averaging and density-weighted averaging were used. The latter relaxes the assumption of small conditional fluctuations of density. The DCMC equation was derived in a general way, relaxing the assumption of high Reynolds number and unity Lewis number. Yet, it must be noted that the high Reynolds number assumption is, to some extent, implicit in the primary closure hypothesis proposed by Klimenko [1990]. On the other hand, the primary closure hypothesis proposed by Bilger [1993a] does not require this assumption.

Equation 3.49 presents the DCMC equation in its most general form, and Eqn. 3.57 is the corresponding enthalpy equation. As such, this equation provides the basis for future developments, and can help to direct future modelling efforts.

It was shown that the derivation of the DCMC equation in the LES-framework was virtually identical to the equation obtained with the *joint-PDF method*. The boundary conditions for the DCMC equation in conditional space were discussed. It was pointed out that the assumption of fixed boundary conditions in progress variable space, mixing

line and the equilibrium composition, could be relaxed introducing an alternatively definition of the progress variable.

# Chapter 4

# Implementation of DCMC for Spray Combustion in RANS and LES

## 4.1 Introduction

In this chapter the implementation of the DCMC model is detailed. The numerical simulation follows an Euler-Lagrangian approach, which constitutes an efficient way to model a two-phase flow with a dispersed liquid phase, modelled according to a point-particle approximation [Balachandar & Eaton, 2010]. The turbulent flow field of the continuous gas phase is modelled in the RANS or LES framework. The dispersed liquid phase is modelled as Lagrangian particles that represent parcels of liquid droplets. The Lagrangian approach can handle poly-disperse droplet clouds and allows for a natural treatment of phenomena like dispersion and particle-wall interactions. The DCMC model presented in Chapter 3 is used to solve the spatial and temporal evolution of the local flame structure. In its role as turbulent combustion model, DCMC provides closure for the mean (or LES-filtered) composition and reaction rate.

The local instantaneous description of a multi-phase flow presented in Section 3.2 is used to derive the Reynolds-averaged and LES-filtered transport equations of the conditioning variables. This approach allows a rigorous derivation of the phase interface terms and ensures consistency with the DCMC equation. The transport equations for the mean and variance of the conditioning variables are first derived and presented in an unclosed form. Closure is provided in a separate step to make evident the modelling assumptions involved. Notably, a dilute spray is assumed, so that the effect of liquid

volume fraction on the conservation equations of the averaged flow variable can be neglected.

The chapter is organised as follows. First, the governing equation for the RANS and the LES framework and closure models are presented. Second, the modelling of the dispersed phase and the interfacing with the gas phase is detailed. Finally, the model implementation is explained. Here, the numerical implementation of the DCMC equation and its interfacing with the flow field solver are presented.

## 4.2 Reynolds-averaged transport equation

In the RANS framework the turbulent flow is described by mean fields (and higher-order moments). Transport equations for the mean flow fields are obtained by *Reynolds-averaging* the local instantaneous balance equations. The Reynolds-average $\bar{(\cdot)}$ is defined as an ensemble-average. Mean fields may depend on space and time.

Applying the Reynolds-average to a two-phase flow, the ensemble average considers observations from both phases. Conversely it is convenient to derive averaged equations for a single phase only. For this purpose *phase-averaging* is introduced:

$$\bar{Y} \equiv \frac{\overline{\overline{\theta Y}}}{\bar{\bar{\theta}}} \tag{4.1}$$

Here, $\overline{\overline{(\cdot)}}$ denotes the ensemble average over the two-phase flow. Since the phase-indicator $\theta = \theta_G$ is unity inside the gas phase and zero otherwise (see Section 3.2), $\bar{\bar{\theta}}$ is the mean volume fraction of the gas phase. Then $\bar{Y}$ is the ensemble average considering only the observations of $Y$ in the gas phase. Hence, the transport equation of $\bar{Y}$ only solves for the average of $Y$ in the gas phase. The dispersed liquid phase is solved separately in a Lagrangian framework and coupling is achieved via source terms in the averaged transport equations. Note that $\bar{\bar{\theta}} \approx 1$ in a dilute spray.

In a reacting flow, density fluctuations are considerable. Density-weighted *Favre-averaging* is practical, since it allows to derive averaged transport equations without the cross-correlation of the variable with density. The Favre-average is defined as

$$\tilde{Y} \equiv \frac{\overline{\rho Y}}{\bar{\rho}} \tag{4.2}$$

where $\bar{\rho}$ is the mean density. Here the Favre-average is applied to the gas-phase only. An instantaneous value $Y$ can be decomposed in a density-weighted mean and a

fluctuation:

$$Y = \widetilde{Y} + Y'', \qquad \widetilde{Y''} = 0 \tag{4.3}$$

### 4.2.1 Reynolds-averaged Navier-Stokes equation

The Reynolds-averaged Navier Stokes (RANS) equation for a single-phase flow can be found in Poinsot & Veynante [2005]. For a two-phase flow, the local instantaneous balance equations for mass, momentum and energy can be found in Kataoka [1986]. Averaging of the continuity equation and the Navier-Stokes equation in a two-phase flow leads to

$$\frac{\partial \bar{\rho}}{\partial t} + \nabla \cdot (\bar{\rho}\tilde{\mathbf{u}}) = \bar{\rho}\widetilde{\Pi} \tag{4.4}$$

$$\frac{\partial \bar{\rho}\tilde{\mathbf{u}}}{\partial t} + \nabla \cdot (\bar{\rho}\tilde{\mathbf{u}}\tilde{\mathbf{u}}) = -\nabla \bar{p} + \nabla \cdot \bar{\boldsymbol{\tau}} - \nabla \cdot (\bar{\rho}\widetilde{\mathbf{u}''\mathbf{u}''}) + \bar{\mathbf{S}}_u \tag{4.5}$$

where it was assumed that the spray is dilute and $\bar{\bar{\theta}} = \bar{\bar{\theta}}_G \approx 1$. In the RANS equation, $\bar{\boldsymbol{\tau}}$ is the mean viscous stress tensor and $\bar{\boldsymbol{\tau}}_T \equiv -\bar{\rho}\widetilde{\mathbf{u}''\mathbf{u}''}$ is the Reynolds stress tensor. The mean evaporation mass source term is given in terms of the volumetric evaporation rate $\widetilde{\Pi}$ (see Section 3.2), and $\bar{\mathbf{S}}_u$ is the mean momentum transfer term coupling the gas phase with the dispersed phase.

The mean viscous stress tensor is computed as [Poinsot & Veynante, 2005]

$$\bar{\boldsymbol{\tau}} = \bar{\mu}\left(\nabla\tilde{\mathbf{u}} + (\nabla\tilde{\mathbf{u}})^{\intercal} - \frac{2}{3}(\nabla \cdot \tilde{\mathbf{u}})\mathbf{I}\right) \tag{4.6}$$

where $\bar{\mu}$ is the mean viscosity. Following Boussinesq's turbulence viscosity assumption [Boussinesq, 1877], the Reynolds stress tensor is closed using the viscous stress tensor for Newtonian fluids [Poinsot & Veynante, 2005]:

$$\bar{\rho}\widetilde{\mathbf{u}''\mathbf{u}''} = -\mu_T\left(\nabla\tilde{\mathbf{u}} + (\nabla\tilde{\mathbf{u}})^{\intercal} - \frac{2}{3}(\nabla \cdot \tilde{\mathbf{u}})\mathbf{I}\right) + \frac{2}{3}\bar{\rho}\tilde{k}\mathbf{I} \tag{4.7}$$

where $\mu_T$ is the turbulent viscosity and $\tilde{k}$ is the turbulent kinetic energy. Note that the last term is added to ensure that $\tilde{k} = (1/2)\sum_{k=1}^{3}\widetilde{u_k''u_k''}$. Closure for $\mu_T$ is provided by the $k$-$\varepsilon$ model.

### 4.2.2 $k$-$\varepsilon$ model

In the $k$-$\varepsilon$ model, developed by Jones & Launder [1972], closed transport equations for the transport of turbulent kinetic energy $\tilde{k}$ and its dissipation rate $\tilde{\varepsilon}$ are solved, and

the turbulent viscosity is computed as

$$\mu_T = \bar{\rho} C_\mu \frac{\tilde{k}^2}{\tilde{\varepsilon}} \tag{4.8}$$

In the present work, the $k$-$\varepsilon$ model is used in the form given by Launder & Spalding [1974] with correction for compressibility suggested by El Tahry [1983] – this is the standard implementation in the CFD toolbox OpenFOAM [2014]. The transport equations for $\tilde{k}$ and $\tilde{\varepsilon}$ in closed form are as follows [OpenFOAM, 2014]:

$$\frac{\partial \bar{\rho}\tilde{k}}{\partial t} + \nabla \cdot (\bar{\rho}\tilde{\mathbf{u}}\tilde{k}) = \nabla \cdot \left[ \left( \bar{\mu} + \frac{\mu_T}{\sigma_k} \right) \nabla \tilde{k} \right] + P_k - \underbrace{\frac{2}{3}\bar{\rho}(\nabla \cdot \tilde{\mathbf{u}})\tilde{k}}_{T_{k,5}} - \bar{\rho}\tilde{\varepsilon} \tag{4.9}$$

$$\begin{aligned} \frac{\partial \bar{\rho}\tilde{\varepsilon}}{\partial t} + \nabla \cdot (\bar{\rho}\tilde{\mathbf{u}}\tilde{\varepsilon}) = \nabla \cdot \left[ \left( \bar{\mu} + \frac{\mu_T}{\sigma_\varepsilon} \right) \nabla \tilde{\varepsilon} \right] + C_{\varepsilon 1} \frac{\tilde{\varepsilon}}{\tilde{k}} P_k - C_{\varepsilon 2} \bar{\rho} \frac{\tilde{\varepsilon}^2}{\tilde{k}} \\ \underbrace{- \left( \frac{2}{3} C_{\varepsilon 1} + C_{\varepsilon 3,\mathrm{RDT}} \right) \bar{\rho}(\nabla \cdot \tilde{\mathbf{u}})\tilde{\varepsilon}}_{T_{\varepsilon,6}} \end{aligned} \tag{4.10}$$

where $P_k$ represents the production of turbulent kinetic energy. The compressibility correction by El Tahry [1983] is introduced though the fifth term of the $\tilde{k}$-equation ($T_{k,5}$) and the last term of the $\tilde{\varepsilon}$-equation ($T_{\varepsilon,6}$); without these terms the standard model for high-Reynolds number flow [Jones & Launder, 1972; Launder & Spalding, 1974] is recovered. The production term is defined as[1]

$$P_k \equiv -\bar{\rho}\, \widetilde{\mathbf{u}''\mathbf{u}''} \colon \nabla \tilde{\mathbf{u}} \tag{4.11}$$

It is closed using the Boussinesq expression for the Reynolds stress tensor (Eqn. 4.7). In the present formulation, the production does not contain pressure terms, which may, however, be significant in closed combustion chambers [Swaminathan & Bray, 2011]. The standard model parameters are [Jones & Launder, 1972; Launder & Spalding, 1974]

$$C_\mu = 0.09, \qquad \sigma_k = 1.0, \qquad \sigma_\varepsilon = 1.3, \qquad C_{\varepsilon 1} = 1.44, \qquad C_{\varepsilon 1} = 1.92, \tag{4.12}$$

[1] In tensor notation $-\bar{\rho}\, \widetilde{\mathbf{u}''\mathbf{u}''} \colon \nabla \tilde{\mathbf{u}} = -\bar{\rho}\, \widetilde{u_i'' u_j''}\, \partial \tilde{u}_i / \partial x_j$

and the additional parameter for compressibility correction is [El Tahry, 1983]

$$C_{\varepsilon 3,\mathrm{RDT}} = -0.33 \tag{4.13}$$

Finally, it should be pointed out that the standard $k$-$\varepsilon$ model used in the present work does not contain any coupling with the dispersed phase. Hence, the only the effect of the dispersed phase on the mean flow ($\bar{\mathbf{S}}_u$ in Eqn. 4.5) is considered, but the effects of turbulence modulation by the dispersed phase, damping or enhancement of $\tilde{k}$, cannot be taken into account with the present modelling framework.

### 4.2.3 Reynolds-averaged equations of $\xi$ and $c$

Reynolds-averaging of the local instantaneous balance equations leads to the transport equations of the mean and variance of mixture fraction and reaction progress variable. Using the definitions of phase-averaging and density-weighted averaging, the following unclosed transport equation for $\tilde{\xi}$, $\tilde{c}$, $\widetilde{\xi''}$ and $\widetilde{c''}$ are obtained:

$$\frac{\partial \overline{\overline{\theta}}\bar{\rho}\tilde{\xi}}{\partial t} + \nabla\cdot\left(\overline{\overline{\theta}}\bar{\rho}\tilde{\mathbf{u}}\tilde{\xi}\right) = -\nabla\cdot(\overline{\overline{\theta}}\bar{\rho}\widetilde{\mathbf{u}''\xi''}) + \nabla\cdot\left(\overline{\overline{\theta}}\ \overline{\rho D\nabla\xi}\right) + \bar{\rho}\widetilde{\Pi} \tag{4.14}$$

$$\begin{aligned}\frac{\partial \overline{\overline{\theta}}\bar{\rho}\widetilde{\xi''^2}}{\partial t} + \nabla\cdot\left(\overline{\overline{\theta}}\bar{\rho}\tilde{\mathbf{u}}\widetilde{\xi''^2}\right) = & -\nabla\cdot(\overline{\overline{\theta}}\bar{\rho}\widetilde{\mathbf{u}''\xi''^2}) + \nabla\cdot\left(\overline{\overline{\theta}}\ \overline{\rho D\nabla\xi''^2}\right)\\ & + 2\,\overline{\overline{\theta}}\ \overline{\xi''\nabla\cdot(\rho D\nabla\tilde{\xi})} - 2\,\overline{\overline{\theta}}\ \overline{\rho D\nabla\xi''\cdot\nabla\xi''} - 2\overline{\overline{\theta}}\bar{\rho}\widetilde{\mathbf{u}''\xi''}\cdot\nabla\tilde{\xi}\\ & + 2\bar{\rho}(\widetilde{\xi\Pi} - \tilde{\xi}\widetilde{\Pi}) - \bar{\rho}(\widetilde{\xi^2\Pi} - \tilde{\xi}^2\widetilde{\Pi})\end{aligned} \tag{4.15}$$

$$\frac{\partial \overline{\overline{\theta}}\bar{\rho}\tilde{c}}{\partial t} + \nabla\cdot\left(\overline{\overline{\theta}}\bar{\rho}\tilde{\mathbf{u}}\tilde{c}\right) = -\nabla\cdot\left(\overline{\overline{\theta}}\bar{\rho}\widetilde{\mathbf{u}''c''}\right) + \nabla\cdot\left(\overline{\overline{\theta}}\ \overline{\rho D\nabla c}\right) + \overline{\overline{\theta}}\bar{\rho}\widetilde{\dot{\omega}_c^*} + \bar{\rho}\widetilde{S_c^-} + \bar{\rho}\widetilde{c\Pi} \tag{4.16}$$

$$\begin{aligned}\frac{\partial \overline{\overline{\theta}}\bar{\rho}\widetilde{c''^2}}{\partial t} + \nabla\cdot\left(\overline{\overline{\theta}}\bar{\rho}\tilde{\mathbf{u}}\widetilde{c''^2}\right) = & -\nabla\cdot(\overline{\overline{\theta}}\bar{\rho}\widetilde{\mathbf{u}''c''^2}) + \nabla\cdot\left(\overline{\overline{\theta}}\ \overline{\rho D\nabla c''^2}\right)\\ & + 2\,\overline{\overline{\theta}}\ \overline{c''\nabla\cdot(\rho D\nabla\tilde{c})} - 2\,\overline{\overline{\theta}}\ \overline{\rho D\nabla c''\cdot\nabla c''} - 2\overline{\overline{\theta}}\bar{\rho}\widetilde{\mathbf{u}''c''}\cdot\nabla\tilde{c} + 2\overline{\overline{\theta}}\bar{\rho}\widetilde{c''\dot{\omega}_c^{*\prime\prime}}\\ & + 2\bar{\rho}(\widetilde{c\dot{S}_c^-} - \tilde{c}\widetilde{S_c^-}) + \bar{\rho}(\widetilde{c^2\Pi} - 2\tilde{c}\widetilde{c\Pi} + \tilde{c}^2\widetilde{\Pi})\end{aligned} \tag{4.17}$$

where $\widetilde{\dot{\omega}_c^*}$, $\widetilde{S_c^-}$ are the averaged form of the terms defined by Eqns 3.16 and 3.19. The physical meaning of the terms can be explained for the progress variable variance equation. On the right-hand side, the first term represents the turbulent transport, the second and third term represent molecular diffusion, the fourth term is the dissipation and the fifth term is the production by mean gradients [Poinsot & Veynante, 2005]. The sixth term is a production term due to chemical reaction and mixing, and the remaining terms are due to spray evaporation. In these equations various terms are unclosed and require modelling. This is discussed in the next section.

### 4.2.4 Reynolds-averaged equations of $\xi$ and $c$ in closed form

A dilute spray is assumed and, consequently $\bar{\bar{\theta}} = \bar{\bar{\theta}}_G \approx 1$. Standard closure models are detailed in Poinsot & Veynante [2005]. For a scalar $\Phi$ closure is provided as follows.

$$\overline{(\rho D \nabla \Phi)} = \frac{\bar{\mu}}{\mathrm{Sc}} \nabla \tilde{\Phi} \tag{4.18}$$

$$-\bar{\rho}\widetilde{\mathrm{u}''\Phi''} = \frac{\mu_T}{\mathrm{Sc}_T} \nabla \tilde{\Phi} \tag{4.19}$$

$$-\bar{\rho}\widetilde{\mathrm{u}''\Phi''} \cdot \nabla \tilde{\Phi} = \frac{\mu_T}{\mathrm{Sc}_T} \nabla \tilde{\Phi} \cdot \nabla \tilde{\Phi} \tag{4.20}$$

where Sc is the Schmidt number for molecular transport and $\mathrm{Sc}_T$ is the turbulent Schmidt number.

The scalar dissipation rate of mixture fraction is modelled as for a passive scalar,

$$\overline{\rho D \nabla \xi'' \cdot \nabla \xi''} = \bar{\rho} C_\xi \frac{\tilde{\varepsilon}}{\tilde{k}} \widetilde{\xi''^2} \tag{4.21}$$

where the model constants $C_\xi = 1$ is used. In the present case of a two-phase flow, the mixture fraction is not a passive scalar in the strict sense, since its balance equation contains a source term due to evaporation. The applicability of this model is discussed in Chapter 6.

The scalar dissipation rate of the reaction progress variable is closed with an algebraic model that takes dilatation effects into account [Kolla et al., 2009] and was subsequently modified for stratified flames [Darbyshire et al., 2010],

$$\bar{\rho}\tilde{\varepsilon}_c = \overline{\rho D \nabla c'' \cdot \nabla c''} = \left[ \left( 2K_c - \tau(\tilde{\xi}) C_4 \right) \frac{S_L^0(\tilde{\xi})}{\delta_L^0(\tilde{\xi})} + C_3 \frac{\tilde{\varepsilon}}{\tilde{k}} \right] \frac{\bar{\rho}\widetilde{c''^2}}{\beta_c} \tag{4.22}$$

with

$$K_c = 0.85\tau(\tilde{\xi}), \qquad C_3 = \frac{1.5\sqrt{\mathrm{Ka}}}{1+\sqrt{\mathrm{Ka}}}, \qquad C_4 = \frac{1.1}{(1+\mathrm{Ka})^{0.4}}, \qquad \mathrm{Ka} = \frac{\delta_Z(\tilde{\xi})}{S_L^0(\tilde{\xi})}\sqrt{\frac{\bar{\rho}\tilde{\varepsilon}}{\bar{\mu}}} \tag{4.23}$$

where $S_L^0$ is the laminar flame speed, $\delta_L^0$ is the thermal flame thickness, $\delta_Z$ is the Zel'dovich flame thickness calculated as $\delta_L^0/\delta_Z = 2(1+\tau)^{0.7}$, $\tau = (T_b - T_u)/T_u$ is the normalised temperature increase, Ka is the Karlovitz number, and $\beta_c = 6.7$ is a model parameter. $S_L^0$, $\delta_L^0$ and $\tau$ depend on mixture fraction, and are pre-computed for freely propagating laminar premixed flames using the commercial software Cosilab [Rotexo GmbH und Co. KG, 2012]. In the model they are evaluated at the local mean mixture fraction $\tilde{\xi}$ [Darbyshire et al., 2010].

This leads to the mean and variance equations of the mixture fraction and reaction progress variable in closed form.

$$\frac{\partial\bar{\rho}\tilde{\xi}}{\partial t} + \nabla\cdot(\bar{\rho}\tilde{\mathbf{u}}\tilde{\xi}) = \nabla\cdot\left[(D_T+\bar{D})\nabla\tilde{\xi}\right] + \bar{\rho}\widetilde{\Pi} \tag{4.24}$$

$$\begin{aligned}\frac{\partial\bar{\rho}\widetilde{\xi''^2}}{\partial t} + \nabla\cdot(\bar{\rho}\tilde{\mathbf{u}}\widetilde{\xi''^2}) = \nabla\cdot\left[(D_T+\bar{D})\nabla\widetilde{\xi''^2}\right] - 2\bar{\rho}\frac{\tilde{\varepsilon}}{\tilde{k}}\widetilde{\xi''^2} + 2D_T\nabla\tilde{\xi}\cdot\nabla\tilde{\xi} \\ + 2\bar{\rho}(\widetilde{\xi\Pi} - \tilde{\xi}\widetilde{\Pi}) - \bar{\rho}(\widetilde{\xi^2\Pi} - \tilde{\xi}^2\widetilde{\Pi})\end{aligned} \tag{4.25}$$

$$\frac{\partial\bar{\rho}\tilde{c}}{\partial t} + \nabla\cdot(\bar{\rho}\tilde{\mathbf{u}}\tilde{c}) = \nabla\cdot\left[(D_T+\bar{D})\nabla\widetilde{\xi''^2}\right] + \bar{\rho}\widetilde{\dot{\omega}_c^*} + \bar{\rho}\widetilde{S_c^-} + \bar{\rho}\widetilde{c\Pi} \tag{4.26}$$

$$\begin{aligned}\frac{\partial\bar{\rho}\widetilde{c''^2}}{\partial t} + \nabla\cdot(\bar{\rho}\tilde{\mathbf{u}}\widetilde{c''^2}) = \nabla\cdot\left[(D_T+\bar{D})\nabla\widetilde{c''^2}\right] - 2\bar{\rho}\tilde{\varepsilon}_c + 2D_T\nabla\tilde{c}\cdot\nabla\tilde{c} + 2\bar{\rho}\widetilde{c''\dot{\omega}_c^{*\prime\prime}} \\ + 2\bar{\rho}(\widetilde{cS_c^-} - \tilde{c}\widetilde{S_c^-}) + \bar{\rho}(\widetilde{c^2\Pi} - 2\tilde{c}\widetilde{c\Pi} + \tilde{c}^2\widetilde{\Pi})\end{aligned} \tag{4.27}$$

where the turbulent and molecular diffusivities are $D_T = \mu_T/\mathrm{Sc}_T$ and $\bar{D} = \bar{\mu}/\mathrm{Sc}$ with $\mathrm{Sc}_T = 0.7$ and $\mathrm{Sc} = 0.7$. Closure for the apparent reaction rate $\widetilde{\dot{\omega}_c^*}$ and the variance source term $\widetilde{c''\dot{\omega}_c''^*}$ is provided by the DCMC model, computing the variable in doubly-conditional space (Eqn. 3.63) and integrating with the presumed PDF as

$$\widetilde{\dot{\omega}_c^*} = \int_0^1\int_0^1 \langle\dot{\omega}_c^*|\eta,\zeta\rangle\ \tilde{p}(\eta,\zeta)\ \mathrm{d}\eta\ \mathrm{d}\zeta \tag{4.28}$$

$$\widetilde{c''\dot{\omega}_c''^*} = \widetilde{c\dot{\omega}_c^*} - \tilde{c}\widetilde{\dot{\omega}_c^*} = \left(\int_0^1 \int_0^1 \zeta \ \langle \dot{\omega}_c^* | \eta, \zeta \rangle \ \tilde{p}(\eta, \zeta) \ \mathrm{d}\eta \ \mathrm{d}\zeta\right) - \tilde{c}\widetilde{\dot{\omega}_c^*} \tag{4.29}$$

The spray term in the $\tilde{\xi}$-equation is exact and directly provided by the evaporation model (Eqn. 4.87). Closure of the other spray terms requires modelling. The $\widetilde{\xi''^2}$-equation contains two spray source terms. While some studies neglected the second term, Giusti & Mastorakos [2017] pointed out that both terms can be of similar size and have a significant impact on the inner flame region. In previous work, $\widetilde{\xi\Pi}$ and $\widetilde{\xi^2\Pi}$ where computed either by summing $\xi_{s,i}^k \dot{m}_{d,i}$ ($k = 1$ or 2) for all droplets in a cell [Demoulin & Borghi, 2000] or by assuming that $\langle \Pi | \eta \rangle$ was a $\delta$-function of the average surface mixture fraction $\langle \xi_s \rangle$ [Tyliszczak et al., 2014]. In both cases it was assumed that $\xi_s \approx Y_{\mathrm{F}s}$, where $Y_{\mathrm{F}s}$ was the fuel mass fraction at saturation conditions calculated at the droplet temperature. However, this assumption is only correct if the droplets evaporate upstream of the flame. A schematic of the general case is shown in Fig. 4.1. The mixture fraction at the droplet surface satisfies $Y_{\mathrm{F}s} \leq \xi_s \leq (Y_{\mathrm{F}}^{\mathrm{Eq}})^{-1}(Y_{\mathrm{F}s})$, where $(Y_{\mathrm{F}}^{\mathrm{Eq}})^{-1}$ is the inverse function of the equilibrium fuel mass fraction $Y_{\mathrm{F}}^{\mathrm{Eq}}(\xi)$, and the relation $Y_{\mathrm{F}s} = \xi$ signifies the mixing line. This reflects the case of a droplet evaporating in burnt gases where some reaction products are present besides the fuel vapour at the droplet surface. In principle, this effect can be accounted for by presuming the the evaporation source term in doubly-conditional space and integrating with the PDF (Eqn. 4.91). This approach requires a model for the doubly-conditional evaporation rate, which was presented in Section 3.7. As a result, closure for the spray terms can be provided by the DCMC model, given the mean evaporation rate and $\langle Y_{\mathrm{F}s} \rangle$ from the evaporation model, for instance

$$\widetilde{\xi\Pi} = \int_0^1 \int_0^1 \eta \ \langle \Pi | \eta, \zeta \rangle \ \tilde{p}(\eta, \zeta) \ \mathrm{d}\eta \ \mathrm{d}\zeta \tag{4.30}$$

and similar for $\widetilde{\xi^2\Pi}$, $\widetilde{cS_c^-}$, $\widetilde{S_c^-}$, $\widetilde{c^2\Pi}$ and $\widetilde{c\Pi}$.

## 4.3 LES-filtered transport equations

In LES the instantaneous flow field is solved for filtered variables. The filter can be defined in the spectral domain or in physical space [Poinsot & Veynante, 2005; Pope, 2000]. Flow structures larger than the filter size are resolved by the filtered fields while fluctuations of smaller scales are averaged out and require modelling. A spatial filtering

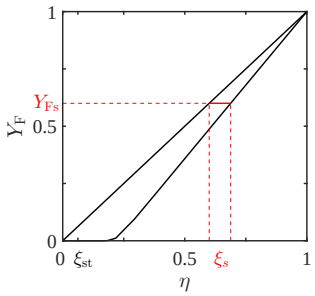


Fig. 4.1 Mixture fraction at the droplet surface. The solid red line indicates the range of possible values for $\xi_s$.

procedure can be defined as [Pope, 2000]

$$\bar{Y}(\mathbf{x},t) \equiv \int_V Y(\mathbf{x}',t)\; G(\mathbf{x}-\mathbf{x}')\; \mathrm{d}V' \tag{4.31}$$

where $G$ is the LES-filter, which satisfies the normalisation condition:

$$\int_V G(\mathbf{x}-\mathbf{x}')\; \mathrm{d}V' = 1 \tag{4.32}$$

The LES-filter $G$ can be defined in different ways, for instance as a Gaussian filter in physical space:

$$G(\mathbf{x}) = \left(\frac{6}{\pi\Delta^2}\right)^{3/2} \exp\left(-\frac{6}{\Delta^2}\|\mathbf{x}\|^2\right) \tag{4.33}$$

where $\Delta$ denotes the filter width. It is notable that generally a filtered variable and a double-filtered quantity (here, denoted as $\overline{\bar{Y}}$, not to be confused with the notation used in phase-averaging) are not equal:

$$\bar{Y} \neq \overline{\bar{Y}}, \qquad \overline{Y'} \neq 0 \tag{4.34}$$

The derivation of the transport equations requires the filter to be commutative with differential operator. In principle this is not possible if the filter size, taken equal to the mesh size, varies in space, but the effects are usually neglected [Poinsot & Veynante, 2005].

For a reacting flow with important density fluctuations, density-weighted filtering can be defined:

$$\tilde{Y}(\mathbf{x},t) \equiv \frac{\int_V \rho(\mathbf{x}',t)\; Y(\mathbf{x}',t)\; G(\mathbf{x}-\mathbf{x}')\; \mathrm{d}V'}{\int_V \rho(\mathbf{x}',t)\; G(\mathbf{x}-\mathbf{x}')\; \mathrm{d}V'} = \frac{\overline{\rho Y}}{\bar{\rho}} \tag{4.35}$$

For a multi-phase phase, phase-weighted filtering is introduced. Then it is convenient to introduce *phase-filtering* and *density-weighted filtering* as

$$\tilde{Y}(\mathbf{x},t) \equiv \frac{\int_V \theta(\mathbf{x}',t)\ \rho(\mathbf{x}',t)\ Y(\mathbf{x}',t)\ G(\mathbf{x}-\mathbf{x}')\ \mathrm{d}V'}{\int_V \theta(\mathbf{x}',t)\ \rho(\mathbf{x}',t)\ G(\mathbf{x}-\mathbf{x}')\ \mathrm{d}V'} = \frac{\overline{\overline{\theta\rho Y}}}{\overline{\overline{\theta\rho}}} \tag{4.36}$$

We further define the phase-filtered density.

$$\bar{\rho} \equiv \frac{\int_V \theta(\mathbf{x}',t)\ \rho(\mathbf{x}',t)\ G(\mathbf{x}-\mathbf{x}')\ \mathrm{d}V'}{\int_V \theta(\mathbf{x}',t)\ G(\mathbf{x}-\mathbf{x}')\ \mathrm{d}V'} = \frac{\overline{\overline{\theta\rho}}}{\overline{\overline{\theta}}} \tag{4.37}$$

This is the filtered density only considering the infinitessimal volume elements $\mathrm{d}V'$ in the gas phase. Hence,

$$\overline{\overline{\theta}}\bar{\rho}\tilde{Y} = \overline{\overline{\theta\rho Y}} \tag{4.38}$$

where $\overline{\overline{\theta}}$ is the filtered volume fraction of the gas phase, $\bar{\rho}$ is the phase-filtered density and $\tilde{Y}$ is the density-weighted filtered variable in the gas phase.

### 4.3.1 LES-filtered Navier-Stokes equation

The LES-filtered Navier-Stokes equation for a single-phase flow can be found in Poinsot & Veynante [2005]. LES-filtering of the continuity and the momentum equation for a two-phase flow leads to

$$\frac{\partial\bar{\rho}}{\partial t} + \nabla\cdot(\bar{\rho}\tilde{\mathbf{u}}) = \bar{\rho}\widetilde{\Pi} \tag{4.39}$$

$$\frac{\partial\bar{\rho}\tilde{\mathbf{u}}}{\partial t} + \nabla\cdot(\bar{\rho}\tilde{\mathbf{u}}\tilde{\mathbf{u}}) = -\nabla\bar{p} + \nabla\cdot\bar{\boldsymbol{\tau}} - \nabla\cdot[\bar{\rho}(\widetilde{\mathbf{u}\mathbf{u}} - \tilde{\mathbf{u}}\tilde{\mathbf{u}})] + \bar{\mathbf{S}}_u \tag{4.40}$$

where it was assumed that the volume fraction occupied by the liquid droplets in each LES-cell is small and that $\overline{\overline{\theta}} = \overline{\overline{\theta}}_G \approx 1$. In the LES-filtered Navier-Stokes equation, the filtered viscous stress tensor is

$$\bar{\boldsymbol{\tau}} = \bar{\mu}\left(\nabla\tilde{\mathbf{u}} + (\tilde{\mathbf{u}})^{\intercal} - \frac{2}{3}(\nabla\cdot\tilde{\mathbf{u}})\mathbf{I}\right) \tag{4.41}$$

and the sub-grid scale Reynolds stress tensor is defined as

$$\bar{\boldsymbol{\tau}}_{\mathrm{sgs}} \equiv -\bar{\rho}(\widetilde{\mathbf{u}\mathbf{u}} - \tilde{\mathbf{u}}\tilde{\mathbf{u}}) \tag{4.42}$$

Closure for $\bar{\boldsymbol{\tau}}_{\mathrm{sgs}}$ is provided with a constant Smagorinsky model.

### 4.3.2 Smagorinsky model

The Smagorinsky model, originally proposed by Smagorinsky [1963], is used to provide closure for the unresolved Reynolds stress tensors. The model can be derived in various ways, including dimensional arguments or based on the equilibrium assumption that the small scales dissipate entirely the energy received from the large scales. The model is widely used for its simple form; in constant density flow $\nu_{\text{sgs}} = (C_s\Delta)^2\|\mathbf{S}\|$, where $\|\bar{\mathbf{S}}\| \equiv (2\bar{\mathbf{S}} : \bar{\mathbf{S}})^{1/2}$ is the Frobenius norm of the resolved strain-rate tensor[2] and $C_s$ is called the Smagorinsky constant, typically $C_s \approx 0.2$ for homogeneous turbulence, but generally dependent on the flow configuration [Ferziger & Perić, 2002; Poinsot & Veynante, 2005].

In the present work, the Smagorinsky model is used with constant parameters, in the form given by Fureby [1996]. The SGS Reynolds stress tensor is closed following the Boussinesq's turbulent viscosity assumption [Boussinesq, 1877] (see also Poinsot & Veynante [2005]):

$$\bar{\boldsymbol{\tau}}_{\text{sgs}} = 2\mu_{\text{sgs}}\widetilde{\mathbf{S}}_{\text{dev}} - \frac{2}{3}\bar{\rho}k_{\text{sgs}}\mathbf{I} \tag{4.43}$$

where $\mu_{\text{sgs}}$ is the sub-grid scale turbulent viscosity, $\tilde{k}_{\text{sgs}}$ is the sub-grid scale kinetic energy and $\widetilde{\mathbf{S}}_{\text{dev}}$ is the deviatoric stain rate tensor. The resolved strain rate tensor is[3]

$$\widetilde{\mathbf{S}} \equiv \frac{1}{2}(\nabla\tilde{\mathbf{u}} + (\nabla\tilde{\mathbf{u}})^{\intercal}) \tag{4.44}$$

and the deviatoric strain rate tensor is $\widetilde{\mathbf{S}}$ minus its trace[4]

$$\widetilde{\mathbf{S}}_{\text{dev}} \equiv \widetilde{\mathbf{S}} - \frac{1}{3}\text{tr}\left(\widetilde{\mathbf{S}}\right)\mathbf{I} = \frac{1}{2}(\nabla\tilde{\mathbf{u}} + (\nabla\tilde{\mathbf{u}})^{\intercal}) - \frac{1}{3}(\nabla\cdot\tilde{\mathbf{u}})\mathbf{I} \tag{4.45}$$

The sub-grid scale turbulent viscosity $\mu_{\text{sgs}}$ is computed as

$$\mu_{\text{sgs}} = C_k\Delta\bar{\rho}k_{\text{sgs}}^{1/2} \tag{4.46}$$

The sub-grid scale turbulent kinetic energy $k_{\text{sgs}}$ is calculated based on the assumption of local equilibrium, where production equals dissipation. In this way, an algebraic

[2] In tensor notation $\bar{\mathbf{S}} : \bar{\mathbf{S}} = \bar{S}_{ij}\bar{S}_{ij}$ using Einstein summation convention.

[3] In tensor notation $\widetilde{S}_{ij} = \frac{1}{2}\left(\frac{\partial\tilde{u}_i}{\partial x_j} + \frac{\partial\tilde{u}_j}{\partial x_i}\right)$ using Einstein summation convention.

[4] $\text{tr}(\mathbf{S}) = \sum_i S_{ii}$

expression for $k_{\text{sgs}}$ is derived (see dissertation by Zhang [2015, p. 36]):

$$k_{\text{sgs}}^{1/2} = \frac{\frac{2}{3}\text{tr}\left(\widetilde{\mathbf{S}}\right) + \left(\left[\frac{2}{3}\text{tr}\left(\widetilde{\mathbf{S}}\right)\right]^2 + 8C_k C_\varepsilon \widetilde{\mathbf{S}}_{\text{dev}} : \widetilde{\mathbf{S}}\right)^{1/2}}{2C_\varepsilon/\Delta} \tag{4.47}$$

The following model parameters were used [Fureby, 1996]:

$$C_k = 0.02, \qquad C_\varepsilon = 1.048 \tag{4.48}$$

This model does not contain any SGS effects of the droplets on the turbulence. However, the spray can modulate the resolved spectrum of turbulence, if the LES resolution is fine enough and the droplet Reynolds number is sufficiently high.

### 4.3.3 LES-filtered equations for $\xi$ and $c$

LES-filtering of the mixture fraction equation and reaction progress variable leads to Eqns 4.49 and 4.51. In order to derive equations for the sub-grid scale variance, LES-filtered equations for $\widetilde{\xi^2}$ and $\widetilde{c^2}$ are derived and transport equations for $\tilde{\xi}^2$ and $\tilde{c}^2$ are subtracted respectively (Eqns 4.50 and 4.52):

$$\frac{\partial \overline{\bar{\theta}}\bar{\rho}\tilde{\xi}}{\partial t} + \nabla\cdot\left(\overline{\bar{\theta}}\bar{\rho}\tilde{\mathbf{u}}\tilde{\xi}\right) = -\nabla\left(\overline{\bar{\theta}}\bar{\rho}(\widetilde{\mathbf{u}\xi} - \tilde{\mathbf{u}}\tilde{\xi})\right) + \nabla\cdot\left(\overline{\bar{\theta}}\ \overline{\rho D\nabla\xi}\right) + \bar{\rho}\widetilde{\Pi} \tag{4.49}$$

$$\begin{aligned}\frac{\partial \overline{\bar{\theta}}\bar{\rho}[\widetilde{\xi^2} - \tilde{\xi}\tilde{\xi}]}{\partial t} &+ \nabla\cdot\left(\overline{\bar{\theta}}\bar{\rho}\tilde{\mathbf{u}}[\widetilde{\xi^2} - \tilde{\xi}^2]\right) = -\nabla\cdot\left(\overline{\bar{\theta}}\bar{\rho}[\widetilde{\mathbf{u}\xi^2} - \tilde{\mathbf{u}}\widetilde{\xi^2}]\right) + \nabla\cdot\left(\overline{\bar{\theta}}\ \overline{\rho D\nabla[\xi^2]}\right)\\ &+ 2\nabla\cdot\left(\overline{\bar{\theta}}\bar{\rho}\tilde{\xi}[\widetilde{\mathbf{u}\xi} - \tilde{\mathbf{u}}\tilde{\xi}]\right) - 2\left(\overline{\bar{\theta}}\bar{\rho}[\widetilde{\mathbf{u}\xi} - \tilde{\mathbf{u}}\tilde{\xi}]\right)\cdot\nabla\tilde{\xi}\\ &- 2\nabla\cdot\left(\overline{\bar{\theta}}\tilde{\xi}\ \overline{\rho D\nabla\xi}\right) + 2\left(\overline{\bar{\theta}}\ \overline{\rho D\nabla\xi}\right)\cdot\nabla\tilde{\xi} - 2\overline{\bar{\theta}}\ \overline{\rho D\nabla\xi\cdot\nabla\xi}\\ &+ 2\bar{\rho}\left(\widetilde{\xi\Pi} - \tilde{\xi}\widetilde{\Pi}\right) - \bar{\rho}\left(\widetilde{\xi^2\Pi} - \tilde{\xi}^2\widetilde{\Pi}\right)\end{aligned} \tag{4.50}$$

$$\frac{\partial \overline{\bar{\theta}}\bar{\rho}\tilde{c}}{\partial t} + \nabla\cdot(\overline{\bar{\theta}}\bar{\rho}\tilde{\mathbf{u}}\tilde{c}) = \nabla\cdot\left(\overline{\bar{\theta}}\ \overline{\rho D\nabla c}\right) + \overline{\bar{\theta}}\bar{\rho}\widetilde{\dot{\omega}_c^*} + \bar{\rho}\widetilde{S_c^-} + \bar{\rho}\widetilde{c\Pi} \tag{4.51}$$

$$\begin{aligned}\frac{\partial\overline{\overline{\theta}}\bar{\rho}[\widetilde{c^2}-\tilde{c}\tilde{c}]}{\partial t}&+\nabla\cdot\left(\overline{\overline{\theta}}\bar{\rho}\tilde{\mathbf{u}}[\widetilde{c^2}-\tilde{c}^2]\right)=-\nabla\cdot\left(\overline{\overline{\theta}}\bar{\rho}[\widetilde{\mathbf{u}c^2}-\tilde{\mathbf{u}}\widetilde{c^2}]\right)+\nabla\cdot\left(\overline{\overline{\theta}}\ \overline{\rho D\nabla[c^2]}\right)\\&+2\nabla\cdot\left(\overline{\overline{\theta}}\bar{\rho}\tilde{c}[\widetilde{\mathbf{u}c}-\tilde{\mathbf{u}}\tilde{c}]\right)-2\left(\overline{\overline{\theta}}\bar{\rho}[\widetilde{\mathbf{u}c}-\tilde{\mathbf{u}}\tilde{c}]\right)\cdot\nabla\tilde{c}\\&-2\nabla\cdot\left(\overline{\overline{\theta}}\tilde{c}\ \overline{\rho D\nabla c}\right)+2\left(\overline{\overline{\theta}}\ \overline{\rho D\nabla c}\right)\cdot\nabla\tilde{c}-2\overline{\overline{\theta}}\ \overline{\rho D\nabla c\cdot\nabla c}\\&+2\overline{\overline{\theta}}\bar{\rho}[\widetilde{c\dot{\omega}_c^*}-\tilde{c}\widetilde{\dot{\omega}_c^*}]+2\bar{\rho}\left(\widetilde{cS_c^-}-\tilde{c}\widetilde{S_c^-}\right)+\bar{\rho}\left(\widetilde{c^2\Pi}-2\tilde{c}\widetilde{c\Pi}+\tilde{c}^2\widetilde{\Pi}\right)\end{aligned}\tag{4.52}$$

Closure for these LES-filtered equations is discussed in the next section.

### 4.3.4 LES-filtered equations for $\xi$ and $c$ in closed form

The unique definition of the sub-gird variance of a scalar $\Phi$ is based in the filtered PDF [Jiménez et al., 2001]:

$$\widetilde{\Phi''^2}\equiv\widetilde{\Phi^2}-\tilde{\Phi}\tilde{\Phi}\tag{4.53}$$

It is assumed that the filtered volume fraction of the liquid is small and consequently $\overline{\overline{\theta}}\approx 1$. The closure models used for the LES-filtered transport equations of the conditioning variables are as follows. The unresolved scalar flux is closed as

$$-\bar{\rho}(\widetilde{\mathbf{u}\Phi}-\tilde{\mathbf{u}}\tilde{\Phi})=\frac{\mu_{\text{sgs}}}{\text{Sc}_T}\nabla\tilde{\Phi}\tag{4.54}$$

and the diffusion flux is modelled as

$$\overline{\rho D\nabla\Phi}=\bar{\rho}\frac{\bar{\mu}}{\text{Sc}}\nabla\tilde{\Phi}\tag{4.55}$$

These closure models lead to the following transport equations for the LES-filtered value and the SGS variance of the mixture fraction and reaction progress variable:

$$\frac{\partial\bar{\rho}\tilde{\xi}}{\partial t}+\nabla\cdot(\bar{\rho}\tilde{\mathbf{u}}\tilde{\xi})=\nabla\cdot\left(\bar{\rho}(D_T+\bar{D})\nabla\tilde{\xi}\right)+\bar{\rho}\widetilde{\Pi}\tag{4.56}$$

$$\begin{aligned}\frac{\partial\bar{\rho}\widetilde{\xi''^2}}{\partial t}&+\nabla\cdot(\bar{\rho}\tilde{\mathbf{u}}\widetilde{\xi''^2})=\nabla\cdot\left(\bar{\rho}(D_T+\bar{D})\nabla\widetilde{\xi''^2}\right)-2\bar{\rho}\widetilde{N_\xi}\\&+2\bar{\rho}(D_T+\bar{D})\nabla\tilde{\xi}\cdot\nabla\tilde{\xi}\\&+2\bar{\rho}\left(\widetilde{\xi\Pi}-\tilde{\xi}\widetilde{\Pi}\right)-\bar{\rho}\left(\widetilde{\xi^2\Pi}-\tilde{\xi}^2\widetilde{\Pi}\right)\end{aligned}\tag{4.57}$$

$$\frac{\partial \bar{\rho}\tilde{c}}{\partial t} + \nabla \cdot (\bar{\rho}\tilde{\mathbf{u}}\tilde{c}) = \nabla \cdot \left(\bar{\rho}(D_T + \bar{D})\nabla \tilde{c}\right) + \bar{\rho}\widetilde{\dot{\omega}_c^*} + \bar{\rho}\widetilde{S_c^-} + \bar{\rho}\widetilde{c\Pi} \tag{4.58}$$

$$\begin{aligned}\frac{\partial \bar{\rho}\widetilde{c''^2}}{\partial t} + \nabla \cdot (\bar{\rho}\tilde{\mathbf{u}}\widetilde{c''^2}) =& \nabla \cdot \left(\bar{\rho}(D_T + \bar{D})\nabla \widetilde{c''^2}\right) - 2\bar{\rho}\widetilde{N}_c \\ &+ 2\bar{\rho}(D_T + \bar{D})\nabla\tilde{c} \cdot \nabla\tilde{c} + 2\bar{\rho}(\widetilde{c\dot{\omega}_c^*} - \tilde{c}\widetilde{\dot{\omega}_c^*}) \\ &+ 2\bar{\rho}\left(\widetilde{cS_c^-} - \tilde{c}\widetilde{S_c^-}\right) + \bar{\rho}\left(\widetilde{c^2\Pi} - 2\tilde{c}\widetilde{c\Pi} + \tilde{c}^2\widetilde{\Pi}\right)\end{aligned} \tag{4.59}$$

where the molecular and turbulent diffusivities are computed as $\bar{D} = \bar{\mu}/(\bar{\rho}\mathrm{Sc})$ and $D_T = \mu_{\mathrm{sgs}}/(\bar{\rho}\mathrm{Sc}_T)$ with $\mathrm{Sc} = 0.7$ and $\mathrm{Sc}_T = 0.4$ respectively.

The filtered scalar dissipation rates (SDRs), $\widetilde{N}_\xi$ and $\widetilde{N}_c$, are defined as

$$\widetilde{N}_\xi \equiv \frac{\overline{\rho D \nabla\xi \cdot \nabla\xi}}{\bar{\rho}}, \qquad \widetilde{N}_c \equiv \frac{\overline{\rho D \nabla c \cdot \nabla c}}{\bar{\rho}} \tag{4.60}$$

In order to provide closure, the SDRs can be considered as composed of a resolved part and a sub-grid scale contribution, neglecting inter-scale cross-terms [Navarro-Martinez et al., 2005]. Hence, the SDR of the mixture fraction is computed as follows:

$$\widetilde{N}_\xi = \underbrace{\bar{D}\nabla\tilde{\xi} \cdot \nabla\tilde{\xi}}_{\widetilde{N}_{\xi,\mathrm{res}}} + \underbrace{\frac{1}{2}C_N \frac{\mu_{\mathrm{sgs}}}{\bar{\rho}\Delta^2}\widetilde{\xi''^2}}_{\widetilde{N}_{\xi,\mathrm{sgs}}} \tag{4.61}$$

The model for $\widetilde{N}_{\xi,\mathrm{sgs}}$ has been suggested by Branley & Jones [2001], based on dimensional arguments, and similarly by Jiménez et al. [2001], based on the modelling of sub-grid kinetic energy by Yoshizawa & Horiuti [1985]. The model constant $C_N$ can be computed using dynamic procedures [Navarro-Martinez et al., 2005; Pitsch, 2006]. Nevertheless, in many studies various constant values are also used: for instance, Navarro-Martinez & Kronenburg [2009, 2011] used $C_N = 5$, Ihme & See [2010] and Chen et al. [2017] used $C_N = 4$; Garmory & Mastorakos [2011] found $C_N = 42$ after calibration for the Sandia D flame. The value 42 is also used in the present work.

The SDR of the reaction progress variable is

$$\widetilde{N}_c = \underbrace{\bar{D}\nabla\tilde{c} \cdot \nabla\tilde{c}}_{\widetilde{N}_{c,\mathrm{res}}} + \widetilde{N}_{c,\mathrm{sgs}} \tag{4.62}$$

The sub-grid scale contribution needs to be closed with a model that can counterbalance the SGS variance source due to chemical reaction ($\widetilde{c\dot{\omega}_c^*} - \tilde{c}\widetilde{\dot{\omega}_c^*}$). For this reason, the algebraic model by Dunstan et al. [2013] that includes flame dilatation effects is used. This model for the SGS contribution of the SDR is based in the the model for the Reynolds-averaged SDR by Kolla et al. [2009] (Eqn. 4.22). Here the model is used in the version adapted for stratified mixture [Chen et al., 2017]:

$$\widetilde{N}_{c,\mathrm{sgs}} = \left(1 - e^{-0.75\ \Delta/\delta_L^0(\tilde{\xi})}\right)\left[2K_c\frac{S_L^0(\tilde{\xi})}{\delta_L^0(\tilde{\xi})} + (C_3 - \tau(\tilde{\xi})C_4\mathrm{Da}_{\mathrm{sgs}})\frac{2u'_{\mathrm{sgs}}}{3\Delta}\right]\frac{\widetilde{c''^2}}{\beta_c} \tag{4.63}$$

with

$$K_c = 0.79\tau(\tilde{\xi}), \qquad C_3 = \frac{1.5\sqrt{\mathrm{Ka}_{\mathrm{sgs}}}}{1+\sqrt{\mathrm{Ka}_{\mathrm{sgs}}}}, \qquad C_4 = \frac{1.1}{(1+\mathrm{Ka}_{\mathrm{sgs}})^{0.4}}, \tag{4.64}$$

and

$$\mathrm{Da}_{\mathrm{sgs}} = \frac{\Delta}{\delta_L^0(\tilde{\xi})}\frac{S_L^0(\tilde{\xi})}{u'_{\mathrm{sgs}}}, \qquad \mathrm{Ka}_{\mathrm{sgs}} = \left(\frac{u'_{\mathrm{sgs}}}{S_L^0(\tilde{\xi})}\right)^{3/2}\left(\frac{\delta_L^0(\tilde{\xi})}{\Delta}\right)^{1/2} \tag{4.65}$$

where $S_L^0$ is the laminar flame speed, $\delta_L^0$ is the thermal flame thickness, $\tau \equiv (T_b - T_u)/T_u$ is the normalised temperature increase, $\mathrm{Da}_{\mathrm{sgs}}$ is the SGS Darmköhler number and $\mathrm{Ka}_{\mathrm{sgs}}$ is the SGS Karlovitz number. The factor $(1 - e^{-0.75\Delta/\delta_L^0})$ ensures that in the limit of a fully resolved flame the SGS scalar dissipation rate vanishes. $S_L^0$, $\delta_L^0$ and $\tau$ depend on mixture fraction, and are pre-computed for freely propagating laminar premixed flames using the commercial software Cosilab [Rotexo GmbH und Co. KG, 2012]; they are evaluated at the local mean mixture fraction $\tilde{\xi}$ [Chen et al., 2017]. The contribution of the SGS velocity fluctuations in this SDR model and its evaluation was investigated by Langella et al. [2017], who found the best agreement with experimental data when $u'_{\mathrm{sgs}}$ was computed based on the scaled-similarity hypothesis [Pope, 2000] using a test filter of size $2\Delta$. This procedure was also tested for stratified flames by Chen et al. [2017]. In the present work constant value $\beta_c = 7.5$ was used as in Chen et al. [2017].

The LES-filtered reaction rate terms $\widetilde{\dot{\omega}_c^*}$ and $\widetilde{c\dot{\omega}_c^*}$ are closed using DCMC by integrating the conditional moments with the FDF, similar to RANS (Eqns 4.28 and 4.29). The LES-filtered transport equations contain various spray source terms. The spray term in the $\tilde{\xi}$ equation is exact, the other require modelling. Considerations for modelling in LES are similar to RANS (see discussion in Section 4.2.4) and, in principle, the LES-filtered terms can also be evaluated using the DCMC model (Eqn. 4.30). The effect of evaporation on the SGS variance of mixture fraction was only considered in a

few studies [De & Kim, 2013; Giusti et al., 2016; Giusti & Mastorakos, 2017; Tyliszczak et al., 2014]. The corresponding terms were not included in Chapter 7 but their effect was investigated in Appendix D. Modelling of the spray terms in the progress variable equations in Chapter 7 follows the findings in Chapter 6, where simplified models are proposed.

### 4.3.5 LES-filtered equation for $h$ in closed form

Evaporative cooling very directly affects the temperature in the vicinity of droplets, and even small temperature differences can have a strong effect on the evaporation rate. Therefore, the effect needs to be considered locally at small scale, which makes it difficult to consider even with a DCMC approach, since solving the $Q_h$ equation intrinsically involves an averaging procedure. For this reason a transport equation for the LES-filtered enthalpy is solved,

$$\frac{\partial \bar{\rho}\tilde{h}}{\partial t} + \nabla \cdot (\bar{\rho}\tilde{h}\tilde{\mathbf{u}}) = \nabla \cdot \left(\bar{\rho}(a_T + \bar{a})\nabla \tilde{h}\right) + \bar{\rho}\tilde{S}_h \tag{4.66}$$

and $\tilde{h}$ is used to correct the temperature and density locally, as detailed in the following. The filtered values $\bar{\rho}_{\text{cmc}}$, $\tilde{T}_{\text{cmc}}$, $\bar{C}_{p,\text{cmc}}$ and $\tilde{h}_{\text{cmc}}$ are computed by integrating the corresponding conditional variables with the filtered probability density function (FDF). The filtered values, $\bar{\rho}$ and $\tilde{T}$, are obtained by performing a linear correction:

$$\tilde{T} = \tilde{T}_{\text{cmc}} + \frac{\tilde{h} - \tilde{h}_{\text{cmc}}}{\bar{C}_{p,\text{cmc}}}, \qquad \bar{\rho} = \bar{\rho}_{\text{cmc}} \frac{\tilde{T}_{\text{cmc}}}{\tilde{T}} \tag{4.67}$$

This approach is relatively common to correct to temperature in the case of non-adiabatic conditions or evaporation, for instance in the work by Hu & Kurose [2018]. The accuracy of the corrections is acceptable because the temperature difference is small. The enthalpy equation contains a spray source term $\bar{\rho}\tilde{S}_h$, which is computed for each Lagrangian parcel by the evaporation model discussed later. Following a unity Lewis number assumption, in the present work, molecular and turbulent thermal diffusivities, $\bar{a}$ and $a_T$, are identical with the respective mass diffusivities for mixture fraction and progress variable.

## 4.4 Spray modelling

For the dispersed phase equations for position, momentum, mass and temperature are solved considering two-way coupling with the continuous phase: the effect of the gas phase on the droplets is considered via the drag and evaporation model; the effect of the droplets on the gas phase is introduced through source terms to the gas phase equations. No model for secondary break-up was used.

### 4.4.1 Equations of motion

The equations of motion for the position and velocity of a droplet are

$$\frac{\mathrm{d}\mathbf{X}_d}{\mathrm{d}t} = \mathbf{U}_d \tag{4.68}$$

$$\frac{\mathrm{d}\mathbf{U}_d}{\mathrm{d}t} = \frac{1}{m_d}\mathbf{F}_d \tag{4.69}$$

where $m_d = \rho_L(\pi/6)d_d^3$ is the mass of the droplet and $\mathbf{F}_d$ is the sum of forces on the droplet. Since $\rho_L/\bar{\rho} \gg 1$, virtual mass, Bassett history forces, Magnus forces, etc. can be neglected. The gravitational force is neglected for high Froude number. Consequently, the particle force only consists of the drag force $\mathbf{F}_d = \mathbf{F}_D$.

The drag force is modelled as sphere drag using the correlation for the drag coefficient by Schiller & Naumann [1933]:

$$C_D = \begin{cases} \frac{24}{\mathrm{Re}}\,(1 + 0.15\ \mathrm{Re}^{0.687}) & \text{if } \mathrm{Re} \leq 1000 \\ 0.44 & \text{otherwise} \end{cases} \tag{4.70}$$

where Re is the droplet Reynolds number given by

$$\mathrm{Re} = \frac{\|\tilde{\mathbf{u}} - \mathbf{U}_d\|\ d_d}{\nu_G} \tag{4.71}$$

The drag force is computed as

$$\mathbf{F}_D = \frac{1}{2}A_d\rho_G C_D\|\tilde{\mathbf{u}} - \mathbf{U}_d\|(\tilde{\mathbf{u}} - \mathbf{U}_d) \tag{4.72}$$

where $A_d = \pi d_d^2/4$ is the cross-section of the sphere, and $\rho_G$ and $\nu_G$ are the density and kinematic viscosity of the gas phase in the film. The relevant properties of the gas

phase, $\rho_G$ and $\nu_G$, are evaluated according to the 1/3-rule:

$$T_G = T_s + \frac{1}{3}(\tilde{T} - T_s), \qquad Y_G = Y_s + \frac{1}{3}(\tilde{Y} - Y_s) \tag{4.73}$$

where subscript $s$ signifies the droplet surface (in gas phase), and $\tilde{T}$ and $\tilde{Y}$ are the local mean (or LES-filtered) temperature and species mass fraction, taken as representative of the mixture far from the droplet surface.

In LES, sub-grid scale dispersion was neglected due to the low level of SGS-kinetic energy. In RANS, a stochastic dispersion model is applied.

### 4.4.2 Stochastic dispersion in RANS

In RANS, turbulent dispersion is modelled with the Discrete Random Walk (DRW) model or Eddy Interaction model (EIM) by Gosman & Ioannides [1983], implemented in OpenFOAM [2014]. The DWR models turbulent dispersion as the successive interaction of the particles (in the present case, droplets) with discrete turbulent eddies. The particles are made to interact with the instantaneous velocity field ($\tilde{\mathbf{u}} + \mathbf{u}_T$), where $\mathbf{u}_T$ is the random velocity component, instead of the mean velocity field $\tilde{\mathbf{u}}$.

For the turbulent eddies it is assumed that the velocity fluctuations is isotropic and follows a Gaussian probability distribution with standard distribution $(2\tilde{k}/3)^{1/2}$. The turbulent eddies have a characteristic length $L_e$ and a lifetime $\tau_e$, estimated as

$$L_e = C_\mu^{3/4} \frac{\tilde{k}^{3/2}}{\tilde{\varepsilon}}, \qquad \tau_e = \frac{\tilde{k}}{\tilde{\varepsilon}} \tag{4.74}$$

with $C_\mu = 0.09$. Moreover, the transit time $\tau_T$, a particle takes to cross the eddy, can be calculated:

$$\tau_t = \frac{L_e}{\|\mathbf{U}_d - (\tilde{\mathbf{u}} + \mathbf{u}_T)\|} \tag{4.75}$$

A particle interacts with a turbulent eddy over the minimum of eddy lifetime and transit time $\min(\tau_e, \tau_t)$. Then a new $\mathbf{u}_T$ is computed as

$$\mathbf{u}_T = \mathbf{n}\sqrt{\frac{2\tilde{k}}{3}} \tag{4.76}$$

where $\mathbf{n}$ is a vector of random direction and its length follows a Gaussian distribution $\mathcal{N}(0, 1)$.

### 4.4.3 Evaporation model

The evaporation model by Abramzon & Sirignano [1989] with Stefan flow correction, non-unity Lewis number in the film and infinite conductivity for the liquid is used. The model is detailed in the following.

The equations for droplet mass $m_d$ and the droplet temperature $T_d$ are as follows:

$$\frac{\mathrm{d}m_d}{\mathrm{d}t} = -\dot{m}_d = -\pi d_d \rho_G D_G \mathrm{Sh}^* \ln(1 + B_M) \tag{4.77}$$

$$\frac{\mathrm{d}T_d}{\mathrm{d}t} = -\frac{1}{m_d C_L} \frac{\dot{m}_d C_{p\mathrm{F}}}{B_T} (\widetilde{T} - T_d) + \frac{1}{m_d C_L} \dot{m}_d L_V \tag{4.78}$$

where $\rho_G$ and $D_G$ are the average density and diffusivity of the gas phase in the film, $C_{p\mathrm{F}}$ is the heat capacity of the fuel vapour, $C_L$ is the heat capacity of the liquid, $L_V$ is the latent heat of vaporisation, and $d_d$ is the droplet diameter. $\widetilde{T}$ is the mean temperature of the gas phase at the location of the droplet, $\mathrm{Sh}^*$ is a parameter termed "modified Sherwood number", and $B_M$ and $B_T$ are the Spalding mass and heat transfer numbers.

The mass transfer number is calculated as

$$B_M = \frac{Y_{\mathrm{F}s} - \tilde{Y}_\mathrm{F}}{1 - \tilde{Y}_\mathrm{F}} \tag{4.79}$$

where a pure liquid fuel was assumed, $\tilde{Y}_\mathrm{F}$ is the mean mass fraction of fuel in the gas phase at the location of the droplet and $Y_{\mathrm{F}s}$ is the fuel mass fraction at the droplet surface.

The thickening of the thermal and diffusion layer due to surface blowing (Stefan flow) is taken into account via correction factors. Hence, the "modified Sherwood number" and the "modified Nusselt number" are computed as

$$\mathrm{Sh}^* = 2 + (\mathrm{Sh}_0 - 2)/F_M, \qquad \mathrm{Nu}^* = 2 + (\mathrm{Nu}_0 - 2)/F_M \tag{4.80}$$

where $\mathrm{Sh}_0$ and $\mathrm{Nu}_0$ are the Nusselt and Sherwood number respectively, which are calculated according to the well-known correlation by Frössling [1938]:

$$\mathrm{Sh}_0 = 2 + 0.552\ \mathrm{Re}^{1/2}\mathrm{Pr}^{1/2}, \qquad \mathrm{Nu}_0 = 2 + 0.552\ \mathrm{Re}^{1/2}\mathrm{Sc}^{1/2} \tag{4.81}$$

and $F_M$ and $F_T$ are the correction factors for the thermal and diffusion film. The correction factors are approximately given as function of the respective mass and heat

transfer number $F_M = F_M(B_M)$ and $F_T = F_T(B_T)$, with the universal function

$$F = (1+B)^{0.7}\ln(1+B)/B \tag{4.82}$$

The heat transfer number $B_T$ depends on the evaporation rate and heat flux itself and, thus, needs to be computed by iterating

$$B_T = (1+B_M)^{\varphi} - 1 \tag{4.83}$$

where $\varphi$ is a parameter calculated as

$$\varphi = \frac{C_{p\mathrm{F}}}{C_{pG}} \frac{\mathrm{Sh}^*}{\mathrm{Nu}^*} \frac{1}{\mathrm{Le}} \tag{4.84}$$

and then using the newly obtained $B_T$ to compute new values for $\mathrm{Nu}^*$ and $\mathrm{Sh}^*$

The fuel vapour mass fraction at the surface $Y_{\mathrm{F}s}$ is computed from the vapour saturation pressure, given by the Clausius-Clapeyron relation, evaluated at the droplet temperature, assuming an isothermal droplet with infinite liquid conductivity:

$$Y_{\mathrm{F}s} = X_{\mathrm{F}s} \frac{W_{\mathrm{F}}}{\sum_\alpha X_\alpha W_\alpha} \ , \qquad X_{\mathrm{F}s} = \frac{p_{\mathrm{sat}}(T_d)}{\bar{p}} \tag{4.85}$$

The quantities $\rho_L$, $C_L$, $p_{\mathrm{sat}}$ and $L_V$ are evaluated at the droplet temperature $T_d$. The gaseous properties $\rho_G$, $\nu_G$, $\lambda_G$, $D_G$, $C_{pG}$ and $C_{p\mathrm{F}}$ are evaluated at average reference conditions, computed according to the 1/3-rule (Eqn. 4.73). The non-dimensional numbers are computed at these reference conditions:

$$\mathrm{Re} = \frac{\|\tilde{\mathbf{u}} - \mathbf{U}_d\| \ d_d}{\nu_G}, \qquad \mathrm{Sc} = \frac{\nu_G}{D_G}, \qquad \mathrm{Pr} = \frac{\nu_G C_{pG}}{\lambda_G}, \qquad \mathrm{Le} = \frac{\mathrm{Sc}}{\mathrm{Pr}} \tag{4.86}$$

The diameter is computed as $d_d = ((m_d/\rho_L)(6/\pi))^{1/3}$.

### 4.4.4 Source terms

The gas phase is coupled to the dispersed phase via source terms in the (Reynolds-averaged or LES-filtered) transport equations of the continuous phase. Hence two-way coupling of the continuous phase and the dispersed phase is used.

The spray source terms are computed by summing over all droplets in a cell of the discretised flow field (LES or RANS). The source terms to the continuity, momentum

and enthalpy equations are as follows:

$$\bar{\rho}\tilde{\Pi} = -\frac{1}{V_{\text{cell}}}\sum_{i}^{N_d}\frac{\mathrm{d}m_{d,i}}{\mathrm{d}t} \tag{4.87}$$

$$\bar{\mathbf{S}}_u = -\frac{1}{V_{\text{cell}}}\sum_{i}^{N_d}\frac{\mathrm{d}m_{d,i}\mathbf{U}_{d,i}}{\mathrm{d}t} \tag{4.88}$$

$$\bar{\rho}\tilde{S}_h = -\frac{1}{V_{\text{cell}}}\sum_{i}^{N_d}\frac{\mathrm{d}m_{d,i}h_L(T_{d,i})}{\mathrm{d}t} \tag{4.89}$$

where $V_{\text{cell}}$ is the cell volume size of the flow field discretisation. The evaporation mass source term is related to the volumetric evaporation rate per unit volume $\tilde{\Pi}$, used in the transport equations of conditioning variables above. The momentum transfer can be written as the change of momentum of the droplet, only because gravitational force was neglected and the drag is the only force acting on the droplet.

Beside the droplet source terms, the flow field solver and the DCMC model require average droplet properties. The average fuel mass fraction at the droplet surface is computed by averaging over all droplets in a cell, using a weighting based on the evaporation rate of the droplet:

$$\langle Y_{\text{F}s}\rangle = \frac{\sum_i^{N_d}\dot{m}_{d,i}\,Y_{\text{F}s,i}(T_{d,i})}{\sum_i^{N_d}\dot{m}_{d,i}} \tag{4.90}$$

## 4.5 Model implementation

This work used the CFD toolbox OpenFOAM-2.3.1 [OpenFOAM, 2014] for the solution of the flow field. The flow field solver was based on the PIMPLE algorithm. PIMPLE stands for a contraction of PISO-SIMPLE, which is a combination of the PISO (Pressure Implicit with Splitting of Operator) [Issa, 1986] and the SIMPLE (Semi-Implicit Method for Pressure-Linked Equations) [Patankar, 1980] algorithms. More information about these solver strategies are given in Ferziger & Perić [2002] and the implementation in OpenFOAM is described by Holzmann [2018]. The modelling of the dispersed phase used the Lagrangian libraries of OpenFOAM that were adopted for the present work. Notably, the evaporation model by Abramzon & Sirignano [1989] was implemented in OpenFOAM. The flow fields solver is interfaced with the DCMC code that was developed in the present work. The DCMC code is based on an unstructured implementation where the DCMC equation is discretised using a finite

volume formulation. The structure and implementation of the DCMC code are based on and similar to the CMC code presented by Garmory & Mastorakos [2015] and Zhang et al. [2015] with more details given in the dissertation by Zhang [2015].

In the unstructured finite-volume implementation of DCMC, the DCMC equation is discretised on a grid that is significantly coarser than the flow field (RANS or LES) resolution, following common practice in CMC modelling. The DCMC cells are polyhedrons that consist of a number of cells of the flow field discretisation; each cell of the flow field discretisation is associated with a single DCMC cell. The faces of the DCMC cells are constructed of the faces from the flow field mesh. A schematic is shown in Fig. 4.2.

The requirements for the discretisation of the physical space in CMC depend on each individual case and are difficult to determine *a priori*. An exemplary overview for singly-conditional CMC is given below. For RANS of simple non-premixed shear flows a one-dimensional CMC grid in stream-wise direction can be used [Klimenko & Bilger, 1999], and 10 to 20 CMC cells may suffice for attached flames but a finer resolution may be required for lifted flames [Kronenburg & Mastorakos, 2011]. In LES, Navarro-Martinez et al. [2005] used 3M LES cells in combination with 1000 CMC cells for an attached jet flame and 50k CMC cells for a lifted jet flame [Navarro-Martinez & Kronenburg, 2009]. Giusti & Mastorakos [2017] used 5M LES cells and 45k CMC cells to simulate local extinction in a bluff-body spray flame. In premixed CMC, Farrace et al. [2017] used 3.6M LES cells and 470 CMC cells. In DCMC coarser grid may be used, compared to conventional CMC, since gradients of the conditional moments are expected to be smaller [Bushe, 2018].

Figure 4.3 shows a diagram of the solver, detailing the coupling between the flow field solver and the DCMC solver. Unconditional mean (or LES filtered) quantities are obtained by integrating the conditional variable with the PDF (or FDF in LES):

$$\tilde{F}(\mathbf{x},t) = \int_0^1 \int_0^1 \langle F(\mathbf{x},t)|\eta,\zeta\rangle_{\mathrm{cmc}}\ \tilde{p}(\eta,\zeta;\mathbf{x},t)\ \mathrm{d}\eta\ \mathrm{d}\zeta \tag{4.91}$$

where the subscript cmc designates the resolution of the DCMC grid. The PDF is presumed as given by Eqn. 3.71. Note that the mean (or filtered) density is computed as

$$\bar{\rho}_{\mathrm{cmc}}(\mathbf{x},t) = \left( \int_0^1 \int_0^1 \frac{1}{\langle \rho(\mathbf{x},t)|\eta,\zeta\rangle_{\mathrm{cmc}}}\ \tilde{p}(\eta,\zeta;\mathbf{x},t)\ \mathrm{d}\eta\ \mathrm{d}\zeta \right)^{-1} \tag{4.92}$$

which follows from the definition of the density-weighted PDF (Eqn. 3.35). In order to take non-adiabatic effects and evaporative cooling into account, the temperature and density are corrected using the transported enthalpy (Eqn. 4.67).

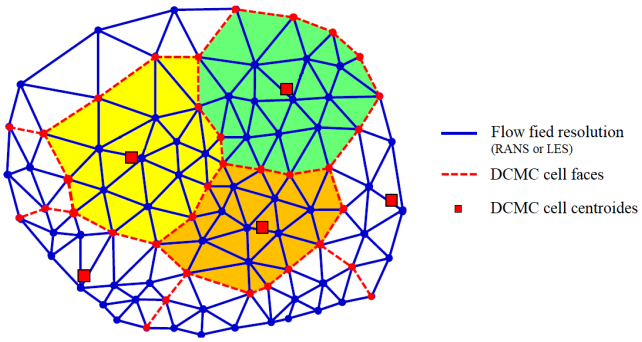


Fig. 4.2 Schematic of the flow field mesh (RANS or LES) and the DCMC mesh. Adapted from Zhang [2015, p. 58].

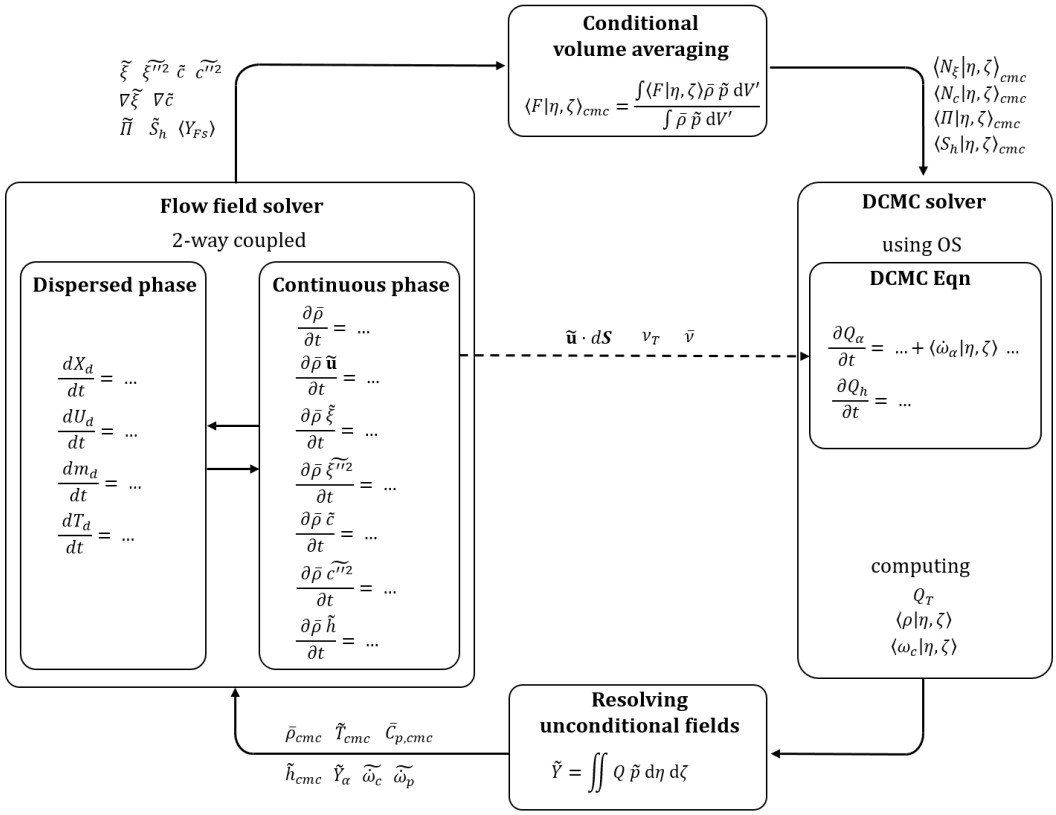


Fig. 4.3 Coupling of the flow field solver and DCMC. Similar to Zhang [2015, p. 58].

In order to map unconditionally averaged quantities from the flow field (RANS or LES) to DCMC a model for the shape of the conditional variable is required. Namely, this is the case for the conditional SDRs and the conditional evaporation rate, and the respective models are detailed in Section 3.7. These models are used to presume the shape of the conditional variables at the flow field (RANS or LES) resolution. The conditional variables at the DCMC resolution are obtained by applying conditional volume averaging:

$$\langle F(\mathbf{x},t)|\eta,\zeta\rangle_{\mathrm{cmc}} = \frac{\int_{V_{\mathrm{cmc}}} \bar{\rho}(\mathbf{x}',t)\ \tilde{p}(\eta,\zeta;\mathbf{x}',t)\ \langle F(\mathbf{x}',t)|\eta,\zeta\rangle\ \mathrm{d}V'}{\int_{V_{\mathrm{cmc}}} \bar{\rho}(\mathbf{x}',t)\ \tilde{p}(\eta,\zeta;\mathbf{x}',t)\ \mathrm{d}V'} \tag{4.93}$$

where $V_{\mathrm{cmc}}$ is the volume of the DCMC cell.

The finite-volume implementation of the DCMC equation is explained next. The DCMC equation (Eqn. 3.62) in integral form is

$$\begin{aligned}
&\int_{V_{\mathrm{cmc}}} \frac{\partial Q_\alpha}{\partial t}\mathrm{d}V' + \int_{V_{\mathrm{cmc}}} \nabla\cdot(\langle\mathbf{u}|\eta,\zeta\rangle Q_\alpha)\,\mathrm{d}V' = \int_{V_{\mathrm{cmc}}} Q_\alpha \nabla\cdot\langle\mathbf{u}|\eta,\zeta\rangle\mathrm{d}V' \\
&\quad - \int_{V_{\mathrm{cmc}}} \frac{1}{\bar{\rho}\tilde{p}}\nabla\cdot(\bar{\rho}\tilde{p}\langle\mathbf{u}''Y_\alpha''|\eta,\zeta\rangle)\mathrm{d}V' + \int_{V_{\mathrm{cmc}}} \frac{1}{\bar{\rho}\tilde{p}}\nabla\cdot(\bar{\rho}\tilde{p}\langle D\nabla Y_\alpha|\eta,\zeta\rangle)\mathrm{d}V' \\
&\quad + \int_{V_{\mathrm{cmc}}} \langle N_\xi|\eta,\zeta\rangle\frac{\partial^2 Q_\alpha}{\partial\eta^2}\mathrm{d}V' + 2\int_{V_{\mathrm{cmc}}} \langle N_{\xi c}|\eta,\zeta\rangle\frac{\partial^2 Q_\alpha}{\partial\eta\partial\zeta}\mathrm{d}V' + \int_{V_{\mathrm{cmc}}} \langle N_c|\eta,\zeta\rangle\frac{\partial^2 Q_\alpha}{\partial\zeta^2}\mathrm{d}V' \\
&\quad + \int_{V_{\mathrm{cmc}}} \langle\dot{\omega}_\alpha|\eta,\zeta\rangle\mathrm{d}V' - \int_{V_{\mathrm{cmc}}} \langle\dot{\omega}_c^*|\eta,\zeta\rangle\frac{\partial Q_\alpha}{\partial\zeta}\mathrm{d}V' \\
&\quad + \int_{V_{\mathrm{cmc}}} (\delta_{\alpha\mathrm{F}} - Q_\alpha)\langle\mathit{\Pi}|\eta,\zeta\rangle\mathrm{d}V' - \int_{V_{\mathrm{cmc}}} \langle S_\xi^-|\eta,\zeta\rangle\frac{\partial Q_\alpha}{\partial\eta}\mathrm{d}V' - \int_{V_{\mathrm{cmc}}} \langle S_c^-|\eta,\zeta\rangle\frac{\partial Q_\alpha}{\partial\zeta}\mathrm{d}V'
\end{aligned} \tag{4.94}$$

Following Zhang [2015, Section 3.3.2], the individual terms are discretised as follows:

- Term $\mathcal{T}_0$ (transient term):

$$\int_{V_{\mathrm{cmc}}} \frac{\partial Q_\alpha}{\partial t}\ \mathrm{d}V' \approx V_{\mathrm{cmc}}\frac{\partial Q_\alpha}{\partial t} \tag{4.95}$$

  Term $\mathcal{T}_1$ (advective term) is rearranged using Gauss's theorem. In discretised form the term is computed by summing over all faces of the (polyhedral) DCMC cells, using the model for the conditional velocity in Eqn. 3.83:

$$\int_{V_{\mathrm{cmc}}} \nabla\cdot(\langle\mathbf{u}|\eta,\zeta\rangle Q_\alpha)\ \mathrm{d}V' = \int_{\partial V_{\mathrm{cmc}}} (\langle\mathbf{u}|\eta,\zeta\rangle Q_\alpha)\cdot\mathbf{n}\,\mathrm{d}S' \approx \sum_i (Q_\alpha\tilde{\mathbf{u}}\cdot\mathbf{n})_i\,\Delta S_i \tag{4.96}$$

  The term is implemented with a first-order upwind scheme.

- Term $\mathcal{T}_2$ (dilatation term):

$$\int_{V_{\text{cmc}}} Q_\alpha \nabla \cdot \langle \mathbf{u} | \eta, \zeta \rangle \, \mathrm{d}V' \approx Q_\alpha \oint_{\partial V_{\text{cmc}}} \langle \mathbf{u} | \eta, \zeta \rangle \cdot \mathbf{n} \, \mathrm{d}S' \approx Q_\alpha \sum_i (\tilde{\mathbf{u}} \cdot \mathbf{n})_i \, \Delta S_i \quad (4.97)$$

- Terms $\mathcal{T}_3$ (turbulent transport) and $\mathcal{T}_4$ (molecular transport):

$$\begin{aligned} -\int_{V_{\text{cmc}}} \frac{1}{\bar{\rho}\tilde{p}} \nabla \cdot (\bar{\rho}\tilde{p} \langle \mathbf{u}'' Y_\alpha'' | \eta, \zeta \rangle) \, \mathrm{d}V' &\approx \oint_{\partial V_{\text{cmc}}} (D_T \nabla Q_\alpha) \cdot \mathbf{n} \, \mathrm{d}S' \\ &\approx \sum_i (D_T \nabla Q_\alpha \nabla \mathbf{n})_i \, \Delta S_i \end{aligned} \quad (4.98)$$

  and

$$\begin{aligned} \int_{V_{\text{cmc}}} \frac{1}{\bar{\rho}\tilde{p}} \nabla \cdot (\bar{\rho}\tilde{p} \langle D \nabla Y_\alpha | \eta, \zeta \rangle) \, \mathrm{d}V' &\approx \oint_{\partial V_{\text{cmc}}} \left( \bar{D} \nabla Q_\alpha \right) \cdot \mathbf{n} \, \mathrm{d}S' \\ &\approx \sum_i (\bar{D} \nabla Q_\alpha \cdot \mathbf{n})_i \, \Delta S_i \end{aligned} \quad (4.99)$$

  whose implementation is second-order accurate.

- The other terms do not contain any derivatives in space or time. The following discretisation is used for the terms 5 to 12, which is representative of the source and transport terms in conditional space, including the chemical reaction, SDRs and evaporation:

$$\int_{V_{\text{cmc}}} \mathcal{T}(\eta, \zeta) \, \mathrm{d}V' \approx V_{\text{cmc}} \mathcal{T}(\eta, \zeta) \quad (4.100)$$

  These terms contain first and second derivatives in $(\eta, \zeta)$-space, which are discretised using finite differences. First derivatives, $\partial/\partial\eta$ and $\partial/\partial\zeta$, were implemented with an upwind scheme. Second derivatives, $\partial^2/\partial\eta^2$, $\partial^2/(\partial\eta\partial\zeta)$ and $\partial^2/\partial\zeta^2$, used a second-order central differencing scheme.

In the DCMC solver an operator splitting (OS) strategy is pursued. In general operator splitting (OS) strategies for reacting flows have been described by Schwer et al. [2003] and their application in CMC was detailed by Kronenburg & Mastorakos [2011]. The principle is to solve the DCMC equation in several fractional steps, for the non-stiff transport terms and the stiff reaction source term. OS errors in CMC were assessed by Wright et al. [2005] and De Paola et al. [2008b] in the case of auto-ignition. They found that the error was non-negligible but could be controlled if the time step was sufficiently small. In DCMC, operator splitting of the transport in conditional space and the reaction source term is indispensable. While conventional CMC typically requires 50

to 100 nodes to discretise the conditional space, in DCMC the discretisation of the two-dimensional conditional space requires about $50 \times 50 = 2500$ nodes, more than one order of magnitude higher than in conventional CMC. Moreover, complex mechanisms used in state-of-the-art simulations have typically more than 50 or even 100 species for heavy hydrocarbons. Then the fully coupled ODE system for a single DCMC cell contains $O(100,000)$ ODEs. Certain chemical processes described by this ODE system have very short time scales, so that the ODE system is mathematically very stiff and costly to solve numerically. In OS strategies, only the non-stiff diffusion processes are solved for the fully coupled system; the stiff chemical processes are solved separately for every node of the conditional space. This strategy reduces the computational effort for the solution of the DCMC equation significantly.

In the present work, the following OS strategy, similar to Wright et al. [2005], is employed:

- First, the terms of transport in physical space, advection $\mathcal{T}_1$, dilatation $\mathcal{T}_2$, turbulent transport $\mathcal{T}_3$, and molecular transport $\mathcal{T}_4$ are solved:

$$\mathcal{T}_0 = -\mathcal{T}_1 + \mathcal{T}_2 + \mathcal{T}_3 + \mathcal{T}_4 \tag{4.101}$$

  This step is integrated in time with a first-order explicit Euler scheme.

- Second, the transport in conditional space and the conditional evaporation source terms are solved together. Transport in conditional space includes the terms $\mathcal{T}_5$, $\mathcal{T}_6$, $\mathcal{T}_7$ and $\mathcal{T}_9^p$, representing the contribution of $\langle \dot{\omega}_p | \eta, \zeta \rangle$ to the apparent reaction rate. The spray source terms are $\mathcal{T}_{10}$, $\mathcal{T}_{11}$ and $\mathcal{T}_{12}$.

$$\mathcal{T}_0 = \mathcal{T}_5 + \mathcal{T}_6 + \mathcal{T}_7 + \mathcal{T}_9^p + \mathcal{T}_{10} + \mathcal{T}_{11} + \mathcal{T}_{12} \tag{4.102}$$

  This step is integrated using the ODE solver VODPK [Brown & Hindmarsh, 1989].

- Third, the chemical reaction source term is solved. The term $\mathcal{T}_9^p$, represents the contribution of $\langle \dot{\omega}_c | \eta, \zeta \rangle$ to the apparent reaction rate.

$$\mathcal{T}_0 = \mathcal{T}_8 + \mathcal{T}_9^c \tag{4.103}$$

  The chemical reactions are solved using the SpeedCHEM library [Perini, 2013].

The OS errors caused by this strategy are assessed in Appendix C. For the time steps used in the present work (Chapters 5, 6 and 7), the OS error on the conditional

temperature and conditional reaction rate is found to be less than 2 % of the conditional variable.

## 4.6 Summary and discussion

This chapter presented the implementation of the DCMC model for RANS and LES. Local instantaneous balance equations for the two-phase flow were used to rigorously derive the Reynolds-averaged and LES-filtered transport equations of the conditioning variables, mixture fraction and reaction progress variable. It was assumed that the mean liquid volume fraction and LES-filtered liquid volume fraction were small, and could be neglected in the averaged transport equations. In RANS the assumption can be expected to hold in a dilute spray where the mean liquid volume fraction is very small. The LES-filtered liquid volume fraction is a instantaneous value and depends on the droplet size and filter width. In the case of finely resolved LES and large droplets this assumptions might reach its limit. Notably, this issue is not considered in most recent spray combustion LES. In a mean sense, considering time-averaged fields, the error is expected to be small.

In LES, the transport equation for the filtered enthalpy is solved, to consider the effect of evaporative cooling and the feedback on the evaporation rate itself. Since DCMC involves an averaging procedure, this correction is necessary to correct the temperature locally.

The modelling of the spray within a Lagrangian framework was presented. The spray is two-way coupled with the gaseous phase. Secondary break-up was not considered.

The implementation of the DCMC model and the interfacing with the flow field solver was presented. The unstructured finite-volume implementation of the DCMC equation is flexible and well-suited for complex domains. This unstructured implementation is computationally efficient, since it allows using a much coarser spatial discretisation for DCMC than for the flow field solver. In DCMC the number of nodes used to discretise the doubly-conditional space increases considerably compared to singly-conditional space, typically by one to two orders of magnitude. Consequently, it is imperative to use a operator splitting technique. An assessment of the operator splitting errors is given in Appendix C. For the conditional temperature and reaction rate the error was found to be below 2 % of the conditional variable.

# Chapter 5

# DCMC-0D

## 5.1 Introduction

In this chapter the solutions of the DCMC equation are explored in the special case of spatial homogeneity with prescribed scalar dissipation rates, denoted as "DCMC-0D". The model equation for DCMC-0D is formally similar to the multi-dimensional flamelet equation derived by Nguyen et al. [2010] and Mittal et al. [2012].

It is instructive to conduct this *a priori* study before simulating a flame with DCMC coupled to RANS or LES. Furthermore, a steady-state solution of the DCMC-0D is used as initial condition and inlet boundary condition for the DCMC solver and, thus, is a prerequisite for applications of DCMC with RANS or LES.

## 5.2 Numerical set-up

The combustion of n-heptane and air is considered. For the mixture fraction, zero and one represent air and pure fuel vapour respectively. The air temperature was 298 K and the fuel vapour temperature was 371.58 $K$ corresponding to the boiling point of heptane [Green & Perry, 2008] – theoretically, $\xi = 1$ can only be reached in the case of a boiling liquid. The reaction progress variable is based on $CO_2$. The chemical mechanism by Smallbone et al. [2009] with 67 species and 315 elementary reactions is used. For heptane-air mixture the lean and rich flammability limits are $\xi_{\text{lean}} \approx 0.0339$ and $\xi_{\text{rich}} \approx 0.1996$ [Coward & Jones, 1952]; the stoichiometric mixture fraction is $\xi_{\text{st}} \approx 0.0622$. The solver settings correspond to the ones used in Chapter 7: the doubly-conditional space, $\mathbb{D} = \{(\eta, \zeta) \in \mathbb{R}^2 : 0 \leq \eta \leq 1, 0 \leq \zeta \leq 1\}$, was discretised

with $71 \times 41$ nodes. The time step was $\Delta t = 10^{-6}$ s. Numerical schemes for DCMC were as detailed in Section 4.5. Operators splitting was used.

## 5.3 DCMC-0D without spray terms

First, consider the DCMC equation in the simplified case of DCMC-0D and in absence of spray terms. Then Eqn. 3.62 becomes

$$\begin{aligned}\frac{\partial Q_\alpha}{\partial t} = \langle N_\xi|\eta,\zeta\rangle\frac{\partial^2 Q_\alpha}{\partial\eta^2} + 2\langle N_{\xi c}|\eta,\zeta\rangle\frac{\partial^2 Q_\alpha}{\partial\eta\partial\zeta} + \langle N_c|\eta,\zeta\rangle\frac{\partial^2 Q_\alpha}{\partial\zeta^2} \\ + \langle\dot\omega_\alpha|\eta,\zeta\rangle - \langle\dot\omega_c^*|\eta,\zeta\rangle\frac{\partial Q_\alpha}{\partial\zeta}\end{aligned} \tag{5.1}$$

and the $Q_h$-equation (Eqn. 3.57) becomes

$$\frac{\partial Q_h}{\partial t} = \langle N_\xi|\eta,\zeta\rangle\frac{\partial^2 Q_h}{\partial\eta^2} + 2\langle N_{\xi c}|\eta,\zeta\rangle\frac{\partial^2 Q_h}{\partial\eta\partial\zeta} + \langle N_c|\eta,\zeta\rangle\frac{\partial^2 Q_h}{\partial\zeta^2} - \langle\dot\omega_c^*|\eta,\zeta\rangle\frac{\partial Q_h}{\partial\zeta} \tag{5.2}$$

These equations are formally similar to the multi-dimensional flamelet equation solved by Nguyen et al. [2010]. Using the definition of $\langle\dot\omega_c^*|\eta,\zeta\rangle$ (Eqn. 3.63) to expand this term, Eqn. 5.1 becomes

$$\begin{aligned}\frac{\partial Q_\alpha}{\partial t} = \langle N_\xi|\eta,\zeta\rangle\frac{\partial^2 Q_\alpha}{\partial\eta^2} + 2\langle N_{\xi c}|\eta,\zeta\rangle\frac{\partial^2 Q_\alpha}{\partial\eta\partial\zeta} + \langle N_c|\eta,\zeta\rangle\frac{\partial^2 Q_\alpha}{\partial\zeta^2} + \langle\dot\omega_\alpha|\eta,\zeta\rangle \\ - \frac{1}{\partial Q_\psi/\partial\zeta}\left(\langle N_\xi|\eta,\zeta\rangle\frac{\partial^2 Q_\psi}{\partial\eta^2} + 2\langle N_{\xi c}|\eta,\zeta\rangle\frac{\partial^2 Q_\psi}{\partial\eta\partial\zeta} + \langle N_c|\eta,\zeta\rangle\frac{\partial^2 Q_\psi}{\partial\zeta^2}\right)\frac{\partial Q_\alpha}{\partial\zeta} \\ - \frac{1}{\partial Q_\psi/\partial\zeta}\langle\dot\omega_\psi|\eta,\zeta\rangle\frac{\partial Q_\alpha}{\partial\zeta}\end{aligned} \tag{5.3}$$

and similar for the $Q_h$-equation. In the present case the progress variable source term takes a more complicated form than in the work by Nguyen et al. [2010], only because a normalised progress variable is used.

It can be seen from Eqn. 5.3 that all terms on the right-hand side cancel each other, if $\alpha = \psi$ and, therefore, $\partial Q_\psi/\partial t = 0$. This means that $Q_{\mathrm{CO2}} = \langle Y_{\mathrm{CO2}}|\eta,\zeta\rangle$ is fixed in time in the present case. Thus, $Q_{\mathrm{CO2}}$ automatically satisfies Eqn. 3.12, relating $\xi$ and $c$ with $Y_{\mathrm{CO2}}$, independently of time and space. This is also true when the DCMC equation is solved in space since $\nabla Q_\psi = 0$. Alternative formulations of the DCMC equation with a different definition of progress variable, which is not normalised with

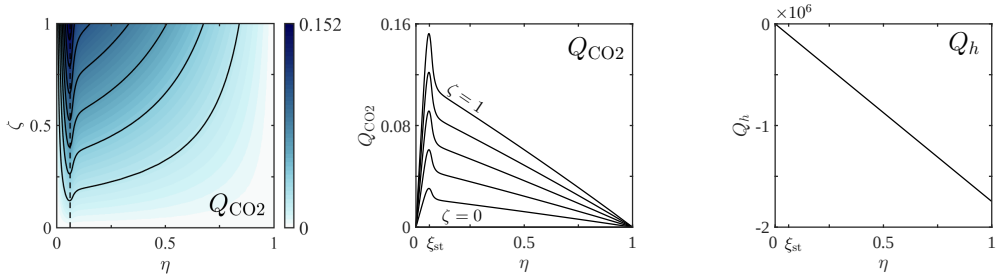


Fig. 5.1 Doubly-conditional moments of $CO_2$ mass fraction, shown as surface plot in $(\eta, \zeta)$-space (left) and as line plots in $\eta$-space for constant $\zeta = 0$, 0.2, 0.4, 0.6, 0.8, 1 (middle), and enthalpy $Q_h$, shown as line plot in $\eta$-space (right). The dashed vertical line marks the stoichiometric mixture fraction $\xi_{st} \approx 0.0622$.

the equilibrium composition but varies in space an time, are possible and details can be found in Appendix B. Since the present chemical mechanism does not include $NO_x$ chemistry and differential diffusion is not considered, all terms on the right-hand side of Eqn. 5.3 also cancel each other for $\alpha = N_2$. Therefore, $Q_{N2}$ is fixed in time and space, conserving its linear shape in mixture fraction space. The conditional moment of enthalpy $Q_h$ evolves linearly in $\eta$-space and, in the present adiabatic case, is invariant with $\zeta$. Then all terms on the right-hand side of the $Q_h$-equation are zero and $Q_h$ is fixed in time and space, and only depends on the boundary conditions in conditional space for $\eta = 0$ and 1. Figure 5.1 shows $Q_{CO2}$, given by the definition of the progress variable (Eqn. 3.12), and $Q_h$; for better understanding, $Q_{CO2}$ is shown as a surface plot in $(\eta, \zeta)$-space, which is the representation used hereafter in the present work, and as line plots in $\eta$-space.

In this *a priori* assessment, the solution from Eqn. 5.3 is compared to a two-dimensional manifold in $(\xi, c)$-space created from a set of one-dimensional freely propagating laminar premixed flames in the range of flammable mixture fractions. These laminar premixed flames were calculated using the commercial software Cosilab [Rotexo GmbH und Co. KG, 2012]. For better comparison with the DCMC model, unity Lewis number was also imposed in the calculation of the laminar premixed flames. Extension of the DCMC model to include differential diffusion effects is not in the scope of the present study, but the suggestions by Kronenburg & Bilger [1997] or Farrace et al. [2018] can be incorporated in future work.

For the conditional SDR $\langle N_c|\eta, \zeta\rangle$ two different models are tested. The first model is the unscaled profile of the SDR from the one-dimensional freely propagating laminar premixed flames $N_c^0(\eta, \zeta)$:

$$\langle N_c|\eta, \zeta\rangle = N_c^0(\eta, \zeta) \tag{5.4}$$

The second model is the algebraic approximation suggested by Nguyen et al. [2010]:

$$\langle N_c|\eta,\zeta\rangle = N_{c,\max} \times G_c(\eta,\zeta) \tag{5.5}$$

where the function $G_c$ is given in Eqn. 3.75. In the present case the scaling factor is set to $N_{c,\max} = 1650\ \mathrm{s}^{-1}$, equal to the maximum obtained for the laminar premixed flames. The conditional SDR given by both models is shown in Fig. 5.2. For $\langle N_\xi|\eta,\zeta\rangle$ the AMC models's [O'Brien & Jiang, 1991] bell curve was used:

$$\langle N_\xi|\eta,\zeta\rangle = N_{\xi,\max} \times G_\xi(\eta) \tag{5.6}$$

where the scaling factor $N_{\xi,\max} = 2\ \mathrm{s}^{-1}$ was used – this is very small compared to the value leading to extinction in a non-premixed transient flamelet, $\approx 335\ \mathrm{s}^{-1}$.

Figure 5.3 shows a comparison of the DCMC-0D results with the two models for the conditional SDR of progress variable, and the 2D manifold constructed from freely propagating premixed laminar flames. Note that the choice of the SDR model has no effect on $Q_{\mathrm{CO2}}$. Both SDR models give similar results and the species, reaction rate and temperature are in reasonable agreement with the premixed flames. Some differences between DCMC-0D and the laminar flames exist for rich mixture, which can be attributed to the low but finite level of $N_\xi$ in DCMC-0D. The good agreement between DCMC-0D and premixed flames suggests that the modelling of $\langle N_c|\eta,\zeta\rangle$ is suitable. This is in line with the observation made by Farrace et al. [2018, 2017] in singly-conditional premixed CMC, where the premixed flame structure was well reproduced by CMC when the correct shape for conditional SDR was used.

Comparing the DCMC-0D simulations with the two SDR models for the progress variable shows that for the algebraic model, the contour of $\langle\dot{\omega}_c|\eta,\zeta\rangle$ is narrower in $\eta$-space. This is due to the fact that $G_c(\eta,\zeta)$ has a much broader shape in $\eta$-space than $N_c^0(\eta,\zeta)$ and overestimates $N_c$ for lean and rich mixtures as evidenced by Fig. 5.2. Nevertheless, the overall prediction of $\langle\dot{\omega}_c|\eta,\zeta\rangle$, in terms of shape in doubly-conditional space and the peak value, is similar in both cases. This suggests that the conditional reaction rate can be predicted with reasonable accuracy, using an algebraic model for the shape of $N_c$ in conditional space, if the peak value, $N_{c,\max}$, at stoichiometric conditions is set correctly, i.e. if the presumed bell shape $G_c(\eta,\zeta)$ is scaled correctly. Necessarily, correct scaling of the presumed shape implies accurate modelling of $\widetilde{N}_c$. Since the reaction rate directly affects the progress variable field of the flame, simple modelling of $\langle N_c|\eta,\zeta\rangle$ may be sufficient to predict the flame shape and temperature.

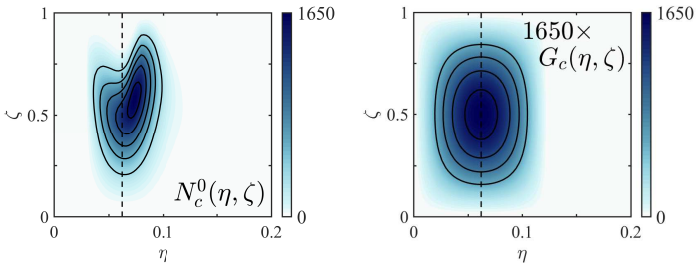


Fig. 5.2 Conditional SDR from freely propagating premixed laminar flames $N_c^0(\eta,\zeta)$ and the approximation with an algebraic model $G_c(\eta,\zeta)$.

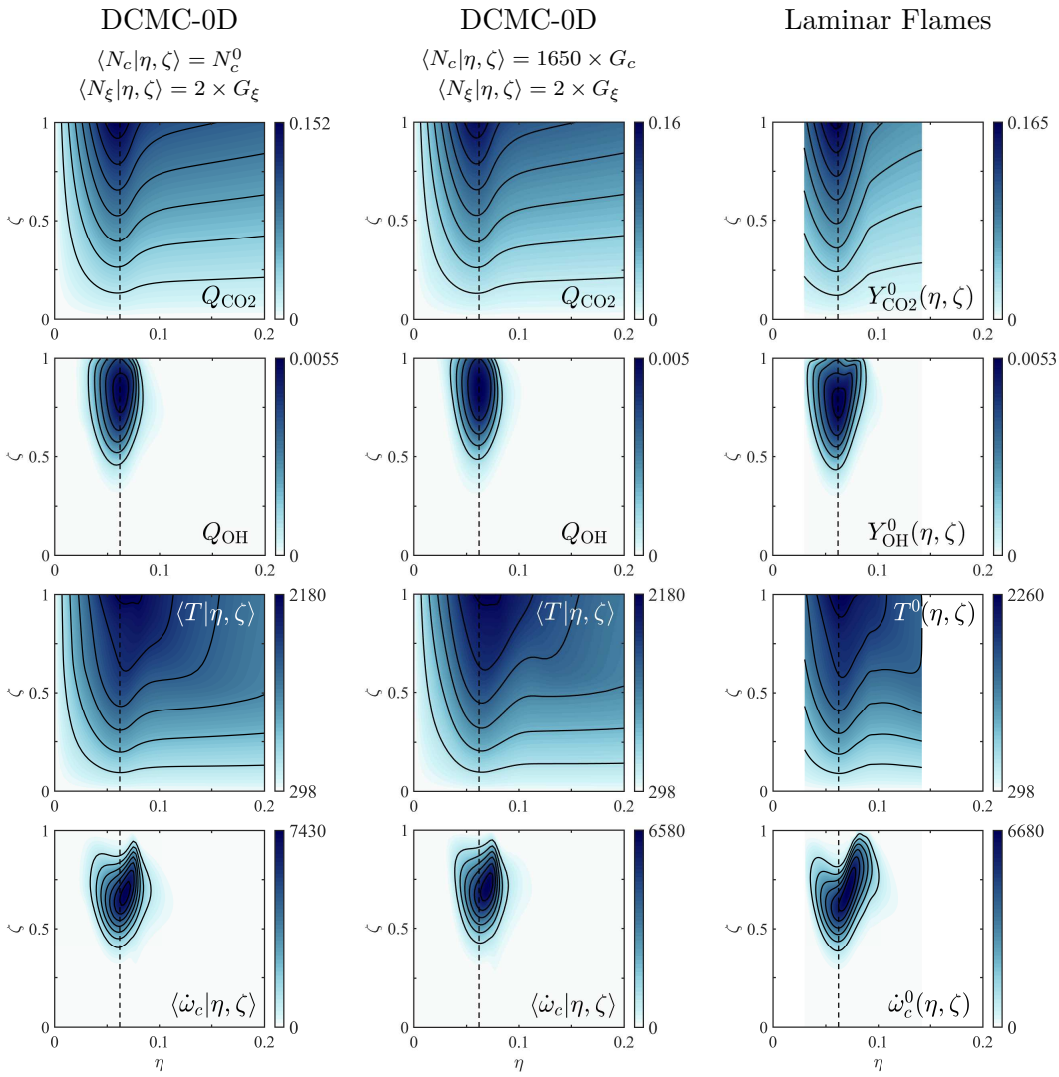


Fig. 5.3 Comparison of steady-state solutions from DCMC-0D with two different models for $\langle N_c|\eta,\zeta\rangle$ (left and middle) and a 2D-manifold from laminar premixed flames (right). Laminar premixed flame calculations are only available for $\xi_{\text{lean}} < \eta < \xi_{\text{rich}}$. The dashed vertical line marks the stoichiometric mixture fraction $\xi_{\text{st}} \approx 0.0622$.

Perhaps for the prediction of pollutants more accurate modelling of SDR may be required.

Figure 5.4 shows the effect of varying the level of SDR on the DCMC-0D solution, also comparing with Fig. 5.3 (left). These simulations used $N_c^0(\eta,\zeta)$ from premixed laminar flames. Increasing $\langle N_c|\eta,\zeta\rangle$, relative to unstrained laminar premixed flames, lowered the peak value of $\langle\dot{\omega}_c|\eta,\zeta\rangle$; slightly increasing $\langle N_\xi|\eta,\zeta\rangle$, from a negligible value, led to a higher peak value of $\langle\dot{\omega}_c|\eta,\zeta\rangle$. Varying the level of the SDRs also affected the profiles of $\langle\dot{\omega}_c|\eta,\zeta\rangle$ in conditional space, for instance widening the peak in $\eta$-space if $N_\xi$ increases. These findings are in line with the discussion by Nguyen et al. [2010].

## 5.4 DCMC-0D with spray terms

Second, consider the effect of the doubly-conditional spray source terms. The governing equation for the DCMC-0D problem then becomes

$$\begin{aligned}\frac{\partial Q_\alpha}{\partial t} &= [\text{r.h.s. of Eqn. 5.1}]\\ &\quad + (\delta_{\alpha\mathrm{F}} - Q_\alpha)\,\langle \mathit{\Pi}|\eta,\zeta\rangle - \langle S_\xi^-|\eta,\zeta\rangle\frac{\partial Q_\alpha}{\partial\eta} - \langle S_c^-|\eta,\zeta\rangle\frac{\partial Q_\alpha}{\partial\zeta}\end{aligned} \tag{5.7}$$

and the $Q_h$-equation becomes

$$\begin{aligned}\frac{\partial Q_h}{\partial t} &= [\text{r.h.s. of Eqn. 5.2}]\\ &\quad + \langle S_h|\eta,\zeta\rangle - \langle \mathit{\Pi}|\eta,\zeta\rangle Q_h - \langle S_\xi^-|\eta,\zeta\rangle\frac{\partial Q_h}{\partial\eta} - \langle S_c^-|\eta,\zeta\rangle\frac{\partial Q_h}{\partial\zeta}\end{aligned} \tag{5.8}$$

Figure 5.5 shows a conditional evaporation term $\langle \mathit{\Pi}|\eta,\zeta\rangle$ for a droplet with a surface vapour mass fraction $Y_{\mathrm{Fs}} = 0.65$, which is presumed as a ridge in $(\eta,\zeta)$-space along an iso-line of the conditional fuel mass fraction $Q_\mathrm{F}$. In this example we further assume that $\langle S_h|\eta,\zeta\rangle = \langle \mathit{\Pi}|\eta,\zeta\rangle \times [-2.2\cdot 10^6\ \mathrm{J/kg}]$ – this is a typical ratio $\widetilde{S}_h/\widetilde{\mathit{\Pi}}$ found in the simulations presented in Chapter 7.

It is notable that the net effect of the spray terms on $Q_\alpha$ is small if $Y_{\mathrm{Fs}} > \xi_{\mathrm{rich}}$, where $Q_\alpha$ drops linearly towards its value at the boundary $\eta = 1$. In the particular cases of $Q_{\mathrm{N2}}$ and $Q_{\mathrm{CO2}}$, which are unambiguously described by $\eta$ and $\zeta$, the three spray terms cancel each other completely, so that their shapes are never affected by evaporation. This is the same as in singly-conditional CMC.

In contrast, there is a significant net effect on $Q_h$ – this is the effect of evaporative cooling. Figure 5.5 shows the conditional moment of fuel mass fraction $Q_\mathrm{F}$, used

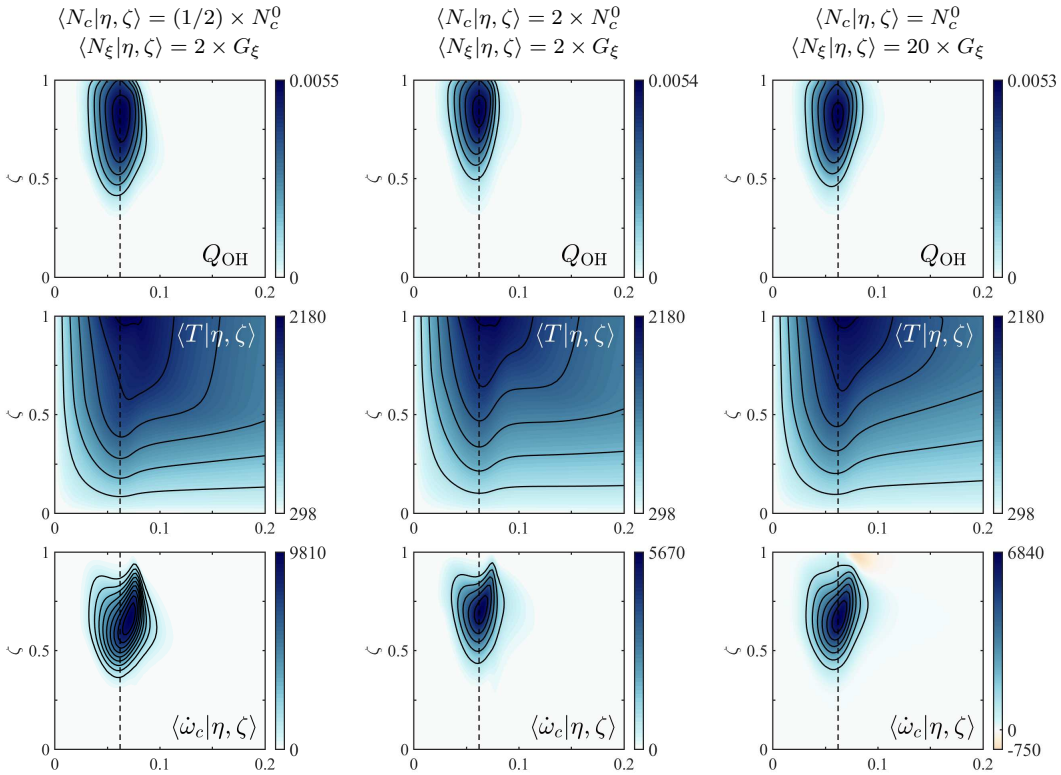


Fig. 5.4 Comparison of steady-state solutions from DCMC-0D with different levels of $N_\xi$ and $N_c$. The dashed vertical line marks the stoichiometric mixture fraction $\xi_{\mathrm{st}} \approx 0.0622$.

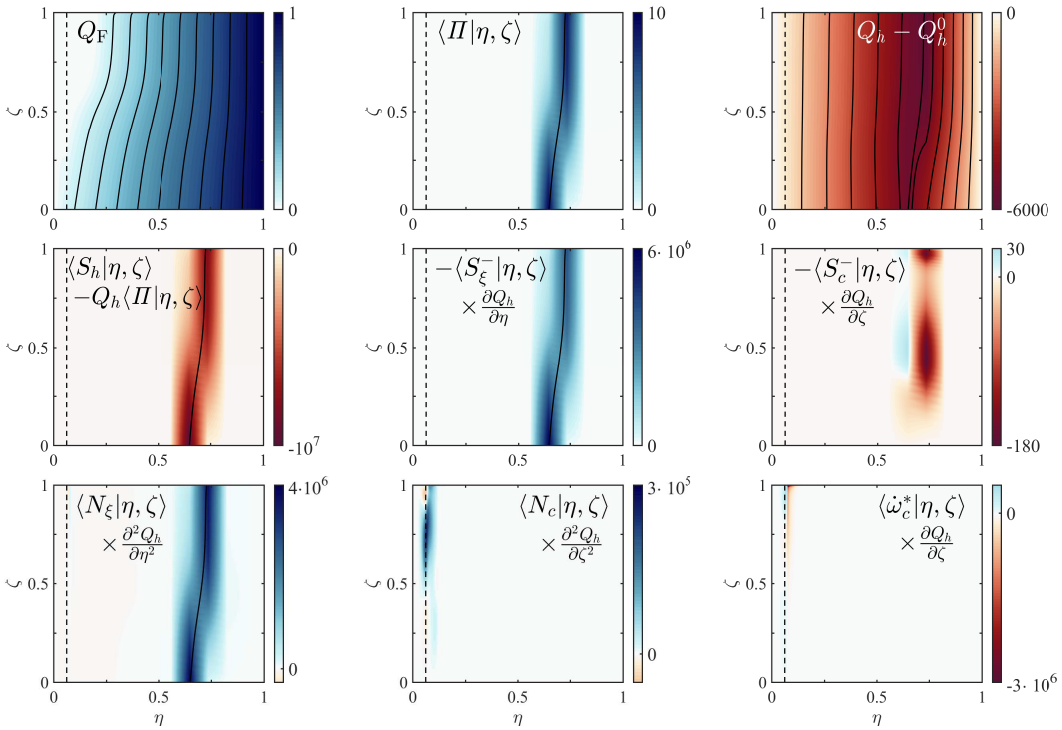


Fig. 5.5 Steady-state solution from DCMC-0D with spray terms for $Q_h$. First row: fuel mass fraction $Q_\mathrm{F}$, conditional spray term $\langle \Pi|\eta,\zeta\rangle$ and conditional enthalpy $Q_h$ relative to the case without spray terms denoted as $Q_h^0$; second and third row: terms of the $Q_h$-equation. The dashed vertical line marks $\xi_\mathrm{st} \approx 0.0622$.

to presume the shape of $\langle \Pi | \eta, \zeta \rangle$, and the net effect of the evaporation term on $Q_h$, shown relative to its initial un-deformed shape $Q_h^0(\eta, \zeta)$. The first spray term ($\langle S_h | \eta, \zeta \rangle - Q_h \langle \Pi | \eta, \zeta \rangle$) is partly compensated by the second one, $-\langle S_\xi^- | \eta, \zeta \rangle \, \partial Q_h / \partial \eta$. The third term, $-\langle S_c^- | \eta, \zeta \rangle \, \partial Q_h / \partial \zeta$, representing the effect of evaporation on $c$ is negligible by comparison. The net spray term is eventually counter-balanced by the SDR of the mixture fraction, which dissipates the evaporation source term in $\eta$-space and leads to the distortion of $Q_h$. In the limit of steady state, $Q_h$ decreases linearly in the interval $\eta \in [0, Y_{\mathrm{Fs}}]$. This suggests that the effect of evaporative cooling on the reaction zone, in terms of $\Delta h$ and $\Delta T$, is progressively smaller for hotter droplets when $Y_{\mathrm{Fs}} > \xi_{\mathrm{rich}}$. Vice versa, cold droplets at first contact with the flame can be expected to have the largest effect on the flame.

## 5.5 Conclusions

In this chapter solutions of the DCMC equation in the case of spatial homogeneity were explored. Analysis of terms in the DCMC equation showed that the conditional moments of $CO_2$, $N_2$ and $h$ are fixed in time and space because terms of the corresponding DCMC equations are zero or cancel each other. For $Q_{\mathrm{CO2}}$ this is a consequence of the progress variable definition, which is automatically fulfilled; for $Q_{\mathrm{N2}}$ and $Q_h$ this is only true due to the absence of $NO_x$ chemistry and due to the present adiabatic case, respectively, and in absence of differential diffusion.

In an *a priori* assessment the DCMC model, given the right conditional SDRs, successfully reproduced the conditional reaction rate and temperature from freely propagating laminar premixed flames. This confirms the validity of the DCMC model in this limit case of small $N_\xi$ and supports the choice of sub-models used for the doubly-conditional SDR of reaction progress variable.

A simple algebraic model for $\langle N_c | \eta, \zeta \rangle$ was tested and found to provide reasonable results in terms of the conditional temperature and reaction rate, similar to the ones obtained using $N_c^0(\eta, \zeta)$ from laminar premixed flames, if scaled correctly. In a parameter study the effect of varying the SDRs was investigated. Increasing $\langle N_c | \eta, \zeta \rangle$, relative to unstrained premixed flames, led to lower conditional reaction rates, and slightly increasing $\langle N_\xi | \eta, \zeta \rangle$ led to a higher peak value of the conditional reaction rates.

The effect of spray terms on the $Q_h$-equation was demonstrated. At steady state, a balance to leading order is reached between the conditional enthalpy spray term, the mixture fraction spray term and the mixture fraction SDR term.

# Chapter 6

# Simulation of a Piloted Spray Flame

## 6.1 Introduction

This chapter presents an application of the DCMC approach with RANS. The model is applied to a piloted ethanol spray flame recently studied experimentally in Cambridge [Kariuki & Mastorakos, 2017]. This experimental work studied the combustion of a mixture of air and uniformly dispersed droplets in a turbulent flow. The flame is stabilised on a burner but has the same characteristics as a flame propagating in a droplet-air mixture. Due to substantial pre-vaporisation and premixing the flame behaves similarly to premixed flames.

Spray flames of this type have so far been out of reach for CMC modelling. Mortensen & Bilger [2009] derived the CMC equation for spray combustion based on the mixture fraction concepts. Consequently, conventional CMC has been limited to spray flames whose behaviour was dominated by non-premixed combustion modes. More recently, CMC has been developed for premixed flames [Amzin et al., 2012]. However, in spite of their premixed flame-like behaviour these spray flames are still characterised by strong small-scale mixture inhomogeneities and steep mixture fraction gradients near the droplet surface. Recent DNS work has shown significant differences in the flame of propagating spray flames and fully premixed flames [Wacks & Chakraborty, 2016b; Wacks et al., 2016]. This shows the necessity for a Doubly Conditional Moment Closure model to reproduce the behaviour of a flame propagating in an inhomogeneous mixture. Therefore, the flame studied experimentally by Kariuki & Mastorakos [2017] constitutes a suitable candidate to test the present DCMC model.

The objective of the chapter is to present the first application of the DCMC model in a RANS framework. The chapter is organised as follows. First, the experimental test case and the numerical set-up of the simulations are described. Second, the results from two preliminary cold flow simulations are shown, which were used to estimate the level of pre-vaporisation in the burner. Third, velocity and droplet distributions from the simulation are compared to experimental measurements. Fourth, the doubly-conditional moments in different locations of the flames are compared. Fifth, the flame shape from the simulations is compared to OH-PLIF measurments in the experiment. Finally, the term balance in the mean and variance equations of the conditioning variables are discussed.

## 6.2 Experimental set-up

The test flames simulated in the present chapter were studied experimentally by Kariuki & Mastorakos [2017]. Figure 6.1 shows a schematic of the burner and Fig 6.2 shows a photo of the nozzle and pilot, and photos of the flames at the three conditions studied. Air is supplied through four holes at the the bottom of the burner. A perforated plate (4 mm holes) and a pack of bearing balls ensures a flat flow profile upstream of the atomiser. The ethanol spray is injected into the main flow of air approximately 380 mm upstream of the nozzle to allow for dispersion and partial pre-vaporisation. The spray injector is an air-assist external mix atomiser (Delavan AL-06), operating with a secondary air supply to break up the liquid fuel. The droplets are injected in a solid cone with a cone angle of 18°.

The main air flow rate was 220 L/min and the secondary air flow rate supplied to the atomiser was 15 L/min. The experiments considered three flames with different fuel flow rates, 24.4 mL/min, 28.4 mL/min and 23.4 mL/min, corresponding to the overall equivalence ratios (based on liquid fuel mass and total air mass flow rate) $\phi_{\text{ov}} = 0.62$, 0.72 and 0.82. Cold flow measurements used the fuel flow rate of the richest flame. The final section of the nozzle has a diameter 41 mm; in the experimental work the diameter was measured at the exit plane including a narrow chamfer (see detail in Fig. 6.1) and a nominal nozzle diameter of 42 mm was reported. The flame is stabilised at the exit plane of the nozzle on an annular pilot of diameter $\approx 51$ mm and width $\approx 6$ mm. The pilot is an open premixed methane-air flame with an approximately stoichiometric fuel-air ratio; the air flow rate was 30 L/min and the methane flow rate was 3.5 L/min. The flames have the character of a pilot-stabilised turbulent premixed jet flames with a bulk velocity $U_b \approx 3.04$ m/s, based on the diameter 41 mm. The

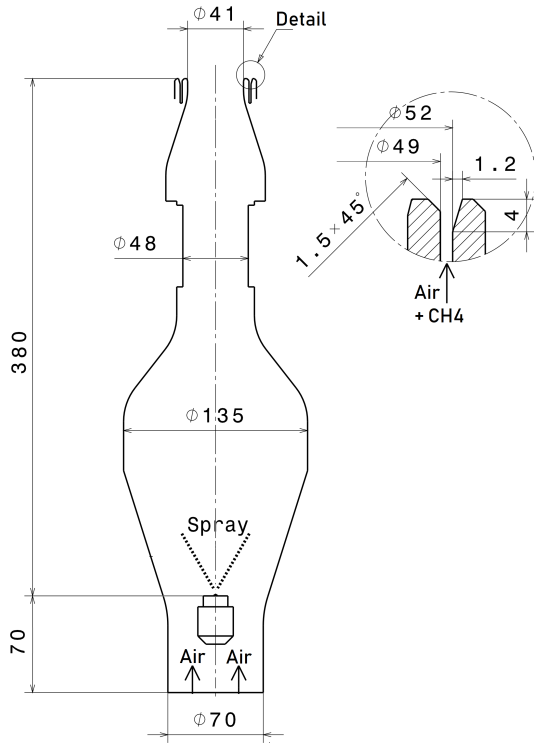


Fig. 6.1 Schematic of the burner and detail view of the pilot.

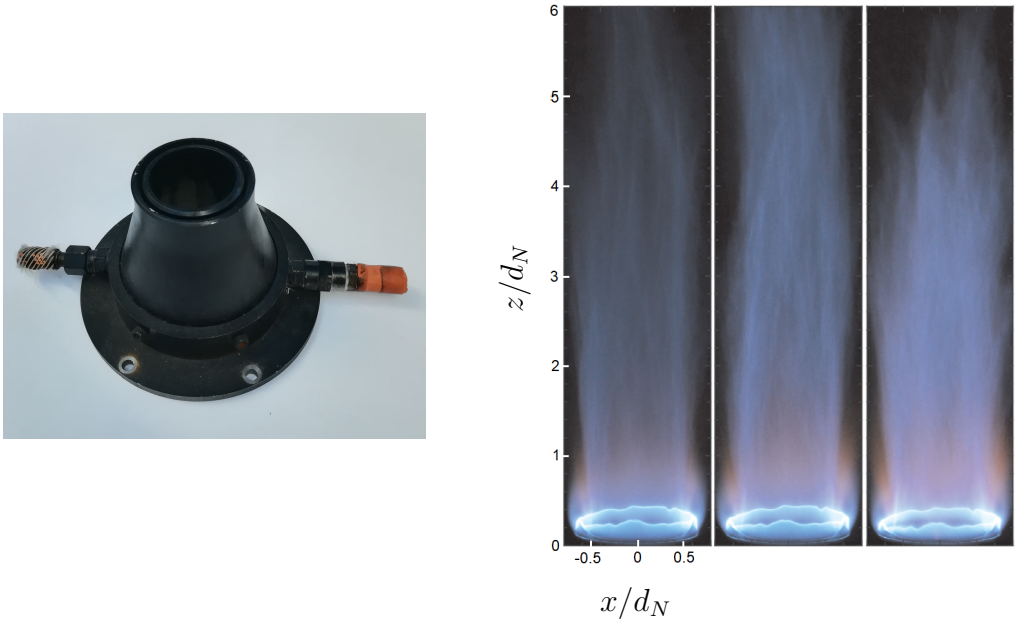


Fig. 6.2 Photo of the burner (left) and the flames (right). Flames with overall equivalence ratio $\phi_{ov} = 0.62$, 0.72 and 0.82 from left to right. At the base of the flames the annular pilot is visible. Photos of the flames from Kariuki & Mastorakos [2017], reused under Creative Commons Attribution License (CC BY).

coordinates of measurement locations, (axial distance from the exit plane of the nozzle $z$ and radial distance $r$ or cross-stream coordinate $x$, with $r = 0$ corresponding to $x = 0$, see Fig. 6.2), are normalised with the nominal nozzle diameter $d_N = 42$ mm, for direct comparison with the experiments [Kariuki & Mastorakos, 2017].

The experimental database contains Phase Doppler Anemomentry (PDA) and Laser Doppler Anemometry (LDA) measurements of the droplet diameter and velocity (in directions $x$ and $z$, as defined in Fig.6.2), simultaneous measurements of OH Planar Laser Induced Fluorescence (OH-PLIF) and Mie scattering, $OH^*$ chemiluminescence imaging and $CH_2O$-PLIF.

In the present work, two reacting cases with overall equivalence ratios $\phi_{\text{ov}} = 0.62$ and 0.82, correspond to $\xi \approx 0.065$ and 0.084 respectively (for ethanol-air mixture the stoichiometric mixture fraction is $\xi_{\text{st}} \approx 0.1005$ and the flammability limits are $\xi_{\text{lean}} \approx 0.05$ and $\xi_{\text{rich}} \approx 0.2$ [Coward & Jones, 1952]), and the non-reacting case were considered.

## 6.3 Simulation set-up

### 6.3.1 Model equations

In the present chapter the DCMC equation was solved without the conditional spray terms:

$$\begin{aligned}\frac{\partial Q_\alpha}{\partial t} + \nabla\cdot(Q_\alpha\langle\mathbf{u}|\eta,\zeta\rangle) &= Q_\alpha\ \nabla\cdot\langle\mathbf{u}|\eta,\zeta\rangle + D_T\nabla Q_\alpha \\ &+ \langle N_\xi|\eta,\zeta\rangle\frac{\partial^2 Q_\alpha}{\partial\eta^2} + \langle N_c|\eta,\zeta\rangle\frac{\partial^2 Q_\alpha}{\partial\zeta^2} + \langle N_{\xi c}|\eta,\zeta\rangle\frac{\partial^2 Q_\alpha}{\partial\eta\partial\zeta} + \langle\dot\omega_\alpha|\eta,\zeta\rangle \\ &- \frac{\partial Q_\alpha}{\partial\zeta}\frac{1}{\partial Q_\psi/\partial\zeta}\left(\langle N_\xi|\eta,\zeta\rangle\frac{\partial^2 Q_\psi}{\partial\eta^2} + \langle N_c|\eta,\zeta\rangle\frac{\partial^2 Q_\psi}{\partial\zeta^2} + \langle N_{\xi c}|\eta,\zeta\rangle\frac{\partial^2 Q_\psi}{\partial\eta\partial\zeta}\right) \\ &- \frac{\partial Q_\alpha}{\partial\zeta}\frac{1}{\partial Q_\psi/\partial\zeta}\langle\dot\omega_\psi|\eta,\zeta\rangle\end{aligned} \tag{6.1}$$

where the third and fourth line contain the terms of the conditional apparent reaction rate $\langle\dot\omega_c^*|\eta,\zeta\rangle$ (Eqn. 3.52). Details can be found in Section 3.7. For $\langle N_c|\eta,\zeta\rangle$ the model based on two bell curves with the presumed shape $G_c(\eta,\zeta)$ (Eqn. 3.75) suggested by Nguyen et al. [2010] was used. This model constitutes an approximation of a more complicated modelling approach where the doubly-conditional SDR is constructed from premixed laminar flames. Still, with an analytic expression for the presumed shape, the model can be conveniently used. This choice was made for simplicity in this

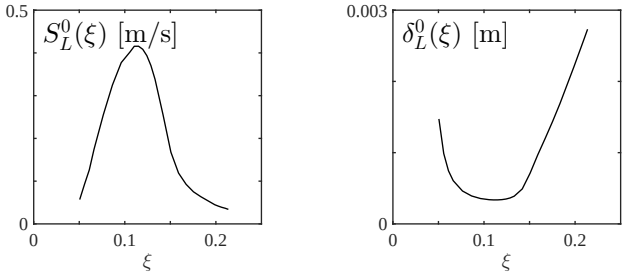


Fig. 6.3 Laminar flame speed and laminar flame thickness; $\xi_{\mathrm{st}} \approx 0.1005$.

application of the DCMC model. The other sub-models for the DCMC equation are as discussed in Section 3.7. The assumption of statistical independence of $\xi$ and $c$ is used for simplicity. Accurate modelling of the joint-PDF would be very complicated, considering the case of a three-stream problem, including one hot pilot stream, and droplet evaporation, and is beyond the scope of this work. The assumption may not be strictly valid close to the pilot, but given that the pilot stream is small compared to the main flow, it can be a reasonable modelling choice in the main flame region sufficiently far from the pilot. The assumption of conditional independence for the velocity was used since mixture fraction gradients are small in the present flame.

Figure 6.3 shows the laminar flame thickness $\delta_L^0$ and laminar flame speed $S_L^0$ used by the model for $\widetilde{N}_c$ (Eqn. 4.63). These quantities were computed for freely propagating laminar premixed flames using the commercial software Cosilab [Rotexo GmbH und Co. KG, 2012]. The transport equations of the mean and variance of the conditional variables, $\tilde{\xi}$, $\tilde{c}$, $\widetilde{\xi''}$ and $\widetilde{c''}$, were solved including all spray terms (see Eqns 4.24, 4.25, 4.26, and 4.27). In this chapter these spray terms are denoted as

$$S_{\widetilde{\xi''^2}} = 2(\widetilde{\xi\Pi} - \tilde{\xi}\tilde{\Pi}) - (\widetilde{\xi^2\Pi} - \tilde{\xi}^2\tilde{\Pi}) \tag{6.2}$$

$$S_{\tilde{c}} = \widetilde{S_c^-} + \widetilde{c\Pi} \tag{6.3}$$

$$S_{\widetilde{c''^2}} = 2(\widetilde{cS_c^-} - \tilde{c}\widetilde{S_c^-}) + (\widetilde{c^2\Pi} - 2\tilde{c}\widetilde{c\Pi} + \tilde{c}^2\widetilde{\Pi}) \tag{6.4}$$

These spray terms were computed by integration in conditional space (Eqn. 4.30), using the presumed shape of the conditional evaporation rate, $G_\pi(\eta, \zeta)$ (Section 3.7.6).

### 6.3.2 Numerical set-up

The three-dimensional computational domain stretches $-1 < z/d_N < 19$ along the burner axis, where $z = 0$ is the position of the nozzle outlet and the pilot (see definition of the coordinate axes in Fig. 6.2). The main flow inlet is retracted by one nozzle diameter. The diameter of the entire domain is $33d_N$. The domain is discretised using an unstructured tetrahedral mesh with approximately 4.5M cells. A three-dimensional domain was used to conform with the three-dimensional unstructured implementation of the DCMC code. The associated loss in computational performance is marginal since the cost of solving the flow field is negligible compared to the online solution of the chemistry in DCMC. The numerical domain and the mesh resolution are shown in Fig. 6.4.

The boundary conditions were set as follows. The turbulence level in the main flow is set according to Laser Doppler Anemometry (LDA) measurements. From the experiments velocity measurements in the axial direction, $u_z$, and horizontal cross-stream direction, $u_x$, are available (see Fig. 6.2). Assuming that $\mathrm{RMS}(u_x) \approx \mathrm{RMS}(u_y)$, the turbulent kinetic energy at the inlet is estimated as

$$\tilde{k} \approx [\mathrm{RMS}(u_z)]^2 + 2\ [\mathrm{RMS}(u_x)]^2 \tag{6.5}$$

which corresponds to a turbulent velocity fluctuation of $u' = (2\tilde{k}/3)^{1/2} \approx 0.51$ m/s or 15 % of the bulk velocity. Furthermore, the turbulent length scale is estimated as $L_T \approx d_N/3$ leading to an estimation of the turbulent dissipation rate according to

$$\tilde{\varepsilon} \approx u'^3/L_T \tag{6.6}$$

This provides an approximate value of 9.7 $\mathrm{m}^2/\mathrm{s}^3$.

Since the degree of pre-vaporisation of the ethanol spray was not measured in the experiment, the mixture fraction at the inlet had to be estimated. For this purpose separate RANS simulations of the interior of the burner, upstream of the nozzle, were performed. The set-up of these simulations is detailed in Section 6.3.4 and the results are shown in Section 6.4.1. According to these simulation of the upstream part of the burner the inlet boundary condition for the mixture fraction was set to $\tilde{\xi} = 0.04$ and $\widetilde{\xi''^2} = 0$. Even though the injected amount of liquid fuel is smaller in the leaner case, the same boundary condition is also used for the simulation of the flame with $\phi_{\mathrm{ov}} = 0.62$. This will allow us to explore the sensitivity of the simulation results to the level of pre-vaporisation and premixing in the upstream region of a spray flame. In the

rich flame almost half the fuel is pre-vaporised compared to two thirds in the leaner flame. For the main flow, the inlet boundary condition for the reaction progress variable upstream of the nozzle is set to $\tilde{c} = 0$ and $\widetilde{c''^2} = 0$. For the purpose of the present application whose aim is to discuss the model and its application, the uncertainty related to the inlet boundary condition is considered satisfactory.

In the framework of the present simulation the pilot requires modelling. The pilot is an open methane-air flame, which is not retracted relative to the main flow. Hence, dilatation in the pilot flame does not lead to a significant increase of the mean axial velocity but to an increase in width of the hot pilot stream as it would be expected for a usual triangular flame. Following a single mixture fraction based approach in the present simulations, the precise composition of a methane-air pilot cannot be taken into account. Instead the pilot is modelled as a premixed stoichiometric ethanol-air flame. The annular pilot flame itself is not resolved but instead modelled as a uniform inlet boundary condition with a laminar inflow of burnt gases, i.e. $\tilde{\xi} = \xi_{\mathrm{st}}$, $\widetilde{\xi''^2} = 0$, $\widetilde{c} = 1$ and $\widetilde{c''^2} = 0$, with a mass flow rate corresponding to the experimental configuration.

For the modelling of the spray, Lagrangian particles are injected on the surface of the main flow inlet. Figure 6.5 shows the droplet size distributions measured at the exit of the nozzle in the three cases considered. The cumulative number distribution, $N_d(d_d)$, is defined as the fraction of droplets smaller than diameter $d_d$, and then $\mathrm{d}N_d/\mathrm{d}d_d$ can be interpreted as the droplet size probability density function. The cumulative volume distribution, $Q_d(d_d)$, is defined as the fraction of the total liquid volume in droplets of diameter less than $d_d$ [Lefebvre, 1989]. The number distribution can be computed from the number increment $\Delta N_{d,i}$, i.e. the number of droplets in the size class $d_{d,i} - \Delta d_{d,i}/2 \leq d_d < d_{d,i} + \Delta d_{d,i}/2$. The volume distributions can be computed from the volume increment within $\Delta d_{d,i}$:

$$\Delta Q_{d,i} = \left( \Delta N_{d,i} \frac{\pi}{6} d_{d,i}^3 \right) \tag{6.7}$$

The distributions can be represented by histograms, which are constructed by plotting $\Delta N_{d,i}/\Delta d_{d,i}$ and $\Delta Q_{d,i}/\Delta d_{d,i}$ versus $d_{d,i}$. In Fig. 6.5, the number and volume distributions are plotted as histograms, normalised by the total number of droplets $N_{d,\mathrm{tot}}$ and total liquid volume $Q_{d,\mathrm{tot}}$. For the case of $\phi_{\mathrm{ov}} = 0.62$ the droplet number and volume distributions is plotted for different radial locations across the nozzle in the range $-18 \leq x \leq 18$ mm. The distributions collapse onto each other. This shows that the droplet size distribution is independent of the radial position. The shape of the distributions cannot be approximated accurately with a standard Rosin-Rammler

distribution. Consequently, a general shape is used for the volume distribution, discretising the experimentally measured size distribution on a grid and using piece-wise linear interpolation between the grid nodes (spacing of nodes = 2 $\mu$m). For each case an average droplet distribution is constructed from experimental data by averaging the distribution from the measurement points with $z = 6$ mm. The droplets are injected randomly at the main flow inlet surface.

In the experimental set-up the annulus that stabilises the pilot is very narrow, and the pilot flow is broadened by the dilatation across the flame while the velocity of the hot stream does not increase significantly. In the present work the pilot is modelled as a uniform inlet of hot gases with the mass flow rate of the experiment. Yet, fixing the mass flow rate according to the experiment, while using the geometric area of the annulus as uniform inlet, the velocity of the pilot stream is greatly overestimated. Therefore, the surface of the annulus is increased by a factor of three to match the momentum of the pilot stream with the experiment as well. A small laminar co-flow of 0.1 m/s is set around the burner nozzle, where $\tilde{\xi} = 0$ and $\tilde{c} = 1$. Walls are considered adiabatic.

A one-dimensional DCMC grid was used to discretise the physical domain with 35 DCMC cells along the burner axis for $0 < z/d_N < 5$; the DCMC cells were spaced at an axial distance of 5 mm. A steady-state solution from DCMC-0D was used as initial condition and inlet boundary condition. In the present case, a very weakly strained solution from DCMC-0D was used, notably $N_{\xi,\max} = 1$ s$^{-1}$ and $N_{c,\max} = 200$ s$^{-1}$. Zero-gradient boundary conditions were used for the DCMC equation at the walls and the outlet.

The doubly-conditional space, $\mathbb{D} = \{(\eta, \zeta) \in \mathbb{R}^2 : 0 \leq \eta \leq 1, 0 \leq \zeta \leq 1\}$, was discretised with 51 $\eta$-nodes, clustered around the stoichiometric mixture fraction $\eta = \xi_{\text{st}}$ (for the reaction of ethanol with air $\xi_{\text{st}} \approx 0.1006$) and 41 $\zeta$-nodes, which are more closely spaced at $\zeta = 1$. Dirichlet boundary conditions are set on all four sides of the doubly-conditional domain, mixing line and equilibrium condition for $\zeta = 0$ and 1 respectively, air at $\eta = 0$ and fuel vapour at the boiling point (351.4 K for ethanol [Green & Perry, 2008]) at $\eta = 1$. The equilibrium condition was approximated by solving singly-conditional, non-premixed CMC-0D equation, similar to the non-premixed flamelet equation, with a very low scalar dissipation rate $N_{\xi,\max} = 1$ s$^{-1}$, compared to the critical scalar dissipation rate of approximately 367 s$^{-1}$ leading to extinction [Giusti et al., 2016]. The discretisation of the doubly-conditional space and the shape of $Q_{\text{CO2}}$ are shown in Fig. 6.6.

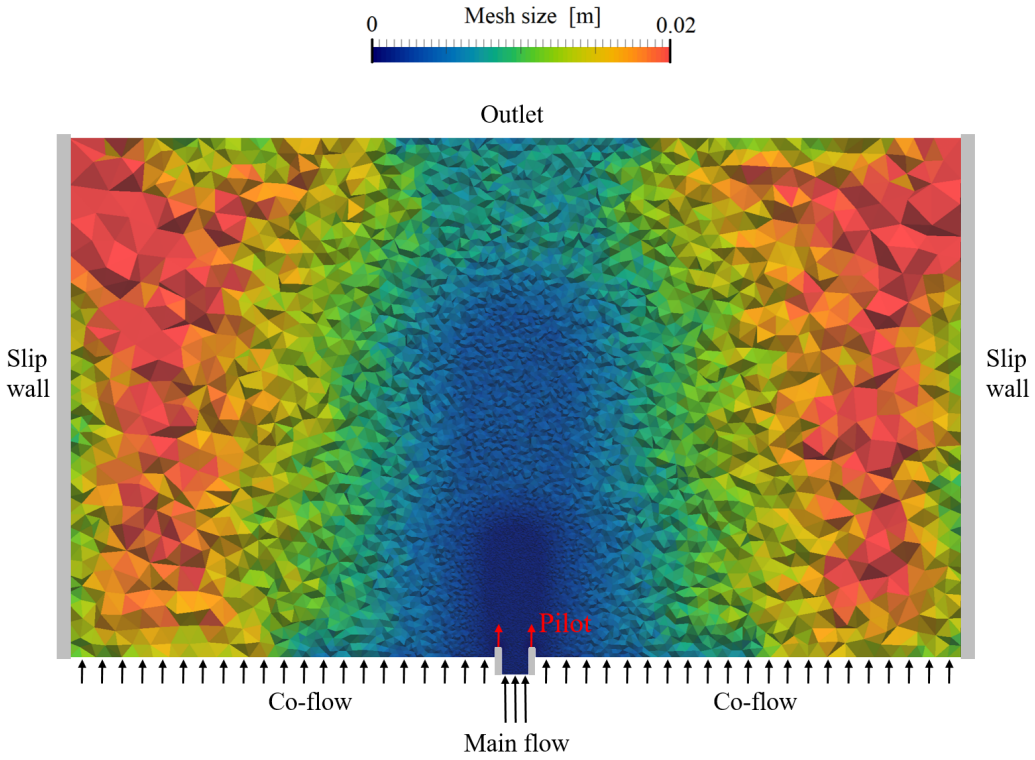


Fig. 6.4 Numerical domain and mesh resolution used for the simulation of the flames, shown in the $xz$-cut plane.

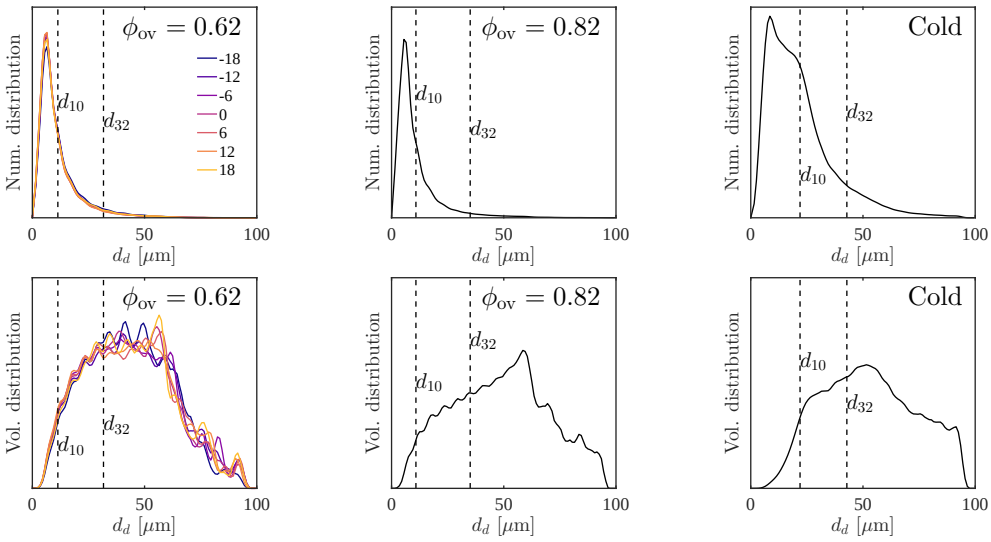


Fig. 6.5 Normalised droplet distributions from PDA measurements at the exit of the nozzle. For $\phi_{ov} = 0.62$ (left) the different lines indicate the $x$-coordinate [mm] of the measurement location. Dashed lines mark the mean diameter $d_{10}$ and the Sauter mean diameter $d_{32}$. In the three cases (from left to right) $d_{10} \approx 11.5$, 10.8 and 21.9 $\mu$m, and $d_{32} \approx 31.5$, 35.1 and 42.8 $\mu m$.

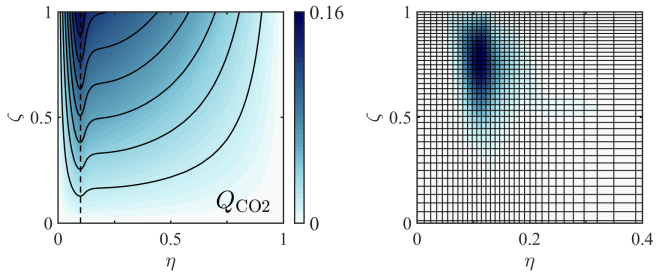


Fig. 6.6 Conditional moment $Q_{CO2}$ and discretisation of the doubly-conditional space. The reaction rate $\dot{\omega}_c$ is indicated on top of the grid. For $\eta > 0.4$ the $\eta$-grid is approximately uniform.

The flow field was solved with unsteady RANS (URANS) using the $k$-$\varepsilon$ model with standard parameters. The time step for URANS was $5 \cdot 10^{-6}$ s. To keep operator splitting errors small, the DCMC equation was solved in five sub-steps of $10^{-6}$ s, employing the operator splitting strategy discussed in Section 4.5 in each sub-step. Numerical schemes for the flow field solver were of second order in space and first order in time. Numerical schemes for DCMC were as detailed in Section 4.5.

### 6.3.3 Chemistry

A detailed chemical mechanism for ethanol combustion [Marinov, 1999] with 57 species and 383 reversible reactions is used. The mechanism performs well in predicting ignition delays and laminar flame speeds at ambient pressure when compared to experimental data. It has been successfully used in a CMC simulation by Giusti & Mastorakos [2017].

### 6.3.4 Numerical set-up of preliminary simulation

In this section the numerical set-up of the cold flow simulations used for the estimation of the level of pre-vaporisation is detailed. The numerical domain included the inside of the burner upstream of the nozzle up to the atomiser. An unstructured tetrahedral mesh with 3.5M cells was used. The relevant parts of the domain and the mesh resolution are shown in Fig. 6.7. A coarsely meshed cylindrical domain which was attached downstream of the nozzle is not shown here.

For the main air flow a uniform inflow velocity corresponding to the main air flow rate was applied at the bottom surface of the domain. The secondary air supplied to the atomiser is injected from the atomiser. In reality the air is injected through a small orifice with very high velocities to break up the liquid. This region where the spray is

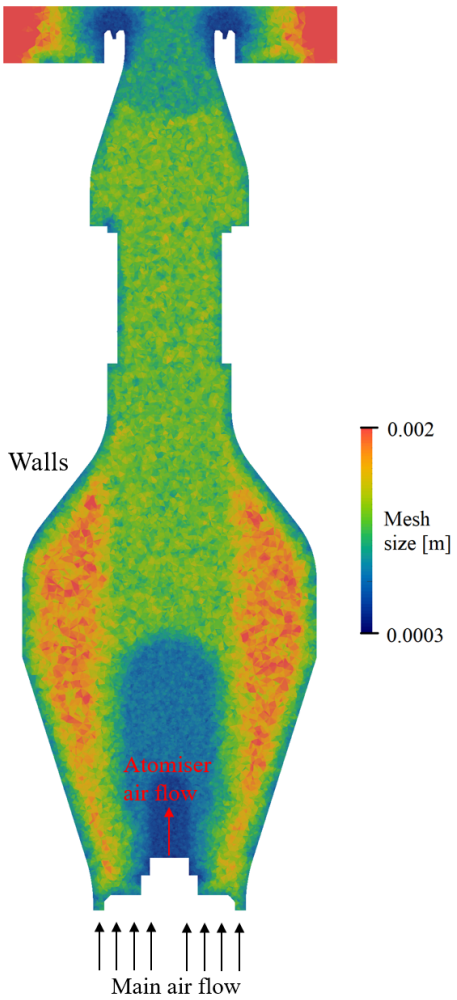


Fig. 6.7 Numerical domain and mesh resolution for preliminary non-reacting simulations, shown in the $xz$-cut plane.

dense cannot be resolved with the present modelling framework. Instead the atomiser air flow is modelled as a uniform velocity inlet with a diameter of 3 mm. The droplets are injected in the centre of this jet. Since the experiment did not provide the droplet distributions at close distance from the injector, the droplets were injected with the distribution measured at the nozzle exit. This assumption is considered acceptable for the purpose of the present simulation, to estimate the pre-vaporisation in the burner. No-slip wall boundary conditions were applied at the outer walls of the burner and the pieces of the atomisation system, and standard wall functions are used.

## 6.4 Results and discussion

### 6.4.1 Estimation of pre-vaporisation

In order to estimate the level of pre-vaporisation in the burner, separate non-reacting simulations of the region upstream of the nozzle are performed. The results are shown in Fig. 6.8. The mean mixture fraction at the nozzle exit shows the level of pre-vaporisation. In the richer case with $\phi_{\text{ov}} = 0.82$, the mean mixture fraction at the nozzle is $\tilde{\xi} \approx 0.038$, and in the lean case with $\phi_{\text{ov}} = 0.62$ it is $\tilde{\xi} \approx 0.035$. Note that complete evaporation would give a mean mixture fraction of 0.084 and 0.065 respectively. The level of pre-vaporised fuel vapour is much closer in both cases than the overall equivalence rations. Moreover, the mean mixture fraction hardly increases in the last diameter upstream of the nozzle. Both observations suggest that the vapour-air mixture approaches saturation condition. The simulations also show that the profiles of $\tilde{u}_z$, $\tilde{k}$ and $\tilde{\xi}$ at the exit of the nozzle are flat. This is in line with the PDA measurements for velocity and turbulence intensity. Furthermore, it can be observed that $\tilde{k}$ is almost solely generated by the atomiser. The turbulence intensity decays along the pipe but is eventually enhance by the contraction leading to the exit of the nozzle. This explains the mechanism behind the generation of a high turbulence level, $u'/U_b \approx 0.15$, at relatively low bulk velocity.

These simulations show that $\tilde{\xi} = 0.04$ is a reasonable value for the fuel vapour mass fraction in the gas phase. This value corresponds approximately to the pre-vaporisation in the richer case. It lies below the lean flammability limit, so that enhanced evaporation at contact with the hot gases is essential to maintain the flame, but a premixed character of the flame can be expected. Using the same level of vapour in the leaner flame overestimates the pre-vaporisation in this case. Therefore, the

leaner case can demonstrate how a slight enhancement of pre-vaporisation affects the flame.

### 6.4.2 Velocity and droplet statistics

Figure 6.9 shows the radial profiles of the mean axial velocity of the gas phase for cold flow and the two flames considered here. The results are compared to Phase Doppler Anemometry (PDA) measurements of the mean axial velocity of the droplets in the range $0 \leq r/d_N \leq 0.5$, not including the pilot stream, by Kariuki & Mastorakos [2017]. In the cold case, the effect of the pilot stream is small and the flow spreads like a turbulent jet with a radial profile similar to a Gaussian bell curve. In contrast, for both flames studied, the axial mean velocity is almost constant for $r/d_N < 0.5$. This feature is well reproduced by the simulation.

Next the droplet size information from the simulations is compared to the PDA measurements [Kariuki & Mastorakos, 2017]. Figure 6.10 compares the droplet volume distributions, represented by a normalised histograms, i.e. $(\Delta Q_{d,i}/Q_{\mathrm{d,tot}})/\Delta d_{d,i}$ versus $d_{d,i}$. The spray is injected far upstream of the nozzle and experimental measurements show that the droplet distributions are very similar at different radial positions in the core of the main flow, even for reacting cases. Thus, droplet distributions are only shown for different axial positions, considering the experimental data from all measurement points with $r < 0.75 \times (d_N/2)$. For the simulations, the droplet volume distributions at the inlet were set equal to the experimental ones from the axial position $z = 6$ mm. In general, a reasonable agreement between the experimental volume distributions and the simulation results is achieved. In both flames, the droplet volume distribution flattens in the range of small droplets ($d_d < 30$ $\mu$m) while it increases for larger droplets (40 $\mu$m $< d_d <$ 70 $\mu$m). This can be explained by (i) a shorter heating-up period and thus quicker evaporation of smaller droplets and (ii) a faster decrease in diameter for smaller droplets when their temperature is nearly constant and $d_d^2$ is known to decrease approximately linearly in time [Williams, 1985b]. The phenomenon is slightly over-predicted in the simulations but can also be observed in the PDA data, in particular, for the richer flame.

### 6.4.3 Analysis in doubly-conditional space

In Fig. 6.11 the conditional moments of $CO_2$, OH, $CH_2O$ and temperature are shown for different locations in both flames. Figure 6.12 shows the conditional scalar dissipation rates and apparent reaction reaction rate for some of these locations. Note that $Q_{\mathrm{CO2}}$ is

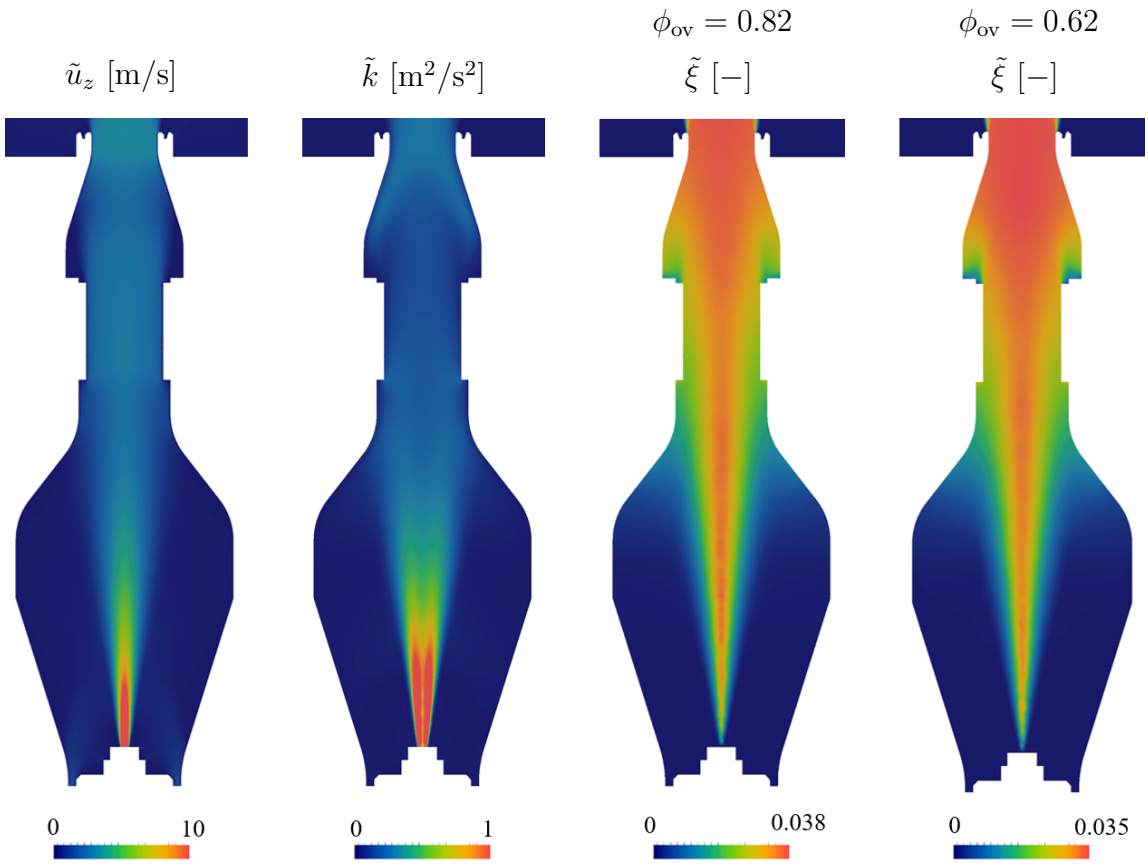


Fig. 6.8 Mean velocity, turbulent kinetic energy and mean mixture fraction upstream of the nozzle. The mean velocity and $\tilde{k}$ are very similar in both cases. The scale for velocity is capped at 10 m/s and for $\tilde{k}$ at 1 m$^2$/s$^2$.

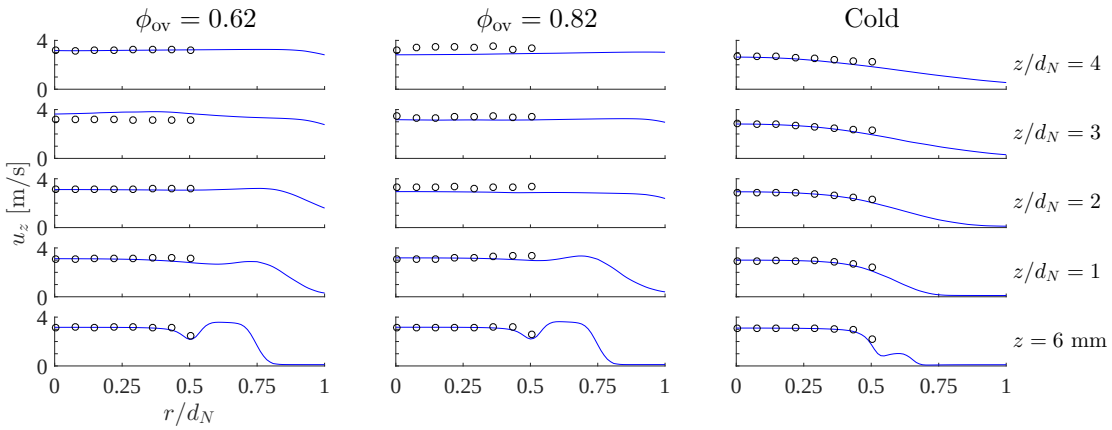


Fig. 6.9 Radial profiles of mean axial velocity from PDA measurements, $\langle u_z \rangle$ (symbols ∘), and from the RANS simulation, $\widetilde{u}_z$ (line –), at 5 axial locations for the cold flow and the flames.

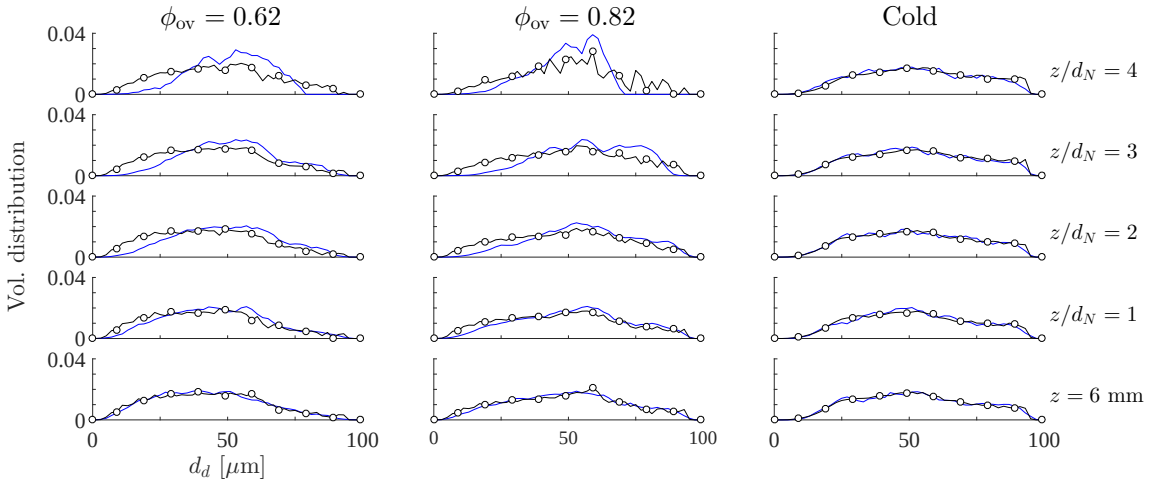


Fig. 6.10 Droplet volume distributions from PDA measurements (line with symbols ∘) and from the RANS simulations (line –) at 5 axial locations for the cold flow and the flames. The distributions are represented by normalised histograms, $(\Delta Q_{d,i}/Q_{d,\mathrm{tot}})/\Delta d_{d,i}$.

fixed for all DCMC cells equal to its shape defined by Eqn. 3.12, as a direct consequence of the definition of the progress variable based on the mass fraction of $CO_2$. The DCMC cell at $z = 0$ is located at the exit of the nozzle very close to the inlet and the scalar dissipation rates upstream of the flame are low. Hence, the structure of a weakly strained flame is mostly influenced by the advective term of the DCMC equation. For $\eta = \xi_{\mathrm{st}}$ the temperature rises quickly for $0 \leq \zeta < 0.5$ and then flattens out for higher $\zeta$, slowly approaching the temperature at equilibrium condition. In contrast, the DCMC cell at $z/d_N = 1$ contains the flame and thus experiences increased scalar dissipation rates. In particular, a high $\widetilde{N}_c$ diffuses reactants in conditional space. Consequently, $Q_T$ rises almost linearly from $\zeta = 0$ to 1 at $\eta = \xi_{\mathrm{st}}$.

The conditional moments observed at the locations $z/d_N = 1$ and 2 are very similar and the gradient of the doubly-conditional moments is low. This weak dependence on physical space suggests that the entire flame is already well parametrised by the doubly-conditional space. Furthermore, there are strong similarities between the richer and the leaner flame. Both show the same evolution of the flame structure in axial direction: increasing $N_c$ and decreasing $\dot{\omega}_c^*$. This trend was already discussed in Chapter 5. The similarity between the flame structure in both flames suggests that the difference in equivalence ratio is partly considered via the mixture fraction space in the doubly-conditional parametrisation. This means that the difference in the mean flame shape are due to the differences in the mixture fraction PDF, while the doubly-conditional flame structure is similar in both cases, because the flow conditions, turbulence level etc. are the same for both flames.

The conditional apparent reaction rate computed at the two locations previously discussed are shown in Fig. 6.13. They are compared to $\dot{\omega}_c^0(\eta, \zeta)$, the reaction rate from a 2D-manifold created for freely propagating laminar premixed flames. The laminar flames were computed using the commercial software Cosilab [Rotexo GmbH und Co. KG, 2012]. In the weakly strained case at $z/d_N = 0$ the conditional reaction rate reaches significantly higher values than for the location at $z/d_N = 1$. This shows how the conditional reaction rate adjusts as the scalar dissipation rates increase. The apparent reaction rate $\langle \dot{\omega}_c^* | \eta, \zeta \rangle$ also takes negative values. This is due to the contribution of the non-premixed term, which is also shown in Fig. 6.13. Figure 6.11 showed that the doubly-conditional flame structure is very similar at different axial locations and in the leaner flame. This can also be observed for the reaction rate which is very similar and, thus, is not shown here.

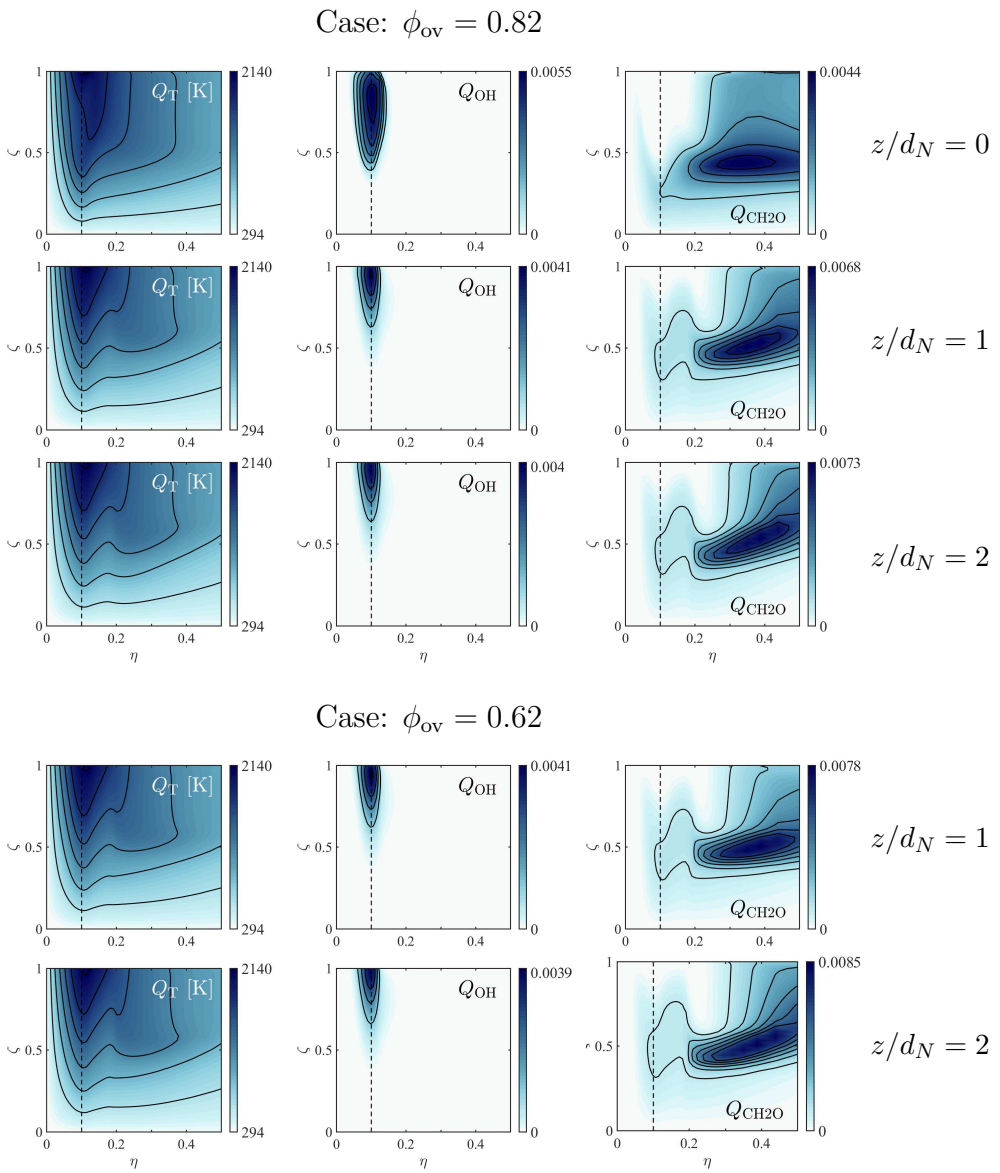


Fig. 6.11 Conditional moments of $T$, $Y_{OH}$ and $Y_{CH2O}$ in different locations for the case with $\phi_{ov} = 0.82$ and the case with $\phi_{ov} = 0.62$. The dashed line marks the stoichiometric mixture fraction $\xi_{st} \approx 0.1005$

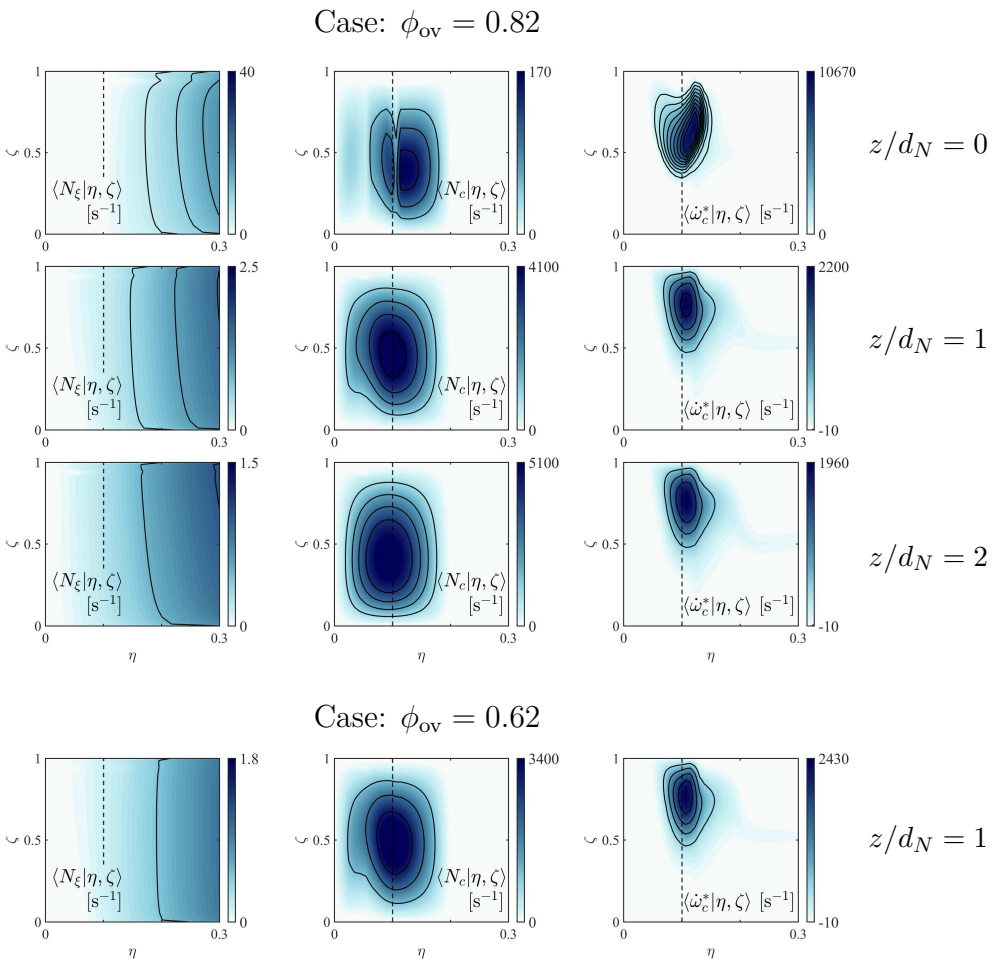


Fig. 6.12 Conditional scalar dissipation rates and conditional reaction rate in different locations for the case with $\phi_{ov} = 0.82$ and the case with $\phi_{ov} = 0.62$. The dashed line marks the stoichiometric mixture fraction $\xi_{st} \approx 0.1005$.

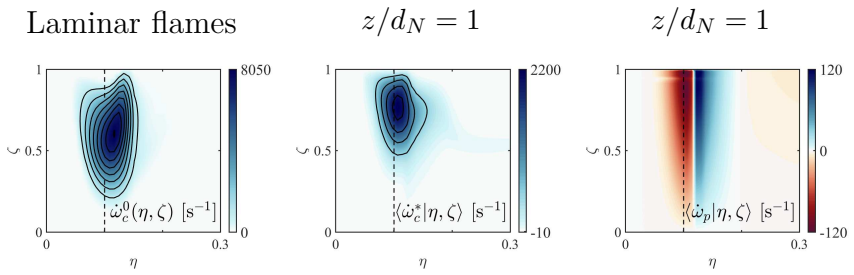


Fig. 6.13 Conditional reaction progress variable source term. From left to right: $\dot{\omega}_c^0(\eta,\zeta)$ from laminar premixed flames, $\langle\dot{\omega}_c^*|\eta,\zeta\rangle$ and $\langle\dot{\omega}_p|\eta,\zeta\rangle$ at the location $z/d_N = 1$, for the case with $\phi_{ov} = 0.82$.

### 6.4.4 Flame shape

Next the shape of the flames is assessed. Figures 6.14 and 6.15 shows ensemble averaged OH planar laser-induced fluorescence (OH-PLIF) images and isolines of ensemble-averaged progress variable $\langle c \rangle$ determined from experimental data [Kariuki & Mastorakos, 2017], in comparison to $\tilde{Y}_{\mathrm{OH}}$ and $\tilde{c}$ isolines from the simulations. Note that the OH-PLIF signal intensity is not directly related to OH mass fraction [Eckbreth, 1996]. Therefore, only a qualitative comparison is possible and no scale is shown for the mean OH PLIF intensity. Note also that in the experiment the instantaneous field of progress variable was determined by tracking the flame front through a thresholding procedure applied to the OH-PLIF images, which is different from the definition of the progress variable based on $CO_2$ mass fraction used in the simulations.

For the richer flame with an overall equivalence ratio $\phi_{\mathrm{ov}} = 0.82$ (Fig. 6.15), the mean flame brush is relatively broad, occupying the range $1 < z/d_N < 2.5$ along the burner axis, where the mean progress variable increases from 0.1 to 0.9. The simulation predicts a slightly longer flame but a thinner flame brush, stretching over the range $2.1 < z/d_N < 2.8$. Moreover, $\tilde{Y}_{\mathrm{OH}}$ in the burnt gases, downstream of the flame is lower than in the pilot stream, while this trend is not observed in the OH-PLIF signal intensity. The simulation results also show that a significant proportion of fuel is not burned and the presence of this fuel in the hot combustion products leads to the production of $CH_2O$ downstream of the flame. The leaner flame (Fig. 6.14) with an overall equivalence ratio $\phi_{\mathrm{ov}} = 0.62$ is longer and experiments showed that the mean flame brush is present in the range $2.5 < z/d_N < 3.5$ on the burner axis. This flame length is well predicted by the simulation. Moreover, the simulation also predicts a lower $\tilde{Y}_{\mathrm{OH}}$ in the main flow compared to the pilot stream. Indeed, this behaviour is also found in the OH-PLIF signal of the leaner flame. However, this feature is less pronounced in this case and the simulations, unexpectedly, predict that the combustion products of the leaner flame contain more $\tilde{Y}_{\mathrm{OH}}$ than in the case of the richer flame. Since the pre-vaporised fraction of fuel is different in both cases, this feature can be directly related to the droplet terms in the transport equations of the conditioning variables, which will be discussed next.

### 6.4.5 Term balance for conditioning variables

In the following, some information on the relative magnitude of the various terms in the transport equations of $\tilde{\xi}$, $\widetilde{\xi''^2}$, $\tilde{c}$, $\widetilde{c''^2}$ and the DCMC equation is given. Figure 6.16 shows the field of the mean mixture fraction and its variance for the richer flame with

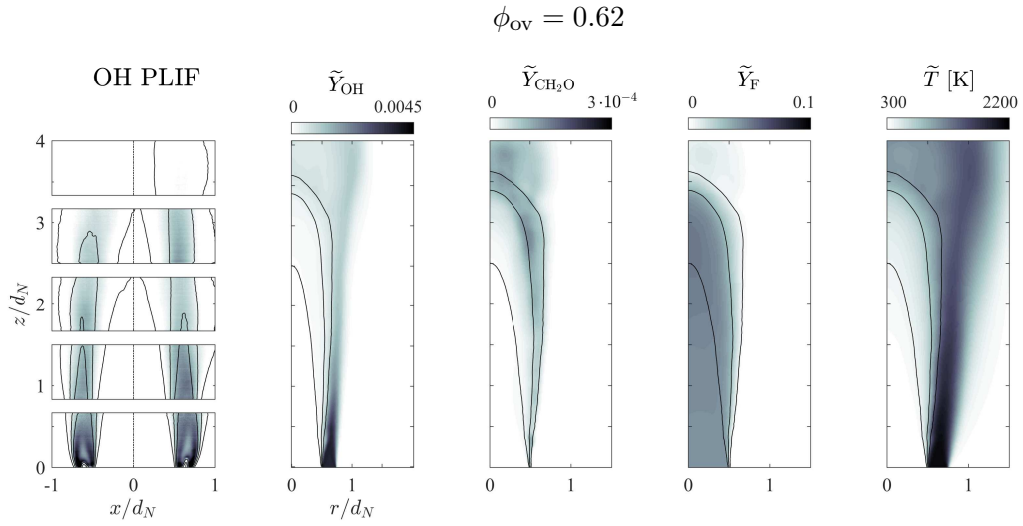


Fig. 6.14 Simulation results for $\tilde{Y}_{OH}$ and $\tilde{c}$-isolines compared to ensemble-averaged OH-PLIF and experimental $\langle c \rangle$ isolines for the flame with $\phi_{ov} = 0.62$. The isolines are for the values 0.1, 0.5 and 0.9. Fields of $\tilde{Y}_{CH2O}$, $\tilde{Y}_F$, $\tilde{T}$ from the simulation are also shown.

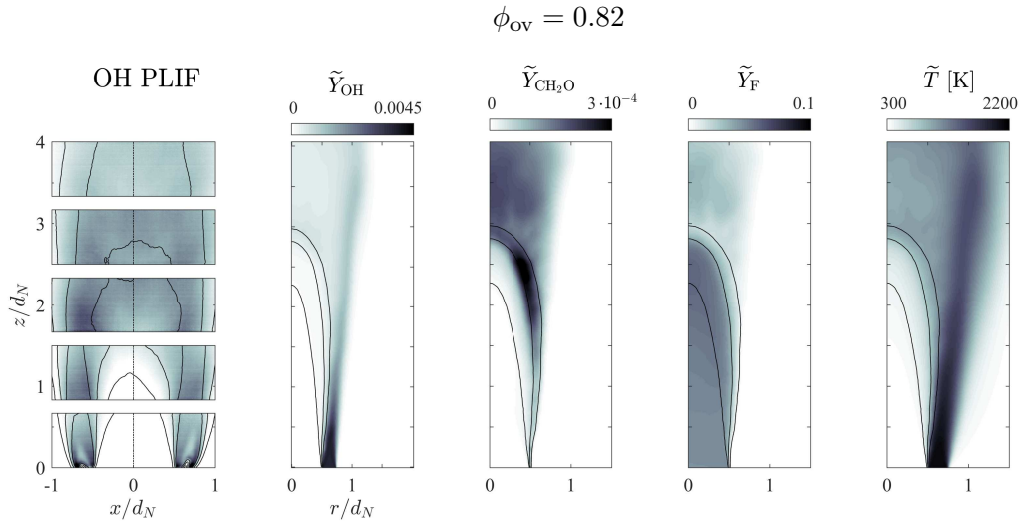


Fig. 6.15 Simulation results for $\tilde{Y}_{OH}$ and $\tilde{c}$ isolines compared to ensemble-averaged OH-PLIF and experimental $\langle c \rangle$ isolines for the flame with $\phi_{ov} = 0.82$. The isolines are for the values 0.1, 0.5 and 0.9. Fields of $\tilde{Y}_{CH2O}$, $\tilde{Y}_F$, $\tilde{T}$ from the simulation are also shown.

$\phi_{\mathrm{ov}} = 0.82$. The mean mixture fraction set at the inlet, one nozzle diameter upstream of the burner exit, is below the lean flammability limit of an ethanol air mixture ($\xi_{\mathrm{lean}} \approx 0.05$). Upstream of the flame the mean temperature is low and the evaporation rate $\widetilde{\Pi}$ is low. Nevertheless $\tilde{\xi}$ increases along the burner axis, first slowly to $\tilde{\xi} \approx 0.048$ at $z/d_N = 1$ and then faster, reaching 0.59 at $z/d_N = 2$ in the preheat zone of the flame. Even though the evaporation rate is highest in the range of $0.5 < \tilde{c} < 0.9$, some droplets still exist downstream of the flame brush and $\widetilde{\Pi}$ takes significant values until $z/d_N = 3.5$. Droplet evaporation is also the dominant source in the mixture fraction variance equation (Eqn. 4.25) and the production due to mean mixture fraction gradients is negligible in the flame investigated in this work. In contrast to $\widetilde{\Pi}$, the mixture fraction variance source source term is very small upstream of the $\tilde{c} = 0.1$ isoline because the droplets evaporating in this region have a low $T_d$ and thus $\xi_s$ is not much larger than $\tilde{\xi}$. Consequently, $\widetilde{\xi''^2}$ rises significantly in the region of the mean flame brush. In particular, this increase of $\widetilde{\xi''^2}$ is not directly counterbalanced by the scalar dissipation rate term, since a model for passive scalar mixing (Eqn. 4.21), was used due to the lack of alternatives. Even though the scalar dissipation rate is globally of the same order of magnitude as the droplet source of $\widetilde{\xi''^2}$, we note that $\widetilde{\xi''^2}$ is locally over-predicted. In particular, this is the case in the core of the main flow for $2.5 < z/d_N < 3.5$, where the production of variance outweighs its destruction. This high level of mixture fraction variance in the post flame region of the richer flame explains low levels of $\tilde{Y}_{\mathrm{OH}}$ in the main flow of the richer flame, compared to the pilot stream (Fig. 6.15): for high $\widetilde{\xi''^2}$ a broad $\beta$-PDF is presumed and the probability of finding flammable mixture that can react to form OH is low. This connection is also demonstrated by the unexpected fact that the simulations show higher $\tilde{Y}_{\mathrm{OH}}$ for the leaner flame. Since the mass fraction of pre-vaporised fuel is $\tilde{\xi} = 0.04$ for both flames, in the lean case two thirds of fuel mass are fully premixed. Hence, evaporation produces lower levels of $\widetilde{\xi''^2}$ in the lean case leading to higher $\tilde{Y}_{\mathrm{OH}}$. For the same reason $\bar{\rho}$ is over-predicted leading to an under-prediction of $\tilde{u}_z$ at downstream locations.

In addition to the mean reaction source term, the $\tilde{c}$-equation (Eqn. 4.26) also contains a droplet source term, which is computed as detailed in Eqn. 6.3. As previously discussed, this source term is zero as long as the droplets evaporate in unburned mixture. On a global scale $S_{\tilde{c}}$ is also two orders of magnitude lower than the apparent reaction rate $\widetilde{\dot{\omega}_c^*}$ and, thus, it only has a small effect on the shape of the flame brush. The same applies to the total evaporation variance source term $S_{\widetilde{c''^2}}$ compared to $\widetilde{c''\dot{\omega}_c^{*\prime\prime}}$, so that the effect of evaporation on the $\widetilde{c''^2}$-equation is negligible in the present case. In contrast, the $S_{\tilde{c}}$ plays an important role in the region downstream

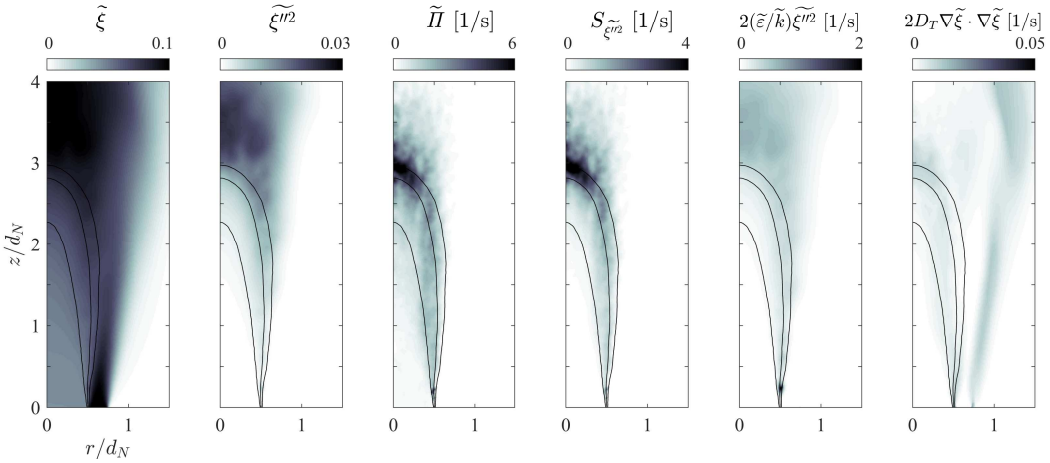


Fig. 6.16 Fields of $\tilde{\xi}$ and $\widetilde{\xi''^2}$ and source/sink terms of their transport equations for the flame with $\phi_{\text{ov}} = 0.82$. $S_{\widetilde{\xi''^2}}$ is the droplet source in the $\widetilde{\xi''^2}$ equation and $2(\tilde{\varepsilon}/\tilde{k})\widetilde{\xi''^2}$ is the scalar dissipation rate term. Isolines of $\tilde{c} = 0.1$, 0.5 and 0.9 mark the flame brush.

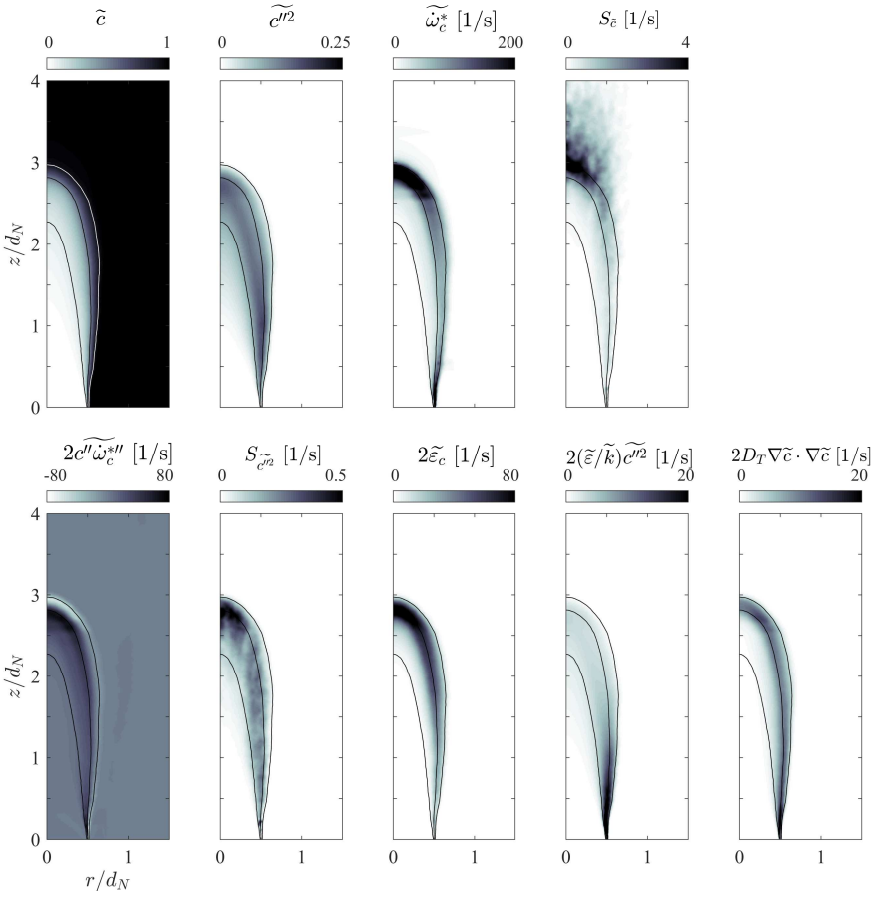


Fig. 6.17 Fields of $\tilde{c}$ and $\widetilde{c''^2}$ and source/sink terms of their transport equations for the flame with $\phi_{\text{ov}} = 0.82$. $S_{\tilde{c}}$ and $S_{\widetilde{c''^2}}$ are the droplet sources terms of the $\tilde{c}$ and $\widetilde{c''^2}$ equations respectively. $\tilde{\varepsilon}_c$ is the scalar dissipation from the model by Kolla et al. [2009]. Isolines of $\tilde{c} = 0.1$, 0.5 and 0.9 mark the flame brush.

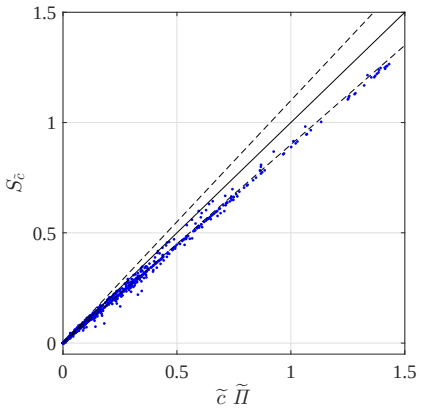


Fig. 6.18 Scatter plot of $S_{\tilde{c}}$ versus $\widetilde{\tilde{c}\Pi}$. The solid line represents equality. The dashed lines are for +10 % and −10 %. Simulation data from the case with $\phi_{\mathrm{ov}} = 0.82$.

of the flame, where it counter-balances a large fraction of the decrease in $\tilde{c}$, otherwise caused by the evaporative mass source acting on the mean density. For this purpose, a simplified model for this term can be proposed by comparing $S_{\tilde{c}}$ to $\widetilde{\tilde{c}\Pi}$. Figure 6.18 shows that instead of using Eqn. 6.3, a simplified model,

$$S_{\tilde{c}} = \widetilde{S_c^-} + \widetilde{c\Pi} \approx \tilde{c}\widetilde{\Pi} \tag{6.8}$$

can be used for this purpose.

This leaves the reaction source $\widetilde{c''\dot{\omega}_c^{*\prime\prime}}$ and the production due to mean progress variable gradients as the main source terms in the $\widetilde{c''^2}$-equation. Note that $\widetilde{c''\dot{\omega}_c^{*\prime\prime}}$ locally also takes the role of an important variance sink term as the reaction reaches completion. On the side of the sink terms Fig. 6.17 shows a comparison of the mean scalar dissipation rate $\widetilde{\varepsilon_c}$, as computed in the present work using the model by Kolla et al. [2009] (Eqn. 4.22), and an *a postiori* evaluation of the SDR model for a passive scalar applied to the reaction progress variable. The latter takes the largest values in the thinnest part of the reacting shear layer that forms between the main flow and the pilot stream, but takes much smaller values than $\tilde{\varepsilon}_c$ in the region where the flame closes. Indeed, in the present simulations it was not possible to stabilise a flame using $2(\tilde{\varepsilon}/\tilde{k})\widetilde{c''^2}$ to model the scalar dissipation rate, so that the model by Kolla et al. [2009] was employed.

## 6.5 Conclusions

In a first application, DCMC was used to simulate the behaviour of a piloted ethanol spray flame at two operating conditions. The velocity field and the droplet distributions showed good agreement with experimental data, and the trend of flame length with the overall equivalence ratio for the two flames was reproduced.

The doubly-conditional flame structure did not vary strongly along the burner axis. Furthermore, similarity of the flame structure in both flames suggests weak sensitivity to the overall equivalence ratio.

The term balance in the Reynolds-averaged mean and variance equations of the conditioning variables was investigated. The reaction source was dominant on $\widetilde{c''^2}$. The term could not be balanced by a linear relaxation model for SDR and instead a model that includes dilatation effects was used. The Reynolds-averaged spray terms in the mean and variance equations of the conditioning variables were modelled using the presumed shape for the conditional evaporation rate. The spray source term was dominant in the evolution of $\widetilde{\xi''^2}$. This is in line with the findings of previous studies. The SDR, given by the linear relaxation model, was of the same order of magnitude as the spray term, but did not balance the source term. This led to high levels of variance, which could be related to mismatches between experiment and simulation. Spray terms had only a very small effect on $\tilde{c}$ and $\widetilde{c''^2}$. Nevertheless, the spray source to $\tilde{c}$ is representative of the principle of conservation of mass, and simple modelling for this term was suggested.

# Chapter 7

# LES-DCMC of a Lifted Spray Flame

## 7.1 Introduction

This chapter presents an application of the LES-DCMC approach to simulate a heptane spray flame recently studied experimentally in Rouen [Shum-Kivan et al., 2017; Verdier et al., 2018, 2017]. The flame has the characteristics of a lifted jet flame, stabilised in the shear layer of a turbulent jet.

LES constitutes the state-of-the-art for the modelling of turbulent flows in practical applications of engineering interest. LES-CMC, where CMC acts as the sub-grid scale combustion model, has been very successful predicting complex combustion problems in both non-premixed and fully premixed applications (see review in Section 2.4.4). LES-CMC even performed well in some cases, where the overall correlation of the reactive scalars with the mixture fraction was weakened, e.g. Garmory & Mastorakos [2011]. However, this flame had a predominantly non-premixed character and the fluctuations were associated with transient effects in response to temporal fluctuations of the SDR, while the local instantaneous description of the flame remained well correlated with the mixture fraction. In order to simulate flames where non-premixed and premixed combustion modes co-exist, a doubly conditional approach is required. Co-existence of multiple combustion modes is the case in turbulent spray flames, as discussed in Section 2.3.4.

The objectives of this chapter is the validation of LES-DCMC for spray combustion. The present test flame has previously been simulated using various modelling approaches: LES with the Artificially Thickened Flame (ATF) model in the limit of a resolved flame [Shum-Kivan et al., 2017], LES with the Stochastic Fields (SF) method [Noh

et al., 2018], LES with Filtered Tabulated Chemistry [Chatelier et al., 2017] and RANS with Flamelet Generated Manifolds (FGM) [Both, 2017]. Hence, this flame constitutes a suitable benchmark case to validate the LES-DCMC approach.

The chapter is organised as follows. First, the numerical set-up of the simulation is described. Second, cold flow results are compared to experimental measurements to assess the accuracy of the LES without combustion model. Third, comparisons between simulation results and experimental data for the test flame under investigated are shown for validation of the present modelling approach and features of the flame are discussed. Fourth, the DCMC modelling approach is discussed. DCMC results are compared to results obtained using a space- and time-invariant flame structure. Moreover, the temporal evolution of the flame structure parametrised in doubly conditional space is analysed.

## 7.2 Experimental set-up

The test case studied in the present work is a lifted n-heptane spray jet flame open to the atmosphere. The burner is described by Shum-Kivan et al. [2017] and Verdier et al. [2018, 2017].

The burner consists of a plenum, a nozzle without swirl and a spray injector located in the centre of the nozzle. Figure 7.1 shows a drawing of the burner and Fig. 7.2 shows photos of the burner and the flame. Air is supplied to the burner through four inlets and two meshes installed at the bottom of the plenum ensure a uniform flow upstream of the nozzle. The nozzle has a conical shape with an annular cross-section. At the exit of the nozzle, the inner and outer diameter are 10 and 20 mm respectively. The burner is operated with an air mass flow rate of 6 g/s, which gives a bulk velocity of 21.58 m/s (at $p = 1$ atm and $T = 298$ K) and a jet Reynolds number (based on the hydraulic diameter of the annulus) of about 13,900. The atomiser (Danfoss 1.35 kg/h, 80° hollow cone) is a pressurised swirl injector with an injector orifice with diameter 200 $\mu$m and 8 bar pressure, injecting the spray in a hollow-cone with a half-angle of 40°. The fuel mass flow rate is 0.28 g/s. At a distance of 10 mm from the injector, the spray has a Sauter mean diameter of 32 $\mu$m.

This flame is a test case of the *Workshop on Turbulent Combustion of Sprays* (TCS, www.tcs-workshop.org). The experimental database contains Phase Doppler Anemomentry (PDA) measurements of the mean and the root mean square (RMS) of the droplet velocity and the diameter, OH Planar Laser Induced Fluorescence (OH-PLIF) imaging [Shum-Kivan et al., 2017], measurements of the droplet temperature with

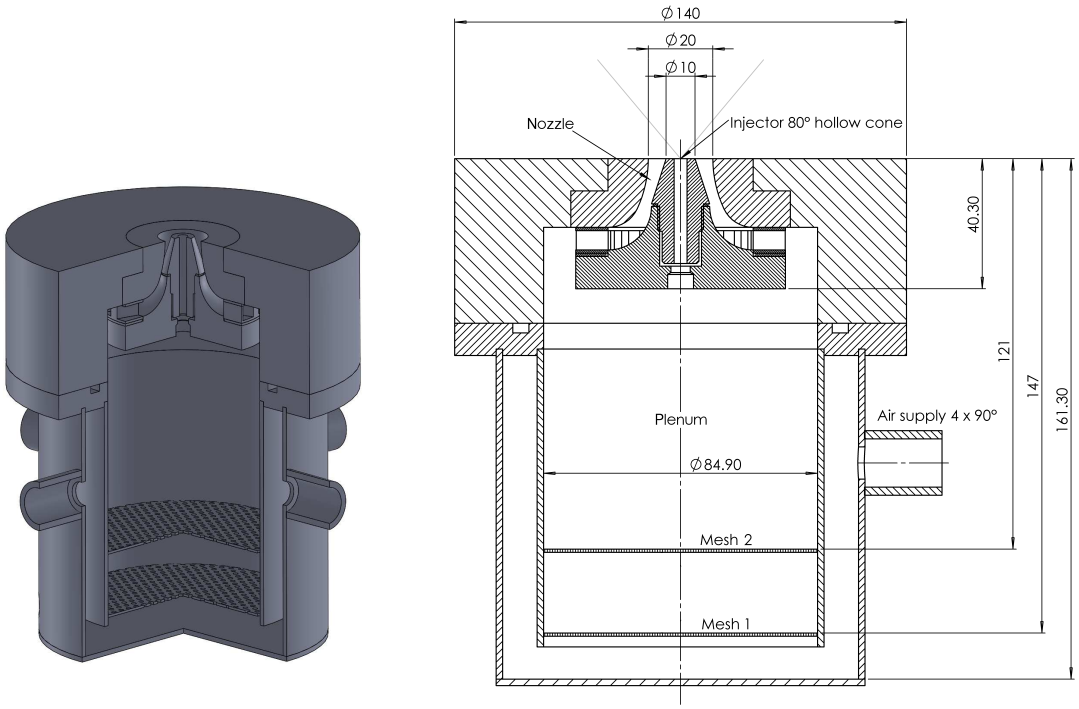


Fig. 7.1 Isometric view and technical drawing of the of the burner. The technical drawing is simplified; not shown are the injector, the fuel pipe to the injector and closed-off pipe inlets. The 3D-geometry was provided by Dr B. Renou.

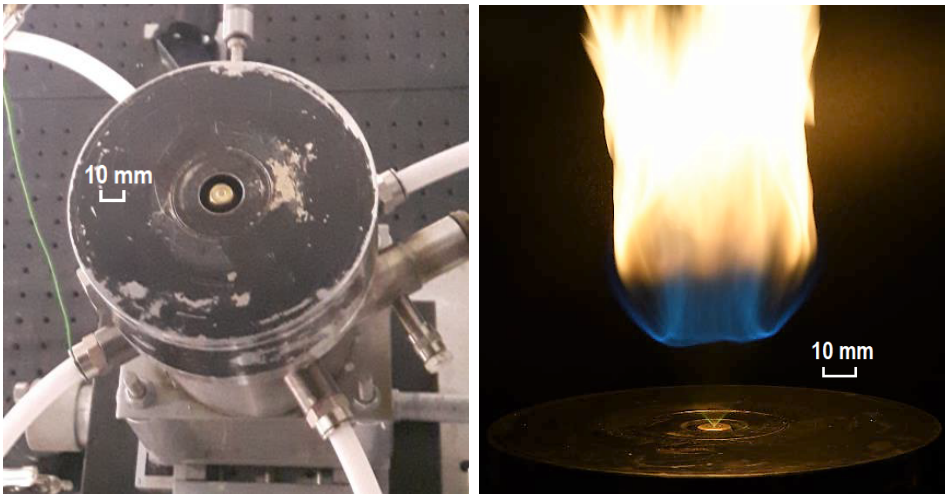


Fig. 7.2 Photos of the burner and the flame. Photos provided by Dr B. Renou.

Global Rainbow Refractometry Technique (GRT) [Verdier et al., 2017] and simultaneous high-speed OH-PLIF and high-speed Particle Image Velocimetry (PIV) [Verdier et al., 2018]. PDA data is available for a reacting and a non-reacting case. Assuming that small droplets closely follow the gas flow, PDA measurements are used to provide measurements of the gas phase velocity.

## 7.3 Simulation set-up

### 7.3.1 Model equations

The DCMC equation used in the present chapter was

$$\begin{aligned}\frac{\partial Q_\alpha}{\partial t} + \nabla\cdot(\langle\mathbf{u}|\eta,\zeta\rangle Q_\alpha) &= Q_\alpha\nabla\cdot\langle\mathbf{u}|\eta,\zeta\rangle + \frac{1}{\bar\rho\tilde p}\nabla\cdot\left(\bar\rho\tilde p(D_T+\bar D)\nabla Q_\alpha\right)\\ &+ \langle N_\xi|\eta,\zeta\rangle\frac{\partial^2 Q_\alpha}{\partial\eta^2} + 2\langle N_{\xi c}|\eta,\zeta\rangle\frac{\partial^2 Q_\alpha}{\partial\eta\partial\zeta} + \langle N_c|\eta,\zeta\rangle\frac{\partial^2 Q_\alpha}{\partial\zeta^2}\\ &+ \langle\dot\omega_\alpha|\eta,\zeta\rangle - \langle\dot\omega_c^*|\eta,\zeta\rangle\frac{\partial Q_\alpha}{\partial\zeta}\\ &+ (\delta_{\alpha\mathrm{F}}-Q_\alpha)\langle\Pi|\eta,\zeta\rangle - \langle S_\xi^-|\eta,\zeta\rangle\frac{\partial Q_\alpha}{\partial\eta} - \langle S_c^-|\eta,\zeta\rangle\frac{\partial Q_\alpha}{\partial\zeta}\end{aligned} \tag{7.1}$$

Details can be found in Section 3.7. For $\langle N_c|\eta,\zeta\rangle$ the SDR from freely propagating premixed laminar flames $N_c^0(\eta,\zeta)$ was used. Figure 7.3 shows the shape of $N_c^0$ and the laminar flame thickness $\delta_L^0$ and laminar flame speed $S_L^0$ used in the model for the SGS scalar dissipation rate $\widetilde{N}_{c,\mathrm{sgs}}$ (Eqn. 4.22). These quantities were computed for freely propagating laminar premixed flames using the commercial software Cosilab [Rotexo GmbH und Co. KG, 2012]. The mixture fraction is defined to be 0 for air and 1 for for pure fuel vapour. For the combustion of heptane and air, the stoichiometric mixture fraction is $\xi_{\mathrm{st}} \approx 0.0622$, and the lean and rich flammability limits are $\xi_{\mathrm{lean}} \approx 0.0339$ and $\xi_{\mathrm{rich}} \approx 0.1996$ respectively [Coward & Jones, 1952]. The air temperature is 298 K and the temperature of pure fuel vapour is set at 371.58 $K$, corresponding to the boiling point of n-heptane [Green & Perry, 2008].

The LES-filtered transport equations are as shown in Section 4.3.4. Spray source terms were not included in the $\widetilde{\xi''^2}$-equation. In the $\tilde c$-equation the spray source term was modelled as $\widetilde{S_c^-} + \widetilde{c\Pi} \approx \tilde c\widetilde{\Pi}$, and the spray source term to the $\widetilde{c''^2}$-equation was neglected, as discussed in Chapter 6.

The spray source term in the $\widetilde{\xi''^2}$-equation was not included, since currently available models for $\widetilde{N}_{\xi,\mathrm{sgs}}$ (Eqn. 4.61) seem unsuitable to balance the production of variance in

regions with low turbulence level. The evaporation in regions with lower turbulence intensity constitutes a main difference between the present case and the flame studied by Giusti & Mastorakos [2017] who successfully included this source term. The effect of this source term on the results is investigated in Appendix D.

### 7.3.2 Numerical set-up

The numerical domain is shown in Fig. 7.4 (left). It includes the nozzle and plenum of the burner (see Fig. 7.1). Downstream of the nozzle, the domain was of cylindrical shape with a diameter of 800 mm and a length of 500 mm. The plenum was included up to the plate with holes 121 mm upstream of the nozzle exit (Mesh 2 in Fig. 7.1). A constant air mass flow rate was set as inlet boundary condition to the plenum. A slip wall boundary condition was applied at the sides of the cylindrical domain and a small co-flow of 0.1 m/s was set around the outer dimensions of the burner, only for $r > 70$ mm, which reflects the dimensions of the burner.

An unstructured tetrahedral LES mesh with 18M cells was used. It was refined in the nozzle and the region of the flame to a minimum size of 0.35 mm in the nozzle and 0.4 mm around the stabilisation point of the flame. Four prism layers were applied to the walls in the nozzle with a thickness of the first layer of 0.045 mm, which increasing by a factor of 1.25 in each layer. The resolution of the LES mesh is shown in Fig. 7.5.

Besides the LES mesh, a coarser DCMC mesh with 644 cells, arranged in an O-grid was used. In the region of interest the DCMC cells were spaced with an increment of 2.5 mm in axial direction; 3 layers of cells were used in radial direction, assuring that the outer and the inner flame were resolved by different DCMC cells, and 7 cells were used in each circumference of the O-grid. At the inlets a set of conditional moments obtained from DCMC-0D (see Chapter 5) corresponding to a weakly strained flame, similar to the tabulation of freely propagating premixed laminar flames, were set as the boundary condition. The same set of conditional moments was also used as the initial condition. Zero-gradient boundary conditions, $\nabla Q_\alpha = 0$, were set at the outlet and the walls.

The doubly-conditional space $\mathbb{D} = \{(\eta, \zeta) \in \mathbb{R}^2 : 0 \leq \eta \leq 1, 0 \leq \zeta \leq 1\}$ was discretised with $71 \times 41$ nodes. The $\eta$-nodes were clustered in the flammable mixture fraction region and the $\zeta$-nodes were spaced progressively more closely for $\zeta$ approaching 1. The discretisation of the doubly-conditional space and the shape of $Q_{\mathrm{CO2}}$ are shown in Fig. 7.6.

The time step was $10^{-6}$ s. Numerical schemes for LES were of second order in space and first order in time. Numerical schemes for DCMC were as detailed in Section 4.5.

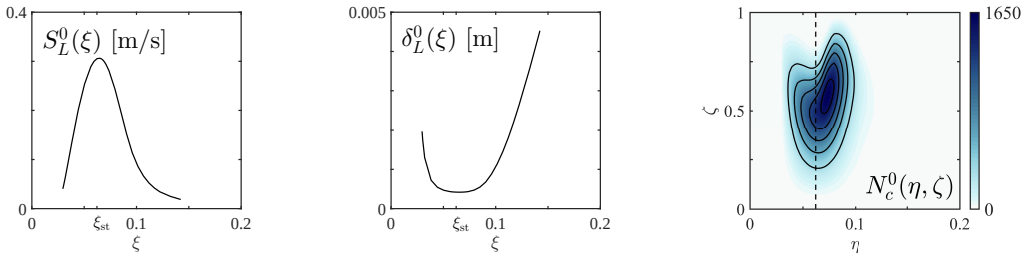


Fig. 7.3 Laminar flame speed, laminar flame thickness and conditional SDR from freely propagating premixed laminar flames $N_c^0(\eta, \zeta)$.

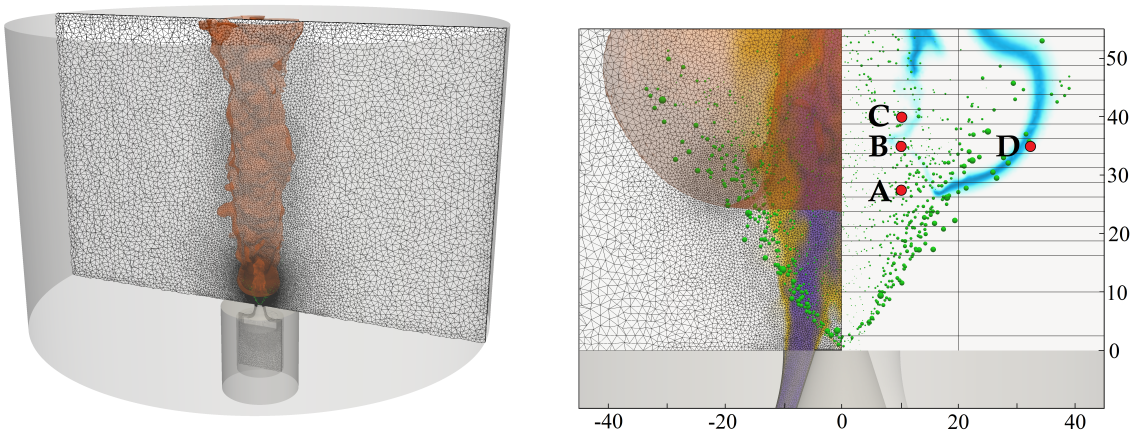


Fig. 7.4 Numerical domain (left) and detail view of the region of interest (right). The position of the flame is indicated by the red iso-contour for $\tilde{c} = 0.1$. The detail view shows the LES mesh (left half) and outlines of DCMC cells (right half). Additionally, droplets and contours of axial velocity and OH mass fraction are shown. The locations A at $(r, z) = (10\ \text{mm}, 27.5\ \text{mm})$, B at $(10\ \text{mm}, 35\ \text{mm})$, C at $(10\ \text{mm}, 40\ \text{mm})$ and D at $(30\ \text{mm}, 35\ \text{mm})$ are selected for detailed analysis.

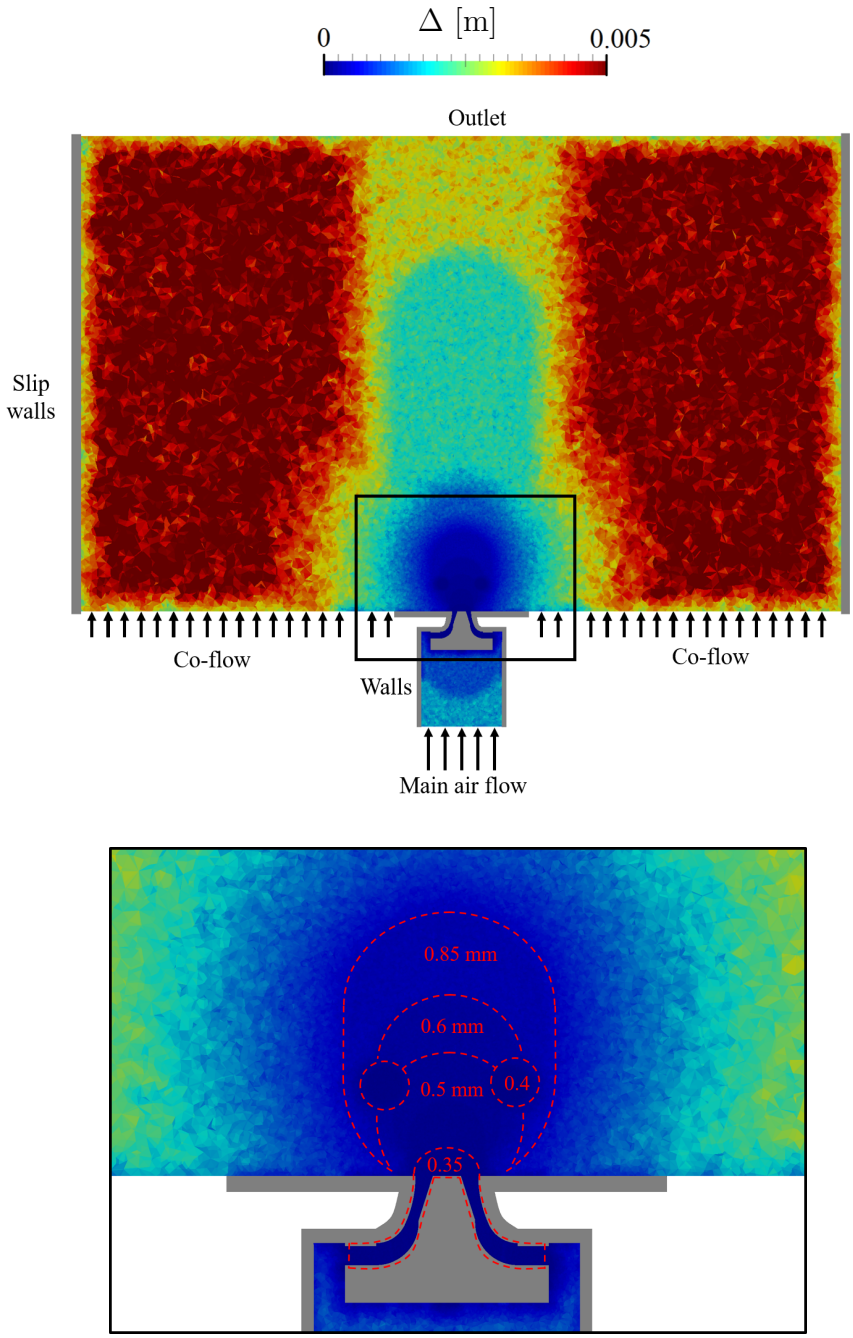


Fig. 7.5 Resolution of the LES mesh and boundary conditions. Entire domain (top) and detail view (bottom). $\Delta$ is the LES filter size calculated as the cubic-root of the cell volume.

Operators splitting was used. The simulation ran on a Cray XC30 system using 432 2.7 GHz processors; 1 ms of physical time took about 12,000 CPU hours on wall-clock time. Time-averages were collected over 10 ms, corresponding to three flow-through times.

### 7.3.3 Spray injector modelling

The spray injector was modelled as a hollow cone injection. A general volume distribution was used to sample the size of the injected droplets in the range $1 < d_d < 80$ $\mu$m. The volume distribution of the injected droplets was computed from raw PDA measurements at $z = 10$ mm, averaging the results from various measurement locations in the range $0 \leq r \leq 13$ mm. Comparing the volume distributions at axial locations $z = 7$, 10 and 13 mm showed little differences for $z \geq 10$ mm, suggesting that the spray distribution was fully developed at this location. Figure 7.7 shows the injected volume distribution and the corresponding number distribution. The mean diameter is $d_{10} \approx 21$ $\mu$m and the Sauter mean diameter is $d_{32} \approx 32$ $\mu$m. The droplets were injected with a random half angle between 35° and 50° and an initial velocity in the range $25 < U_d < 33$ m/s depending on the initial diameter: $U_d = 33$ m/s for small droplets ($d_d \leq 10$ $\mu$m) decreasing linearly with diameter to $U_d = 25$ m/s for large droplets ($d_d > 55$ $\mu$m). These choices were made so that the simulation matched the spray measurements at the first available location.

### 7.3.4 Chemical mechanism

The simulation used a complex chemical mechanism for the combustion of n-heptane and air with 67 species and 315 elementary reactions [Smallbone et al., 2009]. The mechanism reproduces flame speed and ignition temperatures well at ambient conditions. The mechanism does not include $NO_x$-chemistry and $N_2$ acts as an inert species. The same mechanism was used in the simulation of the present test flame by Shum-Kivan et al. [2017].

## 7.4 Results and discussion

### 7.4.1 Cold flow results

First, the non-reacting case is discussed. A cold flow solution is used to assess the resolution of the LES mesh. Figure 7.8 shows the instantaneous field of the filtered

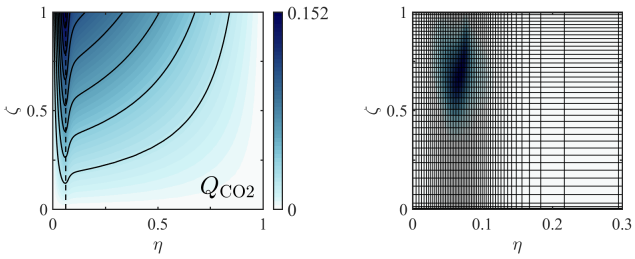


Fig. 7.6 Conditional moment $Q_{CO2}$ and discretisation of the doubly-conditional space. The reaction rate $\dot{\omega}_c$ is indicated on top of the grid. For $\eta > 0.3$ the $\eta$-grid is uniform.

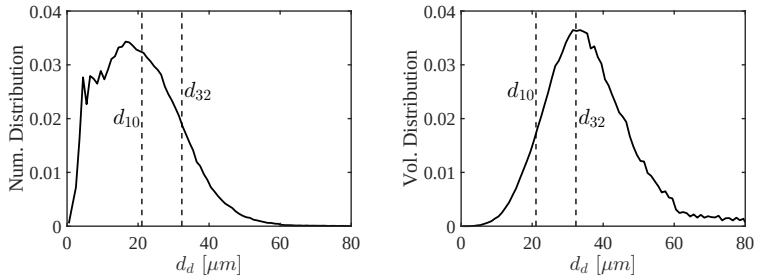


Fig. 7.7 Number distribution (left) and volume distribution (right) of the injected droplets. Dashed lines indicate the mean diameter $d_{10} \approx 21$ $\mu$m and the Sauter mean diameter $d_{32} \approx 32$ $\mu$m of the distribution.

axial velocity $\tilde{u}_z$, its time average $\langle \tilde{u}_z \rangle$ and the RMS value, computed as

$$\mathrm{RMS}(\tilde{u}_z) = \Big( \Big\langle (\tilde{u}_z - \langle \tilde{u}_z \rangle)^2 \Big\rangle \Big)^{1/2} \tag{7.2}$$

and the SGS velocity fluctuation, computed as $u'_{\mathrm{sgs}} = (2k_{\mathrm{sgs}}/3)^{1/2}$, where $k_{\mathrm{sgs}}$ is the kinetic energy of sub-grid scale turbulent motion, computed by the SGS turbulence model (Eqn. 4.47).

The spatial resolution of the LES is assessed following the suggestion made by Pope [2000]. For this purpose the residual $M$ is calculated:

$$M \equiv \frac{k_{\mathrm{sgs}}}{K + k_{\mathrm{sgs}}} \tag{7.3}$$

where $K$ is the kinetic energy of the resolved eddies, calculated as

$$K = \frac{1}{2} \Big\langle (\tilde{\mathbf{u}} - \langle \tilde{\mathbf{u}} \rangle) \cdot (\tilde{\mathbf{u}} - \langle \tilde{\mathbf{u}} \rangle) \Big\rangle \tag{7.4}$$

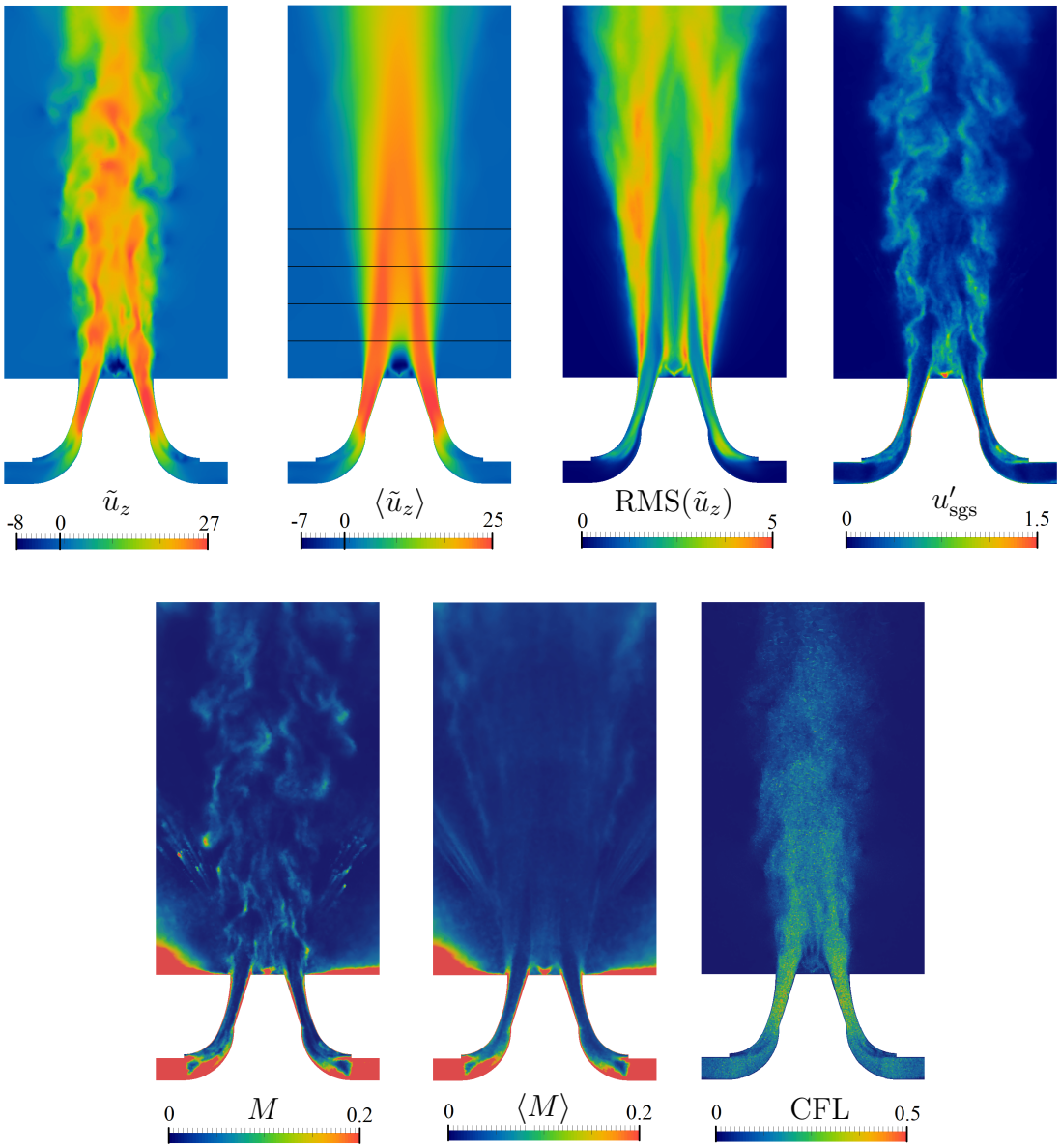


Fig. 7.8 Surface plots of cold flow fields: instantaneous filtered axial velocity $\tilde{u}_z$, time-averaged axial velocity $\langle\tilde{u}_z\rangle$ and RMS($\tilde{u}_z$), instantaneous SGS velocity fluctuation $u'_{\mathrm{sgs}}$, instantaneous residual $M$ (Eqn. 7.3) and its time-average $\langle M\rangle$ and instantaneous CFL number (Eqn. 7.3). Black lines indicate the axial locations of the profiles shown in Fig. 7.9.

The residual $M$ measures the fraction of the total turbulent kinetic energy that is unresolved by the LES. According to Pope [2000], an LES should resolve at least 80 % of the turbulent kinetic energy. Figure 7.8 shows the instantaneous and time-averaged value of $M$. The present simulation fulfils this criterion in the whole region of interest, resolving at least 95 % of turbulent kinetic energy in the region of interest; only the upstream part of the nozzle and the region of the injection could not be resolved at this level. Anyhow, close to the injection the spray is dense and the present modelling framework is not expected to resolve this region accurately. Furthermore, the cold flow simulation was used to assess the wall mesh in the nozzle. The thickness of the first prism layer in the nozzle corresponds to $y^+ = yu_\tau/\nu \approx 1.4$. The laminar sub-layer was resolved by three cells. Figure 7.8 also shows the Courant-Fiedrichs-Lewy (CFL) number at one time instant. In OpenFOAM [2014] the CFL number for each cell is computed as

$$\mathrm{CFL} = \frac{1}{2}\frac{\Delta t \ \sum_i (\bar{\rho}\tilde{\mathbf{u}})_i \cdot \mathbf{n}_i \Delta S_i}{\bar{\rho} V_{\mathrm{les}}} \tag{7.5}$$

where the mass flow is summed over all faces $\Delta S_i$ of an LES cell of volume $V_{\mathrm{les}}$. The stability of explicit time integration schemes requires the CFL number to be below unity. For the time step $\Delta t = 10^{-6}$ s, the CFL number is below 0.3 in most of the region of interest.

For validation the LES results for the non-reacting case are compared with velocity measurements from PDA. Figure 7.9 shows a good agreement between the predictions of the simulation and the experimental data. This suggests that the mesh resolution, numerical schemes and boundary conditions are suitable.

The modelling of the spray injection is validated next. Figure 7.10 compares LES results and experimental data for droplet diameter, temperature and velocity in the non-reacting case. Error-bars represent the RMS values around the mean for simulation and experiment (temperature measurements for $z = 10$ mm and RMS values for temperature were not available). The good agreement between LES and the experimental data for the droplet velocity and diameter at the location $z = 10$ mm suggests that the modelling of the injector was suitable.

Discrepancies exist for the droplet temperature. The experiment predicts a local maximum of droplet temperature at the burner axis, which is not reproduced by the simulation. Considering that the droplet diameter and velocity is well predicted and that the present case is non-reacting, leaves the evaporation model as the driving factor behind the temperature prediction. The Abramzon & Sirignano [1989] model is an equilibrium evaporation model and potentially non-equilibrium effects could play a

role. However, Noh et al. [2018] recently tested three evaporation models, including a non-equilibrium evaporation model, but did not find this local maximum with either one of them. A detailed study of the evaporation model is not intended in the present work and the overall results for sprays are considered satisfactory.

### 7.4.2 Flow field and spray statistics in the flame

Figure 7.11 shows profiles of the mean velocity and its RMS from LES and from PDA measurements in the flame. The dilatation due to the flame increases the width of the jet for $z \geq 30$ mm compared to the cold flow results (Fig. 7.9). The good agreement shows that the LES also predicts the velocity field in the reacting case well.

In Fig. 7.12 droplet diameter, temperature and velocity in the flame are shown. Large droplets behave in a ballistic sense and significant slip velocities persist beyond $z = 20$ for $r > 15$ mm and, in particular, at the flame anchoring point. Consequently, the flame benefits from enhanced evaporation to provide gaseous fuel (e.g. for a droplet of diameter 30 $\mu$m with a slip velocity of 5 m/s the evaporation rate increases by almost a factor of two). In general, LES results for velocity and diameter agree well with the experiment, with minor differences at $z = 40$ mm; the overall agreement is comparable to the results by Noh et al. [2018]. Some differences between LES and experiment are found for the mean droplet temperature. Along the burner axis the simulation finds nearly constant mean droplet temperature, increasing from 281 to 282 K between $z = 10$ and 40 mm, in contrast to a local maximum observed in the experiments. This was already discussed for the non-reacting case. These droplets are not in contact with the flame and the reasoning remains the same. Moreover, the simulation predicts a faster and eventually greater heat-up at contact with the hot gases. At $z = 30$ mm the simulation finds a maximum mean temperature of 345 K compared to 320 K in the experiment, but at $z = 40$ mm the difference is smaller. The reason is not clear. Similar discrepancies with the experiment were observed in other modelling attempts of this flame with various combustion models [Both, 2017; Chatelier et al., 2017; Noh et al., 2018]. This suggests that the effect is not related to the combustion model. It is notable that modelling of the SGS effect of evaporation by including the evaporation terms in the $\widetilde{\xi''^2}$-equations would lead to lower gas temperature around, which could decrease the droplet temperature. In general, the agreement for the reacting case is also considered satisfactory.

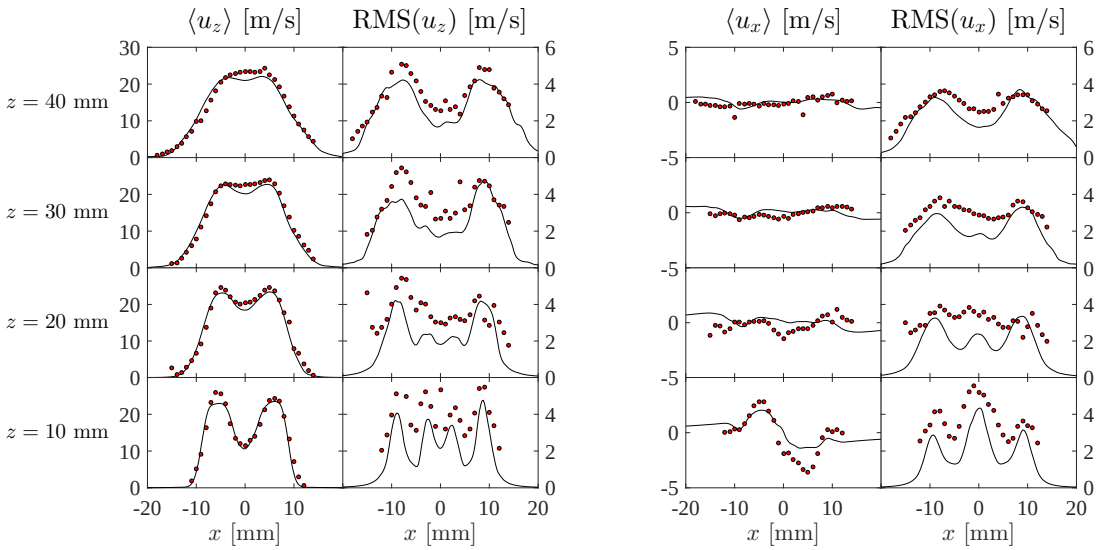


Fig. 7.9 Profiles of the gas velocity in the non-reacting case. Mean and RMS from LES (line) are compared to PDA measurements [Shum-Kivan et al., 2017] (symbols).

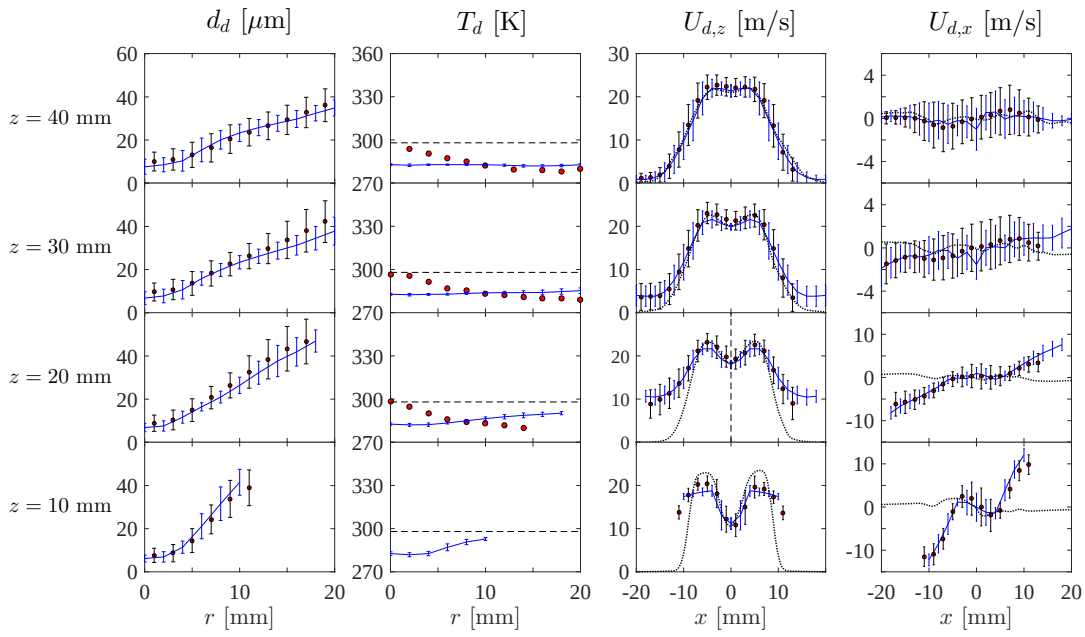


Fig. 7.10 Profiles of mean droplet diameter, temperature and velocity in the non-reacting case. Results from LES (blue line) are compared to PDA [Shum-Kivan et al., 2017] and GRT [Verdier et al., 2017] measurements (symbols). Error bars represent the RMS value from LES and experiment at a given location (no RMS was available for GRT measurements). Black dotted lines indicate the mean gas velocity and mean gas temperature in the respective graphs. Black dashed lines mark the initial droplet temperature 298 K.

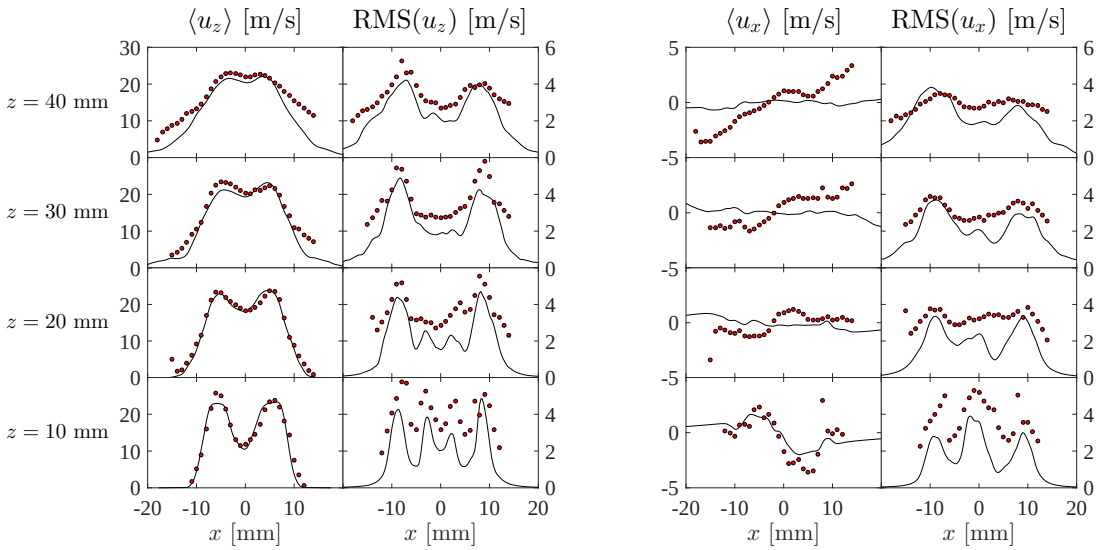


Fig. 7.11 Profiles of the gas velocity in the flame from LES and experiment. Mean and RMS from LES (line) are compared to PDA measurements [Shum-Kivan et al., 2017] (symbols).

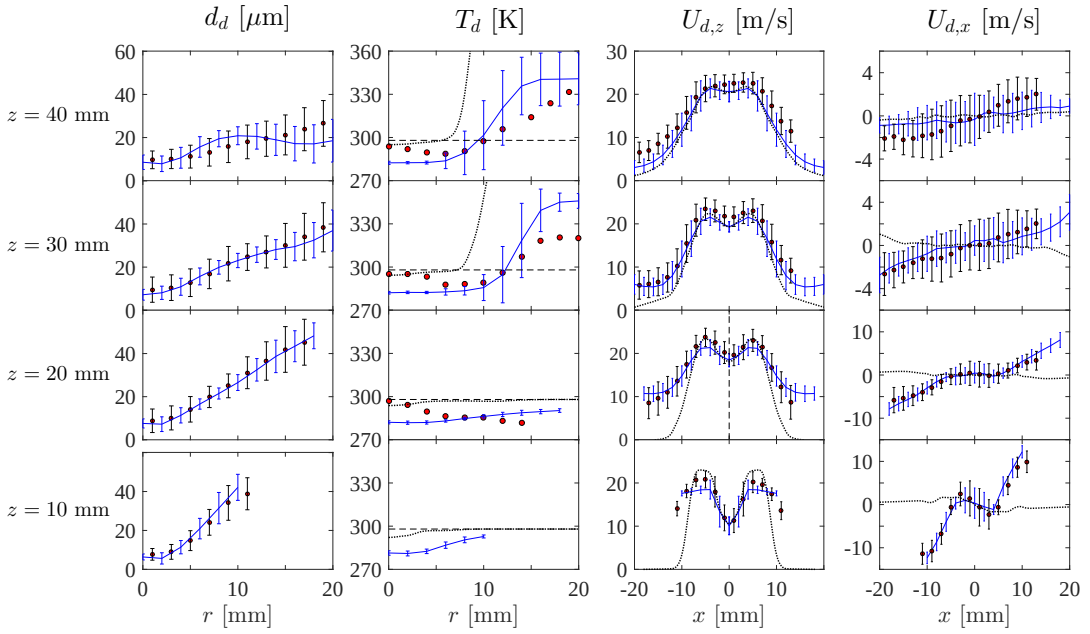


Fig. 7.12 Profiles of droplet diameter, temperature and velocity in the flame. Results from LES (blue line) are compared to PDA [Shum-Kivan et al., 2017] and GRT [Verdier et al., 2017] measurements (symbols). Error bars represent the RMS value from LES and experiment at a given location (no RMS was available for GRT measurements). Black dotted lines indicate the mean gas velocity and mean gas temperature in the respective graphs. Black dashed lines mark the initial droplet temperature 298 K.

### 7.4.3 Flame shape and anchoring point

The shape of the flame is discussed next. First, LES results for OH mass fraction are compared to OH-PLIF images. Figure 7.13 compares the instantaneous fields. Note that the OH-PLIF signal is not directly related to the filtered OH mass fraction [Eckbreth, 1996]. Therefore, the comparison is only qualitative. The flame consists of a smooth quasi-laminar outer reaction zone, where OH is present in a thick layer, and a thin inner reaction zone that is heavily wrinkled by the turbulent jet with some parts of the flame detached from its main body. The two branches are connected at the upstream tip of the flame, located in the dominant trajectory of the droplets, as will be discussed later. In Fig. 7.14 time-averages and time-based RMS of OH mass fraction and OH-PLIF signal intensity are shown. The simulation predicts a lift-off height of approximately 26 mm, which is in good agreement with the experiment, where values in the range from 24 to 26 mm were observed. The present results can be compared to the lift-off height predictions of 25 mm obtained with the SF model and the Abramzon-Sirignano model [Noh et al., 2018] and ≈ 19 mm by Shum-Kivan et al. [2017] as presented at the TCS workshop. The flame is anchored in the shear layer of the turbulent jet at the radial position $r \approx 17$ mm. The time-based RMS values of the OH field appear to be of the same order of magnitude as local mean values, which suggests that the flame is thin compared to the width of flame brush. While the RMS of OH mass fraction from LES is qualitatively similar to the RMS of OH-PLIF signal for the inner flame brush, the simulation does not detect strong fluctuations for the outer flame branch. This can be attributed to low mean velocities in this region where the flame is laminar. Consequently, characteristic time scales for the outer flame are very long, $\sim 0.1$ s, as evidenced by 10 Hz OH-PLIF recordings from the experimental database, which is challenging to explore with high-fidelity LES.

More details about the flame structure can be inferred from the instantaneous fields of relevant quantities shown in Fig. 7.15. For better orientation relative to the position of the flame, the images are overlaid with iso-contours of $\tilde{c}$. In the present spray flame at atmospheric condition significant evaporation rates are only achieved where droplets are submerged in hot gases. Hence, $\tilde{\xi}$ reaches its peak value downstream of the flame's tip. In this region surrounded by the flame the overall mixture is rich. The SGS variance of the mixture fraction is small, since the effect of spray evaporation was not included in its transport equation. Consequently, $\widetilde{N_\xi}$ is dominated by its resolved contribution. The reaction progress variable reaches its highest values in the quasi-laminar outer flame, where its SGS variance is negligible. In contrast, the turbulent inner flame branch sees high variance, $\widetilde{N_c}$ and $\widetilde{\dot{\omega}_c^*}$. The chemical contribution

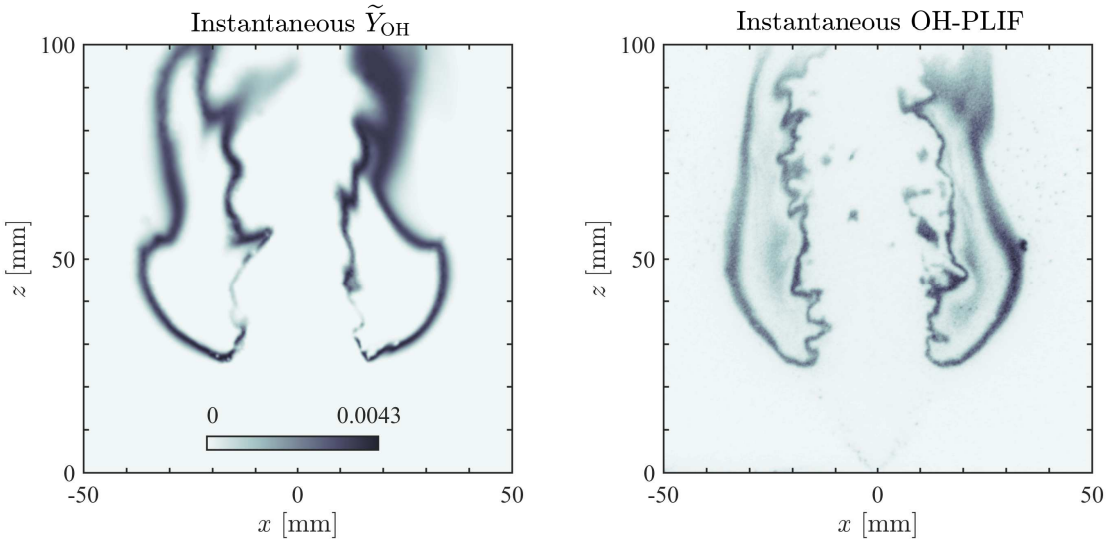


Fig. 7.13 Instantaneous field of $\widetilde{Y}_{OH}$ from LES (left) compared to instantaneous OH-PLIF intensity from the experiment (right). Note that the OH-PLIF signal is not directly related to $\widetilde{Y}_{OH}$; comparisons of instantaneous fields are only qualitative.

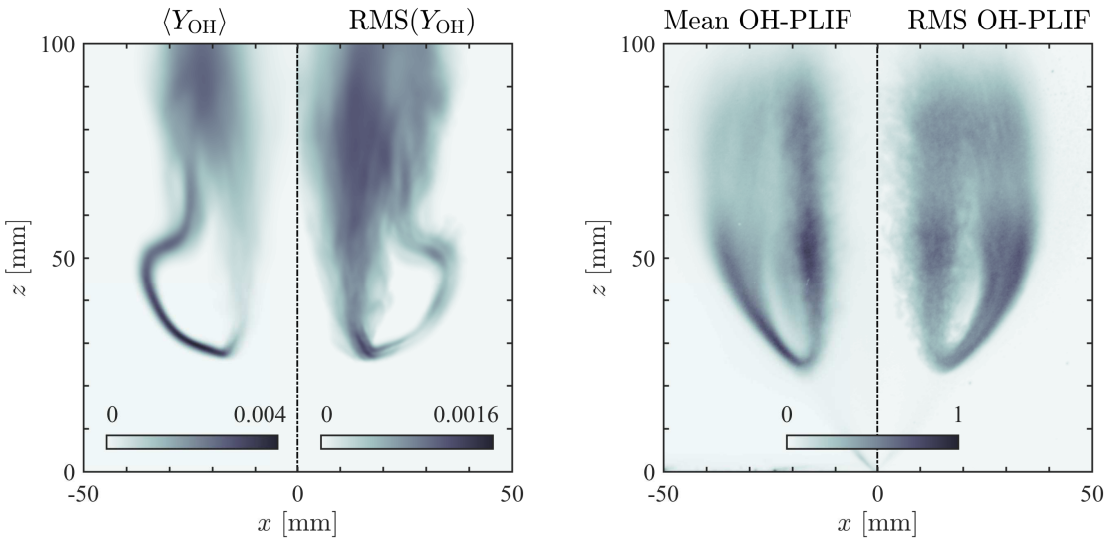


Fig. 7.14 Time-averaged OH mass fraction $\langle Y_{OH} \rangle$ and corresponding RMS from LES (left) compared to time-averaged OH-PLIF intensity and its RMS from the experiment (right). For mean OH-PLIF and its RMS the same colour map is used.

to the apparent reaction rate $\widetilde{\dot{\omega}_c}$ is up to an order of magnitude higher in the inner flame branch. The contribution of passive mixing $\widetilde{\dot{\omega}_p}$ is predominantly negative. As droplets cross the flame front an increase in reaction progress is naturally associated with enhanced evaporation and higher $N_\xi$, leading to even lower $\widetilde{\dot{\omega}_p}$. Negative $\widetilde{\dot{\omega}_p}$ delays the completion of the reaction and thickens the flame.

The region between the outer and inner flame branch is fuel-rich and the temperature is also high. Thus, intermediate species like $C_2H_2$ are produced through pyrolysis and the heat release rate (HRR) is negative. Significant amounts of fuel mass fraction are only found for very rich mixture in the centre between the outer and inner flame branch and also around the upstream tip of the flame when the evaporation rate of a droplet is high enough to create fuel blobs that are – to a certain extent – resolved by the LES. Furthermore, high levels of $CH_2O$ and CO are found in the rich region. Substantial differences between the outer and inner flame are visible. In the outer branch levels of $C_2H_2$ and OH are relatively higher, whereas the inner branch contains more $CH_2O$. In particular, the interaction of turbulence with the flame leads to regions of low $\widetilde{Y}_{\mathrm{OH}}$ in the inner flame brush, which was also observed in the experiment using high-speed OH-PLIF [Verdier et al., 2018].

Furthermore, the results shown in Fig. 7.15 allow to comment on modelling choices. Only low $\tilde{Y}_{\mathrm{F}} = \tilde{Y}_{\mathrm{C7H16}}$ is found in the flame brush apart from the fuel pockets around droplets with strong evaporation rates. Conversely, the presence of pure fuel is expected near the surface of every droplet, even if this is not resolved by the LES. This is a sub-grid scale effect that requires special treatment of the spray terms in the $\widetilde{\xi''^2}$-equation discussed by Giusti & Mastorakos [2017], which were not included in the present work. Future work on the sub-grid scale modelling of spray effects will be necessary.

In order to better understand the stabilisation of the flame, we consider the time-averaged fields shown in Fig. 7.16. The time-averaged mixture fraction $\langle\xi\rangle$ is very similar to the instantaneous one, with significant variance only occurring in the turbulent inner flame branch. In the outer flame branch the turbulent velocity fluctuation, $u' = [(2/3)\ (K + \langle k_{\mathrm{sgs}}\rangle)]^{1/2}$, is very low, which shows that the flow is laminar in this region. The time-averaged fields indicate the presence of the dispersed phase, hence of liquid fuel and evaporation. Dashed black lines mark representative droplet trajectories and the region of the highest liquid volume fraction $\langle\theta_L\rangle$ shows the dominant pathway of the droplets, crossing through the tip of the flame. Since the droplets behave in a ballistic way, moving relative to the gas phase (Fig. 7.12), they penetrate through the flame and the highest mean evaporation rate $\langle\rho\Pi\rangle$ occurs in the region of hot gases downstream of the tip of the flame. In contrast, the mean mixture fraction is very

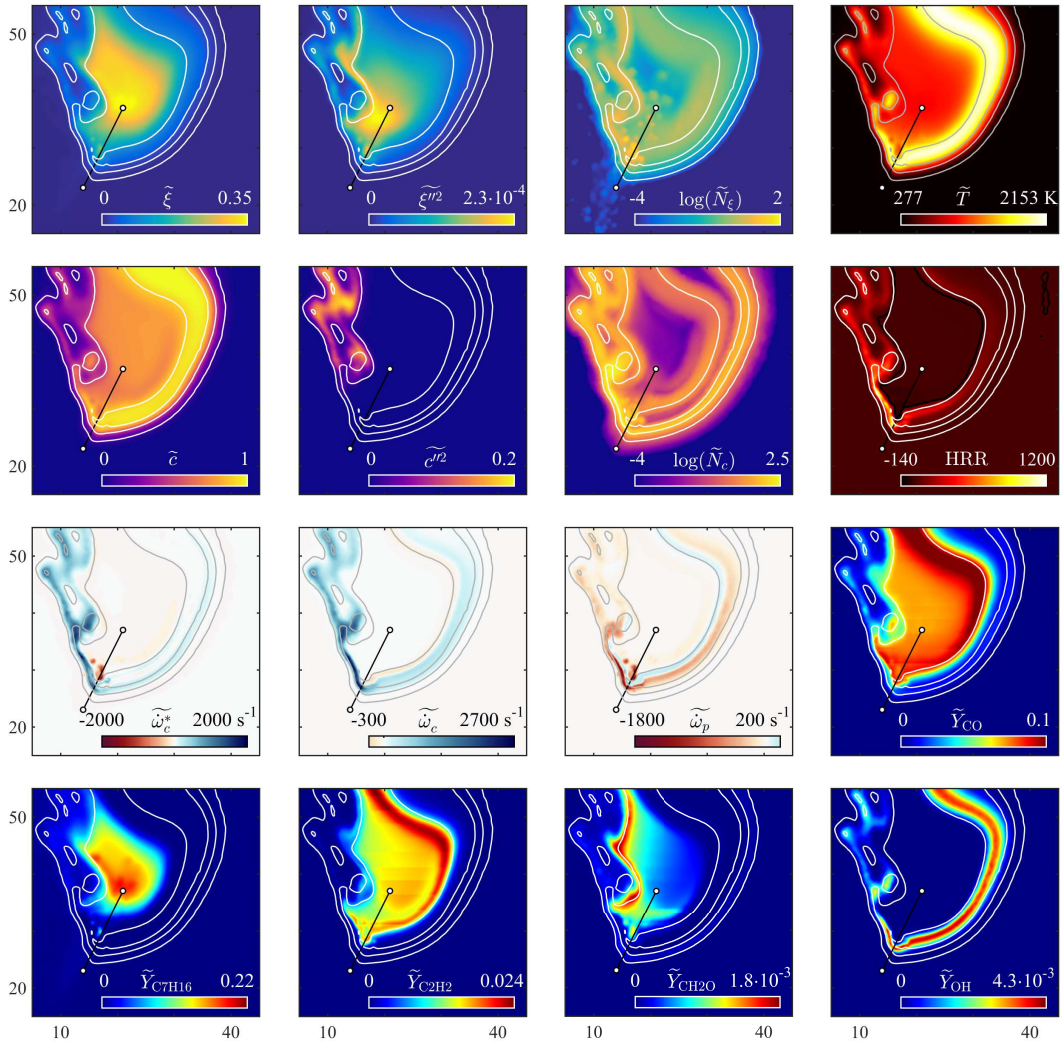


Fig. 7.15 Instantaneous fields for various LES-filtered quantities. White (grey in the case of a light background) contour lines are iso-lines of $\tilde{c} = 0.1$, 0.5, 0.9. The HRR is given in MW/m$^3$; SDRs are given in s$^{-1}$, logarithmic scales are clipped at -4. Thick, black lines mark the areas of negative HRR in the respective image. A black line between white circles marks the orientation of the cut used in Fig. 7.17.

low in the cold gases upstream of the flame, as indicated by iso-contours. This shows that in the present case the flame itself "creates" the gaseous fuel required. Finally, Fig. 7.16 also reveals that the spray is indeed very dilute in the region occupied by the flame and that the highest average evaporation rate $\langle \rho \Pi \rangle$ is observed near the tip of the flame.

A detailed view of the flame's profile at its anchoring point can be obtained from Fig. 7.17. The profiles are drawn over the line indicated in Figs 7.15 and 7.16, perpendicular to the mean position of the flame. Primarily, these profiles highlight the low level of gaseous fuel available in the cold gases upstream of the flame, and the ongoing evaporation in the post flame region. An intermediate peak of $\tilde{\xi}$ and fuel in the instantaneous profiles indicates the location of a parcel of droplets that crosses the tip of the flame, creating a pocket of rich mixture. Besides these pockets, the time-averaged profile shows that the fuel mass fraction is low in the vicinity of the reaction zone indicated by the peak of OH. Instead $C_2H_2$ and $C_2H_4$ are present in the hot post-flame region where negative HRR is observed. In this region, the existence of $O_2$ suggests incomplete combustion.

Figure 7.18 (A) shows a cut through an instantaneous iso-surface of the stoichiometric mixture fraction. This reveals again large differences between the inner and outer branch of the flame. In general, temperature and $\tilde{Y}_{\mathrm{OH}}$ are lower at the inner flame brush but higher HRR indicates chemical reaction. Furthermore, the iso-contour is strongly wrinkled around the base of the flame due to the evaporation of droplets penetrating the flame. Typically, these are spots of lower temperature but are also surrounded by regions of high HRR.

It is notable that a wide range of temperatures and species mass fractions is observed on the stoichiometric mixture fraction contour. Since $\widetilde{\xi''^2}$ is small in the present simulation (Fig. 7.15), these variations can be directly associated with variations of progress variable. In a singly-conditional framework based on mixture fraction, these variations would be fluctuations around the conditional mean. Therefore, conventional CMC would not be able to resolve these small-scale variations to the same level as the present DCMC approach. LES-CMC could potentially reproduce certain aspects of these variations by the transient response of the flame structure to strong variations of the SDR when droplets penetrate the flame. Effectively, these variations are equivalent to the holes in the flame caused by droplets, in the simulation by Giusti & Mastorakos [2017]. Reproducing these effects with LES-CMC requires a very fine discretisation in physical space and a large number of CMC cells. In contrast, in the present DCMC approach the progress variable provides an additional degree of freedom in the

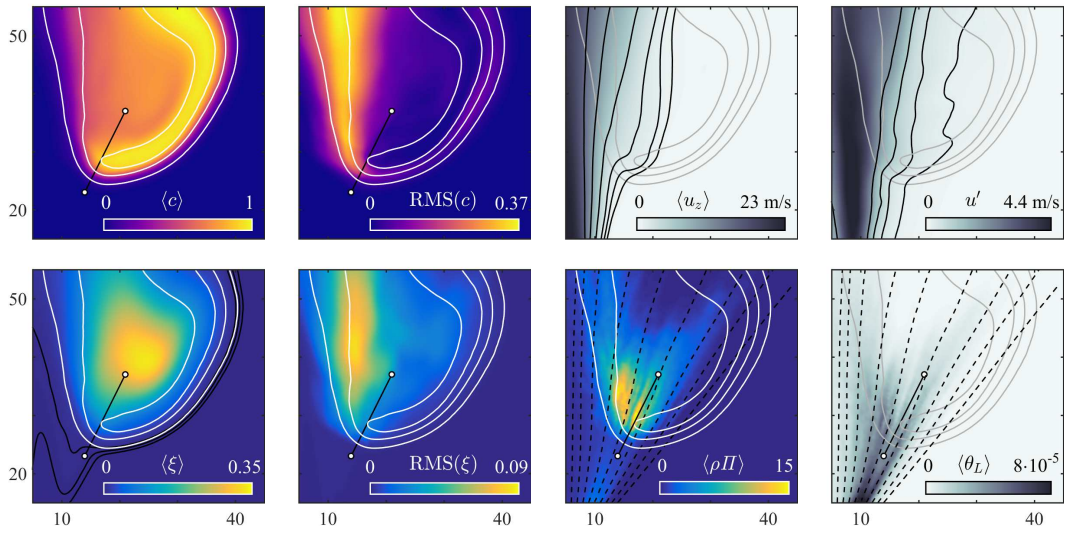


Fig. 7.16 Time-averaged fields of various LES-filtered quantities. White (grey in images with light background) iso-lines are for $\langle c \rangle = 0.1$, 0.5 and 0.9; solid black iso-lines are for mean axial velocity $\langle u_z \rangle = 0.5$, 1, 2, 5, 10, 15 m/s, turbulent velocity fluctuation $u' = 0.2$, 0.5, 1, 2, and mean mixture fraction $\langle \xi \rangle = 0.001$, 0.002, 0.004, in the respective images. Dashed black lines show representative droplet trajectories. A black line between white circles marks the orientation of the cut used in Fig. 7.17.

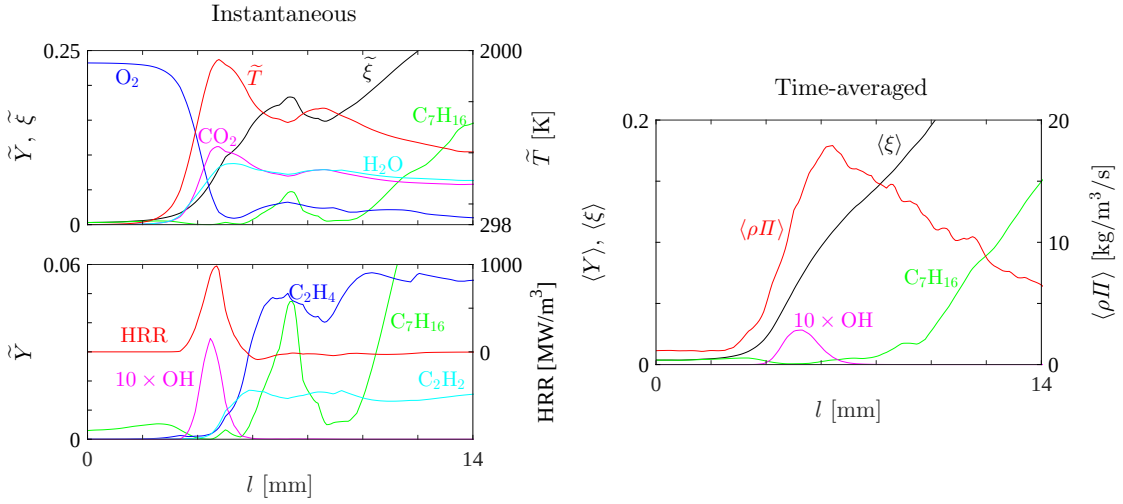


Fig. 7.17 Instantaneous and time-averaged profiles of the flame through the anchoring point, perpendicular to the $\langle c \rangle = 0.5$ iso-contour.

conditional space that allows the resolution of small-scale variations of temperature, HRR and species, using a moderate number of DCMC cells.

In Fig. 7.18 (B) a cut through two $\tilde{c}$ iso-contours ($\tilde{c} = 0.1$ and 0.6) shows that very little fuel evaporates upstream of the flame. Gaseous fuel is only generated by evaporation in response to the heat released by chemical reaction. Moreover, Fig. 7.18 highlights that most droplets penetrate through flame and continue to evaporate in the hot gases.

### 7.4.4 DCMC versus constant flame structure

In this section, the effect of solving the DCMC equation to capture the evolution of the flame structure is assessed. For this purpose, the LES-DCMC results are compared to an LES that uses a constant flame structure, invariant in space and time. This simulation uses the flame structure computed in the *a priori* assessment of DCMC-0D (Fig. 5.3, left), instead of solving the DCMC equation. All other models and settings of the simulation are unchanged.

Figure 7.20 compares the results of the two simulations. The position of the flame and its shape are hardly affected. Both simulations show a lift-off hight of about 26 mm. This suggests that the lift-off height of this particular flame may be determined by the spray injection and evaporation rather than the combustion model. The gas velocities and spray statistics are unchanged compared to Figs 7.11 and 7.12 (not shown). The fields of mean temperature from both simulations are overall similar, which explains the unchanged spray statistics and gas velocity.

The present flame is not exposed to very high levels of turbulence intensity and the SDR is relatively low. Hence, large differences due to the local variations in strain rate are not expected. Some differences can be observed at the turbulent inner flame branch, where LES-DCMC predicts higher mean temperature and mean HRR. Differences are also observed for most chemical species, in particular, for radical species. Here only OH mass fraction is shown, since a comparison to experimental OH-PLIF measurements is possible. LES-DCMC predicts $\langle Y_{\mathrm{OH}} \rangle \approx 0.001$ in the inner flame brush, which is about three times higher than the mean OH in the simulation with constant flame structure. At the same time LES-DCMC predicts a lower level of OH in the outer flame branch. Hence, the LES-DCMC results appear to be more similar to the integrated OH-PLIF measurements that found comparable intensity in both flame branches (see Fig 7.14).

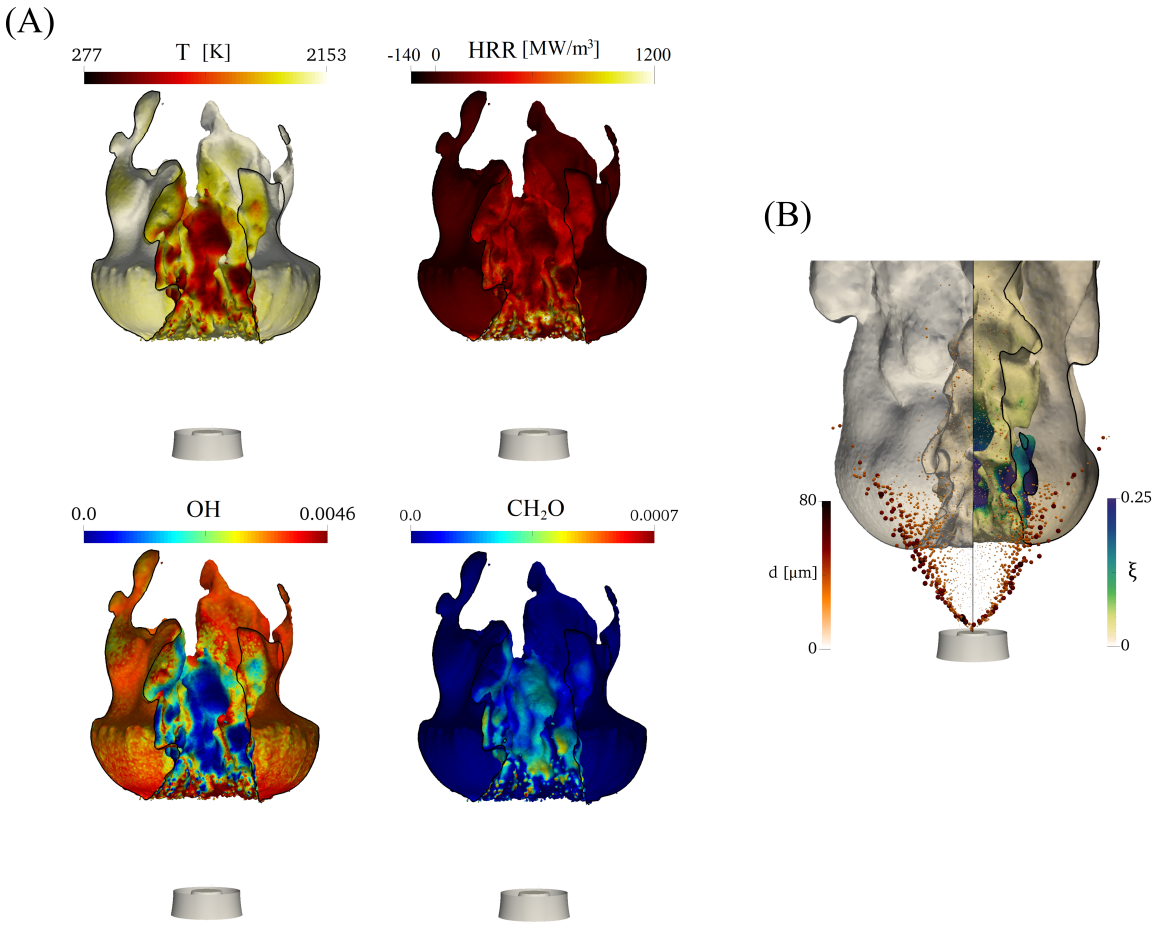


Fig. 7.18 (A) Cut through the stoichiometric mixture fraction iso-surface; coloured by LES-filtered temperature, heat release rate and mass fractions of OH and $CH_2O$. The contour in the cut-plane is indicated by a black iso-line. (B) Cut through the reaction progress variable iso-surfaces $\tilde{c} = 0.1$ (left) and $\tilde{c} = 0.6$ (right), coloured by mixture fraction; the colour of droplets indicates their size.

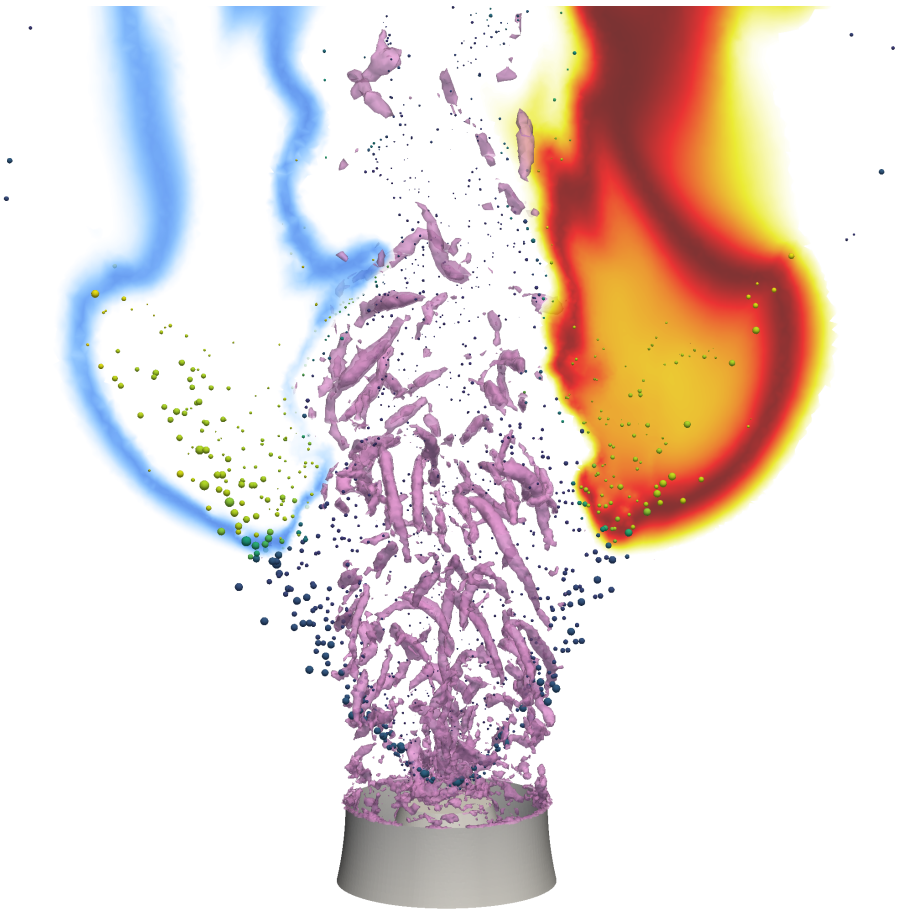

Fig. 7.19 Qualitative snapshot of the flame. Contours of OH mass fraction (left) and temperature (right) indicate the location of the flame. Droplets are only shown in the cut plane, coloured by droplet temperature. Iso-surfaces of Q-criterion (second invariant of the velocity gradient tensor) $4 \cdot 10^7$ s$^{-2}$ indicate the turbulence field.

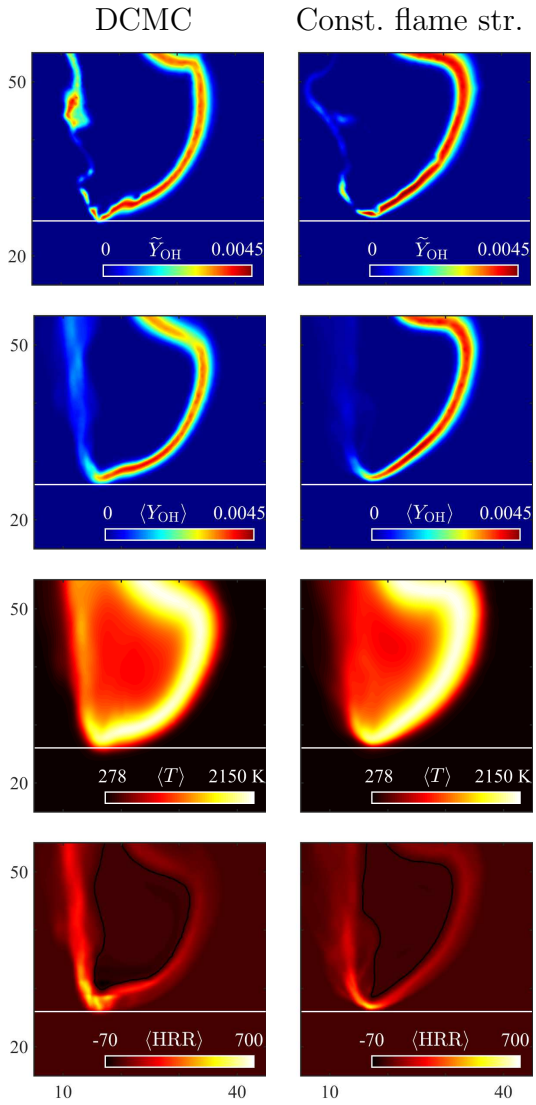


Fig. 7.20 Comparison of results from LES-DCMC (left) and LES with space- and time-invariant flame structure (right), for instantaneous $\tilde{Y}_{OH}$ and the time-averaged fields $\langle Y_{OH} \rangle$, $\langle T \rangle$ and $\langle HRR \rangle$. HRR is given in MW/m$^3$. The white horizontal line at $z = 26$ mm indicates the lift-off height obtained from LES-DCMC. A black line encompasses the region with negative mean HRR in the respective plots.

### 7.4.5 Analysis in doubly-conditional space

The previous analysis showed that the evolution of the doubly-conditional flame structure, solved in space and time by the DCMC equation, had a noticeable effect on the prediction of OH, HRR and even temperature in the flame. The spatial and temporal evolution of the flame structure in DCMC is investigated next.

Figure 7.21 shows instantaneous doubly-conditional moments for three different locations, at the tip, the inner and the outer branch of the flame (see Fig. 7.4). Note that $Q_{\mathrm{CO2}}$ (Fig. 7.6) is fixed in the entire domain according to the definition in Eqn. 3.12. At the locations A and B the conditional moments of temperature, $O_2$ and OH are relatively similar. Using the doubly-conditional parametrisation, the conditional means of major species seem to be less sensitive to location than they are in singly-conditional CMC. At the same time, significant differences persist for the reaction rates, suggesting that the balance of minor species are more sensitive to location. Larger differences are observed when comparing the inner and outer flame branch (locations B and D).

The balance of terms in the DCMC equation is analysed here focusing on the radical species OH. It was shown previously that solving for the evolution of the flame structure with DCMC has an effect on the prediction of OH in the inner flame branch. Figure 7.22 shows the instantaneous terms of the DCMC equation for OH at the location of the anchoring point of the flame (location A). The conditional moment $Q_{\mathrm{OH}}$ itself and $\langle \dot{\omega}_c | \eta, \zeta \rangle$ are displayed in Fig. 7.21 (location A). In contrast to singly-conditional CMC (for instance, Fig. 11 in Zhang & Mastorakos [2017]), the present case, the terms representative of transport in physical space, advection, dilatation and diffusion, do not play an important role in the balance of terms. This is in line with the reduced sensitivity of $Q_{\mathrm{OH}}$ to spatial location and relatively lower gradients in physical space, as compared to singly-conditional CMC. This can partly be related to the fact that this flame does not exhibit a very strong transient behaviour, so that the flame structure parametrised in doubly-conditional space evolves only gradually in space. More generally, the progress variable provides an additional degree of freedom in conditional space that can be seen as representative for the spatial evolution across the flame. The reduced sensitivity of certain doubly-conditional moments on location has recently been discussed by Bushe [2018].

Amongst the terms of transport in physical space the diffusion term is more than one order of magnitude smaller than the advective term (not shown) since more than 95 % of turbulent kinetic energy is resolved by the LES. At the same time molecular and turbulent diffusion are of comparable size, suggesting that the term of molecular diffusion in the DCMC equation should not be neglected.

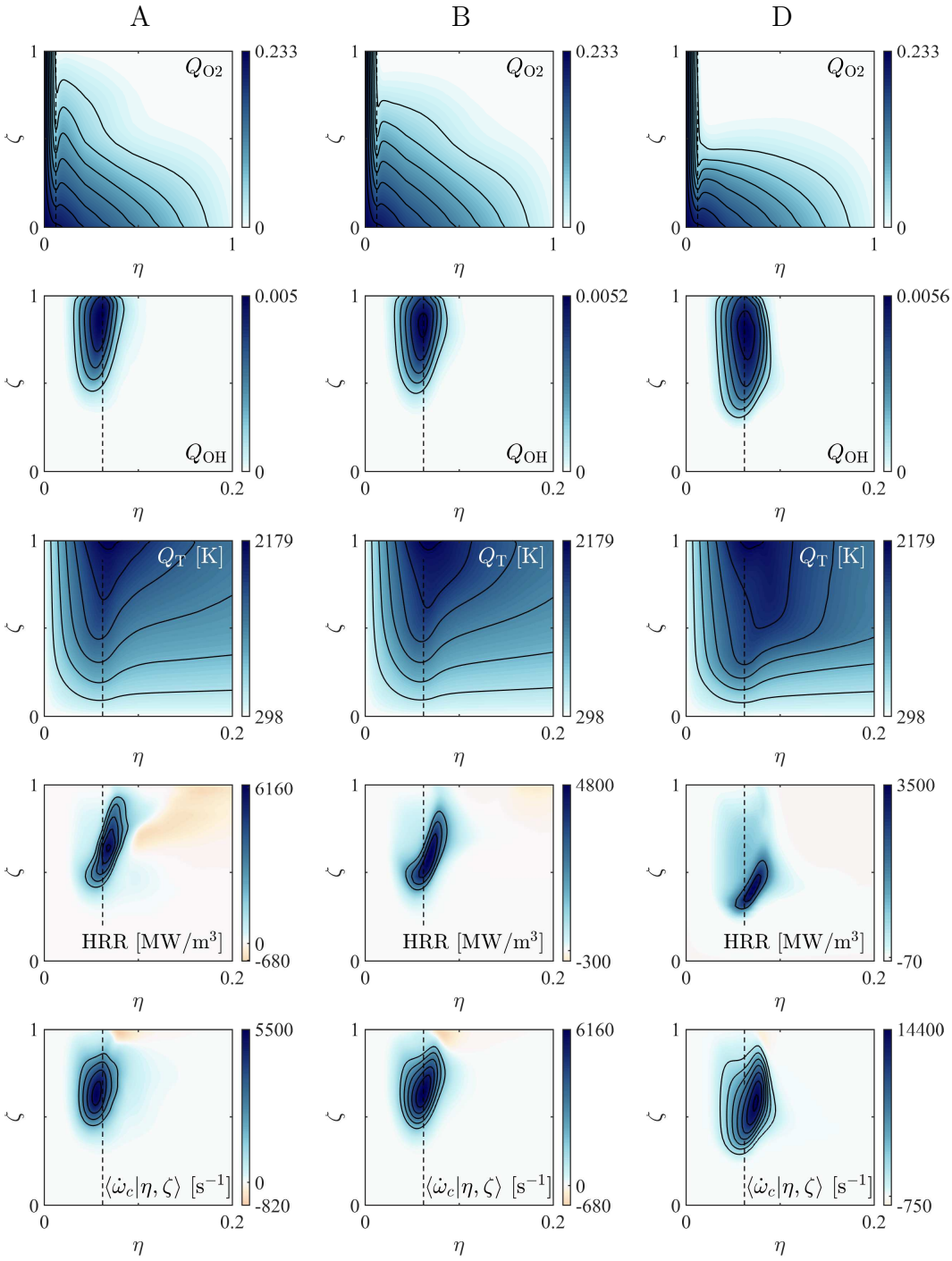


Fig. 7.21 Instantaneous doubly-conditional moments from the tip of the flame at location A (left), the inner flame branch at location B (middle) and the outer flame branch at location D (right). The dashed vertical line marks $\xi_{st}$.

The most prominent terms shown in Fig. 7.22 are related to chemical reaction and $N_\xi$ (including $\dot{\omega}_p$). This suggests that non-premixed burning modes are important in the region of the anchoring point of this flame. While the effect of $N_c$ is overall smaller, the term acts most strongly by transporting OH from intermediate to earlier stages of the reaction zone ($\zeta \approx 0.4$). Thus, it establishes the reaction-diffusion balance responsible for the flame structure in $\zeta$-space that can be expected to have a direct effect on the conditional reaction rate.

The source term $\dot{\omega}_p$ represents the diffusion of species $Y_\psi = Y_{\mathrm{CO2}}$ in mixture fraction space. Since $\dot{\omega}_p$ is a source term to the conditioning variable $c$, it appears as an "advective" term in $\zeta$-space. It is notable that $\langle \dot{\omega}_p | \eta, \zeta \rangle < 0$ for stoichiometric mixture fraction because $\partial^2 Q_{\mathrm{CO2}} / \partial \eta^2 = \zeta (\partial^2 Y^{\mathrm{Eq}}_{\mathrm{CO2}} / \partial \eta^2) < 0$ for $\eta \approx \xi_{\mathrm{st}}$.

The direct effect of evaporation on $Q_{\mathrm{OH}}$ appears to be marginal. The highest spray source terms occur for hot droplets, but then the doubly-conditional spray source acts in the fuel-rich region of $\eta$-space, where $Q_{\mathrm{OH}}$ is zero and, thus, is unaffected. However, evaporative cooling, as indicated by $(Q_h - Q_h^0)$, may affect the chemical reaction balance indirectly.

As mentioned earlier, the flame structure parametrised in doubly-conditional space varies much less in time and physical space than usual in conventional singly-conditional CMC. This is, in particular, true for major species and temperature. The instantaneous reaction rate is more strongly affected by small changes of SDR and, consequently, larger variations are observed both in terms of spatial differences and temporal fluctuations. This is summarised in Fig. 7.23, showing the temporal evolution of the peak value of the doubly-conditional reaction rate for different locations. First, $\langle \dot{\omega}_c | \eta, \zeta \rangle$ is investigated at the locations A, B and C, which distinguish each other in terms of their axial distance from the nozzle (Fig. 7.4). Moreover, time-averages of the conditional reaction rate $\langle \langle \dot{\omega}_c | \eta, \zeta \rangle \rangle$ and the corresponding RMS are shown. At location D, in the outer flame branch, fluctuations are negligible and the time-averaged conditional reaction rate at D is identical with the instantaneous one shown in Fig. 7.21.

Since the highest SDRs occur close to the tip of the flame (Fig. 7.15), the region around location A experiences the highest strain and, thus, exhibits the lowest conditional reaction rate. For all three locations the RMS values are about 10 % of the conditional reaction rate's peak value. Yet the time scales for fluctuations differ significantly: while they are very fast at location A, the flame around point C experiences slow transitions over several milliseconds. Secondly, the conditional reaction rate in various locations with identical radial and axial coordinates but at different azimuthal locations is studied; A1, A2, A3 and A4 share the same radial and

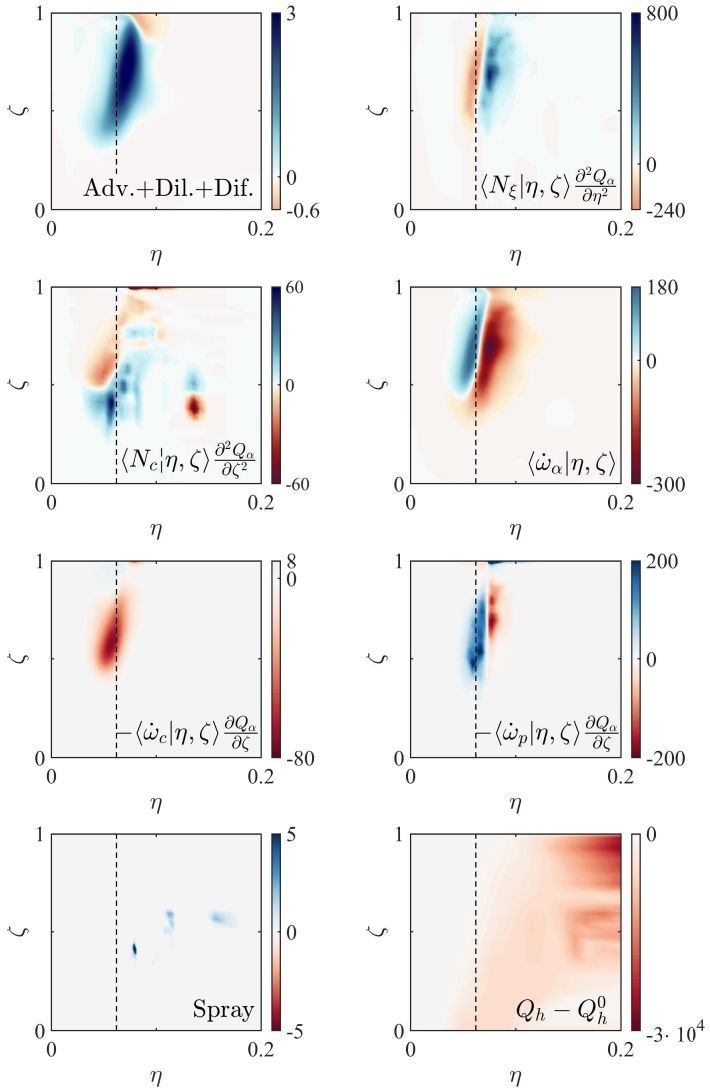


Fig. 7.22 Instantaneous term balance for the DCMC equation of $Q_{\mathrm{OH}}$ for the CMC cell at location A, $(r, z) = (10\ \mathrm{mm}, 27.5\ \mathrm{mm})$. Also shown is $Q_h - Q_h^0$, representing the net effect of the spray term on $Q_h$. The dashed vertical line marks $\xi_{\mathrm{st}}$.

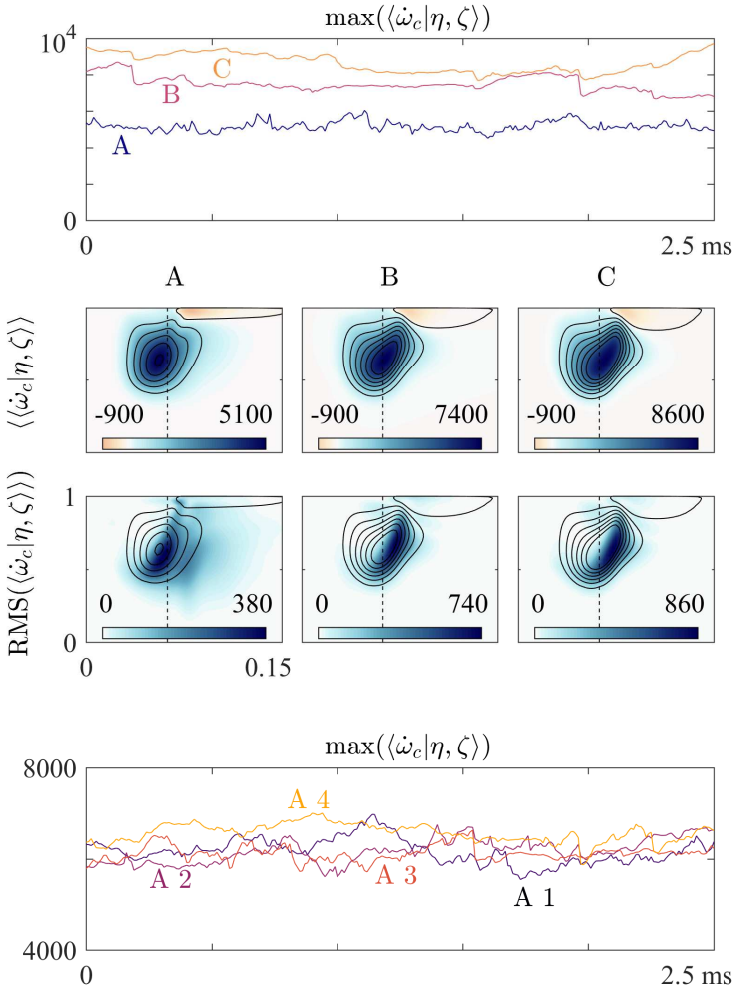


Fig. 7.23 Temporal evolution of $\langle \dot{\omega}_c | \eta, \zeta \rangle$ for locations A, B and C (top). For locations A, B and C time averages of the conditional reaction rate $\langle \langle \dot{\omega}_c | \eta, \zeta \rangle \rangle$ and the time-based RMS are shown (middle). Note that the RMS is overlaid with contour lines of the temporal mean. In comparison, the evolution for the locations A1, A2, A3 and A4 with the same radial and axial position as A, but different azimuthal locations, 0°, 51°, 103° and 154° respectively, are shown (bottom). The dashed vertical line marks $\xi_{\mathrm{st}}$.

axial coordinate with location A and occupy consecutive azimuthal positions. In spite of the burner's geometry, the test flame only exhibits rotational symmetry in the mean sense. Consequently, the behaviour in neighbouring azimuthal locations is similar, but differences in conditional reaction rate persist at most instances in time.

This analysis demonstrated the following points: (i) gradients of the conditional means in physical space are greatly reduced due to the doubly-conditional parametrisation of the flame structure; (ii) spatial differences and temporal fluctuations of the conditional means of minor species and reaction rates persist on top of the doubly-conditional parametrisation, even in the relatively stable test flame studied here; and (iii) this underlines the necessity for a sufficient resolution in terms of DCMC cells.

## 7.5 Conclusions

In this chapter an application of the LES-DCMC modelling approach was presented. Doubly-conditional spray terms have been included in the DCMC equation to introduce the effect of evaporation on the reaction zone. LES-DCMC was employed to simulate a lifted spray jet flame using a detailed chemical mechanism for n-heptane fuel. The study found good agreement between simulation results and experiments in terms of instantaneous as well as time-averaged flame shape and droplet statistics. In particular, droplet statistics and lift-off height obtained in the present work were similar to the predictions with the SF model by Noh et al. [2018].

Analysing iso-contours of stoichiometric mixture fraction showed strong variations of temperature, heat release rate and species in the inter-droplet region. This showed that the doubly-conditional parametrisation of the flame allowed to resolve local effects due to droplet evaporation. At the same time, iso-contours of progress variable showed that the flame experienced a wide range of mixture compositions, from lean to very rich, involved in the flame. These variations were associated with both mixture inhomogeneity in the range from lean to very rich and small-scale variations of reaction progress.

The DCMC approach allowed for a detailed analysis of the flame and its anchoring point. In the DCMC equation of OH, the conditional reaction rate was found to be primarily balanced by the terms associated with the SDR of mixture fraction. This suggested that non-premixed burning modes are prominent at the anchoring point of the flame.

Furthermore, it was found that advective and diffusive transport were less important in DCMC than in the conventional singly-conditional CMC. This is attributed to the

fact, that the additional dimension in conditional space reduces the dependency of the flame structure on physical space and the gradients of the doubly-conditional moments in physical space are lower. While conditional moments of temperature and major species are similar in large parts of the domain, the conditional reaction rate has a significant dependence on the location in the flame. Moreover, it exhibits temporal fluctuations of about 10 % of its local mean, whose time scales depend on the location.

The benefit of solving for the flame structure with DCMC was assessed by comparing the results from LES-DCMC with a second LES that used a space- and time-invariant flame structure. While both simulations predicted the same lift-off height, some differences were found for OH, HRR and temperature in the turbulent inner flame branch.

# Chapter 8

# Conclusions and Recommendations

## 8.1 DCMC model development

Doubly Conditional Moment Closure (DCMC) was developed as a modelling approach for turbulent spray combustion. This approach is founded in the well-established Conditional Moment Closure (CMC) modelling framework for turbulent combustion. In contrast to commonly used CMC modelling, the present DCMC formulation is based on two conditioning variables, mixture fraction and reaction progress variable. This formulation allows to parametrise the entire range from non-premixed to fully premixed flames. This is, in particular, necessary in the modelling of spray combustion, where the interplay of evaporation, mixing and reaction manifests in a diverse palette of combustion regimes, and premixed and non-premixed burning modes may occur simultaneously within a single flame.

In Chapter 3 the model derivation and closure were presented. The DCMC equation was derived using a *separated flow model* as formalism for the description of multi-phase flows. In this way the spray source terms were derived, which represent the effect of evaporation on the flame structure in the DCMC equation. It was attempted to derive the DCMC equation in a general way, and to relax commonly made assumptions where possible. Namely the assumption of unity Lewis and the explicit assumption of high Reynolds number were relaxed, leaving the *primary closure hypothesis* of CMC as the main assumption. Therefore, the derivation provides a complete view of the physical effects on the flame structure and their representation by terms in the DCMC equation, including differential diffusion and low Reynolds number effects. This may provide the basis for future modelling efforts.

A set of closure models for the DCMC equation was suggested. The models were generalisations of commonly used sub-models for singly-conditional CMC, or

adaptations from other mixture fraction-progress variable approaches. In particular, a model for the doubly-conditional spray source term was suggested. The model is based on theoretical considerations and constitutes a generalisation of the $\delta$-function used in previous work with singly-conditional CMC.

## 8.2 DCMC-0D

In Chapter 5, the solutions of the DCMC equation were explored in the special case of spatial homogeneity, denoted as DCMC-0D. Features of the DCMC equation were discusses. Notably the conditional moment of $CO_2$, the species used as the progress variable, was fixed in time and space, so that the definition of the progress variable was automatically satisfied. Moreover, the conditional moments of $N_2$ and enthalpy are fixed in the case of unity Lewis number and absence of $NO_x$ chemistry, and under adiabatic conditions and in the absence of spray terms.

In an *a priori* assessment, the results from DCMC-0D were compared to a two-dimensional manifold constructed of freely-propagating laminar premixed flames. In the case of small $N_\xi$ and using a model for $\langle N_c|\eta,\zeta\rangle$ based on the tabulation of laminar premixed flames, DCMC-0D reproduced the flame structure and reaction rate from the laminar premixed flames reasonably well. This confirms the validity of DCMC, the solver strategy and the modelling of $\langle N_c|\eta,\zeta\rangle$ in the limit case of $N_\xi \to 0$. An alternative algebraic model for $\langle N_c|\eta,\zeta\rangle$ was tested and it was shown that it can provide reasonable results, in terms of the conditional temperature and reaction rate, if correctly scaled. The algebraic model does not require the pre-computation of laminar flames and could be used as a simple alternative to more sophisticated models for predictions of flame shape and temperature – predicting pyrolysis or pollutant formation may require a more accurate model for the conditional SDR. The effect of the SDRs on the reaction rate was examined. Increasing $N_c$ relative to unstrained premixed flames led to lower conditional reaction rate; a slight increases of $N_\xi$ led to a higher peak value of the conditional reaction rate. These findings are in line with previous work.

The context of DCMC-0D was also used to demonstrate the modelling and effect of the spray source terms. The effect of spray evaporation on the doubly-conditional moments of species mass fraction is small. In particular, for $CO_2$ and $N_2$ the spray terms cancel each other. In contrast, a significant effect is found on the conditional moment of enthalpy – this is the effect of evaporative cooling. Analysing the term balance for the $Q_h$ equation showed that at steady state, a balance to first order is

established between the enthalpy spray term, the mixture fraction spray term and the $N_\xi$ term.

## 8.3 DCMC and RANS of a piloted spray flame

In Chapter 6, DCMC was used in combination with RANS to simulate a piloted ethanol spray flame at two operating conditions. This constituted the first application of DCMC to a lab-scale flame. The investigated flames were of the type of propagating spray flames with similar behaviour to premixed flames, but also with significant small-scale mixture inhomogeneities. Therefore, this flame posed a suitable test case for the DCMC method. The velocity field and the droplet distributions showed good agreement with experimental data and the flame shape prediction was promising in revealing the experimental trend, due to overall equivalence ratio.

The flame structure and its parametrisation in the doubly-conditional space were investigated. The doubly-conditional flame structure was found to be relatively insensitive to axial location in the flame. This indicates that the entire flame was nearly sufficiently parametrised by the doubly-conditional space – a result of a simple flow field and low turbulence levels. Moreover, strong similarities of the flame structure in two flames with different overall equivalence ratio suggested that the parametrisation based on mixture fraction could account for these differences in the overall mixture. These findings show that the $(\xi, c)$ parametrisation of a flame is very general, and suggest that a coarse discretisation of the physical space can be sufficient for DCMC.

The term balance of the Reynolds-averaged mean and variance equations for the conditioning variables was analysed. First, the reaction source term in the $\widetilde{c''^2}$ equation was found to be dominant, and could not be balanced by the SDR given by the linear relaxation model for passive scalar mixing. This showed the need to use a model for the SDR of progress variable that takes flame dilatation effects into account. Second, the presumed shape of the spray source in conditional space was used to close the spray source terms in the mean and variance equations of mixture fraction and progress variable, and study their effect on the term balance. Apart from the mean mixture fraction equation, these source terms have a complicated form and require modelling. In the $\widetilde{\xi''^2}$ equation, the evaporation was the dominant source term and the linear relaxation model for passive scalar mixing model seemed inadequate to counter-balance this source term. In the $\widetilde{c''^2}$ equation, the evaporation source term was small, and due to its limited spatial effect it can be neglected. In the $\tilde{c}$ equation, the effect of spray evaporation is also small, but reflects the principle of conservation of mass for the

species used as basis for the progress variable, and, thus, should not be neglected. A simple model for this term was suggested to provide closure without integration of the spray term in doubly-conditional space. Insight gained from this analysis was used in Chapter 7.

## 8.4 LES-DCMC of a lifted spray jet flame

In Chapter 7, the modelling of a spray jet flame with LES-DCMC was presented. This was the first application of LES with DCMC acting as the SGS combustion model. The doubly-conditional spray terms have been included in the DCMC equation, thus introducing the direct effect of evaporation on the reaction zone. The study found very good agreement between simulation and experiments in terms of instantaneous as well as time-averaged flame shape and droplet statistics. As a result, the present case validates the LES-DCMC approach for turbulent spray combustion. Furthermore, since the present flame is a test case of the *Workshop on Turbulent Combustion of Sprays*, which has been simulated with various combustion models, it allows us to benchmark LES-DCMC. In particular, the droplet statistics and lift-off height obtained in the present work are similar to the prediction with Stochastic Fields by Noh et al. [2018].

The doubly-conditional parametrisation of the flame structure in DCMC was found to resolve local small-scale effects of the spray on the flame. These effects manifested as local instantaneous variations of temperature and heat release rate in regions where droplets interact with the flame. The variations were associated with both mixture inhomogeneity in the range from lean to very rich and small-scale variations of reaction progress. Variations of the latter type can not easily be resolved with singly-conditional CMC, which demonstrates the need for a doubly-conditional parametrisation of the flame in the modelling of turbulent spray combustion.

The benefit of solving the DCMC equation online to obtain the temporal and spatial evolution of the flame structure was assessed by comparing the results obtained from LES-DCMC with a second LES that used a space and time-invariant flame structure. While both simulations predicted the same lift-off height, some differences were found for OH, heat release rate and temperature in the turbulent inner flame branch.

For LES-DCMC, the evolution of the doubly-conditional flame structure in space and time was investigated in detail. Spatial gradients of the doubly-conditional flame structure were generally small, and convective transport was found to play a minor role on the flame structure compared to the effects of micro-mixing and chemical reaction in the DCMC equation. Notably, the terms of convective transport are less important

in DCMC than in conventional singly-conditional CMC. Still, micro-mixing affected the reaction-diffusion balance locally, leading to significant spatial variations of the conditional reaction rate. Temporal fluctuations of the conditional reaction rate were approximately 10 % of their time-based mean, and their time scale increasing with axial distance from the burner nozzle.

Finally, analysing the term balance of the DCMC equation allowed to conclude that non-premixed burning modes were most prominent at the anchoring point of the simulated flame. This suggests that the doubly-conditional description of the flame could be used as the basis to create a metric that reveals the driving mechanism of flame stabilisation.

## 8.5 General conclusions

In the present work, the DCMC method for spray flames has been developed and tested. The doubly-conditional parametrisation of the flame structure was found to resolve the effects of local instantaneous fluctuations of mixture fraction and progress variable.

The applications of the DCMC method showed a reduced spatial dependence of the doubly-conditional flame structure and small spatial gradients of the conditional moments. Consequently, a very coarse DCMC mesh may still be sufficient to capture strong transient effects. In the present applications, the DCMC method has already demonstrated the ability to handle large chemical mechanisms efficiently, due to the employment of an operator splitting technique. Considering the reduced requirements in terms of spatial resolution for DCMC, the approach may have the potential for increased computational efficiency using detailed chemistry.

While this work focused on DCMC as an approach for modelling spray combustion, it can also be employed to tackle other problems of turbulent combustion modelling. In principle, the method is "ideally suited for partially premixed flames" [Kronenburg & Mastorakos, 2011, p. 103]. As such, the present work provides the tool for the modelling of partially premixed combustion with a CMC method, which had so far been out of reach. Moreover, the capabilities of DCMC to predict extinction and ignition has already been demonstrated in *a priori* studies relative to DNS. This shows the potential for future applications of the method. At the same time, computational cost and accuracy gain are important factors to consider.

## 8.6 Recommendations

Based on the findings presented in this thesis, the following recommendations for future work are made.

- Further validation of the DCMC method and the closure sub-models is necessary. Test flames with partially premixed combustion and cases with extinction and ignition are particularly recommended.

- Validation of the doubly-conditional sub-models, notably the scalar dissipation rates, against DNS data is recommended. The sub-models used in the present work are mostly based on theoretical considerations, but in most cases the models have not been evaluated against DNS data yet.

- The modelling of the covariance $\widetilde{\xi'' c''}$, its effects on the PDF and the modelling of the cross-scalar dissipation rate (CDR) should be considered. In LES the effect of SGS covariance on the local FDF might be small. However, the filtered CDR may have a significant resolved part and the conditional CDR may play an important role in the prediction of extinction [Kronenburg, 2004]. Modelling of the conditional CDR could be performed as suggested in Eqn. 3.78.

- Differential diffusion should be included in the DCMC equation. In cases with a strongly premixed behaviour, the modelling of differential diffusion would be required to predict the conditional reaction rate accurately. In order to include differential diffusion in DCMC, it might be possible to incorporate the suggestions by Kronenburg & Bilger [1997] and Farrace et al. [2018].

- Further work on spray modelling should focus on the effect of evaporation on the mixture fraction variance, the conditional spray source terms and the SDR. The conditional spray source terms have so far only been considered in a small number of publications. Correct modelling also entails the modelling of PDF and conditional SDR.

- The findings of the present work suggest that a very coarse discretisation of physical space can be sufficient for DCMC. Consequently, there is a potential to increase the computational efficiency considerably if the DCMC grid was adapted accordingly and coarsened in regions with small gradients. This optimisation strategy should be considered to conduct large-scale simulations with detailed chemistry.

- From a theoretical point of view, the treatment of the parts of the conditional space with zero probability should be examined, since it is not clear how to model advective and diffusive fluxes in this case. This is already a significant question for LES-CMC where CMC cells are small, as pointed out by Kronenburg & Mastorakos [2011, p. 113f]: for instance, CMC cells far from the fuel injection may have close-to-zero probability of finding fluid with finite mixture fraction. The issue becomes even more important in DCMC: for instance, a DCMC cell upstream of a lifted flame has zero probability of finding mixture with finite progress variable. Hence, the PDF is zero in most of the doubly-conditional space.

# References


Abdel-Gayed, R. G., Bradley, D., & Lung, F. K.-K. (1989). Combustion regimes and the straining of turbulent premixed flames. *Combustion and Flame*, 76(2):213–218.

Abramzon, B. & Sirignano, W. A. (1989). Droplet vaporization model for spray combustion calculations. *International Journal of Heat and Mass Transfer*, 32(9):1605–1618.

Agarwal, A. K. (2007). Biofuels (alcohols and biodiesel) applications as fuels for internal combustion engines. *Progress in Energy and Combustion Science*, 33(3):233 – 271.

Aggarwal, S. K. (2014). Single droplet ignition: Theoretical analyses and experimental findings. *Progress in Energy and Combustion Science*, 45:79–107.

Airbus SAS (2017). Global Market Forecast 2017 / 2036. www.airbus.com/company/market/forecast/. Accessed 20 June 2018.

Amzin, S. & Swaminathan, N. (2013). Computations of turbulent lean premixed combustion using conditional moment closure. *Combustion Theory and Modelling*, 17(6):1125–1153.

Amzin, S., Swaminathan, N., Rogerson, J. W., & Kent, J. H. (2012). Conditional moment closure for turbulent premixed flames. *Combustion Science and Technology*, 184(10–11):1743–1767.

Apte, S. V., Mahesh, K., & Moin, P. (2009). Large-eddy simulation of evaporating spray in a coaxial combustor. *Proceedings of the Combustion Institute*, 32(2):2247–2256.

Balachandar, S. (2003). Parameterization of force on a particle/bubble/droplet. *Multiphase Science and Technology*, 15(1–4):157–171.

Balachandar, S. (2009). A scaling analysis for point–particle approaches to turbulent multiphase flows. *International Journal of Multiphase Flow*, 35(9):801–810.

Balachandar, S. & Eaton, J. K. (2010). Turbulent dispersed multiphase flow. *Annual Review of Fluid Mechanics*, 42(1):111–133.

Ballal, D. R. & Lefebvre, A. H. (1981). Flame propagation in heterogeneous mixtures of fuel droplets, fuel vapor and air. *Symposium (International) on Combustion*, 18(1):321–328.

Bardina, J., Ferziger, J. H., & Reynolds, W. C. (1980). Improved subgrid-scale models for large-eddy simulation. 13th Fluid and Plasma Dynamics Conference, 14–16 July 1980, Snowmass, CO, USA.

Barlow, R. S. & Frank, J. H. (1998). Effects of turbulence on species mass fractions in methane/air jet flames. *Symposium (International) on Combustion*, 27(1):1087–1095.

Behzadi, J. J., Talei, M., Bolla, M., Hawkes, E. R., Lucchini, T., D'Errico, G., & Kook, S. (2018). A conditional moment closure study of chemical reaction source terms in SCCI combustion. *Flow, Turbulence and Combustion*, 100(1):93–118.

Bekdemir, C., Somers, L. M. T., & de Goey, L. P. H. (2011). Modeling diesel engine combustion using pressure dependent flamelet generated manifolds. *Proceedings of the Combustion Institute*, 33(2):2887–2894.

Bhattacharjee, S. & Haworth, D. C. (2013). Simulations of transient n-heptane and n-dodecane spray flames under engine-relevant conditions using a transported PDF method. *Combustion and Flame*, 160(10):2083–2102.

Bilger, R. W. (1975). A note on Favre averaging in variable density flows. *Combustion Science and Technology*, 11(5–6):215–217.

Bilger, R. W. (1976). The structure of diffusion flames. *Combustion Science and Technology*, 13(1–6):155–170.

Bilger, R. W. (1989). The structure of turbulent nonpremixed flames. *Symposium (International) on Combustion*, 22(1):475–488.

Bilger, R. W. (1992). Advanced laser diagnostics: implications of recent results for advanced combustor models. In Lee, R. S. L., Whitelaw, J. H., & Wung, T. S., editors, *Aerothermodynamics in Combustors*. Springer-Verlag, Berlin, Heidelberg. IUTAM Symposium, 3–5 June 1991, Taipei, Taiwan.

Bilger, R. W. (1993a). Conditional moment closure for turbulent reacting flow. *Physics of Fluids A*, 5(2):436–444.

Bilger, R. W. (1993b). Conditional Moment Closure Modelling and Advanced Laser Measurements. In Takeno, T., editor, *Turbulence and Molecular Processes in Combustion*, pages 267–285. Elsevier Science Publishers, Amsterdam. Sixth Toyota Conference, 11–14 October 1992, Shizuoka, Japan.

Bilger, R. W. (2011). The role of combustion technology in the 21st century. In Echekki, T. & Mastorakos, E., editors, *Turbulent Combustion Modelling*, pages 3–18. Springer, Dordrecht, Heidelberg, London, New York.

Bini, M. & Jones, W. P. (2008). Large-eddy simulation of particle-laden turbulent flows. *Journal of Fluid Mechanics*, 614:207–252.

Blaschek, H. P., Ezeji, T. C., & Scheffran, J. (2010). *Biofuels from Agricultural Waste and Byproducts*. Wiley-Blackwell, Oxford.

Bolla, M., Farrace, D., Wright, Y. M., Boulouchos, K., & Mastorakos, E. (2014). Influence of turbulence–chemistry interaction for n-heptane spray combustion under diesel engine conditions with emphasis on soot formation and oxidation. *Combustion Theory and Modelling*, 18(2):330–360.

Bolla, M., Wright, Y. M., Boulouchos, K., Borghesi, G., & Mastorakos, E. (2013). Soot formation modeling of n-heptane sprays under diesel engine conditions using the conditional moment closure approach. *Combustion Science and Technology*, 185(5):766–793.

Borghesi, G., Mastorakos, E., Devaud, C. B., & Bilger, R. W. (2011). Modeling evaporation effects in conditional moment closure for spray autoignition. *Combustion Theory and Modelling*, 15(5):725–752.

Borghi, R. (1985). On the structure and morphology of turbulent premixed flames. In Casci, C. & Bruno, C., editors, *Recent Advances in the Aerospace Sciences*, pages 117–138. Springer US, Boston, MA.

Borghi, R. (1988). Turbulent combustion modelling. *Progress in Energy and Combustion Science*, 14(4):245–292.

Borghi, R. P. (1996a). Background on droplets and sprays. In *Combustion and Turbulence in Two-phase Flows. Lecture series 1996-02*. Von Karman Institute for Fluid Dynamics.

Borghi, R. P. (1996b). The links between turbulent combustion and spray combustion. In Chang, S. H., editor, *Transport Phenomena in Combustion*. Taylor and Francis.

Both, A. (2017). RANS-FGM simulation of n-heptane spray flame in OpenFOAM. MSc thesis, Delft University of Technology.

Bottone, F., Kronenburg, A., Gosman, D., & Marquis, A. (2012). The numerical simulation of diesel spray combustion with LES-CMC. *Flow, Turbulence and Combustion*, 89(4):651–673.

Boussinesq, J. (1877). *Essai sur la théorie des eaux courantes*. Imprimerie Nationale, Paris.

BP plc (2017a). BP Statistical Review of World Energy June 2017. https://www.bp.com/en/global/corporate/energy-economics/statistical-review-of-world-energy.html. Accessed 20 June 2018.

BP plc (2017b). Energy Outlook. https://www.bp.com/content/dam/bp/pdf/energy-economics/energy-outlook-2017/bp-energy-outlook-2017.pdf. Accessed 20 June 2018.

Bradley, D., Emerson, D. R., Gaskell, P. H., & Gu, X. J. (2002). Mathematical modeling of turbulent non-premixed piloted-jet flames with local extinctions. *Proceedings of the Combustion Institute*, 29(2):2155–2162.

Bradley, D., Kwa, L. K., Lau, A. K. C., Missaghi, M., & Chin, S. B. (1988). Laminar flamelet modeling of recirculating premixed methane and propane-air combustion. *Combustion and Flame*, 71(2):109–122.

Bradley, D., Lawes, M., Liao, S., & Saat, A. (2014). Laminar mass burning and entrainment velocities and flame instabilities of i-octane, ethanol and hydrous ethanol/air aerosols. *Combustion and Flame*, 161(6):1620 – 1632.

Branley, N. & Jones, W. P. (2001). Large eddy simulation of a turbulent non-premixed flame. *Combustion and Flame*, 127(1):1914 – 1934.

Bray, K. N. C. (1996). The challenge of turbulent combustion. *Symposium (International) on Combustion*, 26(1):1–26.

Bray, K. N. C., Champion, M., & Libby, P. A. (1989). The interaction between turbulence and chemistry in premixed turbulent flames. In Borghi, R. & Murthy, S. N. B., editors, *Turbulent Reactive Flows*, pages 541–563. Springer US, New York.

Bray, K. N. C., Domingo, P., & Vervisch, L. (2005). Role of the progress variable in models for partially premixed turbulent combustion. *Combustion and Flame*, 141(4):431–437.

Bray, K. N. C., Libby, P. A., & Moss, J. B. (1985). Unified modeling approach for premixed turbulent combustion–Part I: General formulation. *Combustion and Flame*, 61(1):87–102.

Bray, K. N. C. & Moss, J. B. (1977). A unified statistical model of the premixed turbulent flame. *Acta Astronautica*, 4(3):291–319.

Brown, P. N. & Hindmarsh, A. C. (1989). Reduced storage matrix methods in stiff ODE systems. *Applied Mathematics and Computation*, 31:40–91.

Brown, R. J. & Bilger, R. W. (1998). Experiments on a reacting plume – 2. conditional concentration statistics. *Atmospheric Environment*, 32(4):629–646.

Burgoyne, J. H. & Cohen, L. (1954). The effect of drop size on flame propagation in liquid aerosols. *Proceedings of the Royal Society of London A*, 225(1162):375–392.

Bushe, W. K. (2018). Spatial gradients of conditional averages in turbulent flames. *Combustion and Flame*, 192:314–339.

Bushe, W. K. & Steiner, H. (1999). Conditional moment closure for large eddy simulation of nonpremixed turbulent reacting flows. *Physics of Fluids*, 11(7):1896–1906.

Butler, T. D. & O'Rourke, P. J. (1977). A numerical method for two dimensional unsteady reacting flows. *Symposium (International) on Combustion*, 16(1):1503–1515.

Candel, S., Lacas, F., Darabiha, N., & Rolon, J.-C. (1999). Group combustion in spray flames. *Multiphase Science and Technology*, 11(1):1–18.

Cant, R. S. (2011). RANS and LES modelling of premixed turbulent combustion. In Echekki, T. & Mastorakos, E., editors, *Turbulent Combustion Modelling*, pages 63–90. Springer, Dordrecht, Heidelberg, London, New York.

Cant, R. S. & Mastorakos, E. (2008). *An Introduction to Turbulent Reacting Flows*. Imperial College Press, London.

Cekalin, E. K. (1961). Propagation of flame in turbulent flow of two-phase fuel-air mixture. *Symposium (International) on Combustion*, 8(1):1125–1129.

Cha, C. M., Kosály, G., & Pitsch, H. (2001). Modeling extinction and reignition in turbulent nonpremixed combustion using a doubly-conditional moment closure approach. *Physics of Fluids*, 13(12):3824–3834.

Chatelier, A., Moureau, V., Bertier, N., & Fiorina, B. (2017). Large eddy simulation of a spray jet flame using filtered tabulated chemistry. *10th Mediterranean Combustion Symposium, 17–21 September 2017, Naples, Italy.*

Chen, H., Chen, S., & Kraichnan, R. H. (1989). Probability distribution of a stochastically advected scalar field. *Physical Review Letters*, 63:2657–2660.

Chen, Z., Ruan, S., & Swaminathan, N. (2015). Simulation of turbulent lifted methane jet flames: Effects of air-dilution and transient flame propagation. *Combustion and Flame*, 162(3):703–716.

Chen, Z., Ruan, S., & Swaminathan, N. (2017). Large eddy simulation of flame edge evolution in a spark-ignited methane-air jet. *Proceedings of the Combustion Institute*, 36(2):1645–1652.

Chen, Z. X., Doan, N. A. K., Ruan, S., Langella, I., & Swaminathan, N. (2018). A priori investigation of subgrid correlation of mixture fraction and progress variable in partially premixed flames. *Combustion Theory and Modelling*, 22(5):862–882.

Chiu, H. H., Kim, H. Y., & Croke, E. J. (1982). Internal group combustion of liquid droplets. *Symposium (International) on Combustion*, 19(1):971–980.

Chiu, H. H. & Liu, T. M. (1977). Group combustion of liquid droplets. *Combustion Science and Technology*, 17(3–4):127–142.

Chrigui, M., Gounder, J., Sadiki, A., Masri, A. R., & Janicka, J. (2012). Partially premixed reacting acetone spray using LES and FGM tabulated chemistry. *Combustion and Flame*, 159(8):2718–2741.

Chrigui, M., Masri, A. R., Sadiki, A., & Janicka, J. (2013). Large eddy simulation of a polydisperse ethanol spray flame. *Flow, Turbulence and Combustion*, 90(4):813–832.

Colin, O., Ducros, F., Veynante, D., & Poinsot, T. (2000). A thickened flame model for large eddy simulations of turbulent premixed combustion. *Physics of Fluids*, 12(7):1843–1863.

Colucci, P. J., Jaberi, F. A., Givi, P., & Pope, S. B. (1998). Filtered density function for large eddy simulation of turbulent reacting flows. *Physics of Fluids*, 10(2):499–515.

Coriton, B., Zendehdel, M., Ukai, S., Kronenburg, A., Stein, O. T., Im, S.-K., Gamba, M., & Frank, J. H. (2015). Imaging measurements and LES-CMC modeling of a partially-premixed turbulent dimethyl ether/air jet flame. *Proceedings of the Combustion Institute*, 35(2):1251–1258.

Coward, H. F. & Jones, G. W. (1952). Limits of flammability of gases and vapors. *Bureau of Mines*, Bulletin 503.

Darbyshire, O. R. & Swaminathan, N. (2012). A presumed joint pdf model for turbulent combustion with varying equivalence ratio. *Combustion Science and Technology*, 184(12):2036–2067.

Darbyshire, O. R., Swaminathan, N., & Hochgreb, S. (2010). The effects of small-scale mixing models on the prediction of turbulent premixed and stratified combustion. *Combustion Science and Technology*, 182(9):1141–1170.

De, S. & Kim, S. H. (2013). Large eddy simulation of dilute reacting sprays: Droplet evaporation and scalar mixing. *Combustion and Flame*, 160(10):2048–2066.

De Paola, G., Kim, I. S., & Mastorakos, E. (2008a). Second-order conditional moment closure simulations of autoignition of an n-heptane plume in a turbulent coflow of heated air. *Flow, Turbulence and Combustion*, 82(4):455–475.

De Paola, G., Mastorakos, E., Wright, Y. M., & Boulouchos, K. (2008b). Diesel engine simulations with multi-dimensional conditional moment closure. *Combustion Science and Technology*, 180(5):883–899.

Deardorff, J. W. (1970). A numerical study of three-dimensional turbulent channel flow at large reynolds numbers. *Journal of Fluid Mechanics*, 41(2):453–480.

Demoulin, F. X. & Borghi, R. (2000). Assumed pdf modeling of turbulent spray combustion. *Combustion Science and Technology*, 158(1):249–271.

DesJardin, P. E. & Frankel, S. H. (1998). Large eddy simulation of a nonpremixed reacting jet: Application and assessment of subgrid-scale combustion models. *Physics of Fluids*, 10(9):2298–2314.

Devaud, C. B., Bilger, R. W., & Liu, T. (2004). A new method of modeling the conditional scalar dissipation rate. *Physics of Fluids*, 16(6):2004–2011.

Devaud, C. B. & Bray, K. N. C. (2003). Assessment of the applicability of conditional moment closure to a lifted turbulent flame: first order model. *Combustion and Flame*, 132(1):102–114.

Domingo, P., Vervisch, L., & Bray, K. N. C. (2002). Partially premixed flamelets in LES of nonpremixed turbulent combustion. *Combustion Theory and Modelling*, 6(4):529–551.

Domingo, P., Vervisch, L., & Réveillon, J. (2005). DNS analysis of partially premixed combustion in spray and gaseous turbulent flame-bases stabilized in hot air. *Combustion and Flame*, 140(3):172–195.

Donini, A., M. Bastiaans, R. J., van Oijen, J. A., & de Goey, L. P. H. (2017). A 5-D implementation of FGM for the large eddy simulation of a stratified swirled flame with heat loss in a gas turbine combustor. *Flow, Turbulence and Combustion*, 98(3):887–922.

Dopazo, C. & O'Brien, E. E. (1974). An approach to the autoignition of a turbulent mixture. *Acta Astronautica*, 1(9):1239–1266.

Dovizio, D., Debbagh, A., & Devaud, C. B. (2016). RANS simulations of a series of turbulent V-shaped flames using conditional source-term estimation. *Flow, Turbulence and Combustion*, 96(4):891–919.

Dovizio, D. & Devaud, C. B. (2016). Doubly conditional source-term estimation (DCSE) for the modelling of turbulent stratified V-shaped flame. *Combustion and Flame*, 172:79–93.

Dovizio, D., Labahn, J. W., & Devaud, C. B. (2015). Doubly conditional source-term estimation (DCSE) applied to a series of lifted turbulent jet flames in cold air. *Combustion and Flame*, 162(5):1976–1986.

Dunstan, T. D., Minamoto, Y., Chakraborty, N., & Swaminathan, N. (2013). Scalar dissipation rate modelling for large eddy simulation of turbulent premixed flames. *Proceedings of the Combustion Institute*, 34(1):1193–1201.

Echekki, T. & Mastorakos, E. (2011). Turbulent combustion: Concepts, governing equations and modeling strategies. In Echekki, T. & Mastorakos, E., editors, *Turbulent Combustion Modelling*, pages 19–39. Springer, Dordrecht, Heidelberg, London, New York.

Eckbreth, A. C. (1996). *Laser Diagnostics for Combustion Temperature and Species, Second Edition*. Gordon and Breach Publishers, Amsterdam.

El-Asrag, H. A., Braun, M., & Masri, A. R. (2016). Large eddy simulations of partially premixed ethanol dilute spray flames using the flamelet generated manifold model. *Combustion Theory and Modelling*, 20(4):567–591.

El-Asrag, H. A., Iannetti, A. C., & Apte, S. V. (2014). Large eddy simulations for radiation-spray coupling for a lean direct injector combustor. *Combustion and Flame*, 161(2):510–524.

El Tahry, S. H. (1983). $k$-$\varepsilon$ equation for compressible reciprocating engine flows. *Journal of Energy*, 7(4):345–353.

Elghobashi, S. (1994). On predicting particle-laden turbulent flows. *Applied Scientific Research*, 52(4):309–329.

Ern, A. & Giovangigli, V. (1994). *Multicomponent Transport Algorithms*, volume 24. Springer Verlag, Heidelberg Berlin.

Faeth, G. M. (1979). Current status of droplet and liquid combustion. In Chigier, N. A., editor, *Energy and Combustion Science*, pages 149–182. Pergamon.

Fairweather, M. & Woolley, R. M. (2004). First-order conditional moment closure modeling of turbulent, nonpremixed methane flames. *Combustion and Flame*, 138(1):3–19.

Fairweather, M. & Woolley, R. M. (2007a). Conditional moment closure calculations of a swirl-stabilized, turbulent nonpremixed methane flame. *Combustion and Flame*, 151(3):397–411.

Fairweather, M. & Woolley, R. M. (2007b). First- and second-order elliptic conditional moment closure calculations of piloted methane diffusion flames. *Combustion and Flame*, 150(1):92–107.

Farrace, D., Chung, K., Bolla, M., Wright, Y. M., Boulouchos, K., & Mastorakos, E. (2018). A LES-CMC formulation for premixed flames including differential diffusion. *Combustion Theory and Modelling*, 22(3):411–431.

Farrace, D., Chung, K., Pandurangi, S. S., Wright, Y. M., Boulouchos, K., & Swaminathan, N. (2017). Unstructured LES-CMC modelling of turbulent premixed bluff body flames close to blow-off. *Proceedings of the Combustion Institute*, 36(2):1977–1985.

Favre, A. (1969). Statistical equations of turbulent gases. In *Problems of Hydrodynamics and Continuum Mechanics*, pages 231–266. Society for Industrial and Applied Matematics, Philadelphia, PA.

Ferziger, J. H. & Perić, M. (2002). *Computational Methods for Fluid Dynamics, 3rd Edition*. Springer-Verlag, Berlin Heidelberg New York.

Frössling, N. (1938). Über die Verdunstung fallender Tropfen. *Gerlands Beiträge zur Geophysik*, 52:170–216.

Fureby, C. (1996). On subgrid scale modeling in large eddy simulations of compressible fluid flow. *Physics of Fluids*, 8(5):1301–1311.

Garmory, A. & Mastorakos, E. (2011). Capturing localised extinction in Sandia Flame F with LES-CMC. *Proceedings of the Combustion Institute*, 33(1):1673–1680.

Garmory, A. & Mastorakos, E. (2015). Numerical simulation of oxy-fuel jet flames using unstructured LES-CMC. *Proceedings of the Combustion Institute*, 35(2):1207–1214.

Ge, H.-W. & Gutheil, E. (2008). Simulation of a turbulent spray flame using coupled PDF gas phase and spray flamelet modeling. *Combustion and Flame*, 153(1–2):173–185.

Germano, M., Piomelli, U., Moin, P., & Cabot, W. H. (1991). A dynamic subgrid-scale eddy viscosity model. *Physics of Fluids A: Fluid Dynamics*, 3(7):1760–1765.

Girimaji, S. S. (1991). Assumed $\beta$-pdf model for turbulent mixing: Validation and extension to multiple scalar mixing. *Combustion Science and Technology*, 78(4–6):177–196.

Girimaji, S. S. (1992a). A mapping closure for turbulent scalar mixing using a time-evolving reference field. *Physics of Fluids A: Fluid Dynamics*, 4(12):2875–2886.

Girimaji, S. S. (1992b). On the modeling of scalar diffusion in isotropic turbulence. *Physics of Fluids A: Fluid Dynamics*, 4(11):2529–2537.

Giusti, A., Kotzagianni, M., & Mastorakos, E. (2016). LES/CMC simulations of swirl-stabilised ethanol spray flames approaching blow-off. *Flow, Turbulence and Combustion*, 97(4):1165–1184.

Giusti, A. & Mastorakos, E. (2016). Numerical investigation into the blow-off behaviour of swirling spray flames using the LES/CMC approach. *11th International ERCOFTAC Symposium on Engineering Turbulence Modelling and Measurements, 21–23 September 2016, Palermo, Italy.*

Giusti, A. & Mastorakos, E. (2017). Detailed chemistry LES/CMC simulation of a swirling ethanol spray flame approaching blow-off. *Proceedings of the Combustion Institute*, 36(2):2625–2632.

Givi, P. (1989). Model-free simulations of turbulent reactive flows. *Progress in Energy and Combustion Science*, 15(1):1–107.

Gosman, A. D. & Ioannides, E. (1983). Aspects of computer simulation of liquid-fueled combustors. *Journal of Energy*, 7(6):482–490.

Green, D. W. & Perry, R. H. (2008). *Perry's Chemical Engineering Handbook, 8th Edition.* McGraw-Hill, New York.

Grimmett, G. & Stirzaker, D. (2001). *Probability and Random Processes, Third Edition.* Oxford University Press, Oxford.

Gutheil, E. (2011). Issues in computational studies of turbulent spray combustion. In Merci, B., Roekaerts, D., & Sadiki, A., editors, *Experiments and Numerical Simulations of Dilute Spray Turbulent Combustion*, pages 1–40. Springer, Dordrecht.

Hawkes, E. R. & Cant, R. S. (2000). A flame surface density approach to large-eddy simulation of premixed turbulent combustion. *Proceedings of the Combustion Institute*, 28(1):51–58.

Hayashi, S., Kumagai, S., & Sakai, T. (1977). Propagation velocity and structure of flames in droplet-vapor-air mixtures. *Combustion Science and Technology*, 15(5–6):169–177.

Hayashi, S. & Mizobuchi, Y. (2011). Future directions. In Swaminathan, N. & Bray, K. N. C., editors, *Turbulent Premixed Flames*, pages 365–406. Cambridge University Press, Cambridge.

Heye, C., Raman, V., & Masri, A. R. (2013). LES/probability density function approach for the simulation of an ethanol spray flame. *Proceedings of the Combustion Institute*, 34(1):1633–1641.

Hollmann, C. & Gutheil, E. (1996). Modeling of turbulent spray diffusion flames including detailed chemistry. *Symposium (International) on Combustion*, 26(1):1731–1738.

Hollmann, C. & Gutheil, E. (1998). Diffusion flames based on a laminar spray flame library. *Combustion Science and Technology*, 135(1–6):175–192.

Holzmann, T. (2018). Mathematics, numerics, derivations and OpenFOAM. http://voluntary.holzmann-cfd.de/publications/mathematics-numerics-derivations-and-openfoam. Accessed 14 July 2018.

Hu, Y. & Kurose, R. (2018). Nonpremixed and premixed flamelets LES of partially premixed spray flames using a two-phase transport equation of progress variable. *Combustion and Flame*, 188:227–242.

IEA (2017). International Energy Agency, Key World Energy Statistics. https://webstore.iea.org/key-world-energy-statistics-2017. Accessed 20 June 2018.

Ihme, M. & Pitsch, H. (2008). Prediction of extinction and reignition in nonpremixed turbulent flames using a flamelet/progress variable model: 1. A priori study and presumed PDF closure. *Combustion and Flame*, 155(1):70–89.

Ihme, M. & See, Y. C. (2010). Prediction of autoignition in a lifted methane/air flame using an unsteady flamelet/progress variable model. *Combustion and Flame*, 157(10):1850–1862.

Irannejad, A., Banaeizadeh, A., & Jaberi, F. (2015). Large eddy simulation of turbulent spray combustion. *Combustion and Flame*, 162(2):431–450.

Ishihara, T., Morishita, K., Yokokawa, M., Uno, A., & Kaneda, Y. (2016). Energy spectrum in high-resolution direct numerical simulations of turbulence. *Physical Review Fluids*, 1:082403.

Issa, R. I. (1986). Solution of the implicitly discretised fluid flow equations by operator-splitting. *Journal of Computational Physics*, 62:40–65.

Jenny, P., Roekaerts, D., & Beishuizen, N. (2012). Modeling of turbulent dilute spray combustion. *Progress in Energy and Combustion Science*, 38(6):846–887.

Jiménez, C., Ducros, F., Cuenot, B., & Bédat, B. (2001). Subgrid scale variance and dissipation of a scalar field in large eddy simulations. *Physics of Fluids*, 13(6):1748–1754.

Jiménez, J., Liñán, A., Rogers, M. M., & Higuera, F. J. (1997). A priori testing of subgrid models for chemically reacting non-premixed turbulent shear flows. *Journal of Fluid Mechanics*, 349:149–171.

Jones, W. P. & Launder, B. E. (1972). The prediction of laminarization with a two-equation model of turbulence. *International Journal of Heat and Mass Transfer*, 15(2):301–314.

Jones, W. P., Lyra, S., & Navarro-Martinez, S. (2011). Large eddy simulation of a swirl stabilized spray flame. *Proceedings of the Combustion Institute*, 33(2):2153 – 2160.

Jones, W. P., Lyra, S., & Navarro-Martinez, S. (2012). Numerical investigation of swirling kerosene spray flames using large eddy simulation. *Combustion and Flame*, 159(4):1539–1561.

Kariuki, J. & Mastorakos, E. (2017). Experimental investigation of turbulent flames in uniform dispersions of ethanol droplets. *Combustion and Flame*, 179:95–116.

Kataoka, I. (1986). Local instant formulation of two-phase flow. *International Journal of Multiphase Flow*, 12(5):745–758.

Khan, N., Cleary, M. J., Stein, O. T., & Kronenburg, A. (2018). A two-phase MMC-LES model for turbulent spray flames. *Combustion and Flame*, 193:424–439.

Kim, I. S. & Mastorakos, E. (2005). Simulations of turbulent lifted jet flames with two-dimensional conditional moment closure. *Proceedings of the Combustion Institute*, 30(1):911–918.

Kim, S. H. (2002). On the conditional variance and covariance equations for second-order conditional moment closure. *Physics of Fluids*, 14(6):2011–2014.

Kim, S. H., Choi, C. H., & Huh, K. Y. (2005a). Second-order conditional moment closure modeling of a turbulent CH4/H2/N2 jet diffusion flame. *Proceedings of the Combustion Institute*, 30(1):735–742.

Kim, S. H. & Huh, K. Y. (2004). Second-order conditional moment closure modeling of turbulent piloted jet diffusion flames. *Combustion and Flame*, 138(4):336–352.

Kim, S. H., Huh, K. Y., & Bilger, R. W. (2002). Second-order conditional moment closure modeling of local extinction and reignition in turbulent non-premixed hydrocarbon flames. *Proceedings of the Combustion Institute*, 29(2):2131–2137.

Kim, S. H., Huh, K. Y., & Dally, B. (2005b). Conditional moment closure modeling of turbulent nonpremixed combustion in diluted hot coflow. *Proceedings of the Combustion Institute*, 30(1):751–757.

Kim, S. H., Huh, K. Y., & Tao, L. (2000). Application of the elliptic conditional moment closure model to a two-dimensional nonpremixed methanol bluff-body flame. *Combustion and Flame*, 120(1):75–90.

Kim, S. H. & Pitsch, H. (2005). Conditional filtering method for large-eddy simulation of turbulent nonpremixed combustion. *Physics of Fluids*, 17(10):105103.

Kim, S. H. & Pitsch, H. (2006). Mixing characteristics and structure of a turbulent jet diffusion flame stabilized on a bluff-body. *Physics of Fluids*, 18(7):075103.

Kim, W. T. & Huh, K. Y. (2002). Numerical simulation of spray autoignition by the first-order conditional moment closure model. *Proceedings of the Combustion Institute*, 29(1):569–576.

Kioni, P. N., Rogg, B., Bray, K. N. C., & Liñán, A. (1993). Flame spread in laminar mixing layers: The triple flame. *Combustion and Flame*, 95(3):276–290.

Klimenko, A. Y. (1990). Multicomponent diffusion of various admixtures in turbulent flow. *Fluid Dynamics*, 25(3):327–334.

Klimenko, A. Y. (1993). Conditional moment closure and large-scale fluctuations of scalar dissipation. *Fluid Dynamics*, 28(5):630–637.

Klimenko, A. Y. (2001). On the relation between the conditional moment closure and unsteady flamelets. *Combustion Theory and Modelling*, 5(3):275–294.

Klimenko, A. Y. & Abdel-Jawad, M. M. (2007). Conditional methods for continuum reacting flows in porous media. *Proceedings of the Combustion Institute*, 31(2):2107–2115.

Klimenko, A. Y. & Bilger, R. W. (1999). Conditional moment closure for turbulent combustion. *Progress in Energy and Combustion Science*, 25(6):595–687.

Klimenko, A. Y. & Pope, S. B. (2003). The modeling of turbulent reactive flows based on multiple mapping conditioning. *Physics of Fluids*, 15(7):1907–1925.

Knudsen, E. & Pitsch, H. (2009). A general flamelet transformation useful for distinguishing between premixed and non-premixed modes of combustion. *Combustion and Flame*, 156(3):678–696.

Knudsen, E. & Pitsch, H. (2012). Capabilities and limitations of multi-regime flamelet combustion models. *Combustion and Flame*, 159(1):242–264.

Kolla, H., Rogerson, J. W., Chakraborty, N., & Swaminathan, N. (2009). Scalar dissipation rate modeling and its validation. *Combustion Science and Technology*, 181(3):518–535.

Kolla, H. & Swaminathan, N. (2010a). Strained flamelets for turbulent premixed flames, I: Formulation and planar flame results. *Combustion and Flame*, 157(5):943–954.

Kolla, H. & Swaminathan, N. (2010b). Strained flamelets for turbulent premixed flames II: Laboratory flame results. *Combustion and Flame*, 157(7):1274–1289.

Kronenburg, A. (2004). Double conditioning of reactive scalar transport equations in turbulent nonpremixed flames. *Physics of Fluids*, 16(7):2640–2648.

Kronenburg, A. & Bilger, R. W. (1997). Modelling of differential diffusion effects in nonpremixed nonreacting turbulent flow. *Physics of Fluids*, 9(5):1435–1447.

Kronenburg, A., Bilger, R. W., & Kent, J. H. (1998). Second-order conditional moment closure for turbulent jet diffusion flames. *Symposium (International) on Combustion*, 27(1):1097–1104.

Kronenburg, A., Bilger, R. W., & Kent, J. H. (2000a). Computation of conditional average scalar dissipation in turbulent jet diffusion flames. *Flow, Turbulence and Combustion*, 64(3):145–159.

Kronenburg, A., Bilger, R. W., & Kent, J. H. (2000b). Modeling soot formation in turbulent methane-air jet diffusion flames. *Combustion and Flame*, 121(1):24–40.

Kronenburg, A. & Mastorakos, E. (2011). The Conditional Moment Closure Model. In Echekki, T. & Mastorakos, E., editors, *Turbulent Combustion Modelling*, pages 91–118. Springer, Dordrecht, Heidelberg, London, New York.

Kronenburg, A. & Papoutsakis, A. E. (2005). Conditional moment closure modeling of extinction and re-ignition in turbulent non-premixed flames. *Proceedings of the Combustion Institute*, 30(1):759–766.

Kronenburg, A. & Stein, O. T. (2017). LES-CMC of a partially premixed, turbulent dimethyl ether jet diffusion flame. *Flow, Turbulence and Combustion*, 98(3):803–816.

Kuznetsov, V. R. & Sabel'nikov, V. A. (1990). *Turbulence and Combustion*. Hemisphere Publishing, New York.

Langella, I. & Swaminathan, N. (2016). Unstrained and strained flamelets for LES of premixed combustion. *Combustion Theory and Modelling*, 20(3):410–440.

Langella, I., Swaminathan, N., Gao, Y., & Chakraborty, N. (2017). Large eddy simulation of premixed combustion: Sensitivity to subgrid scale velocity modeling. *Combustion Science and Technology*, 189(1):43–78.

Langmuir, I. (1918). The evaporation of small spheres. *Physical Review*, 12:368–370.

Launder, B. E. & Spalding, D. B. (1974). The numerical computation of turbulent flows. *Computer Methods in Applied Mechanics and Engineering*, 3(2):269–289.

Law, C. K. (1982). Recent advances in droplet vaporization and combustion. *Progress in Energy and Combustion Science*, 8(3):171–201.

Lefebvre, A. H. (1989). *Atomization and Sprays*. Hemisphere Pub. Corp., New York.

Lefebvre, A. H. & Ballal, D. R. (2010). *Gas Turbine Combustion, Third Edition*. CRC Press, Boca Raton, London, New York.

Li, J. D. & Bilger, R. W. (1993). Measurement and prediction of the conditional variance in a turbulent reactive scalar mixing layer. *Physics of Fluids A*, 5(12):3255–3264.

Li, J. D. & Bilger, R. W. (1994). A simple theory of conditional mean velocity in turbulent scalar mixing layer. *Physics of Fluids*, 6(2):605–610.

Lilly, D. K. (1967). The representation of small-scale turbulence in numerical simulation experiments. In *Proceedings of the IBM Scientific Computing Symposium on Environmental Sciences*, pages 195–210. 14–16 November 1966, Yorktown Heights, NY, USA.

Lin, S. P. & Reitz, R. D. (1998). Drop and spray formation from a liquid jet. *Annual Review of Fluid Mechanics*, 30(1):85–105.

Liu, F., Guo, H., Smallwood, G., Gülder, L., & Matovic, M. (2002). A robust and accurate algorithm of the $\beta$-pdf integration and its application to turbulent methane–air diffusion combustion in a gas turbine combustor simulator. *International Journal of Thermal Sciences*, 41(8):763–772.

Lu, T. & Law, C. K. (2009). Toward accommodating realistic fuel chemistry in large-scale computations. *Progress in Energy and Combustion Science*, 35(2):192–215.

Lyons, K. M. & Watson, K. A. (2000). Partially premixed combustion in lifted turbulent jets. *Combustion Science and Technology*, 156(1):97–105.

Ma, L., Naud, B., & Roekaerts, D. (2016). Transported PDF modeling of ethanol spray in hot-diluted coflow flame. *Flow, Turbulence and Combustion*, 96(2):469–502.

Ma, L. & Roekaerts, D. (2016a). Modeling of spray jet flame under MILD condition with non-adiabatic FGM and a new conditional droplet injection model. *Combustion and Flame*, 165:402–423.

Ma, L. & Roekaerts, D. (2016b). Structure of spray in hot-diluted coflow flames under different coflow conditions: A numerical study. *Combustion and Flame*, 172:20–37.

Ma, L. & Roekaerts, D. (2017). Numerical study of the multi-flame structure in spray combustion. *Proceedings of the Combustion Institute*, 36(2):2603–2613.

Mantel, T. & Bilger, R. W. (1995). Some conditional statistics in a turbulent premixed flame derived from direct numerical simulations. *Combustion Science and Technology*, 110–111(1):393–417.

Marinov, N. M. (1999). A detailed chemical kinetic model for high temperature ethanol oxidation. *International Journal of Chemical Kinetics*, 31(3):183–220.

Martin, S. M., Kramlich, J. C., Kosály, G., & Riley, J. J. (2003). The premixed conditional moment closure method applied to idealized lean premixed gas turbine combustors. *Journal of Engineering for Gas Turbines and Power*, 125(4):895–900.

Masri, A. R. (2015). Partial premixing and stratification in turbulent flames. *Proceedings of the Combustion Institute*, 35(2):1115–1136.

Masri, A. R. & Gounder, J. D. (2010). Turbulent spray flames of acetone and ethanol approaching extinction. *Combustion Science and Technology*, 182(4–6):702–715.

Mastorakos, E. (2017). Forced ignition of turbulent spray flames. *Proceedings of the Combustion Institute*, 36(2):2367–2383.

Mastorakos, E. & Bilger, R. W. (1998). Second-order conditional moment closure for the autoignition of turbulent flows. *Physics of Fluids*, 10(6):1246–1248.

Meneveau, C. & Katz, J. (2000). Scale-invariance and turbulence models for large-eddy simulation. *Annual Review of Fluid Mechanics*, 32:1–32.

Miller, R. S., Harstad, K., & Bellan, J. (1998). Evaluation of equilibrium and non-equilibrium evaporation models for many-droplet gas-liquid flow simulations. *International Journal of Multiphase Flow*, 24(6):1025–1055.

Mittal, V., Cook, D. J., & Pitsch, H. (2012). An extended multi-regime flamelet model for IC engines. *Combustion and Flame*, 159(8):2767–2776.

Mizobuchi, Y., Tachibana, S., Shinio, J., Ogawa, S., & Takeno, T. (2002). A numerical analysis of the structure of a turbulent hydrogen jet lifted flame. *Proceedings of the Combustion Institute*, 29(2):2009–2015.

Mortensen, M. (2004). Implementation of a conditional moment closure for mixing sensitive reactions. *Chemical Engineering Science*, 59(24):5709–5723.

Mortensen, M. & Andersson, B. (2006). Presumed mapping functions for Eulerian modelling of turbulent mixing. *Flow, Turbulence and Combustion*, 76(2):199–219.

Mortensen, M. & Bilger, R. W. (2009). Derivation of the conditional moment closure equations for spray combustion. *Combustion and Flame*, 156(1):62–72.

Mortensen, M. & de Bruyn Kops, S. M. (2008). Conditional velocity statistics in the double scalar mixing layer – a mapping closure approach. *Combustion Theory and Modelling*, 12(5):929–941.

Myers, G. D. & Lefebvre, A. H. (1986). Flame propagation in heterogeneous mixtures of fuel drops and air. *Combustion and Flame*, 66(2):193–210.

Navarro-Martinez, S. & Kronenburg, A. (2007). LES-CMC simulations of a turbulent bluff-body flame. *Proceedings of the Combustion Institute*, 31(2):1721–1728.

Navarro-Martinez, S. & Kronenburg, A. (2009). LES-CMC simulations of a lifted methane flame. *Proceedings of the Combustion Institute*, 32(1):1509–1516.

Navarro-Martinez, S. & Kronenburg, A. (2011). Flame stabilization mechanisms in lifted flames. *Flow, Turbulence and Combustion*, 87(2):377–406.

Navarro-Martinez, S., Kronenburg, A., & Di Mare, F. (2005). Conditional moment closure for large eddy simulations. *Flow, Turbulence and Combustion*, 75(1–4):245–274.

Neophytou, A. & Mastorakos, E. (2009). Simulations of laminar flame propagation in droplet mists. *Combustion and Flame*, 156(8):1627–1640.

Neophytou, A., Mastorakos, E., & Cant, R. S. (2012). The internal structure of igniting turbulent sprays as revealed by complex chemistry DNS. *Combustion and Flame*, 159(2):641–664.

Nguyen, P.-D., Vervisch, L., Subramanian, V., & Domingo, P. (2010). Multidimensional flamelet-generated manifolds for partially premixed combustion. *Combustion and Flame*, 157(1):43–61.

Noh, D., Gallot-Lavallée, S., Jones, W. P., & Navarro-Martinez, S. (2018). Comparison of droplet evaporation models for a turbulent, non-swirling jet flame with a polydisperse droplet distribution. *Combustion and Flame*, 194:135–151.

Nomura, H., Koyama, M., Miyamoto, H., Ujiie, Y., Sato, J., Kono, M., & Yoda, S. (2000). Microgravity experiments of flame propagation in ethanol droplet-vapor-air mixture. *Proceedings of the Combustion Institute*, 28(1):999 – 1005.

O'Brien, E. E. (1980). The probability density function (pdf) approach to reacting turbulent flows. In Libby, P. A. & Williams, F. A., editors, *Turbulent Reacting Flows*, pages 185–218. Springer, Berlin, Heidelberg.

O'Brien, E. E. & Jiang, T. (1991). The conditional dissipation rate of an initially binary scalar in homogeneous turbulence. *Physics of Fluids A: Fluid Dynamics*, 3(12):3121–3123.

OpenFOAM (2014). The OpenFOAM Foundation Ltd., OpenFOAM-2.3.1. https://openfoam.org/. Accessed 20 June 2018.

Patankar, S. V. (1980). *Numerical Heat Transfer and Fluid Flow*. Hemisphere Publishing Corporation, New York.

Pei, Y., Hawkes, E. R., & Kook, S. (2013). Transported probability density function modelling of the vapour phase of an n-heptane jet at diesel engine conditions. *Proceedings of the Combustion Institute*, 34(2):3039–3047.

Pei, Y., Hawkes, E. R., Kook, S., Goldin, G. M., & Lu, T. (2015). Modelling n-dodecane spray and combustion with the transported probability density function method. *Combustion and Flame*, 162(5):2006–2019.

Pera, C., Réveillon, J., Vervisch, L., & Domingo, P. (2006). Modeling subgrid scale mixture fraction variance in LES of evaporating spray. *Combustion and Flame*, 146(4):635–648.

Perini, F. (2013). The SpeedCHEM project. http://www.federicoperini.info/speedchem. Accessed 20 June 2018.

Peters, N. (1984). Laminar diffusion flamelet models in non-premixed turbulent combustion. *Progress in Energy and Combustion Science*, 10(3):319–339.

Peters, N. (1988). Laminar flamelet concepts in turbulent combustion. *Symposium (International) on Combustion*, 21(1):1231–1250.

Peters, N. (2000). *Turbulent Combustion*. Cambridge University Press, Cambridge.

Pierce, C. D. & Moin, P. (1998). A dynamic model for subgrid-scale variance and dissipation rate of a conserved scalar. *Physics of Fluids*, 10(12):3041–3044.

Pierce, C. D. & Moin, P. (2004). Progress-variable approach for large-eddy simulation of non-premixed turbulent combustion. *Journal of Fluid Mechanics*, 504:73–97.

Pitsch, H. (2006). Large-eddy simulation of turbulent combustion. *Annual Review of Fluid Mechanics*, 38(1):453–482.

Pitsch, H. & Steiner, H. (2000). Large-eddy simulation of a turbulent piloted methane/air diffusion flame (Sandia flame D). *Physics of Fluids*, 12(10):2541–2554.

Poinsot, T. & Veynante, D. (2005). *Theoretical and Numerical Combustion, Second Edition*. R. T. Edwards, Inc., Philadelphia.

Poinsot, T., Veynante, D., & Candel, S. (1991). Diagrams of premixed turbulent combustion based on direct simulation. *Symposium (International) on Combustion*, 23(1):613–619.

Polymeropoulos, C. E. & Das, S. (1975). The effect of droplet size on the burning velocity of kerosene-air sprays. *Combustion and Flame*, 25:247–257.

Pope, S. B. (1976). The probability approach to the modelling of turbulent reacting flows. *Combustion and Flame*, 27:299–312.

Pope, S. B. (1985). PDF methods for turbulent reactive flows. *Progress in Energy and Combustion Science*, 11(2):119–192.

Pope, S. B. (1991). Computations of turbulent combustion: Progress and challenges. *Symposium (International) on Combustion*, 23(1):591–612.

Pope, S. B. (2000). *Turbulent Flows*. Cambridge University Press.

Popp, S., Hunger, F., Hartl, S., Messig, D., Coriton, B., Frank, J. H., Fuest, F., & Hasse, C. (2015). LES flamelet-progress variable modeling and measurements of a turbulent partially-premixed dimethyl ether jet flame. *Combustion and Flame*, 162(8):3016–3029.

Prasad, V. N., Masri, A. R., Navarro-Martinez, S., & Luo, K. H. (2013). Investigation of auto-ignition in turbulent methanol spray flames using Large Eddy Simulation. *Combustion and Flame*, 160(12):2941–2954.

Press, W. H., Teukolsky, S. A., Vetterling, W. T., & Flannery, B. P. (1992). *Numerical Recipes in Fortran 77, Second Edition*. Cambridge University Press.

Réveillon, J. & Demoulin, F. X. (2007). Evaporating droplets in turbulent reacting flows. *Proceedings of the Combustion Institute*, 31(2):2319–2326.

Réveillon, J. & Vervisch, L. (2005). Analysis of weakly turbulent dilute-spray flames and spray combustion regimes. *Journal of Fluid Mechanics*, 537:317–347.

Reynolds, O. (1895). IV. On the dynamical theory of incompressible viscous fluids and the determination of the criterion. *Philosophical Transactions of the Royal Society of London. (A.)*, 186:123–164.

Richardson, E. S., Chakraborty, N., & Mastorakos, E. (2007). Analysis of direct numerical simulations of ignition fronts in turbulent non-premixed flames in the context of conditional moment closure. *Proceedings of the Combustion Institute*, 31(1):1683–1690.

Rittler, A., Proch, F., & Kempf, A. M. (2015). LES of the sydney piloted spray flame series with the PFGM/ATF approach and different sub-filter models. *Combustion and Flame*, 162(4):1575–1598.

Roomina, M. R. & Bilger, R. W. (1999). Conditional moment closure modelling of turbulent methanol jet flames. *Combustion Theory and Modelling*, 3(4):689–708.

Roomina, M. R. & Bilger, R. W. (2001). Conditional moment closure (CMC) predictions of a turbulent methane-air jet flame. *Combustion and Flame*, 125(3):1176–1195.

Rotexo GmbH und Co. KG (2012). Cosilab Collection, Version 3.3.2. http://rotexo.com. Accessed 20 June 2018.

Ruan, S., Swaminathan, N., Bray, K. N. C., Mizobuchi, Y., & Takeno, T. (2012). Scalar and its dissipation in the near field of turbulent lifted jet flame. *Combustion and Flame*, 159(2):591–608.

Ruan, S., Swaminathan, N., & Darbyshire, O. (2014). Modelling of turbulent lifted jet flames using flamelets: a priori assessment and a posteriori validation. *Combustion Theory and Modelling*, 18(2):295–329.

Sacomano Filho, F. L., Chrigui, M., Sadiki, A., & Janicka, J. (2014). LES-based numerical analysis of droplet vaporization process in lean partially premixed turbulent spray flames. *Combustion Science and Technology*, 186(4–5):435–452.

Sacomano Filho, F. L., Kuenne, G., Chrigui, M., Sadiki, A., & Janicka, J. (2017). A consistent artificially thickened flame approach for spray combustion using LES and the FGM chemistry reduction method: Validation in lean partially pre-vaporized flames. *Combustion and Flame*, 184:68–89.

Salehi, F., Talei, M., Hawkes, E. R., Bhagatwala, A., Chen, J. H., Yoo, C. S., & Kook, S. (2017). Doubly conditional moment closure modelling for HCCI with temperature inhomogeneities. *Proceedings of the Combustion Institute*, 36(3):3677–3685.

Salehi, M. M. & Bushe, W. K. (2010). Presumed PDF modeling for RANS simulation of turbulent premixed flames. *Combustion Theory and Modelling*, 14(3):381–403.

Sazhin, S. S. (2006). Advanced models of fuel droplet heating and evaporation. *Progress in Energy and Combustion Science*, 32(2):162–214.

Schiller, L. & Naumann, A. Z. (1933). Über die grundlegende Berechnung bei der Schwerkraftaufbereitung. *Zeitschift des Vereins Deutscher Ingenieure*, 77:318–320.

Schroll, P., Mastorakos, E., & Bilger, R. W. (2010). Simulations of spark ignition of a swirling n-heptane spray flame with conditional moment closure. *48th AIAA Aerospace Science Meeting, 4–7 January 2010, Orlando, Florida.*

Schumann, U. (1989). Large-eddy simulation of turbulent diffusion with chemical reactions in the convective boundary layer. *Atmospheric Environment*, 23(8):1713–1727.

Schwer, D. A., Lu, P., Green Jr., W. H., & Semião, V. (2003). A consistent-splitting approach to computing stiff steady-state reacting flows with adaptive chemistry. *Combustion Theory and Modelling*, 7(2):383–399.

Shum-Kivan, F., Marrero Santiago, J., Verdier, A., Riber, E., Renou, B., Cabot, G., & Cuenot, B. (2017). Experimental and numerical analysis of a turbulent spray flame structure. *Proceedings of the Combustion Institute*, 36(2):2567–2575.

Silverman, I., Greenberg, J. B., & Tambour, Y. (1993). Stoichiometry and polydisperse effects in premixed spray flames. *Combustion and Flame*, 93(1):97–118.

Sirignano, W. A. (1983). Fuel droplet vaporization and spray combustion theory. *Progress in Energy and Combustion Science*, 9(4):291–322.

Sitte, M. P. & Mastorakos, E. (2017). Modelling of spray flames with doubly conditional moment closure. *Flow, Turbulence and Combustion*, 99(3):933–954.

Sitte, M. P. & Mastorakos, E. (2019). Large eddy simulation of a spray jet flame using doubly conditional moment closure. *Combustion and Flame*, 199:309–323.

Smagorinsky, J. (1963). General circulation experiments with primitive equations. *Monthly Weather Review*, 91(3):99–164.

Smallbone, A. J., Liu, W., Law, C. K., You, X. Q., & Wang, H. (2009). Experimental and modeling study of laminar flame speed and non-premixed counterflow ignition of n-heptane. *Proceedings of the Combustion Institute*, 32(1):1245–1252.

Smith, N. S. A., Bilger, R. W., & Chen, J.-Y. (1992). Modelling of nonpremixed hydrogen jet flames using a conditional moment closure method. *Symposium (International) on Combustion*, 24(1):263–269.

Spalding, D. B. (1955). *Fundamentals of Combustion*. Butterworths Scientific, London.

Sreedhara, S. & Huh, K. Y. (2005). Modeling of turbulent, two-dimensional non-premixed CH4/H2 flame over a bluffbody using first- and second-order elliptic conditional moment closures. *Combustion and Flame*, 143(1):119–134.

Sreedhara, S. & Huh, K. Y. (2007). Conditional statistics of nonreacting and reacting sprays in turbulent flows by direct numerical simulation. *Proceedings of the Combustion Institute*, 31(2):2335–2342.

Sreedhara, S., Lee, Y., Huh, K. Y., & Ahn, D. H. (2008). Comparison of submodels for conditional velocity and scalar dissipation in CMC simulation of piloted jet and bluff-body flames. *Combustion and Flame*, 152(1–2):282–286.

Sreznevsky, B. I. (1882). Ob isparenii zhidkostey [On the evaporation of liquids]. *Zhurnal Russkogo Physico-khimicheskogo obshchestva, Chast'physicheskaya, Sankt-Peterburg*, 14:390–391.

Stanković, I., Mastorakos, E., & Merci, B. (2013). LES-CMC simulations of different auto-ignition regimes of hydrogen in a hot turbulent air co-flow. *Flow, Turbulence and Combustion*, 90(3):583–604.

Swaminathan, N. & Bilger, R. W. (1998). Conditional variance equation and its analysis. *Symposium (International) on Combustion*, 27(1):1191–1198.

Swaminathan, N. & Bilger, R. W. (1999a). Assessment of combustion submodels for turbulent nonpremixed hydrocarbon flames. *Combustion and Flame*, 116(4):519–545.

Swaminathan, N. & Bilger, R. W. (1999b). Study of the conditional covariance and variance equations for second order conditional moment closure. *Physics of Fluids*, 11(9):2679–2695.

Swaminathan, N. & Bilger, R. W. (2001). Analyses of conditional moment closure for turbulent premixed flames. *Combustion Theory and Modelling*, 5(2):241–260.

Swaminathan, N. & Bray, K. N. C. (2005). Effect of dilatation on scalar dissipation in turbulent premixed flames. *Combustion and Flame*, 143(4):549–565.

Swaminathan, N. & Bray, K. N. C. (2011). Fundamentals and challenges. In Swaminathan, N. & Bray, K. N. C., editors, *Turbulent Premixed Flames*, pages 1–40. Cambridge University Press, Cambridge.

Tennekes, H. & Lumley, J. L. (1972). *A First Course in Turbulence*. MIT Press, Cambridge, Massachusetts.

Thornber, B., Bilger, R. W., Masri, A. R., & Hawkes, E. R. (2011). An algorithm for LES of premixed compressible flows using the conditional moment closure model. *Journal of Computational Physics*, 230(20):7687–7705.

Tian, L. & Lindstedt, R. P. (2019). Evaluation of reaction progress variable – mixture fraction statistics in partially premixed flames. *Proceedings of the Combustion Institute*, 37(2):2241–2248.

Triantafyllidis, A., Mastorakos, E., & Eggels, R. L. G. M. (2009). Large eddy simulations of forced ignition of a non-premixed bluff-body methane flame with conditional moment closure. *Combustion and Flame*, 156(12):2328–2345.

Tsui, H. P. & Bushe, W. K. (2014). Linear-eddy model formulated probability density function and scalar dissipation rate models for premixed combustion. *Flow, Turbulence and Combustion*, 93(3):487–503.

Tyliszczak, A. (2015). LES-CMC study of an excited hydrogen flame. *Combustion and Flame*, 162(10):3864–3883.

Tyliszczak, A., Cavaliere, D. E., & Mastorakos, E. (2014). LES/CMC of blow-off in a liquid fueled swirl burner. *Flow, Turbulence and Combustion*, 92(1–2):237–267.

Tyliszczak, A. & Mastorakos, E. (2013). LES/CMC predictions of spark ignition probability in a liquid fuelled swirl combustor. *51st AIAA Aerospace Science Meeting, 7–10 January 2013, Grapevine, Texas*.

Ukai, S., Kronenburg, A., & Stein, O. T. (2013). LES-CMC of a dilute acetone spray flame. *Proceedings of the Combustion Institute*, 34(1):1643–1650.

Ukai, S., Kronenburg, A., & Stein, O. T. (2014). Simulation of dilute acetone spray flames with LES–CMC using two conditional moments. *Flow, Turbulence and Combustion*, 93(3):405–423.

Ukai, S., Kronenburg, A., & Stein, O. T. (2015). Large eddy simulation of dilute acetone spray flames using CMC coupled with tabulated chemistry. *Proceedings of the Combustion Institute*, 35(2):1667–1674.

Valiño, L. (1998). A field Monte Carlo formulation for calculating the probability density function of a single scalar in a turbulent flow. *Flow, Turbulence and Combustion*, 60(2):157–172.

van Oijen, J. A. & de Goey, L. P. H. (2000). Modelling of premixed laminar flames using flamelet-generated manifolds. *Combustion Science and Technology*, 161(1):113–137.

van Oijen, J. A. & de Goey, L. P. H. (2004). A numerical study of confined triple flames using a flamelet-generated manifold. *Combustion Theory and Modelling*, 8(1):141–163.

Verdier, A., Marrero Santiago, J., Vandel, A., Godard, G., Cabot, G., & Renou, B. (2018). Local extinction mechanisms analysis of spray jet flame using high speed diagnostics. *Combustion and Flame*, 193:440–452.

Verdier, A., Marrero Santiago, J., Vandel, A., Saengkaew, S., Cabot, G., Grehan, G., & Renou, B. (2017). Experimental study of local flame structures and fuel droplet properties of a spray jet flame. *Proceedings of the Combustion Institute*, 36(2):2595–2602.

Vikhansky, A. & Cox, S. M. (2007). Conditional moment closure for chemical reactions in laminar chaotic flows. *AIChE Journal*, 53(1):19–27.

Wacks, D., Konstantinou, I., & Chakraborty, N. (2018). Effects of Lewis number on the statistics of the invariants of the velocity gradient tensor and local flow topologies in turbulent premixed flames. *Proceedings of the Royal Society of London A*, 474(2212).

Wacks, D. H. & Chakraborty, N. (2016a). Flame structure and propagation in turbulent flame-droplet interaction: A direct numerical simulation analysis. *Flow, Turbulence and Combustion*, 96(4):1053–1081.

Wacks, D. H. & Chakraborty, N. (2016b). Statistical analysis of the reaction progress variable and mixture fraction gradients in flames propagating into droplet mist: A direct numerical simulation analysis. *Combustion Science and Technology*, 188(11-12):2149–2177.

Wacks, D. H., Chakraborty, N., & Mastorakos, E. (2016). Statistical analysis of turbulent flame-droplet interaction: A direct numerical simulation study. *Flow, Turbulence and Combustion*, 96(2):573–607.

Wang, H., Hawkes, E. R., Savard, B., & Chen, J. H. (2018). Direct numerical simulation of a high ka $CH_4$/air stratified premixed jet flame. *Combustion and Flame*, 193:229–245.

Williams, A. (1973). Combustion of droplets of liquid fuels: A review. *Combustion and Flame*, 21(1):1–31.

Williams, F. A. (1985a). 3. Turbulent Combustion. In Buckmaster, J. D., editor, *The Mathematics of Combustion*, pages 97–131. Society for Industrial and Applied Matematics, Philadelphia, PA.

Williams, F. A. (1985b). *Combustion Theory, Second Edition*. CRC Press, Boca Raton.

Wright, Y. M., De Paola, G., Boulouchos, K., & Mastorakos, E. (2005). Simulations of spray autoignition and flame establishment with two-dimensional CMC. *Combustion and Flame*, 143(4):402–419.

Yamashita, H., Shimada, M., & Takeno, T. (1996). A numerical study on flame stability at the transition point of jet diffusion flames. *Symposium (International) on Combustion*, 26(1):27–34.

Yoshizawa, A. & Horiuti, K. (1985). A statistically-derived subgrid-scale kinetic energy model for the large-eddy simulation of turbulent flows. *Journal of the Physical Society of Japan*, 54(8):2834–2839.

Yuan, R., Kariuki, J., & Mastorakos, E. (2018). Measurements in swirling spray flames at blow-off. *International Journal of Spray and Combustion Dynamics*, 10(3):185–210.

Zhang, H. (2015). *Extinction in Turbulent Swirling Non-premixed Flames*. PhD thesis, University of Cambridge.

Zhang, H., Garmory, A., Cavaliere, D. E., & Mastorakos, E. (2015). Large eddy simulation/conditional moment closure modeling of swirl-stabilized non-premixed flames with local extinction. *Proceedings of the Combustion Institute*, 35(2):1167–1174.

Zhang, H., Giusti, A., & Mastorakos, E. (2019). LES/CMC modelling of ignition and flame propagation in a non-premixed methane jet. *Proceedings of the Combustion Institute*, 37(2):2125–2132.

Zhang, H. & Mastorakos, E. (2016). Prediction of global extinction conditions and dynamics in swirling non-premixed flames using LES/CMC modelling. *Flow, Turbulence and Combustion*, 96(4):863–889.

Zhang, H. & Mastorakos, E. (2017). Modelling local extinction in Sydney swirling non-premixed flames with LES/CMC. *Proceedings of the Combustion Institute*, 36(2):1669–1676.

Zhu, M., Bray, K. N. C., Rumberg, O., & Rogg, B. (2000). PDF transport equations for two-phase reactive flows and sprays. *Combustion and Flame*, 122(3):327–338.

# Appendix A

# Derivation of LES-DCMC

## A.1 Introduction

For completeness, this Appendix contains additional comments and definitions required for the derivation of the DCMC equation in the LES framework. The derivation of LES-DCMC is based on the definition of the conditional filter [Bushe & Steiner, 1999]. In the present doubly-conditional case, the conditionally filtered value of an arbitrary flow variable $F$ is defined as

$$\langle F(\mathbf{x},t)|\eta,\zeta\rangle = \frac{\int_V F(\mathbf{x}',t)\ \delta(\eta-\xi(\mathbf{x}',t))\ \delta(\zeta-c(\mathbf{x}',t))\ G(\mathbf{x}-\mathbf{x}')\ \mathrm{d}V'}{p(\eta,\zeta;\mathbf{x},t)} \tag{A.1}$$

where $G$ is the LES-filter and $p(\eta,\zeta;\mathbf{x},t)$ is the filtered density function (FDF). In the conditional filtering procedure the fine-grained PDF occurs, which is defined as

$$\Psi(\eta,\zeta;\mathbf{x},t) \equiv \delta(\eta-\xi(\mathbf{x},t))\ \delta(\zeta-c(\mathbf{x},t)) \tag{A.2}$$

In the LES-framework the FDF takes the role of a spatially filtered PDF. The FDF was first defined by Pope [1991]. In the present doubly-conditional case, the FDF is defined as

$$p(\eta,\zeta;\mathbf{x},t) = \int_V \Psi(\eta,\zeta;\mathbf{x}',t)\ G(\mathbf{x}-\mathbf{x}')\ \mathrm{d}V' \tag{A.3}$$

## A.2 Derivation

First, phase-weighted and density-weighted filtering are introduced. The conditional filter which considers volume elements in both phases is defined as

$$\overline{\overline{\langle F(\mathbf{x},t)|\eta,\zeta\rangle}} = \frac{\int_V F(\mathbf{x}',t)\ \Psi(\eta,\zeta;\mathbf{x}',t)\ G(\mathbf{x}-\mathbf{x}')\ \mathrm{d}V'}{\overline{\overline{p}}(\eta,\zeta;\mathbf{x},t)} \tag{A.4}$$

where $\overline{\overline{p}}$ is the corresponding FDF, which considers volume elements in both phases. It is defined as

$$\overline{\overline{p}}(\eta,\zeta;\mathbf{x},t) = \int_V \Psi(\eta,\zeta;\mathbf{x}',t)\ G(\mathbf{x}-\mathbf{x}')\ \mathrm{d}V' \tag{A.5}$$

The conditional filter which only considers volume elements in the gaseous phase is defined as

$$\overline{\langle F(\mathbf{x},t)|\eta,\zeta\rangle} = \frac{\int_V \theta(\mathbf{x}',t)\ F(\mathbf{x}',t)\ \Psi(\eta,\zeta;\mathbf{x}',t)\ G(\mathbf{x}-\mathbf{x}')\ \mathrm{d}V'}{\overline{\overline{\langle\theta(\mathbf{x},t)|\eta,\zeta\rangle}}\ \overline{\overline{p}}(\eta,\zeta;\mathbf{x},t)} \tag{A.6}$$

where $\overline{\overline{\langle\theta(\mathbf{x},t)|\eta,\zeta\rangle}}$ is the conditionally filtered phase-indicator function.

The density-weighted filter of the gaseous phase (only considering volume elements in the gas phase) is defined as

$$\widetilde{\langle F(\mathbf{x},t)|\eta,\zeta\rangle} = \frac{\int_V \theta(\mathbf{x}',t)\ \rho(\mathbf{x}',t)\ F(\mathbf{x}',t)\ \Psi(\eta,\zeta;\mathbf{x}',t)\ G(\mathbf{x}-\mathbf{x}')\ \mathrm{d}V'}{\overline{\overline{\langle\theta(\mathbf{x},t)|\eta,\zeta\rangle}}\ \overline{\langle\rho(\mathbf{x},t)|\eta,\zeta\rangle}\ \overline{\overline{p}}(\eta,\zeta;\mathbf{x},t)} \tag{A.7}$$

The FDF of the gas phase is defined as

$$\bar{p}(\eta,\zeta;\mathbf{x},t) = \frac{\overline{\overline{\langle\theta(\mathbf{x},t)|\eta,\zeta\rangle}}\ \overline{\overline{p}}(\eta,\zeta;\mathbf{x},t)}{\overline{\overline{\theta}}(\mathbf{x},t)} \tag{A.8}$$

The density-weighted FDF of the gas phase is defined as

$$\tilde{p}(\eta,\zeta;\mathbf{x},t) = \frac{\bar{p}(\eta,\zeta;\mathbf{x},t)\ \overline{\langle\rho(\mathbf{x},t)|\eta,\zeta\rangle}}{\bar{\rho}(\mathbf{x},t)} \tag{A.9}$$

Applying the filter (over all phases) to the fine-grained PDF leads to the following result. First the definitions of the phase-weighted and density-weighted filtering were applied. Then the definition of the density-weighted FDF of the gas phase was used to re-arrange the result.

$$\int_V \theta\rho F\Psi G\ \mathrm{d}V' = \overline{\overline{\langle\theta|\eta,\zeta\rangle}}\ \overline{\langle\rho|\eta,\zeta\rangle}\ \widetilde{\langle F|\eta,\zeta\rangle}\ \overline{\overline{p}} = \overline{\overline{\theta}}\bar{\rho}\widetilde{\langle F|\eta,\zeta\rangle}\tilde{p} \tag{A.10}$$

The DCMC equation is derived starting form the transport equation of the fine-grained PDF (Eqn. 3.31) and Eqn. 3.38. The LES-filter is applied, i.e. the equations are multiplied with $G$ and volume-integrated. If the filter width $\Delta$ is constant in time and independent of space, the filter commutes with differentiation in time and space. The filter is independent of $\eta$ and $\zeta$ and thus commutes with the differentiation in conditional space. This leads to the following equations.

$$\begin{aligned}\frac{\partial \int_V \theta\rho\Psi G \,\mathrm{d}V'}{\partial t} + \nabla\cdot(\int_V \theta\rho\mathbf{u}\Psi G \,\mathrm{d}V') = \\ - \nabla\cdot\left(\frac{\partial}{\partial\eta}(\int_V \Psi G\theta\rho D\nabla\xi \,\mathrm{d}V')\right) - \nabla\cdot\left(\frac{\partial}{\partial\zeta}(\int_V \Psi G\theta\rho D\nabla c \,\mathrm{d}V')\right) \\ - \frac{\partial^2}{\partial\eta^2}(\int_V \Psi G\theta\rho N_\xi \,\mathrm{d}V') - \frac{\partial^2}{\partial\zeta^2}(\int_V \Psi G\theta\rho N_c \,\mathrm{d}V') \\ - 2\frac{\partial^2}{\partial\eta\partial\zeta}(\int_V \Psi G\theta\rho N_{\xi c} \,\mathrm{d}V') - \frac{\partial}{\partial\zeta}(\int_V \Psi G\theta\rho\dot{\omega}_c^* \,\mathrm{d}V') \\ - \frac{\partial}{\partial\eta}(\int_V \Psi G\rho S_\xi^- \,\mathrm{d}V') - \frac{\partial}{\partial\zeta}(\int_V \Psi G\rho S_c^- \,\mathrm{d}V') + \int_V \Psi G\rho\Pi\end{aligned} \tag{A.11}$$

$$\begin{aligned}\frac{\partial \int_V \theta\rho Y_\alpha\Psi G \,\mathrm{d}V'}{\partial t} + \nabla\cdot(\int_V \theta\rho\mathbf{u}Y_\alpha\Psi G \,\mathrm{d}V') = \nabla\cdot(\int_V \Psi G\theta\rho D_\alpha\nabla Y_\alpha \,\mathrm{d}V') \\ - \nabla\cdot\left(\frac{\partial}{\partial\eta}(\int_V \Psi G\theta\rho Y_\alpha D\nabla\xi \,\mathrm{d}V')\right) - \nabla\cdot\left(\frac{\partial}{\partial\zeta}(\int_V \Psi G\theta\rho Y_\alpha D\nabla c \,\mathrm{d}V')\right) \\ + \frac{\partial}{\partial\eta}(\int_V \Psi G\theta\rho(D+D_\alpha)\nabla\xi\cdot\nabla Y_\alpha \,\mathrm{d}V') \\ + \frac{\partial}{\partial\zeta}(\int_V \Psi G\theta\rho(D+D_\alpha)\nabla c\cdot\nabla Y_\alpha \,\mathrm{d}V') \\ - \frac{\partial^2}{\partial\eta^2}(\int_V \Psi G\theta\rho Y_\alpha N_\xi \,\mathrm{d}V') - \frac{\partial^2}{\partial\zeta^2}(\int_V \Psi G\theta\rho Y_\alpha N_c \,\mathrm{d}V') \\ - 2\frac{\partial^2}{\partial\eta\partial\zeta}(\int_V \Psi G\theta\rho Y_\alpha N_{\xi c} \,\mathrm{d}V') \\ + \int_V \Psi G\theta\rho\dot{\omega}_\alpha \,\mathrm{d}V' - \frac{\partial}{\partial\zeta}(\int_V \Psi G\theta\rho\dot{\omega}_c^* \,\mathrm{d}V') + \int_V \Psi G\rho Y_\alpha\Pi \,\mathrm{d}V' \\ + \int_V \Psi G\rho Y_\alpha\hat{V}_\alpha \,\mathrm{d}V' - \frac{\partial}{\partial\eta}(\int_V \Psi G\rho S_\xi^- \,\mathrm{d}V') - \frac{\partial}{\partial\zeta}(\int_V \Psi G\rho S_c^- \,\mathrm{d}V')\end{aligned} \tag{A.12}$$

Using the definitions of the conditional filter operations, and the phase-weighted and density weighted FDF, the LES-filtered PDF transport equation and LES-filtered

DCMC equation take the same form as Eqns 3.37 and 3.39 respectively. Further operations carried out in Section 3.3 are identical in both cases. Thus, the derivation of the DCMC equation in the LES-framework leads to the same result as obtained in Section 3.3 (Eqn. 3.49) and for the $Q_h$ equation (Eqn. 3.57).

## A.3 Summary

This Appendix gave details about the derivation of the DCMC equation in an LES-framework. The conditional filtering procedures were introduced, analogue to averaging-procedures presented in Section 3.3. It was shown that the LES-filtered DCMC equation takes the same form as the equation derived in Section 3.3, if the LES-filter commutes with differentiation in time and space.

# Appendix B

# DCMC Equation with an Alternative Progress Variable

## B.1 Introduction

For the purpose of generality, in this Appendix we present the DCMC-0D equation where the boundaries at $\zeta = 0$ and 1 are not fixed to the mixing line and the equilibrium composition respectively, but are left to evolve in time and space. This extension may be useful in flames with non-adiabatic effects or cases where the equilibrium composition is not representative.

## B.2 Derivation

Alternatively to a general definition of reaction progress variable by Bray et al. [2005], a progress variable can be defined relative to burned composition that is only valid locally and at a given time instant. Note that this is not a reaction progress variable in the common sense, since 1 does not necessarily represent fully burnt mixture. To avoid confusion we denote it as $c^\dagger$ defined as,

$$c^\dagger(\mathbf{x},t) = c^\dagger_\psi(\xi(\mathbf{x},t), Y_\psi(\mathbf{x},t); x, t) = \frac{Y^0_\psi(\xi(\mathbf{x},t);\mathbf{x},t) - Y_\psi(\mathbf{x},t)}{Y^0_\psi(\xi(\mathbf{x},t);\mathbf{x},t) - Y^1_\psi(\xi(\mathbf{x},t);\mathbf{x},t)} \tag{B.1}$$

where $Y^0_\psi$ and $Y^1_\psi$, denoting the composition for $c^\dagger = 0$ and 1 respectively, are allowed to change in time and space.

The transport equation for $c^\dagger$, ignoring spray terms for simplicity, is

$$\begin{aligned}\frac{\partial \theta\rho c^\dagger}{\partial t} + \nabla\cdot(\theta\rho c^\dagger \mathbf{u}) = \nabla\cdot(\theta\rho D_c \nabla c^\dagger) \\ + \frac{\theta\rho}{\partial Y_\psi/\partial c^\dagger}\left[\dot\omega_\psi + N_\xi\frac{\partial^2 Y_\psi}{\partial\xi^2} + 2N_{\xi c}\frac{\partial^2 Y_\psi}{\partial\xi\partial c^\dagger} + N_c\frac{\partial^2 Y_\psi}{\partial c^{\dagger 2}}\right] \\ - \frac{\rho}{\partial Y_\psi/\partial c^\dagger}\left[\mathbf{u}\cdot\nabla Y_\psi + \frac{\partial Y_\psi}{\partial t}\right]\end{aligned} \tag{B.2}$$

Since $c^\dagger$ evolves linearly between $Y^0_\psi = Y_\psi|_{c=0}$ and $Y^1_\psi = Y_\psi|_{c=1}$,

$$\frac{\partial Y_\psi}{\partial t} = c^\dagger\frac{\partial Y_\psi}{\partial t}\Big|_{c^\dagger=1} + (1-c^\dagger)\frac{\partial Y_\psi}{\partial t}\Big|_{c^\dagger=0} \tag{B.3}$$

$$\nabla Y_\psi = c^\dagger\nabla Y_\psi\Big|_{c^\dagger=1} + (1-c^\dagger)\nabla Y_\psi\Big|_{c^\dagger=0} \tag{B.4}$$

The apparent reaction rate then becomes,

$$\begin{aligned}\dot\omega^\dagger_c = \frac{1}{\partial Y_\psi/\partial c^\dagger}\left[\dot\omega_\psi + N_\xi\frac{\partial^2 Y_\psi}{\partial\xi^2} + 2N_{\xi c}\frac{\partial^2 Y_\psi}{\partial\xi\partial c^\dagger} + N_c\frac{\partial^2 Y_\psi}{\partial c^{\dagger 2}}\right] \\ - \frac{\rho}{\partial Y_\psi/\partial c^\dagger}\left[\mathbf{u}\cdot\nabla Y_\psi + \frac{\partial Y_\psi}{\partial t}\right]\end{aligned} \tag{B.5}$$

Re-deriving the DCMC equation for this new definition of $c^\dagger$, it remains unchanged, except for $\dot\omega^*_c$ being replaced by $\dot\omega^\dagger_c$. In order to show the changes to the DCMC equation we consider the simple case of DCMC-0D and focus on temporal variations.

$$\begin{aligned}\frac{\partial Q_\alpha}{\partial t} &= \langle N_\xi|\eta,\zeta\rangle\frac{\partial^2 Q_\alpha}{\partial\eta^2} + 2\langle N_{\xi c}|\eta,\zeta\rangle\frac{\partial^2 Q_\alpha}{\partial\eta\partial\zeta} + \langle N_c|\eta,\zeta\rangle\frac{\partial^2 Q_\alpha}{\partial\zeta^2} \\ &- \frac{\partial Q_\alpha}{\partial\zeta}\frac{1}{\partial Q_\psi/\partial\zeta}\left[\langle N_\xi|\eta,\zeta\rangle\frac{\partial^2 Q_\psi}{\partial\eta^2} + 2\langle N_{\xi c}|\eta,\zeta\rangle\frac{\partial^2 Q_\psi}{\partial\eta\partial\zeta} + \langle N_c|\eta,\zeta\rangle\frac{\partial^2 Q_\psi}{\partial\zeta^2}\right] \\ &+ \langle\dot\omega_\alpha|\eta,\zeta\rangle - \frac{\partial Q_\alpha}{\partial\zeta}\frac{1}{\partial Q_\psi/\partial\zeta}\langle\dot\omega_\psi|\eta,\zeta\rangle \\ &- \frac{\partial Q_\alpha}{\partial\zeta}\frac{1}{\partial Q_\psi/\partial\zeta}\frac{\partial Q_\psi}{\partial t}\end{aligned} \tag{B.6}$$

where

$$\frac{\partial Q_\psi}{\partial t} = \zeta\frac{\partial Q_\psi}{\partial t}\Big|_{\zeta=1} + (1-c)\frac{\partial Q_\psi}{\partial t}\Big|_{\zeta=0} \tag{B.7}$$

Solving this equation the Dirichlet boundary conditions at $\zeta = 0$ and 1 can be replaced by the boundary conditions imposing $\partial Q_\alpha/\partial\zeta = 0$ and $\partial^2 Q_\alpha/\partial\zeta^2 = 0$.

## B.3 Summary

The DCMC equation was re-derived using an alternative definition of the reaction progress variable, which is not normalised by constant mixing line and equilibrium composition, but instead allows for a time and space dependent normalisation. This allows to relaxes the assumption of constant Dirichlet boundary conditions at $\zeta = 0$ and 1, which could be necessary, for instance, in non-adiabatic cases.

# Appendix C

# Assessment of DCMC Operator Splitting Errors

## C.1 Introduction

In this Appendix the operator splitting procedure of the DCMC solver is assessed. The operator splitting procedure is described in Section 4.5. In the first sub-step the transport in physical space is solved, in the second sub-step the transport in conditional space is integrated and in the third sub-step the chemical reaction is computed.

In this Appendix only the second and third sub-steps are assessed using DCMC-0D. In Chapter 7 it is shown that gradients of the conditional means in physical space are small and the convective transport terms do not play an important role in the balance of terms in the DCMC equation. Therefore, it can be expected that the first sub-step does not contribute strongly to the total splitting errors.

## C.2 Approach

In conventional CMC, the accuracy of operator splitting is often assessed using the auto-ignition delay or the critical SDR leading extinction. Conversely, in DCMC ignition and extinction transients are parametrised by the second conditioning variable Kronenburg [2004], and temporal variations of the doubly-conditional moments are gradual and much smaller than in conventional CMC. As a result, ignition/extinction events cannot be identified as a strong transient of the doubly-conditional flame structure, and a different strategy needs to be used.

In order to assess the operator splitting errors, the step response of the DCMC-0D to a change of the SDR is investigated. Operator splitting errors are decrease for smaller time steps. The standard DCMC time step used in the present work was $\Delta t_1 = 10^{-6}$ s. Splitting errors are assessed by comparing against computations with the smaller time step $\Delta t_2 = 10^{-7}$ s. The initial conditional is the steady-state solution for DCMC-0D presented in Section 5.3 with $\langle N_\xi|\eta,\zeta\rangle = 2 \times G_\xi$ and $\langle N_c|\eta,\zeta\rangle = N_c^0$ (Fig 5.3, left).

The following metric is defined

$$\Delta Q = Q_{\Delta t_1} - Q_{\Delta t_2} \tag{C.1}$$

where $Q_{\Delta t_1}$ is the conditional moment computed with $\Delta t_1 = 10^{-6}$ $s$, and $Q_{\Delta t_2}$ with $\Delta t_2 = 10^{-7}$ $s$. Assuming that splitting errors is much smaller in the case of $\Delta t_2$, $\Delta$ provides an estimate of the operator splitting error.

## C.3 Results

Figure C.1 (left) shows responses to several step changes of $\langle N_c|\eta,\zeta\rangle$, alternating between $1 \times N_c^0$ and $2 \times N_c^0$; Fig. C.1 (right) shows response to step changes of $\langle N_\xi|\eta,\zeta\rangle$ between $2 \times G_\xi$ and $20 \times G_\xi$. These values of the SDRs correspond to the states studied in Fig. 5.4.

The conditional reaction rate is used in this comparison because it is most sensitive to changes of the SDR. For the smaller time step, and consequently lower splitting errors, a slightly slightly higher conditional reaction rate is achieved. The evolution of $\max(\langle\dot{\omega}_c|\eta,\zeta\rangle)$ is very similar for both time steps; the difference is less than 2 %. It is notable that the operator-splitting error during the transient is comparable to the error in the steady state. This is confirmed by the time-evolution of $\max(\Delta\langle\dot{\omega}_c|\eta,\zeta\rangle)$, which measures the largest difference between the conditional reaction rate obtained for both time steps. Therefore, it provides an upper limit for the error of the mean (or filtered) values of the reaction rate and temperature. Furthermore, the evolution of $\max(\Delta\langle\dot{\omega}_c|\eta,\zeta\rangle)$ shows that the operator-splitting error is stable and does not increase in time.

Figure C.2 shows the effect of the operator-splitting error in doubly-conditional space for the reaction rate and the temperature. The local relative error, $\Delta Q_T/Q_T$, is less than 2 % in the entire conditional space. Local relative errors for $\langle\dot{\omega}_c|\eta,\zeta\rangle$ are larger in certain regions up to 2.5 %. The local OS error $\Delta\langle\dot{\omega}_c|\eta,\zeta\rangle$ seems to be strongly

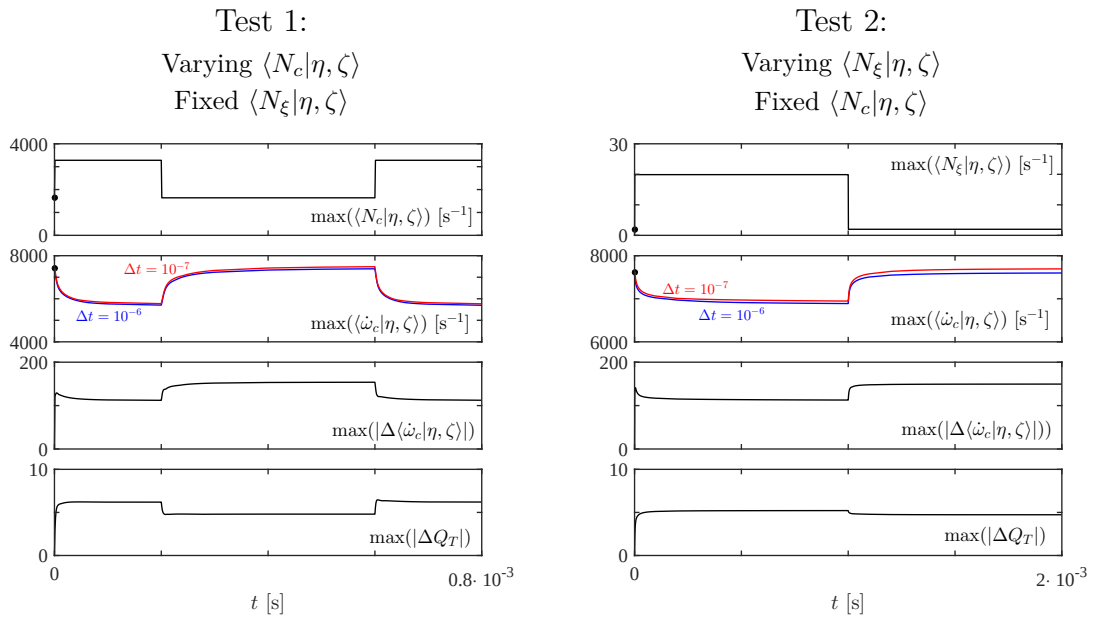


Fig. C.1 Effect of the time step on the step response of DCMC-0D for changes of $\langle N_c|\eta,\zeta\rangle$ (left) and $\langle N_\xi|\eta,\zeta\rangle$ (right). The black dot marks the initial value.

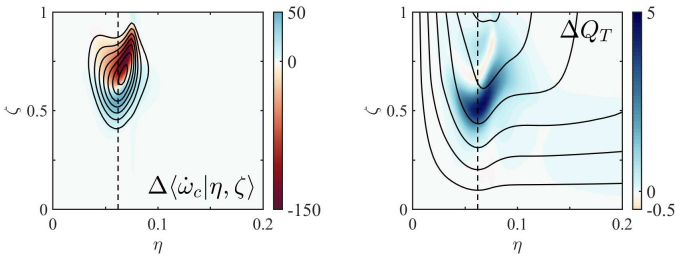


Fig. C.2 Estimate of the OS error $\Delta$ for the conditional reaction rate and temperature for computations with $\Delta t = 10^{-6}$ and $10^{-7}$ s. Instantaneous values for test 1 (Fig. C.1), $t = 0.4 \cdot 10^{-3}$ s. The surface plot for $\Delta$ is overlaid with contour lines of the conditional variable itself. Contour lines are spaced in steps of 1000 s$^{-1}$ for $\dot{\omega}_c$ and 300 K for $T$.

related to the conditional reaction rate $\langle\dot{\omega}_c|\eta,\zeta\rangle$ itself. The error has a positive sign where $\partial\langle\langle\dot{\omega}_c|\eta,\zeta\rangle/\partial\zeta > 0$ and is negative where $\partial\langle\langle\dot{\omega}_c|\eta,\zeta\rangle/\partial\zeta < 0$. This may suggest that the first-order scheme used for $\partial Q/\partial\zeta$ contributes strongly to the OS errors.

## C.4 Summary and discussion

The operator splitting error of the DCMC solver were investigated. In DCMC, operator splitting is essential due to the large number of nodes required for the discretisation of the doubly-conditional space. It was shown that the OS strategy employed in this work kept the OS error bounded at approximately 2 %. The findings of this study suggest that the advective term in progress variable space, $\langle\dot{\omega}_c|\eta,\zeta\rangle\ \partial Q_\alpha/\partial\zeta$, contributes strongly to the OS error.

The accuracy demonstrated for the OS strategy is sufficient for the stable test flames studied in the present work. For LES-DCMC (Ch. 7) it was shown that the temporal fluctuations were weak. For flames with strong transient behaviour, the OS strategy should be re-evaluated. Potentially, a fractional step or different splitting strategy are necessary.

# Appendix D

# SGS Effects of Spray Evaporation

## D.1 Introduction

In this Appendix, the modelling of the effect of droplet evaporation on the sub-grid scale (SGS) variance of mixture fraction is assessed. The correct prediction of the SGS variance of mixture fraction is essential for all presumed PDF methods. In LES of single-phase flows the SGS variance is often modelled, assuming local equilibrium of production and dissipation [Pierce & Moin, 1998].

In two-phase flows, the mixture fraction is also generated by evaporation. Unresolved scalar gradients around the droplet and their interaction with the unresolved scales of turbulence leads to an additional source of SGS variance. The SGS variance equation of mixture fraction in a dilute two-phase flow is

$$\begin{aligned}\frac{\partial\bar{\rho}\widetilde{\xi''^2}}{\partial t}+\nabla\cdot(\bar{\rho}\tilde{\mathbf{u}}\widetilde{\xi''^2}) = \nabla\cdot\left(\bar{\rho}(D_T+\bar{D})\nabla\widetilde{\xi''^2}\right)\\ +2\bar{\rho}(D_T+\bar{D})\nabla\tilde{\xi}\cdot\nabla\tilde{\xi}-2\bar{\rho}\widetilde{N}_\xi\\ +2\bar{\rho}\left(\widetilde{\xi\Pi}-\tilde{\xi}\widetilde{\Pi}\right)-\bar{\rho}\left(\widetilde{\xi^2\Pi}-\tilde{\xi}^2\widetilde{\Pi}\right)\end{aligned} \tag{D.1}$$

Two spray source terms appear in the third line. In most LES of two-phase flows, the effect of these source terms is not considered, e.g. Apte et al. [2009], Chrigui et al. [2012] and Ukai et al. [2013].

In an *a priori* study Pera et al. [2006] found a significant effect of the spray evaporation on the SGS variance of mixture fraction, and developed an algebraic model, based on the assumption of local equilibrium,

$$2\bar{\rho}D_T\nabla\tilde{\xi}\cdot\nabla\tilde{\xi}-2\bar{\rho}\widetilde{N}_{\xi,\mathrm{sgs}}+2\bar{\rho}\left(\widetilde{\xi\Pi}-\tilde{\xi}\widetilde{\Pi}\right)=0 \tag{D.2}$$

where the SDR was modelled as $\widetilde{N}_\xi = \bar{D}\nabla\xi \cdot \nabla\xi + \widetilde{N}_{\xi,\mathrm{sgs}}$ with the SGS contribution $\widetilde{N}_{\xi,\mathrm{sgs}} \propto (\Delta^2/\nu_T)\widetilde{\xi''^2}$ (Eqn. 4.61), and the second spray source term was neglected. This leads to the following algebraic model for the SGS variance

$$\widetilde{\xi''^2} \propto \Delta^2 \nabla\tilde{\xi} \cdot \nabla\tilde{\xi} + 2\left(\widetilde{\xi\Pi} - \tilde{\xi}\widetilde{\Pi}\right)\frac{\Delta^2}{\nu_T} \tag{D.3}$$

The spray term was modelled as $(\widetilde{\xi\Pi} - \tilde{\xi}\widetilde{\Pi}) \propto \widetilde{\xi''^2}(\widetilde{\Pi}/\tilde{\xi})$ following the suggestion by Hollmann & Gutheil [1996].

More recently, De & Kim [2013], Tyliszczak et al. [2014] and Giusti & Mastorakos [2017] considered the effect of spray evaporation on the SGS variance, including the source terms in the transport equation for the SGS variance. De & Kim [2013] observed significantly higher SGS variance when the spray source terms were included, and a necessity for a higher SDR model constant to balance the addition variance source. Giusti & Mastorakos [2017] pointed out that both spray terms need to be considered since they may be of comparable size[1].

De & Kim [2013] closed the spray source terms with an exact relation, similar to the model suggested by Demoulin & Borghi [2000]. A similar approach was also followed by Tyliszczak et al. [2014] and Giusti & Mastorakos [2017], who modelled the spray term as

$$\widetilde{\xi\Pi} = \langle\xi_s\rangle\widetilde{\Pi}, \qquad \widetilde{\xi^2\Pi} = \langle\xi_s\rangle^2\widetilde{\Pi} \tag{D.4}$$

where $\xi_s$ is the mixture fraction at the droplet surface, which can be approximated by the fuel mass fraction at the droplet surface.

In simulations presented in Chapter 7, the spray effect on the SGS variance was not included. In this Appendix, the effect of the spray terms on the case considered in Chapter 7 is considered. For this investigation, the LES is performed using a space and time-invariant two-dimensional manifold is used as a SGS combustion model (see Section 7.4.4). Other simulation settings are as detailed in 7.

## D.2 Case 1

First, the case is investigated, where the spray source terms are included in the SGS variance equation, while the standard linear relaxation model for $N_{\xi,\mathrm{sgs}}$ (Eqn. 4.61) is used – this corresponds to the configuration used by Giusti & Mastorakos [2017].

[1] A. Giusti: personal communication, 20 August 2018

Fig D.1 (top) shows the results of the simulation. The flame structure is substantially changed compared to the results in Chapter 7. Instantaneous and time-averaged OH mass fraction does not exhibit two branches any more. Instead, the whole flame is filled with varying mass fraction of OH, but the level is much lower. The agreement with the experimental observation is significantly worsened compared to the results obtained without the additional spray terms.

The difference between the present case and the study by Giusti & Mastorakos [2017], who successfully included the spary source term, is the level of turbulence in the region where evaporation takes place. In the previous studies, the level of turbulence was high and the linear relaxation model, $N_{\xi,\mathrm{sgs}} \sim \widetilde{\xi''^2}/\tau_T$, dissipated the variance produced by the spray terms. In the present case, the droplet also evaporate in quasi-laminar flow, where the linear relaxation model predicts close-to-zero SDR and cannot counter-balance the source term.

## D.3 Case 2

A second simulation with spray source terms included is performed. Instead of the standard linear relaxation model, the following *ad hoc* correction is introduced,

$$\widetilde{N_\xi} = \bar{D}\nabla\tilde{\xi}\cdot\nabla\tilde{\xi} + \frac{1}{2}\max\left(C_{NT}\frac{\mu_{\mathrm{sgs}}}{\Delta^2}, C_{NL}\frac{\bar{\mu}}{\Delta^2}\right)\widetilde{\xi''^2} \tag{D.5}$$

where $C_{NT} = 42$, and for the purpose of this demonstration $C_{NL} = 1$.

This model reflects that in absence of turbulent mixing, small-scale scalar fluctuations are still dissipated by molecular diffusion. To consider this effect a second time scale is introduced $\propto \Delta^2/\bar{\mu}$, beside the turbulent eddy turn-over time, $\Delta^2/\mu_{\mathrm{sgs}}$, in the standard linear relaxation model. In the modified SDR model, the minimum of the two time scale is chosen. This ensures that in a turbulent flow the correction for molecular diffusion is without effect. Only when turbulent time scale is longer than the molecular time scale this correction starts to act. A correction of this type was first used by De & Kim [2013].

Figure D.1 shows the results, in comparison to the Case 1. The SGS variance is higher than in the LES-DCMC simulation in Ch. 7, but lower than in the case without modified SDR model. The LES results show the characteristic flame shape with an outer and an inner flame branch observed in the experiment and in Ch. 7. At the same time, the lift-off height is slightly increased compared to Ch. 7. This could be due to

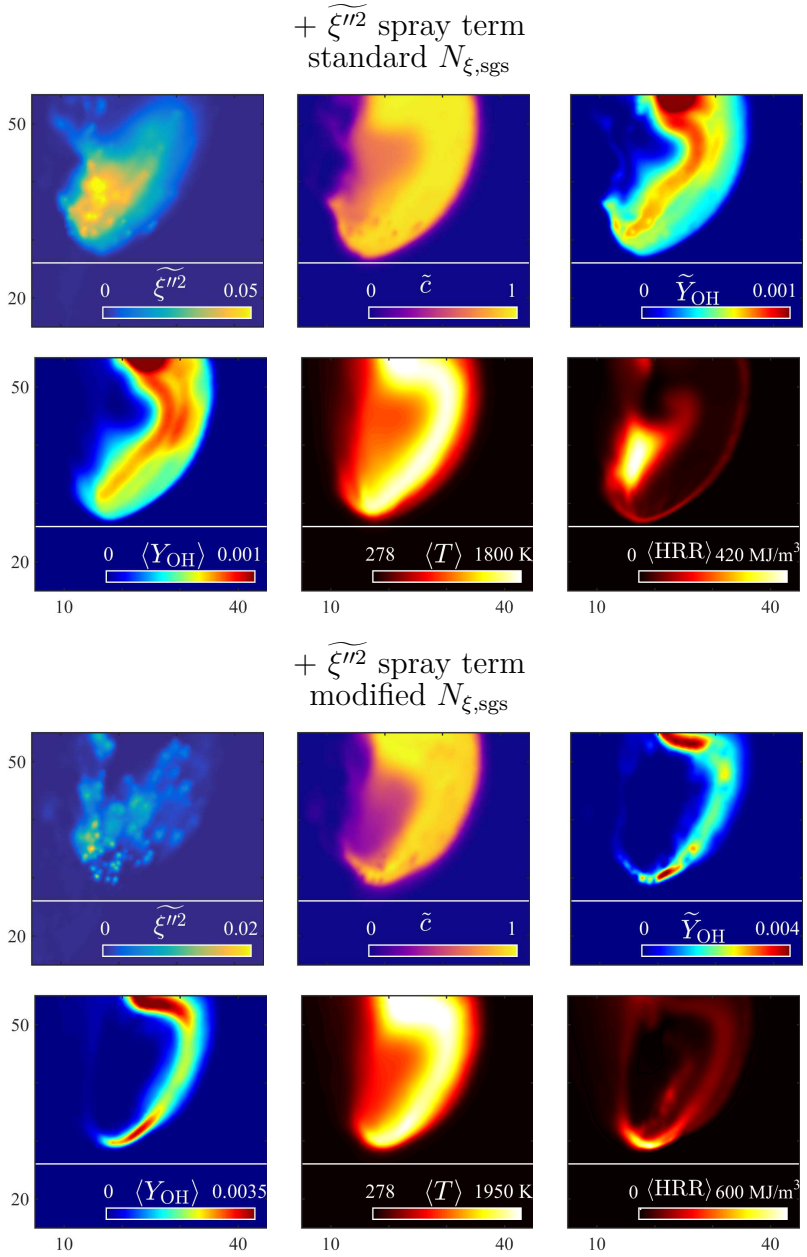


Fig. D.1 Comparison of results with the $\widetilde{\xi''^2}$ spray source term. The white horizontal line indicates the lift-off obtained with LES-DCMC in Ch. 7.

the slower heating of the droplets at contact with the flame, caused by the increased SGS variance and lower temperature in the near field of the droplets.

## D.4 Summary and discussion

In this Appendix the effect of spray source terms in the transport equation of the SGS variance of mixture fraction was investigated. In general the SGS variance of mixture fraction impacts on the flame in two ways: (i) direct effects of the variance are related to the PDF and impact on the resolved temperature, species and reaction rate, and (ii) indirect effects of the variance on the SDR and from the SDR on the flame structure. Using LES with constant flame structure, effects of the second type cannot be investigated in this Appendix. These effect would crucial, for instance, for the correct prediction of extinction and require the online solution of the flame structure, but are not in the scope of the present investigation.

The present study found increased levels of SGS variance due to the inclusion of the spray source terms. The standard linear relaxation model for $N_{\xi,\mathrm{sgs}}$ was found to be insufficient to balance the production of variance in the case of low-intensity turbulence. An *ad hoc* correction was suggested. The modified SDR model considering the time scale of molecular mixing, besides the eddy turn-over time. Using the modified SDR model reasonable results were achieved, but the lift-off height increased slightly.